Transport Properties of Thermoelectric Materials Displaying Structural Phase Transition

by

Müjde Yahyaoğlu

A Dissertation Submitted to the
Graduate School of Sciences and Engineering
in Partial Fulfillment of the Requirements for
the Degree of

Doctor of Philosophy

in

Materials Science and Engineering

KOÇ ÜNİVERSİTESİ

May 25, 2023

Transport Properties of Thermoelectric Materials Displaying Structural Phase Transition

Koç University

Graduate School of Sciences and Engineering

This is to certify that I have examined this copy of a doctoral dissertation by

Müjde Yahyaoğlu

and have found that it is complete and satisfactory in all respects,
and that any and all revisions required by the final
examining committee have been made.

Committee Members:

Assoc. Prof. Umut Aydemir (Advisor)

Assoc. Prof. Uğur Ünal

Prof. Sedat Ballikaya

Asst Prof. Safacan Kölemen

Asst. Prof. Enes Kılınç

Date: May 25, 2023

To my lovely family…

ABSTRACT

Transport Properties of Thermoelectric Materials Displaying Structural Phase Transition

Müjde Yahyaoğlu

Doctor of Philosophy in Materials Science and Engineering

May 25, 2023

Developing renewable, sustainable, and environmentally friendly energy conversion technologies is essential to overcome the current and upcoming energy crisis. The inefficient utilization of energy resources results in the wastage of over 65% of the energy produced globally in the form of heat. Recovering waste heat has emerged as a promising solution to support global energy sustainability via thermoelectric (TE) materials due to their ability to convert heat into electricity or be used as vibration- and noise-free solid-state coolers with no-moving parts without hazardous gas emissions. The thermoelectric efficiency depends on the dimensionless thermoelectric figure of merit $zT = S^2\sigma T/\kappa$, where S, σ, T, and κ are the Seebeck coefficient, electrical conductivity, absolute temperature, and total thermal conductivity, respectively. Achieving optimum values of zT in thermoelectric materials is a complex and challenging task due to the transport properties' interdependence. This study investigates synthesis, characterization, and thermoelectric transport properties of phase-changing binary copper chalcogenides ($Cu_{3-x}Te_2$ and Cu_2Se) and Li_3Sb, along with a study on the p-type half-Heusler compound, NbCoSn.

The synthetic rickardite mineral samples, $Cu_{3-x}Te_2$ (x = 0.2 & 0.1) were successfully synthesized by solid-state synthesis method. Differential Scanning Calorimetry (DSC) analysis revealed that both compositions undergo mainly two main phase transitions at approximately 458 K and 647 K. The high-temperature X-ray diffraction (XRD) measurements done at 300, 473, and 673 K shows that the transitions were confirmed as the following order orthorhombic ↔ tetragonal ↔ hexagonal phases. The effect of these phase transitions was investigated on the electronic and thermal transport properties, revealing that the first transition had minimal effect on the transport data while the second phase transition resulted in a transition from metallic-like to semiconducting-like properties accompanied by a substantial increase in the electrical resistivity and thermopower values, as well as significant decrease in the thermal conductivity values. When these parameters are combined, the higher temperature phase has improved thermoelectric performance compared to the lower temperature phases.

In order to optimize the carrier concentration and study the effect of substitution on phase transition temperatures, a detailed study was performed on Zn- and Ag-substitution on $Cu_{2.9}Te_2$ with the compositions of $M_xCu_{2.9-x}Te_2$. The XRD analysis showed that the targeted phases were obtained with impurities of binaries with increasing substitution amount. Microstructure analysis revealed that all the $Cu_{2.9}Te_2$ samples show strong orientation contrast under the polarized light. A more inhomogeneous grain size distribution was observed for Zn-substituted samples while more homogenous distribution was revealed for Ag-substituted samples. The DSC data showed that all the

compositions displayed the same phase transitions with shifts in their T_{onset}. Zn-substitution had minimal influence on the phase transition temperature while the Ag-substitution had more noticeable effect, resulting in a decrease in the transition temperature with increasing substitution amount. Consequently, the transport properties around the phase transitions were affected by the shifts in the transition temperature via Zn- and Ag-substitution.

Cu_2Se is a widely studied binary copper chalcogenide material in thermoelectrics due to its promising thermoelectric performance at mid-temperatures. Various approaches have been applied to modify the electronic structure and thermal conductivity of Cu_2Se via doping. Herein, two different synthesis approaches have been applied to produce Cu_2Se, hydrothermal and solid-state synthesis methods. The aim of this study is to investigate the effect of nano-B or C-coated nano-B incorporation as a light and non-toxic element into the Cu_2Se compound. The incorporation was done via high-energy ball milling, which lead to an increase in the resistivity values over the entire temperature range. Overall, the thermoelectric efficiency could not be improved due to the higher resistivity values compared to a slight increase in Seebeck coefficient values.

The thermoelectric potential of c-Li_3Sb synthesized by the high-energy ball milling method was evaluated in this study, and the stress/pressure-induced phase transition has been observed in this system, stabilizing the metastable c-Li_3Sb phase at low temperatures. The phase change was observed from h-Li_3Sb to c-Li_3Sb under two different conditions: ball milling and applying low axial pressures. The transport properties of c-Li_3Sb exhibited a degenerate semiconducting behavior characterized by low resistivity values and moderate Seebeck coefficients. The total thermal conductivity values decreased to relatively low values. Despite its favorable electrical and thermal properties, besides its lightweight nature, the air sensitivity of Li_3Sb poses a challenge for its implementation in thermoelectric energy harvesting applications, requiring the design of airtight systems.

A systematic study on synthesizing and addressing the poor thermoelectric performance of the desired p-type NbCoSn material was implemented by a one-step arc-melting synthesis method and explored the effects of Co-deficiency and Zr-substitution on the Nb site. The study aimed to improve the thermoelectric performance of the p-type NbCoSn material by carefully controlling Co-deficiency and introducing Zr-substitution to optimize its electronic and structural properties. The results demonstrate that Zr-substitution is a more effective approach than Co-deficiency in improving the thermoelectric properties of the main phase without altering its composition.

.

ÖZETÇE

Yapısal Faz Geçişi Gösteren Termoelektrik Malzemelerin Taşınım Özellikleri

Müjde Yahyaoğlu

Malzeme Bilimi ve Mühendisliği, Doktora

25 Mayıs 2023

Yenilenebilir, sürdürülebilir ve çevre dostu enerji dönüştürme teknolojilerinin geliştirilmesi, mevcut ve yaklaşmakta olan enerji krizinin üstesinden gelmek için çok önemlidir. Enerji kaynaklarının verimsiz kullanımı, küresel olarak üretilen enerjinin %65'inden fazlasının ısı şeklinde israf olmasına neden olur. Atık ısının geri kazanılması, ısıyı elektriğe dönüştürme veya titreşimsiz ve gürültüsüz, tehlikeli gaz emisyonları olmayan, hareketli parçaları olmayan katı hal soğutucuları olarak kullanılma yetenekleri nedeniyle termoelektrik (TE) malzemeler aracılığıyla küresel enerji sürdürülebilirliğini desteklemek için umut verici bir çözüm olarak ortaya çıkmıştır. TE verimliliği, $zT = S^2\sigma T/\kappa$ 'nin, boyutsuz termoelektrik verimlilik katsayısına bağlıdır; burada S, σ, T ve κ sırasıyla Seebeck katsayısı, elektrik iletkenliği, mutlak sıcaklık ve toplam termal iletkenliktir. Termoelektrik malzemelerde optimum zT değerlerine ulaşmak, taşıma özelliklerinin birbirine bağlı olması nedeniyle karmaşık ve zorlu bir görevdir. Bu çalışma, faz değiştiren ikili bakır kalkojenitlerin ($Cu_{3-x}Te_2$ ve Cu_2Se) ve Li_3Sb'nin sentezi, karakterizasyonu ve termoelektrik taşınım özelliklerinin ayrıntılı bir araştırması ile birlikte p-tipi half-Heusler bileşiği NbCoSn üzerine bir araştırmadır.

Sentetik rikardit minerali olan $Cu_{3-x}Te_2$ (x = 0.2 & 0.1) bileşikleri, katı hal sentez yöntemiyle başarıyla sentezlenmiştir. Diferansiyel Taramalı Kalorimetri (DSC) analizi, her iki bileşimin de yaklaşık olarak 458 K ve 647 K'de iki ana faz geçişine sahip olduğunu ortaya çıkarmıştır. 300, 473 ve 673 K'de yapılan yüksek sıcaklıklı X-ışını kırınımı (XRD) ölçümleri, geçişlerin sırası ile ortorombik ↔ tetragonal ↔ hegzagonal fazlar olduğunu doğruladı. Bu faz geçişlerinin elektronik ve termal taşıma özellikleri üzerindeki etkisi araştırıldı ve ilk geçişin taşıma verileri üzerinde minimum etkiye sahip olduğu, ikinci faz geçişinin ise metalik benzeri özelliklerden yarı-iletken benzeri özelliklere geçişle sonuçlandığı ortaya çıktı. Bu ana faz geçişi, elektriksel direnç ve termogüç değerlerinde artış, ısıl iletkenlik değerlerinde ise önemli düşüşler meydana getirmiştir. Bu parametreler birleştirildiğinde, daha yüksek sıcaklık fazı, daha düşük sıcaklık fazlarına kıyasla daha iyi termoelektrik performansa sahiptir.

Taşıyıcı konsantrasyonunu optimize etmek ve Zn- ve Ag-ikamesinin faz geçiş sıcaklıkları üzerindeki etkisini incelemek için $M_xCu_{2.9-x}Te_2$ bileşikleri üzerine detaylı bir çalışma yapılmıştır. XRD analizi, hedeflenen fazların artan ikame miktarı ile ikili safsızlıklar ile elde edildiğini göstermiştir. Mikro yapı analizi, tüm $Cu_{2.9}Te_2$ numunelerinin polarize ışık altında güçlü yön kontrastı gösterdiğini ortaya koymuştur. Zn ikameli numunelerde daha homojen olmayan bir tane boyutu dağılımı gözlenirken, Ag ikameli olanlarda daha homojen bir dağılım gözlemlenmiştir. DSC verileri, tüm bileşimlerin T_{onset}'lerinde $Cu_{2.9}Te_2$ bileşiğindeki faz geçişine kıyasla kaymalar

sergilediğini gösterdi. Zn ikamesinin faz geçiş sıcaklığı üzerinde minimum etkisi olurken, Ag ikamesinin daha belirgin bir etkisi oldu ve artan ikame miktarı ile geçiş sıcaklığında belirgin bir düşüşe neden oldu. Sonuç olarak, faz geçişleri etrafındaki taşıma özellikleri, Zn- ve Ag-ikame yoluyla geçiş sıcaklığındaki kaymalardan etkilenmiştir.

Cu_2Se, orta sıcaklıklarda umut verici TE performansı nedeniyle yaygın olarak çalışılan bir ikili bakır kalkojenit malzemesidir. Cu_2Se'nin elektronik yapısını ve termal iletkenliğini katkılama yoluyla değiştirmek için çeşitli yaklaşımlar uygulanmıştır. Burada Cu2Se üretmek için hidrotermal ve katı hal sentez yöntemleri olmak üzere iki farklı sentez yaklaşımı uygulanmıştır. Bu çalışmanın amacı, nano-B veya C kaplı nano-B'nin hafif ve toksik olmayan bir element olarak Cu_2Se bileşiğine dahil edilmesinin etkisini araştırmaktır. Bu ekleme, yüksek enerjili bilyeli öğütme kullanılarak yapılmış olup, tüm sıcaklık aralığında özdirenç değerlerinde bir artışa yol açmıştır. Genel olarak, termoelektrik verim, Seebeck katsayısı değerlerindeki hafif bir artışa kıyasla daha yüksek özdirenç değerleri nedeniyle iyileştirilememiştir.

Li_3Sb ile ilgili çalışmada yüksek enerjili bilyeli öğütme yöntemiyle sentezlenen c-Li_3Sb'nin TE potansiyelini değerlendirmek üzere, düşük sıcaklıklarda yarı kararlı c-Li_3Sb fazını stabilize eden, stres/basınç kaynaklı bir faz geçişi gözlemlenmiştir. İki farklı koşul altında (bilyalı öğütme sentezi ve düşük eksenel basınç), hegzagonal yapıdan kübik yapıya bir faz değişimi gözlemlenmiştir. Li_3Sb'nin taşınım özellikleri ölçümleri, nispeten düşük özdirenç değerleri ve orta seviyede Seebeck katsayıları ile karakterize edilen dejenere bir yarı iletken davranışına sahip olduğunu göstermektedir. Buna ek olarak, termal iletkenlik değerleri nispeten düşük değerlere düşmüştür. Elverişli elektriksel ve termal özelliklerine rağmen, hafif yapısının yanı sıra, Li_3Sb'nin hava hassasiyeti, hava geçirmez sistemlerin tasarımını gerektiren TE enerji toplama uygulamalarında uygulanması için bir zorluk teşkil etmektedir.

Bu çalışmanın son kısmında ise, p-tipi NbCoSn malzemesinin sentezlenmesi ve zayıf TE performansının ele alınması üzerine sistematik bir çalışma gerçekleştirilmiştir. Sentez için tek adımlı bir ark eritme sentez yöntemi uygulanmış olup Co-eksikliği ve Nb bölgesine yapılan Zr-ikamesinin taşınım özelliklerine etkileri araştırıldı. Co-eksikliği ve Zr-ikamesi bağımsız bir şekilde dikkatli olarak kontrol edilerek, NbCoSn malzemesinin elektronik ve yapısal özelliklerini optimize edilmesi ve sonuç olarak p-tipi rejimde daha iyi bir termoelektrik performansa ulaşılması amaçlandı. Sonuçlar, Zr ikamesinin, bileşiğin termoelektrik özelliklerini geliştirmede Co-eksiklikten daha pratik bir yaklaşım olduğunu göstermektedir.

AKNOWLEDGEMENTS

I want to thank several people for helping and supporting me during my research. This thesis would not have been possible without their support in various ways.

First and foremost, I would like to thank my supervisor Assoc. Prof. Dr. Umut Aydemir for all his guidance and endless support. He provided me with opportunities and infinite freedom while encouraging and trusting me in my work.

I want to express my sincere thanks to my thesis committee members, Assoc. Prof. Dr. Uğur Ünal, Asst. Prof. Safacan Kölemen, Asst. Prof. Enes Kılınç and Prof. Dr. Sedat Ballıkaya for their valuable comments and help on my research.

I have received valuable assistance from many close collaborators who have made intellectual and experimental contributions to this research. Assoc. Prof. Christophe Candolfi shared his experience with Zintl research. He welcomed me to his research laboratories at Institut Jean Lamour to learn how to use many instruments while I was in my first year of study. I had a chance to work with Prof. G. Jeffrey Snyder in Northwestern University for three months, and I am grateful for all the scientific discussions, guidance and fun time I had in his research group. I want to thank Prof. Yuri Grin, Dr. Yurii Prots, and Dr. Ulrich Burkhardt from Max-Planck Institute CPfS for the collaborating on the main part of my thesis study. Dr. Prots helped us study the crystal structure of the materials and did high-resolution Synchrotron XRD measurements for us. Dr. Burkhardt helped me with the metallography part of this thesis study and WDS measurements. I would like to also thank KUYTAM, especially Dr. Barış Yağcı, for SEM and EDX analysis.

I would like to sincerely thank Prof. Mehmet Somer for his support throughout my B.Sc. and M.Sc. studies and for being a mentor for all these years. I thank all my group members, the KUBAM family, for the research environment and their friendly support

I am very lucky by having a lovely family and grateful for their never ending support. I am thankful to my parents, Yücel & Nebil Yahyaoğlu and my lovely sister, Ülkü Yahyaoğlu for being there for me whenever I need them.

I want to thank TÜBİTAK Bideb 2211/C National Ph.D. Scholarship Program in the Priority Fields in Science and Technology throughout my Ph.D. studies, Bideb 2214/A financial support for my visit to Northwestern University to accompolish a part of this thesis work, and Tübitak ARDEB for the financial support (grant no: 118M371).

TABLE OF CONTENTS

LIST OF TABLES

LIST OF FIGURES

ABBREVIATIONS

DSC	Differential Scanning Calorimetry
DTA	Differential Thermal Analysis
EDX	Energy Dispersive X-ray
HP	Hot Pressing
LFA	Laser Flash Apparatus
OM	Optical Microscopy
PF	Power Factor
PGEC	Phonon-Glass Electron-Crystal
PPM	Parts Per Million
PPMS	Physical Property Measurement System
RTG	Radioisotope Thermoelectric Generator
SEM	Scanning Electron Microscopy
SPS	Spark Plasma Sintering
SS	Solid-State
TE	Thermoelectric
TEG	Thermoelectric Generator
TG	Thermogravimetric Analysis
WDS	Wavelength Dispersive X-ray
XRD	X-ray Diffraction

CHAPTER 1

AN INTRODUCTION

The aim of this thesis study is to conduct a detailed investigation of synthesis, materials characterization, and thermoelectric transport properties of phase-changing binary copper chalcogenides ($Cu_{3-x}Te_2$ and Cu_2Se) and Li_3Sb along with another independent study carried out on the p-type half-Heusler compound; NbCoSn. The information about thermoelectric phenomena and the experimental methods & theoretical concepts were presented in **Chapter 2** and **Chapter 3**, respectively, before the detailed experimental study on $Cu_{3-x}Te_2$, Cu_2Se, Li_3Sb, and NbCoSn presented.

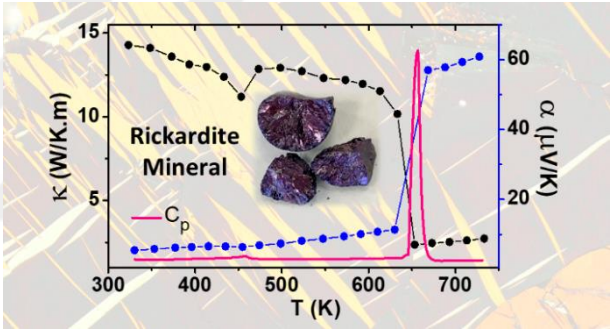

Chapter 4 details the investigation of synthetic polycrystalline rickardite, $Cu_{3-x}Te_2$ (x = 0.1 and 0.2), synthesized by a direct solid-state reaction. The effect of reversible phase transitions at 458 K, 640 K, and 647 K on electronic and thermal transport properties was investigated. These transitions were confirmed by combined analysis of high-temperature X-ray diffraction, differential scanning calorimetry, and specific heat measurements.

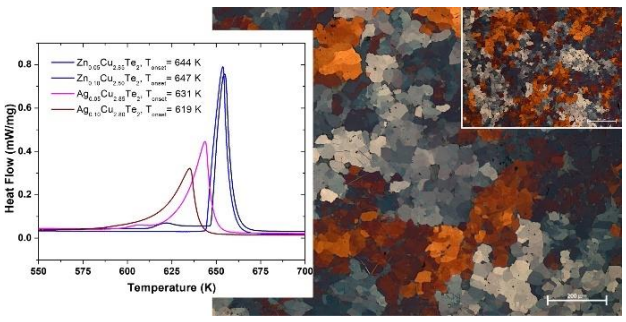

Chapter 5 includes the study of the effect of Zn- and Ag-substitution on the phase transition temperatures of $Cu_{2.9}Te_2$. With the substitution, the shifts in the transition temperatures and the effect on the transport properties were discussed, as well as the crystal structure and the microstructure analysis.

In **Chapter 6**, different synthesis methods, the optimization of Cu_2Se, and the effect of using light-weighted, non-toxic nano-Boron and C-coated nano-Boron incorporation into Cu_2Se and the thermoelectric performance were investigated in detail.

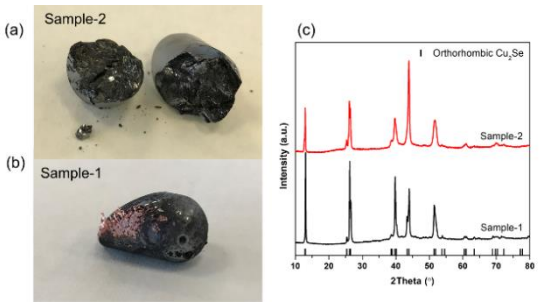

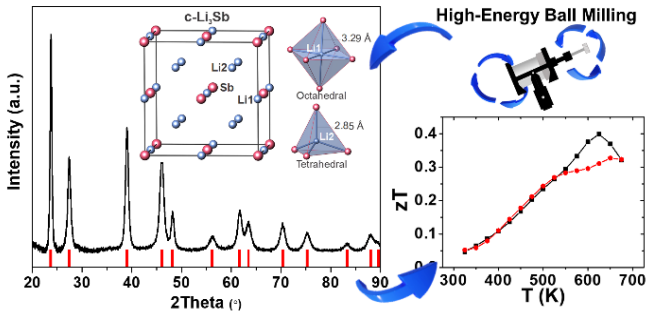

Chapter 7 discusses the thermoelectric potential of c-Li_3Sb, another phase change material. The transport property measurements of Li_3Sb synthesized by high-energy ball-milling were investigated at high temperatures. The discussion includes the phase change variables and their effect on transport properties.

Chapter 8 reports a systematic study of an effort to obtain p-type NbCoSn samples. Different compositions of NbCoSn with Co or Co/Sn deficiency and Zr-substitution on the Nb site were synthesized via the arc-melting method and a high-temperature annealing was applied. The transport properties of these compositions were investigated.

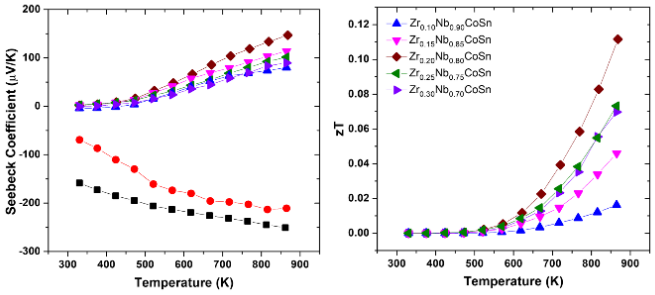

CHAPTER 2

THERMOELECTRIC THEORY AND LITERATURE REVIEW

2.1 Thermoelectric Concepts

The world is currently facing an unprecedented energy crisis, as the demand for energy continues to rise while our traditional sources of energy are depleting at an alarming rate. Fossil fuels, which have been the backbone of our energy production for decades, are not only finite but also contribute significantly to environmental degradation and climate change. As a result, developing renewable, sustainable, and environmentally friendly energy conversion technologies is a key challenge to overcome the upcoming energy crisis. In many studies, it is reported that more than 65 % of the global primary energy consumption is lost during combustion and heat transfer processes as waste heat [1]. Recovering the small fraction of this wasted heat will have high impact on sustainability and significant impact on global energy aspect. Thermoelectric (TE) materials may play an important role in the clean and sustainable energy solution landscape by converting waste heat into electricity and serving as vibration- and noise-free solid-state coolers because of their high reliability without hazardous gas emissions [2, 3]. As shown in Figure 2.1 [4], depending on the waste heat potential and the temperature range of the processes, the thermoelectric technology can be used to utilize the waste heat into useful electrical energy by choosing the best materials for the operation temperature range of the working environment that diversify in a wide range from 100 °C to 1000 °C [5].

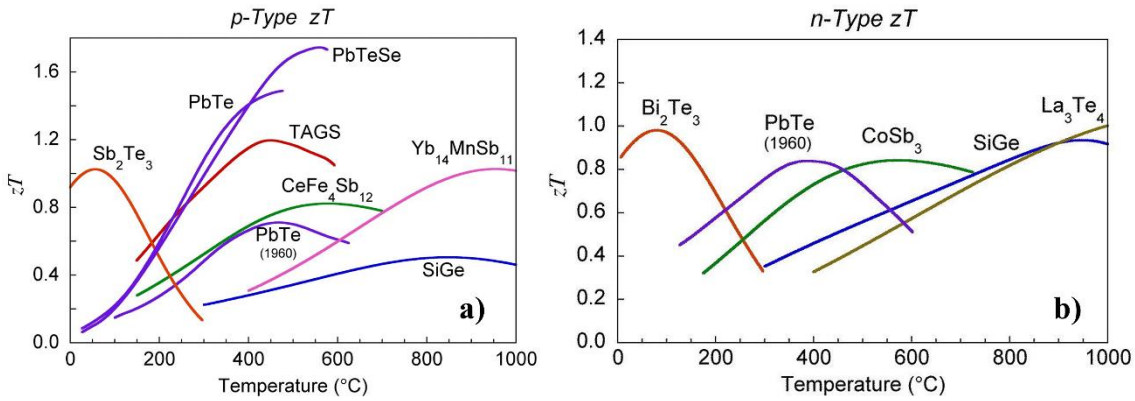

Figure 2.1 The *zT* figure of merit of a) p-type and b) n-type state-of-the-art commercial materials used in specific temperature range for thermoelectric power generation [5].

Even though the conversion efficiency of current thermoelectric devices is relatively low, one of their key advantages is the stable solid-state conversion process without the need for moving parts. These characteristics have made thermoelectric conversion systems which is historically used as radioisotope thermoelectric generators (RTGs) over 40 years, a preferred choice for powering deep space exploration missions since the 1960s when the sunlight is not an option for an energy source. RTGs utilize radioisotope materials, such as ^{238}Pu, as the heat source and outer space as the cold side to generate electrical energy through solid-state thermoelectric conversion, such as in Voyager. This technology has demonstrated the ability to provide sufficient power to space probes for extended periods of time, even lasting decades. The current RTGs, referred to as Multi-Mission Radioisotope Thermoelectric Generators, achieves a conversion efficiency of around 6 %. However, ongoing development efforts at NASA's Jet Propulsion Laboratory (JPL) aim to create the next generation of RTGs with significantly higher conversion efficiencies, reaching up to 15 %. These advancements hold promise for improving the energy output and performance of future deep space exploration missions [6]. In addition to this, thermoelectric materials have been used to make noise-free refrigerators with no moving parts [7], low power electronic devices such as sensors wearable electronics in medical applications [8] at lower temperatures.

The principle of the thermoelectricity is to use the charge carriers within the material for power generation or cooling applications for reverse process. For power generation, when a temperature gradient is applied to the one side of the material driving the majority carriers from hot side to the cold side, a voltage is generated. This phenomena is called the Seebeck effect, named after German physicist and the Seebeck coefficient, *S* is

defined as the amount of potential generated by the material as a result of a temperature gradient (Figure 2.2 a). On the other side, when an electrical field drives the majority charge carriers from cold side to the hot side, a thermal gradient is obtained along the material, this is called Peltier effect by Jean Peltier (Figure 2.2 b) [2, 9, 10].

In a typical thermoelectric device, both n-type and p-type elements are required to create thermoelectric couples, also known as legs shown in Figure 2.2. Many of these couples are connected electrically in series and thermally in parallel to construct a thermoelectric generator (TEG), a device [4]. A TEG uses the heat flow across the temperature gradient to generate power for an electric load through an external circuit. The temperature difference between hot and cold sides of the TEG generate a voltage throught the Seebeck effect while the heat flow drives the electrical current thus determining the overall power output of the TEG.

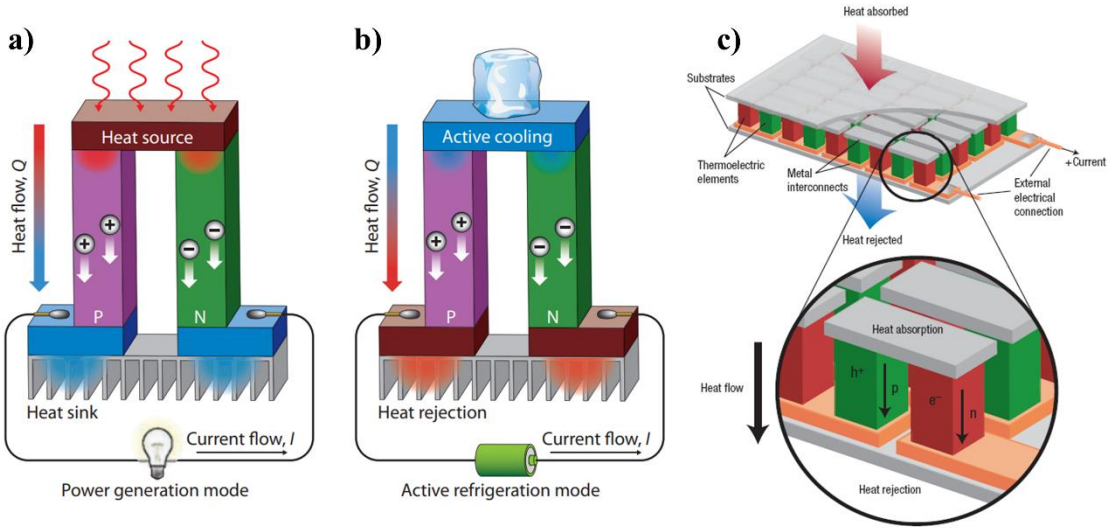

Figure 2.2 Schematic representation of a thermoelectric module for (a) power generation (Seebeck effect), (b) active refrigeration (Peltier effect) [10], and (c) a thermoelectric module [5].

The thermoelectric efficiency of a material is determined by the dimensionless thermoelectric figure of merit;

$$zT = \frac{S^2 \sigma T}{\kappa}$$

where *S*, T, ρ and κ are the Seebeck coefficient (or thermopower), absolute temperature, electrical resistivity, and total thermal conductivity, respectively [2, 4]. To maximize the

efficiency (*zT)* of a material, the numerator which is known as power factor, $PF = S^2\sigma$ should be maximized while minimizing the thermal conductivity. Because of interdepency of these variables, obtaining high zT is challenging. However, there are many reported high zT values through the optimization in both electronic and thermal properties [11-13].

The Seebeck coefficient (*S* or α, thermopower) is strongly correlated with carrier concentration;

$$S = \frac{8\pi^2 {k_B}^2}{3eh^2}\, m^* T \left(\frac{\pi}{3n}\right)^{2/3}$$

where k_B, *e*, *h*, m^*, and *n* is the Boltzman constant, electron charge, Planck constant, carrier effective mass, and carrier concentration, respectively [14]. As seen in the equation, the Seebeck coefficient increases with decreasing carrier concentration, however; the electrical conductivity decreases with decreasing carrier concentration as seen in the following equation;

$$\sigma = ne\mu$$

where *n*, *e*, and μ is the carrier concentration, electron charge, amd carrier mobility, respectively. In the meantime, increasing electrical conductivity lead to increased thermal conductivity as they are interdependent values by considering Wiedemann-Franz law;

$$\kappa_{tot} = \kappa_{elec} + \kappa_{lat}$$
$$\kappa_{elec} = \sigma L T$$

where κ_{tot}, κ_{elec}, κ_{lat}, *L*, and *T* is the total thermal conductivity, electronic thermal conductivity, lattice thermal conductivity, Lorenz constant, and temperature, respectively.

Figure 2.3 a) [15] demonstrates the dependency of Seebeck coefficient, electrical conductivity, and power factor as a function of carrier concentration. In order to obtain a high efficiency thermoelectric material, the optimization of power factor, PF ($S^2\sigma$) is important. Due to the interdepency of the Seebeck coefficient and the electrical conductivity, the optimized power factor can be achieved with carrier concentrations between 10^{19} – 10^{21} cm^{-3}. As seen in Figure 2.3 b) [15], thermal conductivity is also strongly associated with the carrier concentration due to the contribution of the charge

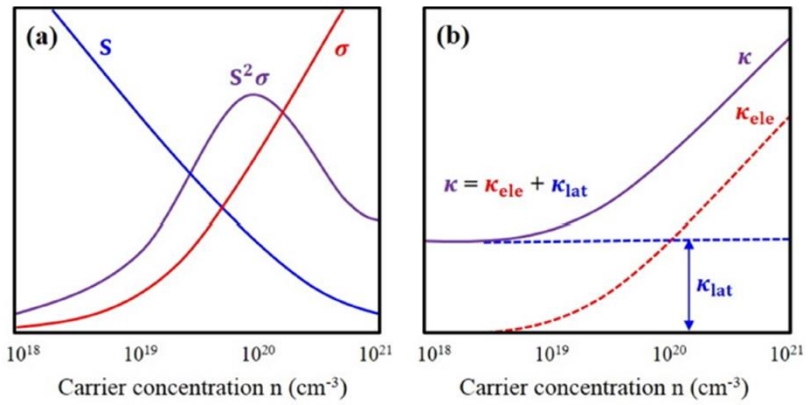

Figure 2.3 Schematic representation of dependency of a) Seebeck coefficient S, electrical conductivity σ, and power factor $S^2\sigma$, b) thermal conductivity as a function of carrier concentration [16].

carriers (electrons and holes) to the thermal conductivity and needs to be optimized for a higher efficiency thermoelectric material. The higher the σ, the higher the κ due to the higher κ_{elec} due to the Wiedemann-Franz law.

Designing thermoelectric materials that can simultaneously satisfy the combination of interdependent properties required for achieving high thermoelectric figure of merit (zT) is a challenging task. This process is not straightforward due to the complex nature of the relationships between different material properties. Up until now, many different studies such as nanostructuring, grain boundary scattering, band structure engineering, point defects, etc. have been implemented to enhance the thermoelectric efficiency by optimizing these interdependent parameters [16-20].

2.2 Phase Changing Cu-Chalcogenides

The phonon-glass electron-crystal (PGEC) concept has been proposed as a possible route to enhancing *zT* by decoupling the interdependent transport parameters. In PGEC materials, structural disorder is desired for achieving low lattice thermal conductivity (phonon-glass) while retaining its crystalline nature for good electronic transport properties (electron-crystal), maximizing the power factor (S^2/ρ) [21]. A fruitful strategy to design such a PGEC material is to seek for crystal structures that can be viewed as two sublattices: one composed of electrically-conducting network while the other behaves as a thermal blocker.

Owing to these decoupled transport properties [22, 23], copper chalcogenides including liquid-like materials (superionic semiconductors) [24-37], diamond-like

compounds[38-42], and layered-structure compounds [43-49] have all recently gained significant attention as promising thermoelectric materials[23]. Cu-based chalcogenides show high thermoelectric efficiency mainly arising from significantly suppressed lattice thermal conductivity stemming from the mobile Cu ions that introduce additional scattering centers, thus, shortening the phonon mean free path [22].

Many studies on binary and ternary Cu-based materials can be found in the literature e.g., $Cu_{2-\delta}X$ (X = S, Se, and Te) [24, 25, 28-33, 50, 51], Cu_8GeSe_6 [34], Cu_5FeS_4 [35], Cu_7PSe_6 [52], $CuCrSe_2$ [53], CuAgSe [36], $CuCrS_2$ [37], etc. In $Cu_{2-\delta}X$ (X = S, Se, and Te), rigid sublattices formed by X atoms provide a crystalline pathway for conducting carriers while disordered Cu atoms with high diffusivity (on the order of 10^{-5} cm^2/s) jump sequentially between equilibrium positions [22]. At high temperatures, the Cu_2X phases possess disordered cubic structures, while they have complex crystal structures at lower temperatures [23]. Stoichiometric compounds such as Cu_2Se and Cu_2S undergo one- and two-phase transitions, respectively. The structural complexity of the Cu_2Te phase is evidenced by the sequential appearance of five phase transitions until a final f.c.c. structure is reached as summarized in Figure 2.4 a [23]. In addition to stoichiometric Cu_2X compounds, many Cu-deficient variants ($Cu_{2-\delta}X$) have been reported [24, 25, 30, 50]. Although the structural complexity further increases upon varying the Cu/X ratio, introducing Cu-deficiency tunes the hole concentration to the optimal value yielding high thermoelectric performance. The fact that Cu-X bonding becomes less polar and weaker from S over Se to Te, Cu deficiencies are more prone to form, leading to high carrier concentrations. Moreover, the lattice thermal conductivity of tellurides is lower than that of selenides or sulfides due to the larger atomic size of Te and weaker Cu-X bonds [23].

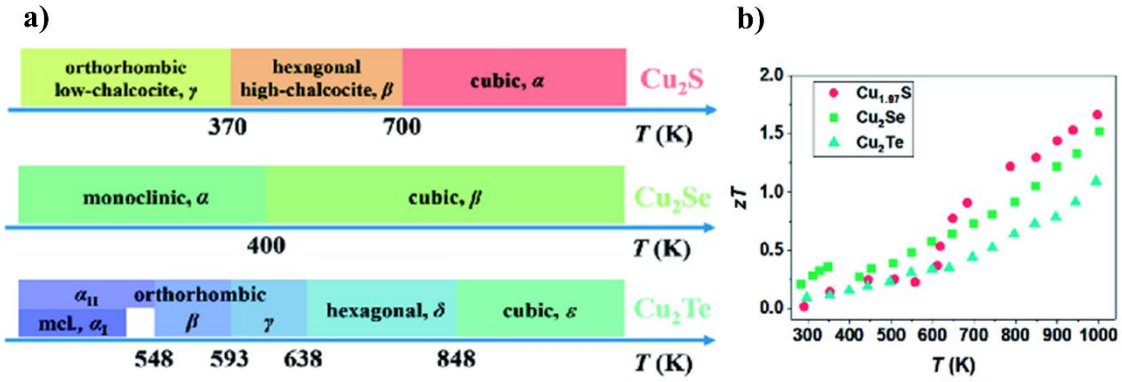

Figure 2.4 a) Different phases and phase change temperatures of Cu_2X compounds, and b) zT values of Cu_2X compounds as a function of temperature [24].

The phase change effect significantly impacts the transport properties of Copper chalcogenidesThe phase transitions involve changes in the crystal lattice arrangement, resulting in alterations in the materials' electronic and thermal transport properties. The transition from the low-temperature phase to the high-temperature phase can lead to variations in the electrical conductivity, Seebeck coefficient, and thermal conductivity of Cu-chalcogenides [23-25, 50, 54], leading to change in thermoelectric efficiency, *zT* as seen in Figure 2.4 b. Understanding and controlling these phase change effects are crucial for optimizing the performance and efficiency of Copper chalcogenide-based thermoelectric and electronic devices [23].

The Cu-Te system is the most complex and least studied Cu-chalcogenide system and even though it is generally represented as $Cu_{2-x}Te$, it has intricate structures and forms different phases such as $Cu_{2-x}Te$ (weissite), CuTe (vulcanite), and $Cu_{3-x}Te_2$ (rickardite) [55]. Due to their physical properties, these compounds are the promising candidates for wide range of applications in various fields such as electronics [56] and solar cells [57-61] beside thermoelectrics [22, 62-64]. However, having many different polymorphic phases and forms of copper telluride complicate to study the principles of crystal structure and electronic band structure of these compounds [65].

Phase diagram of Cu-Te systems has been experimentally studied by many authors [54, 55, 66-70]. One of the complex Cu-Te phases between Cu_2Te and CuTe in the phase diagram is $Cu_{3-x}Te_2$ known as rickardite mineral within the homogeneity range of 40.0 - 41.5 at. % Te and displays an unconventional defective structure with a large amount of vacant metal positions. $Cu_{3-x}Te_2$ ($x \approx 0.2$) phase was reported to be either tetragonal or slightly deformed orthorhombic at room temperature with a close resemblance of the defective tetragonal Cu_2Sb structure type reported by previous studies [71] in which the Cu^{I} (Cu1) atoms occupy the tetrahedral holes while Cu^{II} (Cu2) atoms pseudo octahedral holes of Te lattice [54]. Searching for analogous structure to determine the atomic arrangements of rickardite mineral lead up to Cu_2Sb structure that is tetragonal with the space group *P*4/*mmm* and lattice parameters of a = 3.992 Å and c = 6.091 Å. Lattice parameters of $Cu_{3-x}Te_2$ which is in an agreement with Cu_2Sb structure have been reported as a = 3.94 Å and c = 6.11 Å [68, 71]. Later on, tetragonal phase was found to be stable only above 413 K having partial disordered Cu atoms in octahedral sites with the orthorhombic room temperature to tetragonal phase change [54, 67]. In an another study, unit cell parameters of $Cu_{2.86}Te_2$ ($x = 0.14$) at room temperature were found to be a =

3.991 Å, b = 3.965 Å and c = 6.110 Å and do not vary much within the homogeneity range [68, 72].

To find another Cu-based binary compounds, theory driven experimental research method has been established to guide this study. The crystal structure and thermoelectric properties of the binary compound $Cu_{3-x}Te_2$ have been investigated in detail over a broad range of temperatures (5 – 733 K). The material studied for the transport property measurments was suggested by a machine learning method after using all the information-dense words that are embedded in scientific abstracts. This method enables predicting new potential thermoelectric materials comparing the predicted thermoelectric compositions with available data in the literature.

Among all the Cu-based TE materials, Cu_2Se is known for its reversible phase transition around 400 K, and the phase transition temperature depends on the Cu deficiency in the composition, $Cu_{2-\delta}Se$. The structure of the low-temperature α-phase Cu_2Se is distorted and exhibits lower symmetry with a monoclinic lattice structure. However, the high-temperature β-phase of Cu_2Se crystallizes in the $Fm\bar{3}m$ space group, adopting a face-centered cubic arrangement for the Se^{2-} anions and tetrahedral interstitial sites for the Cu ions. The disorder Cu^+ cations in tetrahedral sites possess liquid-like mobility. Cu_2Se exhibits a specific heat at constant volume, C_v value that falls between the values expected for a solid crystal and a liquid according to the Dulong-Petit law. This suggests a liquid-like characteristic and significantly contributes to the material's thermal conductivity reduction. In contrast to a crystalline materials typically display significant temperature-dependent behavior in terms of lattice thermal conductivity, Cu_2Se does not show intense temperature-dependent behavior in lattice thermal conductivity, supporting its unique properties as a liquid-like semiconductor material. To date, the electronic structures and thermal conductivity of Cu_2Se have been modified by doping using Al, Sn, Sb, Ag, and Li in the Cu sites [49, 73-76], and Te, S, I, and Br in the Se sites [27, 52, 77, 78].

2.3 Li_3Sb, a Zintl Phase

Zintl compounds, classified as phonon-glass electron-crystal (PGEC), are promising thermoelectric candidates for power generation applications at high temperatures [79]. Zintl cations constitute the “phonon-glass” characteristics due to their loosely-ionically-bonded nature, while anionic subunits forming the covalently bonded framework are

responsible for the "electron-crystal" properties [80-82]. Owing to their rich and complex crystal structures with many atoms in the unit cells, Zintl phases exhibit inherently low lattice thermal conductivities [83].

The transport properties of the ternaries $X_{14}MnSb_{11}$ (X = Ca, Yb) [82, 84, 85], $X_5Y_2Sb_6$ (X = Ca, Yb; Y = Al, Ga, In) [86, 87], XY_2Sb_2 (X = Ba, Ca, Sr, Eu, Yb; Y = Ga, Cd, Zn, Mn) [88-96], XMg_2Bi_2 (X = Ca, Eu, Yb) [97, 98], and binary Mg_3X_2 (X = Sb, Bi) [99-104] Zintl phases have been recently shown to be high-efficiency thermoelectric materials. Because of their propensity to show cation vacancies, most of these phases exhibit p-type semiconducting behavior. Only a handful display n-type behavior achieved by either phase boundary mapping or intrinsic or extrinsic doping [105-107].

Along with ternary phases, binary Zintl compounds with cations from group I or II can also crystallize with complex structures preserving PGEC characteristics [108]. Recently, theoretical calculations on the transport properties of lithium-based semiconductor materials revealed that phases containing heavy pnictogens such as Sb or Bi could be promising thermoelectric materials [109]. Up to date, only a few theoretical studies are available in the literature on this family of materials, which are less studied than other alkali pnictide compounds [110-112]. Among the possible Zintl phases, Li_3Sb emerges as an up-and-coming candidate due to its superionic conductivity [113-115], the calculated narrow bandgap of 0.68 eV and low lattice thermal conductivity κ_L of 2.2 W $m^{-1}K^{-1}$ at 300 K, which is significantly lower than $CoSb_3$ (11.5 W $m^{-1}K^{-1}$) [116], n-type half-Heusler $Hf_{0.75}Zr_{0.25}NiSn_{0.99}Sb_{0.01}$ phases (4.0 - 4.6 W $m^{-1}K^{-1}$) [117], and SiGe bulk alloys (2.4 - 28 W $m^{-1}K^{-1}$) [118]. Considering the low κ_L of Li_3Sb, further calculations predicted maximum zTs of 0.87 and 0.39 at 900 K in p-type and n-type Li_3Sb, respectively [109]. Further taking into account the effect of various scattering mechanisms and scattering time τ, zT values as high as 2.4 (1.2) with τ = 5 fs and $n \approx 1.8 \times 10^{20}$ cm^{-3} ($n \approx 6.5 \times 10^{19}$ cm^{-3}) and 3.2 (1.6) with τ = 9 fs and $n \approx 9.6 \times 10^{19}$ cm^{-3} ($n \approx 5.6 \times 10^{19}$ cm^{-3}) in p-type (n-type) materials were predicted at 900 K. All these theoretical findings suggest that both p- and n-type Li_3Sb can show high thermoelectric performance for optimized carrier concentrations [109]. These predictions have been very recently experimentally tested on cubic Li_3Bi (space group $Fm\bar{3}m$) and hexagonal Li_3Sb (h-Li_3Sb; space group $P6_3/mmc$), with a peak zT value of 0.3 at 780 K for the latter. These results suggest that the cubic polymorph of Li_3Sb may exhibit higher thermoelectric performance due to the complexity of the top of the valence bands consisting of three degenerate bands with different effective masses, evidenced by electronic band structure calculations [115]. This

non-trivial topology may result in a high number of warped, non-ellipsoidal Fermi surface that can be beneficial to achieve high *zT* values [119, 120]. In the light of the theoretical studies, the thermoelectric potential of c-Li_3Sb synthesized via ball milling was investigated.

2.4 Half-Heuslers

Half-Heusler (HH) are widely investigated on the field of solar cells [121], magnetism [122], piezoelectricity [123], and thermoelectricity [124-128]. Since HH compounds with 18 valence electrons are semiconducting materials (0 - 4 eV bandgap), they gained attention as potential thermoelectric materials. Semiconducting HH materials have high-temperature stability besides their good mechanical endurance that makes them suitable for application areas [129]. HH are ternary intermetallic compounds that can be stated as the general formula of *XYZ* in the cubic structure where *X* is usually the most electropositive transition metal, *Y* is a less electropositive transition metal and *Z* is a main group element. A typical HH compound has a cubic MgAgAs structure with the F-43m space group. They have three fcc sublattices occupied by different kinds of atoms.

Their valence electron count of component elements is responsible for the materials' physical properties. By controlling each of the three lattice sites, many possibilities can be achieved to alter the electronic and thermal transport properties of the materials [121]. HHs have good electrical properties with high lattice thermal conductivities. To decrease the lattice thermal conductivity of the compounds many procedures can be applied such as alloying, grain size reduction, nanocomposite formation or doping [130].

NbCoSn is recently gained attention because of its high power factor reported S^2/ρ = 3.5 mW m^{-1} K^{-2} and zT = 0.6 at 1000 K in n-type composites of $NbCoSn_{1-x}Sb_x$ ($x \leq 0.15$) [131]. For p-type doping studies, although recent computational studies proposed that Ti, Zr, and Hf can be strong dopants [132], it is reported that Ti and Hf are the weak dopants which lead the compound has low Seebeck coefficients [133, 134]. Recent work on Zr and Ti-doped NbCoSn prepared by only solid-state synthesis method shows that samples are limited by high electrical resistivities and still have low *zT* values [135]. In an efford to obtain a p-type NbCoSn, a fast one-step synthesis method was used as well as long annealings at elevated temperatures via p-type substitution on Nb site and with Co-deficincies. The detailed investigation on thermoelectric transport property measurements was in conducted.

CHAPTER 3

EXPERIMENTAL METHODS & THEORETICAL CONCEPTS

Since some reactants and obtained samples are air or moisture sensitive, all the starting materials and samples were stored in the Argon-filled MBraun glove box. The oxygen and water levels inside the glove box were monitored in parts per million (ppm) and kept less than 0.1 ppm.

3.1 Chemicals and Materials

The chemicals used in this study and their specifications are listed in Table 3.1. All of them were used as it is without any purification except copper (Cu) beads. The surface oxidation on Cu beads was removed after surface reduction.

Table 3.1 Chemicals and their specifications.

Chemicals	Physical State	Company	Purity (%, metals basis)
Cu	beads	Chempur	99.9999
Te	pieces	Alfa Aesar	99.9999
Se	pellets	Aldrich	99.999
I_2	Crystals (resublimed)	Merck	99.5
Zn	powder	GoodFellow	99.9
Ag	powder	Nanografi	99.99
n-B	nano powder	PavTec	99
C-nB	nano powder	PavTec	99
Li	rod	Aldrich	99.9
Sb	shots	Alfa Aesar	99.999
Nb	powder	Chempur	99.9
Co	powder		
Sn	powder	Chempur	99.995
Zr	powder	Nanografi	99.9
Ti	powder	Aldrich	99.5
Ta	foil	Chempur	99.9

3.2 Sample Preparation Methods

The sample preparation methods used in this study include solid-state (SS) synthesis, mechanical alloying, arc melting, and hydrothermal synthesis. After the targeted compositions were synthesized, the samples were densified for further characterization and transport property measurements by spark plasma sintering (SPS) or hot-pressing (HP).

3.2.1 Solid-State Synthesis - Annealing

Solid-state synthesis is a one-step method by mixing the solid elements in a stoichiometric ratio, sealed inside carbon-coated quartz tubes, and melted or/annealed at elevated temperatures. The inside of the quartz tubes used for synthesis was coated with carbon by pyrolysis of acetone using propane/oxygen torch flame to prevent reacting the samples or reactants with the quartz tube. After having a homogenous carbon coating and cleaning inside the tubes, the reactants are loaded into quartz tubes inside the Ar-filled glovebox. The tubes were sealed under vacuum at least a 10^{-2} Torr vacuum to avoid any oxidation formation using a propane/oxygen torch.

Sealed tubes were placed inside muffin furnaces (Protherm) for the reaction, heated up to elevated temperatures above the recrystallization temperature, and kept at that temperature for an appropriate time, followed by cooling with a specific rate or quenching in water. For the quenching case, the tubes are taken out from the muffle furnace at a

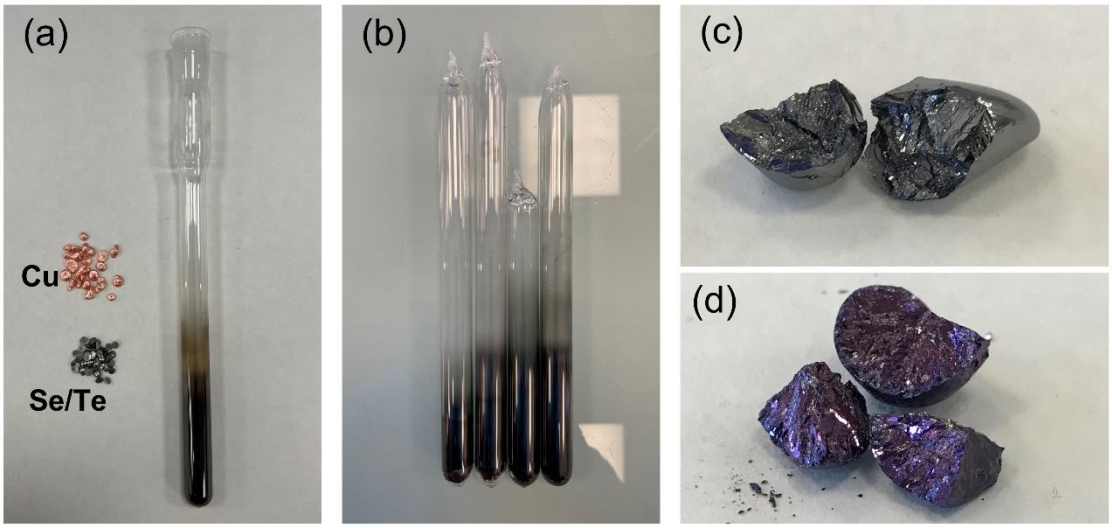

Figure 3.1 (a) C-coated silica tube and the reactants (b) sealed silica tubes under vacuum ready for the heat treatment, (c) Cu_2Se and (d) $Cu_{3-x}Te_2$ ingots synthesized by solid state synthesis method.

specific temperature and water quenched in water for two reasons; to avoid the secondary phase between recrystallization and room temperature (RT) phase or to maintain defects in the structure. If needed, they are put back in furnaces for further annealing at lower temperatures.

3.2.2 Mechanical Alloying

The mechanical alloying technique is used in this research to synthesize, dope, and homogenize the sample before the sintering step and decrease the grain size of the material. High-energy ball milling is one of the mechanical alloying methods that can yield homogenously reacted powder by mixing starting elements in a closed vial. The advantage of this method over the conventional solid-state synthesis method is the control over the stoichiometry in the chemical composition of highly volatile reactants; for example, the synthesis of Li_3Sb.

Mechanical alloying reactions or doping studies by milling are performed by a two-handed (clamps) high-energy ball milling device, SpexSamplePrep 8000D using hardened stainless-steel vials and balls (Figure 3.2). In theory, the clamps holding the vials are shaken back and forth, and solid powders react with one another during the experiment under the influence of G-forces with the help of stainless-steel balls. The preparation steps of the samples, put inside the stainless-steel jars, were always carried out inside the Ar-filled glovebox to avoid oxidation of the activated surface of the samples during milling.

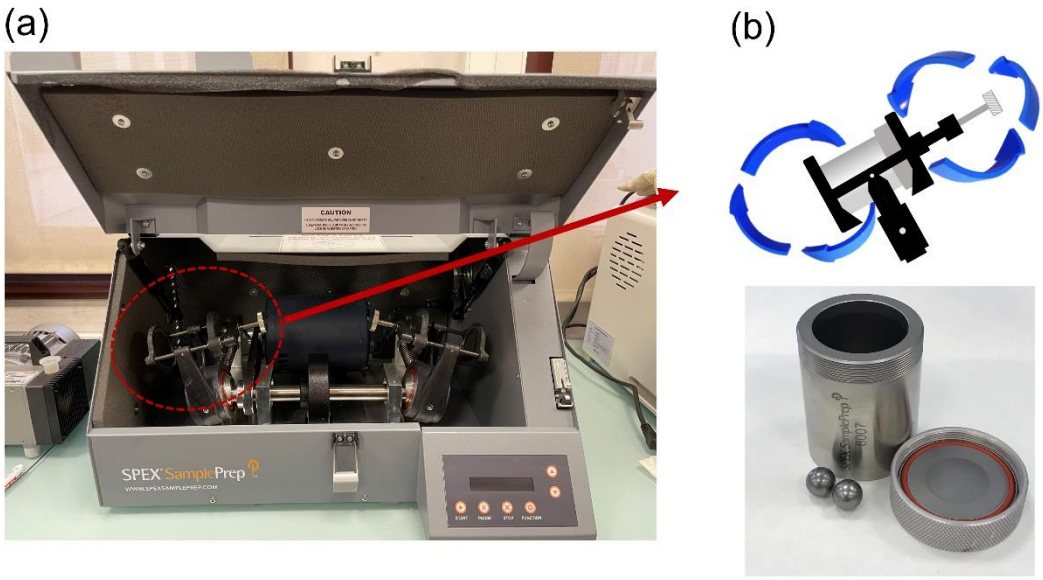

Figure 3.2 (a) SpexSamplePrep 8000D device, and (b) hardened stainless-steel vials used for milling.

3.2.3 Arc Melting

An arc melting furnace is used to synthesize the targeted compounds by reacting the starting elements by melting them together. The arc furnace is placed inside the Ar-filled glovebox and equipped with a water-cooling system and a vacuum pump. The starting elements or pellets made from powders of reactants are placed into water-cooled copper (Cu) plate, the bottom electrode. The tungsten (W) tip, the second electrode, is used above the samples to produce the arc between the sample and the tip by providing an electrical current flowing through the sample and resulting in the melting (Figure 3.3). This procedure is applied for a few seconds on each side of the pellets or chunks of metals and twice for each side to ensure the homogeneity of the samples.

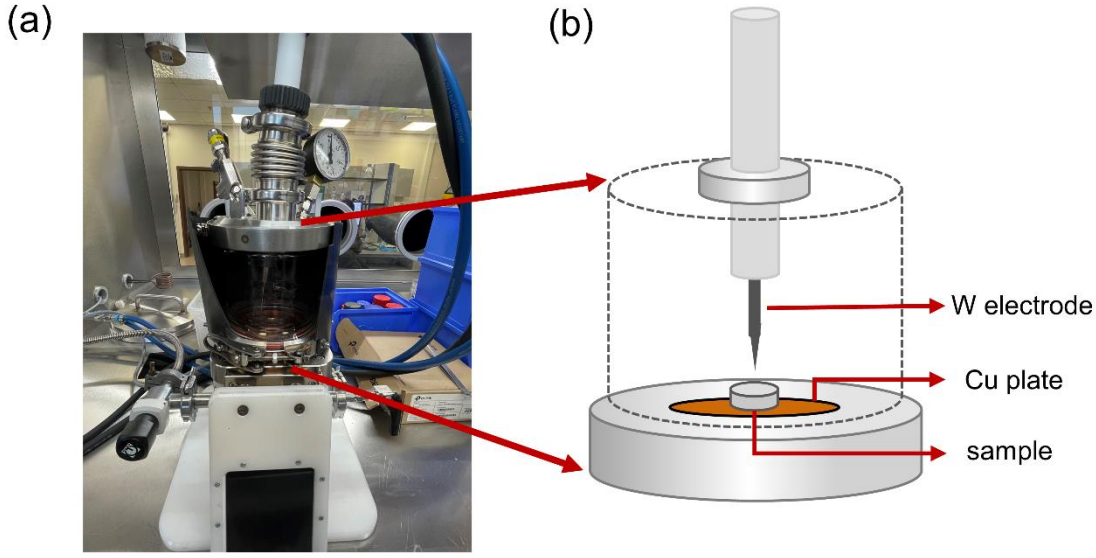

Figure 3.3 Arc melting furnace inside Ar-filled glovebox used for synthesis of some samples and sealing the reaction ampule and (b) schematic representation of arc furnace chamber.

3.2.4 Hydrothermal Method

The hydrothermal synthesis method is a solution synthesis method in that all the reactants are dissolved in a solvent, mainly in water, with a reducing agent for the reaction in an acidic or basic reaction media. As shown in Figure 3.4, the hydrothermal autoclave is composed of two parts: stainless steel outer part and a polypropiolactone (PPL) liner. The prepared solution with reactants and reducing agents were put inside the PPL liner to protect the reaction and the stainless-steel steel hydrothermal autoclave reactor. The PPL

liner is then put inside a stainless-steel hydrothermal autoclave and sealed accordingly with a screw top part. The autoclave is put inside the furnace, and the reaction occurs under elevated temperatures, hence the pressure built inside. The PPL liner is better than Teflon (PTFE) liner because of its higher resistance to alkaline and the acidic environment with higher working temperatures.

Figure 3.4. Hydrothermal stainless-steel (316 L) autoclave reactor and polypropiolactone (PPL) liner.

3.2.5 Consolidation

In the studies, spark plasma sintering (SPS) or hot-press is used to densify the finely powdered samples to get reliable transport property measurements. The density of the resulting pellets from SPS and hot-pressing is measured by geometric density or Archimedes method. After obtaining dense samples, they are used for further characterization and physical property measurements.

Spark Plasma Sintering (SPS)

Spark plasma sintering (SPS) method was used by AGUS-PECS SPS-320Sx from SUGA Co., Ltd. (Figure 3.5). This method uses an electrical current passing through the graphite die and the powder samples inside the die resulting in fast heating with short processing of pulsed electric called spark plasma sintering. The system contains; a vacuum chamber where the atmospheric condition of the process is controlled by a

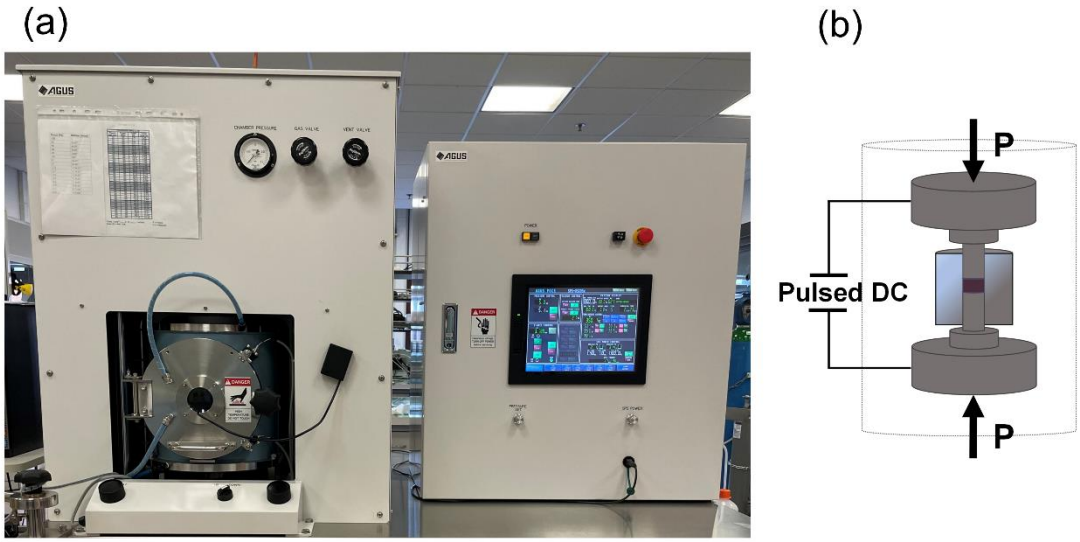

Figure 3.5 (a) Spark plasma sintering (SPS) used for consolidation of the samples and (b) schematic representation of the samples placed into graphite die inside the vacuum chamber.

vacuum pump and inert gas lines, a sintering part where axial pressure is applied through electrode punches, and the DC pulse power supply that controls the sintering process with the help of a thermocouple or an IR camera by measuring the temperature of the graphite die that contains the sample inside. The SPS technique derives advantages from various phenomena, including the generation of plasma, joule heating which is the generation of heat through electrical resistance, the electro-plastic effect, electromigration under the influence of pulsed electric currents, and the application of mechanical pressure.

In contrast to conventional systems, the SPS technique heats the sample from both the outside and inside using pulsed direct currents passed through the graphite dies and the sample inside. When an electrical potential is applied to the sample, generated sparks at the contact points between the particles lead to electron flow and plasma discharge. The sparks instantly cause the local temperature to increase to several thousand degrees Celsius. As a result of Joule heating, the particles' surfaces undergo evaporation and melting, leading to the immediate formation of necks (Figure 3.6) as in the welding process of the particles under axial pressure. In the end, the electro-plastic effect assists the plastic deformation mechanism. It speeds up the densification process by decreasing metals' yield strength when subjected to an electric field [136, 137].

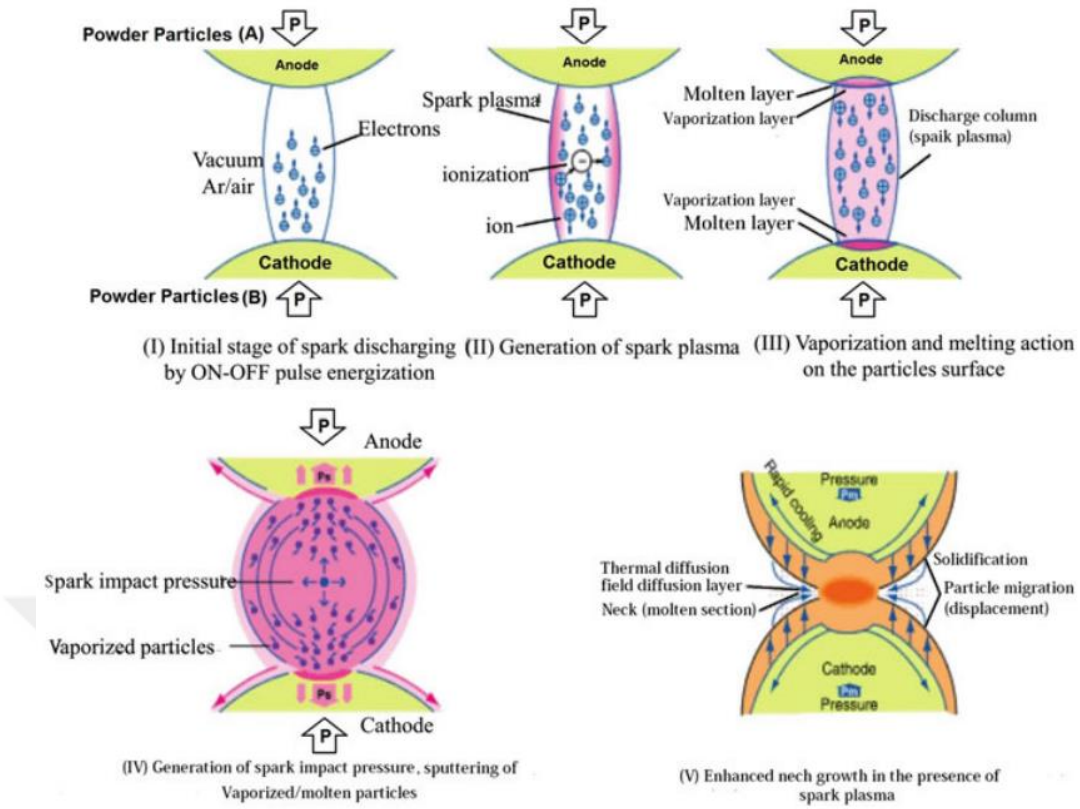

Figure 3.6 Neck formation mechanism by spark plasma [137].

A fine powder sample is loaded inside a graphite die with a 10 mm inner hole inside an Ar-filled glovebox to prevent oxidation of the materials with trapped oxygen inside the powder during the sintering process. The graphite sheets are shaped and put between the sample, and the graphite die as an interlayer before sample loadings to prevent cross contaminations for each sample. The prepared graphite die is placed inside the chamber between electrode plates where the pressure and the current are applied to the sample. The K-type thermocouple is used for temperature readings from the hole of the die placed, or an IR camera is used for measuring the temperature where the sintering is set to a temperature above 850 °C to prevent the thermocouple failure. After placing the graphite die, the chamber is evacuated to prevent oxidation. The program is set by defining applied axial pressure and the sintering time and duration depending on the materials studied.

Hot Pressing

A home-made rapid hot-pressing system is used to consolidate the samples at elevated temperatures by using induction heating in an inert atmosphere at Northwestern University. The finely powdered sample is loaded inside the graphite die in the same procedure as the SPS method. The die is put in the center of the copper induction coil

inside the vacuum chamber of the hot press. The thermocouple (K type) is placed on the graphite die right next to the sample, and the chamber is evacuated down to about 10-5 Torr using a diffusion pump. The set axial pressure is applied to the graphite die under the argon flow, and the set current is applied through the induction coil to heat the die up to a set temperature. The pressing temperature and the duration time depending on the sample studied. When the desired pressing duration is completed, the pressure is released while the temperature gradually decreases to room temperature as the current decreases.

3.2.6 Diamond Wire Saw Cutting

A diamond wire saw was used for cutting the densified samples (pellets) to desired shapes for transport property measurements (Figure 3.7). For the thermal diffusivity tests by using Laser Flash Apparatus (LFA), the thickness of the disc typically should be between 1- 2 mm, depending on the diffusivity limits of the measured samples. For the electrical resistivity and Seebeck measurements using ZEM-3, the samples' desired shape should be cylindrical or rectangular. Since the diameter of the samples should be less than 3 mm in both cases, shaping the samples as a rectangular bar is more effortless with a diamond wire cutting. Overall, each sample obtained as a 10 mm disc (~ 4 – 4.5 mm long) by SPS is glued on its side onto a ceramic or Teflon surface using a polymer wax to cut into ~ a 1.5 mm thick disc shape for LFA. Then, the rest ~2.5 mm thick disc is glued on its round surface to cut a rectangular bar shape piece for ZEM-3 measurements.

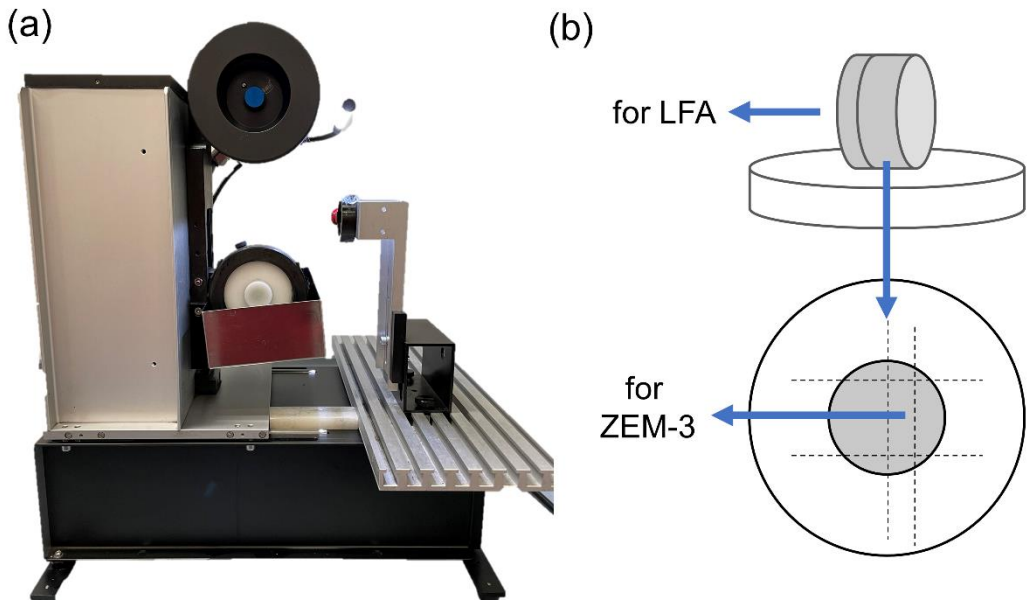

Figure 3.7 (a) Diamond wire saw cutting device used to shape the samples and (b) cutting orientations of each sample.

3.3 Material Characterization Methods

The characterization, crystal structure determination, the phase purity analysis of the samples was performed by using X-ray diffraction (XRD), Single crystal XRD, high-temperature (HT) XRD, and Synchrotron XRD analysis. Besides, microstructural analysis were done by optical microscopy (OM), scanning electron microscopy equipped with energy dispersive X-ray (EDX), and wavelength dispersive X-ray (WDS). Moreover, thermal stability measurements were performed by the simultaneous thermal analyzer (STA).

3.3.1 X-ray Diffraction

X-ray diffraction (XRD) is a non-destructive technique for materials characterization that helps to identify the crystal structures and phase purity of the samples as well as giving information about lattice parameters and grain sizes of the phases. First, x-rays are generated in a cathode ray tube by an electron bombardment of the target material (Cu, Fe, Mo, Ag, or Cr). These produced x-rays are filtered and collimated to have monochromatic concentrated radiation. The collimated x-ray beams are scattered by the periodic lattice of the samples result in constructive and destructive interference only when Bragg's law is fulfilled with the following equation, constructive interference results in a diffraction pattern.

$$2\,d\,\sin\theta = n\,\lambda$$

Powder and bulk samples were characterized by Rigaku MiniFlex XRD with Cu Kα (λ = 1.540598 Å) radiation as an X-ray source by using 40 kV voltage and 15 mA current within the range of $5° \leq 2\theta \leq 90°$, $\Delta 2\theta = 0.02°$. When the sample is air- or moisture-sensitive, a Kapton foil was used to cover the sample inside the Ar-filled glovebox to protect the sample from decomposition. All X-ray powder diagrams were analyzed by STOE WinXPOW software [138] using crystallographic data from the ICSD database [139]. Lattice parameter refinements were calculated using LaB_6 as a correction standard to determine the peak positions. The unit cell parameters were calculated by least-square refinement by using the WinCSD program package [140].

Single-crystal X-ray diffraction (XRD)

For single crystal X-ray analysis, appropriately sized single crystals were picked and mounted on the sharpened end of glass capillaries. The structure data at room temperature were collected with a Rigaku AFC7 diffractometer (Mo Kα radiation, λ = 0.71073 Å) equipped with a Saturn 724 + charge-coupled device detector.

High-Temperature XRD

High-temperature XRD (HTXRD) measurements were carried out in sealed glass capillaries with a high- temperature stage attached to the STOE STADI-MP diffractometer (Mo Kα = 0.71073 Å). Microstructure.

Synchrotron powder X-ray diffraction

Room-temperature and the high-temperature synchrotron powder X-ray diffraction data were collected at the high-resolution beamline ID22 of the European Synchrotron Radiation Facility (ESRF) in Grenoble. Transmission (capillary) measurements were performed at the fixed wavelength of 0.400066 Å between the temperature range of 25 °C to 420 °C.

3.3.2 Scanning Electron Microscopy and Elemental Analysis

Scanning electron microscopy (SEM) is an effective non-destructive method for the determination of the morphology of the microstructure and the chemical compositions (when equipped with EDX or WDX) of a specific material. Variaty of signals are produced to study surface structure by the interactions between the atoms in the sample and the high energy electron beams.

SEM consists of an electron gun, condenser lenses, electron detectors, an objective lens, and a vacuum system. The electron gun or source generates an electron beam that is accelerated along the column. The beam then traverses through a sequence of apertures that modify different characteristics of the beam. During SEM analysis, a highly focused electron beam is directed at the specimen under investigation. SEM operates at a voltage range of 0.1 to 40 keV depending on the sample composition. The interaction between the primary beam and the sample produces various signal types, such as backscattered electrons, secondary electron emission, cathodoluminescence, Auger electrons, and characteristic X-rays, which are detected from defined sample volumes. These signals can be used to investigate diverse sample properties, including surface topography, composition, etc.

The secondary electron signal, which is produced by the ionization of atoms following the interaction between the sample and primary electrons, is the most commonly applied signal in SEM. The secondary electrons have low energy (~5 eV) and provide information about the topography of specimens, allowing surface structures to be resolved down to 10 nm. The brightness of the image is determined by the number of unhindered electrons, whereas blocked electrons result in darker areas. Additionally, backscattered electron signals can provide compositional data in addition to topographic data. When the primary electron beams collide elastically with the sample, they reflect from the surface, maintaining 60-80% of their original energy. The reemitted backscattered signals provide contrast that depends on the atomic number of the sample, as higher atomic numbers with more positive charges result in more backscattered electrons [141, 142].

In this study, the Zeiss Ultra Plus field emission SEM was utilized. Powder samples and the bulk samples were placed onto a carbon tape before loading samples to the vacuum chamber. The bulk samples were finely polished using automatic sample polisher system, Tegramin 30 Struers after mounting the samples using mounting press, Citopress 30 Struers. The elemental composition and distribution were investigated using the elemental mapping feature with Energy Dispersive X-ray Spectroscopy (EDS) and wavelength-dispersive X-ray spectroscopy (WDS, Cameca SX 100, tungsten cathode). Microstructure analysis were performed using optical microscopy (OM, Zeiss Axioplan 2).

3.3.3 Thermal Analysis

Differential scanning calorimetry (DSC) analysis are performed to evaluate the reaction and any kind of phase change (physical or chemical) temperatures beside enthalpy of samples as a function of temperature by measuring the heat flow difference between sample and the reference. The sensors are connected to thermocouples recording the temperature difference between the sample and reference side, which is usually an empty pan.

The thermal stability of the samples was measured using two different DSC devices, Netsch STA 449 F3 Jupiter equipped with thermal gravimetric analysis (TG) and Netsch DSC204 Phoenix. For all the measurements, an inert atmosphere was maintained by flowing N_2 or Ar during the measurements.

3.4 Physical Properties Measurements

The transport property measurements are performed using ZEM-3 for electrical conductivity and Seebeck coefficient determination, hall effect for carrier concentration, laser flash apparatus (LFA) for thermal diffusivity, and magnetic susceptibility test for magnetic property measurements.

3.4.1 Electrical Conductivity and Seebeck Coefficient

The electrical conductivity (σ, or electrical resistivity (ρ)) and the Seebeck coefficient (α) measurements are performed by using ZEM-3 (Ulvac-Riko, Japan, Figure 3.8) using a four-point probe method. The samples used for measurements were cut into rectangular bar shapes with a size approximately 2 mm widths and 6-8 mm heights, and graphite sheets were used between all four probes and the touching surfaces of the samples to avoid contamination and protection of the probes. The sample is placed vertically between the upper and lower electrodes inside the furnace chamber. The chamber is evacuated and refilled with helium (He) at least three times for 15 minutes/cycle to remove oxygen, and a small amount of He is sent to the chamber to keep the environment conductive.

Figure 3.8 Ulvac Zem-3 electrical resistivity and Seebeck measurement system.

During measurements throughout the working temperature range, a constant current is applied to the sample for the resistivity measurements while a heater in the lower block was creating a temperature difference set as 10, 20, and 30 K. The temperature difference and the electromotive force, *dE* were measured by thermocouples. The Seebeck coefficients (*S*) were calculated via the DC method using the following equation;

$$S = \frac{\Delta V}{\Delta T}$$

where ΔV and ΔT are the voltage difference and temperature difference, respectively.

The electrical resistivity (or electrical conductivity) measurements can be done using four terminal merhod by detecting the voltage changes between thermocouples when the current is applied from upper and lower electrodes (Figure 3.9). The electrical resistivity can be calculated using the following formula,

$$\rho = \frac{V}{I}\frac{A}{d}$$

where ρ, A, I, and d are resistivity, the cross-sectional area of the sample, applied current, and the distance between the thermocouple probes, respectively.

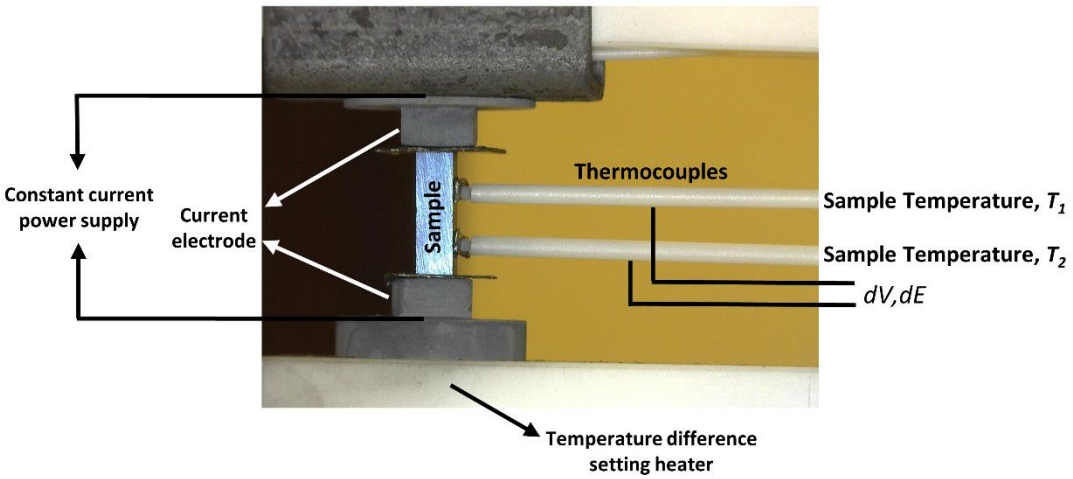

Figure 3.9 Working principle of electrical resistivity and Seebeck measurement system.

3.4.2 Hall Effect

The Hall measurement is a useful method to measure the charge carrier concentration as well as determining the type of the charge carriers as negative for electron ot positive for holes, and the mobility of a material via Hall effect. These properties are used to estimate the band effective mass and the carrier scattering mechanism of the material.

When a magnetic field B is applied to the sample where an electric current flows through, the paths of the charge carriers are diverted to the sides, resulting in the Hall

effect. This phenomenon creates a transverse voltage, V_H which is also known as the Hall effect. The hall constant, R_H can be calculated using the following formula,

$$R_H = \frac{V_H A}{IdB} = \frac{\rho_H}{B}, \qquad R_H = -\frac{1}{n_e}\ (electron),\ R_H = \frac{1}{n_p}\ (hole),$$

where I, d, ρ_H, n_e, n_p, are the current, the transverse dimension of the sample, Hall resistivity, the electron, and the hole concentration, respectively. The Hall mobility, μ_H, of the charge carriers can be calculated using the following formula,

$$n_H = \frac{1}{R_H|e|}, \quad \mu_H = R_H/\rho$$

Hall effect measurements in this study were carried out by using a 4-point probe Van der Pauw (VdP) technique with a home built system in Northerstern University, under a magnetic field of 2 T using pressure-assisted tungsten electrodes. The consolidated dense sample is placed on the alumina sample holder which has heater inside. Four molybdenum probes are placed on the sample and tightened with screws to decrease the contact resistance between probes and the sample. The sample holder is covered with a radiation shield and placed inside the vacuum chamber. The chamber is evacuated down to 10-5 Torr to minimize oxidation during measurement by using rough and turbo pumps.

3.4.3 Thermal Diffusivity and Thermal Conductivity

The laser flash technique is used to measure the diffusivity values of all the samples within the working temperature range under a defined Argon flow. Netsch LFA 467 HT Hyper Flash instrument (Figure 3.10 [143]) was used to measure the thermal diffusivity of the densified 10 mm diameter pellet samples after SPS. With the laser flash method, the lower surface of the sample is heated by a short energy light pulse produced by the Xenon lamp. When there is a temperature change on the upper surface of the samples, the temperature variation is detected by an infrared (IR) detector, which is InSb in the defined instrument. Before loading the samples into the instrument, they were coated with a thin layer of graphite to eliminate the reflection and for better absorption and emission properties to achieve a better signal-to-noise ratio since the LFA is an optical method.

The thermal diffusivity (a) values of the samples were calculated by,

$$a = 0.1388 \frac{d^2}{t_{1/2}}$$

where d is the thickness of the samples and $t_{1/2}$ is half-time at half-signal height.

The total thermal conductivity (κ) values were calculated by using the following equation,

$$\kappa(T) = a(T).C_p(T).\rho(T)$$

where a, C_p, and ρ are the samples' thermal diffusivity, heat capacity, and density, respectively.

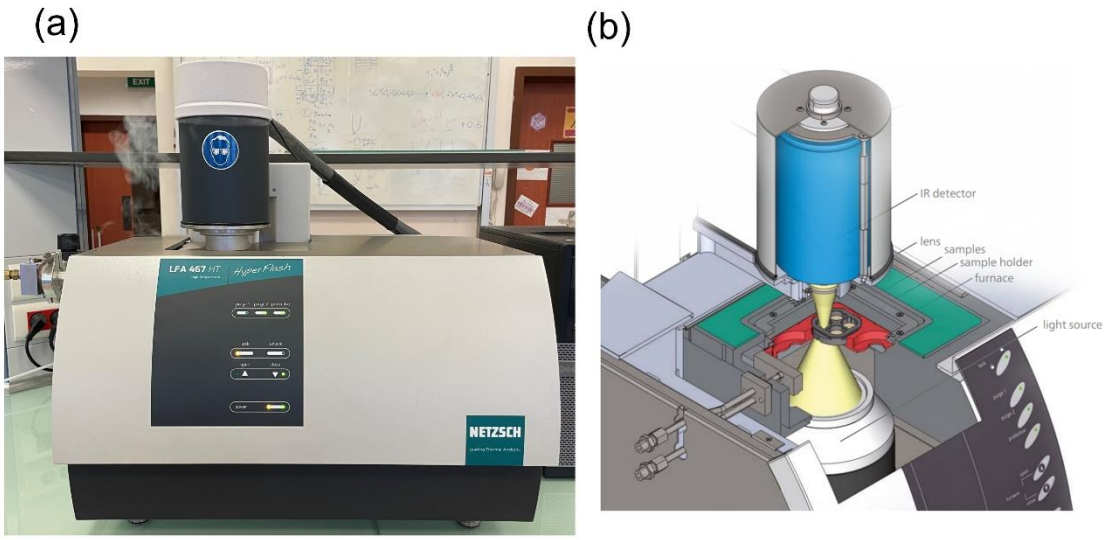

Figure 3.10 (a) Laser flash analysis (LFA 467 HyperFlash) device equipped with liquid N_2 pumping system and (b) the schematic representation of the instrument parts [50].

3.4.4 Heat Capacity

The specific heat capacity, C_p can be obtained by Differential Scanning Calorimetry (DSC) via the ratio method using sapphire as the standard material. C_p is the amount of heat required to increase the temperature of a specific material by a degree for per unit mass. With DSC method, the signals at different temperature is recorded and compared to a reference material simultanously. The reference used in this study is a sapphire

sample with a known C_p and mass. The C_p of the sample is calculated via ratio method evaluated by the software using the following equation,

$$C_{p,sample} = \frac{m_{sapp}}{m_{sample}} \frac{DSC_{sample} - DSC_{baseline}}{DSC_{sapp} - DSC_{baseline}} C_{p,sapp}$$

where m_{sample}, DSC_{sample}, $DSC_{baseline}$, *and* DSC_{sapp} are the sample mass, DSC signal coming from sample, baseline, and sapphire reference, respectively.

When determining C_p is not practical with DSC method, Dulong-Petit law can be used to calculate C_p by taking into account the vibration degrees of freedom of the atoms. Since each atom vibrate in three dimensions, the energy of an atom is $3k_BT$ which is equal to $3k_BTN_A$ for a mole of atom by multiplying the number of atoms in one mole, total inner energy, U. The specific heat, C_p can be found using following formula,

$$C_p = \frac{3NR}{\mathrm{M}}$$

where N, R and M are the total numer of atoms in a chemical formula, the constant which equals to k_BN_A, and the molar mass of the compound, respectively.

3.4.5 Magnetic Properties

Measurements of the magnetic susceptibility, χ, measurements were done using MicroSense. Magnetization curves $M(\mu_0H)$ were measured between 300 and 680 K using a high- temperature vibrating sample magnetometer under magnetic fields, μ_0H, of up to 0.5 T. A polycrystalline piece of ~26 mg was glued onto a silica sample holder using a small amount of nonmagnetic ceramic paste. The magnetic susceptibility, χ, was inferred from the slope of the $M(\mu_0H)$ curves.

CHAPTER 4

PHASE-TRANSITION-ENHANCED THERMOELECTRIC TRANSPORT IN RICKARDITE MINERAL $Cu_{3-x}Te_2$

Majority of this chapter has been published in *Chemistry of Materials, 2021, 33.5, 1832-1841* [144]. The original manuscript has been rearranged to conform to the format requirements of the dissertation.

4.1 Introduction

In an effort to explore other Cu-based binary compounds, we report on a detailed investigation of the crystal structure and thermoelectric properties over a broad range of temperatures (5 – 733 K) of the binary compound $Cu_{3-x}Te_2$. Our experimental study was guided by a machine learning method based on information-dense word (e.g, thermoelectric, *zT* or thermopower) embedded in scientific abstracts. This method enables predicting new potential thermoelectric materials [145, 146], as validated (in part) by comparing the predicted thermoelectric compositions with available computational data sets [147] as well as experimental power factors and *zT* values [148]. $Cu_{3-x}Te_2$ is a naturally occurring mineral known as rickardite with poorly reported structural, chemical and transport properties [68, 149-152]. Motivated by the high thermoelectric performance and potential of commercialization due to low production costs of Cu-based minerals such as $Cu_{2-\delta}S$ [25], $Cu_{26}V_2Ge_6S_{32}$ (colusite) [153], $Cu_{12}Sb_4S_{13}$ (tetrahedrite) [154], and Cu_5FeS_4 (bornite) [35], we investigated the transport properties of synthetic rickardite mineral. In agreement with the complex binary phase diagram of Cu-Te [66] (Figure A 1 and for more close-up look in Figure 4.1), the two different compositions were decided to work on; $Cu_{2.8}Te_2$ and $Cu_{2.9}Te_2$. The first composition was the Cu_7Te_5 ($Cu_{1.4}Te$) which is widely used for the rickardite in the previous studies, and the latter one was picked between the rickardite region between 40 – 41.5 at % Te based on the phase diagram. several reversible phase transitions were evidenced by differential scanning calorimetry and specific heat measurements. The effect of these phase transitions on the transport property measurements were investigated and the high temperature transition leads to a metallic-like to semiconducting-like transitions. The transitions were confirmed as the following order orthorhombic ↔ tetragonal ↔ hexagonal phases by DSC, HTXRD, and the synchrotron high-resolution XRD measurements.

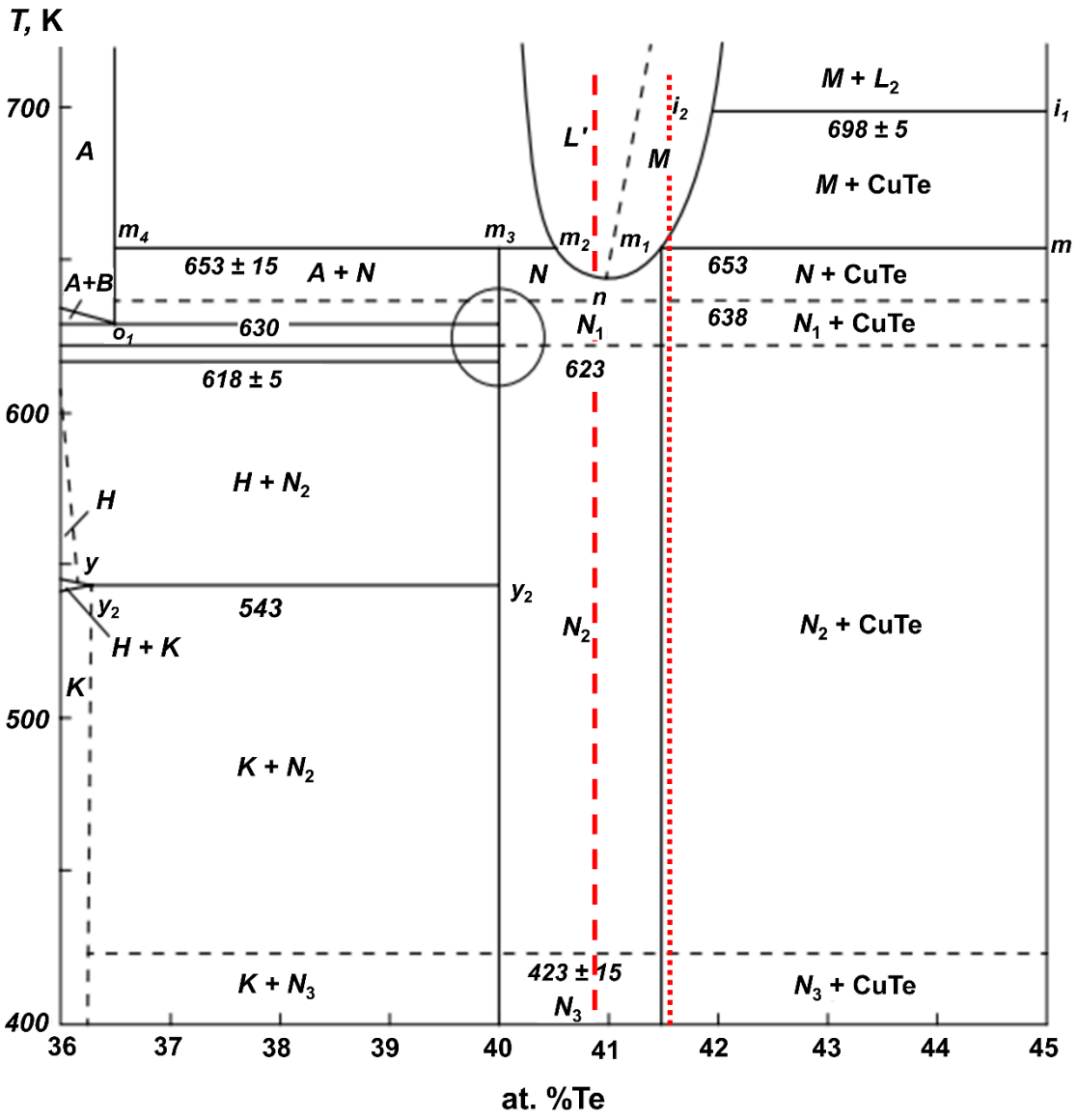

Figure 4.1. A section of binary phase diagram of the Cu-Te system at around $Cu_{3-x}Te_2$ composition region (~ 41 at. % Te) and in the temperature range of 400 – 720 K [66] (––: $Cu_{2.9}Te_2$, ····: $Cu_{2.8}Te_2$).

4.2 Experimental Methods

Copper beads and tellurium pieces were used as starting materials to synthesize polycrystalline $Cu_{3-x}Te_2$ samples. To remove surface oxides, copper beads were put inside an alumina holder, placed in a quartz tube, and kept at 773 K under an H_2/Ar flow for 4 hours. Afterward, $Cu_{3-x}Te_2$ samples were synthesized by reacting cleaned copper

and tellurium in the stoichiometric ratio of $Cu_{2.8}Te_2$ and $Cu_{2.9}Te_2$ by a solid-state synthesis method. Raw materials were sealed into a carbon-coated silica tube under a vacuum. The sealed tube was placed into a muffin furnace and kept at 1223 K for 12 h. After quenching in water at room temperature, the tube was put into a preheated furnace for further annealing at 623 K for 96 h. The final product has a bright purple color, similar to that reported in the literature for $Cu_{3-x}Te_2$. For chemical characterization and transport property measurements, dense cylindrical pellets were obtained by SPS in a graphite die at 623 K for 10 min under a pressure of 65 MPa (Figure 4.2). The densities of the samples were calculated to be 7.35 and 7.43 g/cm$_3$ for $Cu_{2.8}Te_2$ and $Cu_{2.9}Te_2$, respectively, from geometrical dimensions and weight of the consolidated pellets. Considering the crystallographic density of the phase $Cu_{2.8}Te_2$ with 7.54 g/cm^3, the relative densities amount 97 and 99 %, respectively. Based on these results, we consider that the transport data collected on SPS-treated samples give reliable intrinsic behavior of the rickardite phase.

Single-crystal X-ray diffraction (XRD) analysis, phase purity analysis by powder XRD, the crystal structure refinements as well as lattice parameter calculations, High-temperature XRD (HTXRD) analysis, microstructure analyses (optical microscopy, SEM), chemical composition analysis (EDX, WDS), the phase transition temperatures by DSC, heat capacity (Cp) measurements were performed as explained in section 3.3. To determine the speed of phase transitions, an additional Cp measurement (calculated according to DIN 51007) was performed using a DSC apparatus (NETZSCH 403 F3) with a heating rate of 20 K min^{-1} and using sapphire as the standard material.

Electrical and thermal transport properties were measured between 5 and 733 K on polycrystalline dense samples cut with a diamond-wire saw into appropriate shapes and dimensions. Low-temperature measurements (5−300 K) of the electrical resistivity, Seebeck coefficient, and thermal conductivity measurements were carried out on a bar-shaped sample with the thermal transport option of a physical property measurement system (PPMS, Quantum Design, San Diego, CA, USA). Four copper leads were brazed onto the sample using a low-melting-point braze. Hall effect measurements were performed on the same sample using the AC transport option of the PPMS. A five-probe configuration was used by brazing five copper wires onto the sample with a low-melting-point braze. The transverse electrical resistivity ρ_{xy} was measured by sweeping the

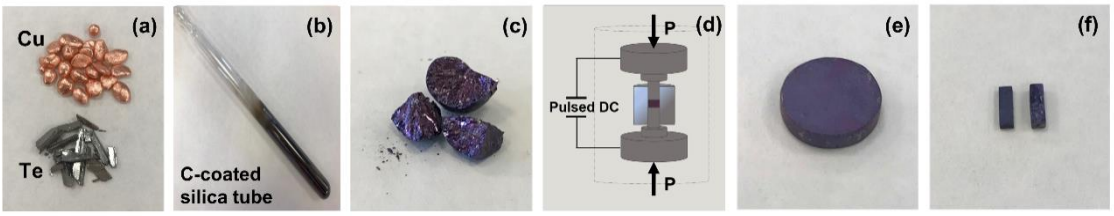

Figure 4.2 Synthesis and sample preparation procedures of $Cu_{2.8}Te_2$ and $Cu_{2.9}Te_2$, (a) raw materials of Cu and Te, (b) C-coated silica tube used for annealing, (c) synthesized $Cu_{2.9}Te_2$, (d) schematic representation of SPS Process, (e) dense pellets obtained after SPS for thermal transport measurements, and (f) samples cut for electrical transport measurements.

magnetic field $\mu_0 H$ between −1 and +1T. The Hall resistivity ρ_H was calculated following the formula $\rho_H = [\rho_{xy}(+\mu_0 H) - \rho_{xy}(-\mu_0 H)]/2$ to dismiss possible magnetoresistive contributions. The Hall charges carrier concentration n_H and Hall mobility μ_H were inferred from the single-band formulas $n_H = -1/R_H e$ and $\mu_H = R_H/\rho$, where e is the elementary charge, and R_H is the Hall coefficient determined from the slope of the $\rho_H(\mu_0 H)$ data for $\mu_0 H \rightarrow 0$. The specific heat measurement was performed under zero magnetic field on a small dense piece of approximately 20 mg using the ^{4}He specific heat option of the PPMS. The piece was glued onto the platform of the sample holder by using a minute amount of Apiezon N grease to ensure good thermal contact between the sample and the platform. At high temperatures (300 − 733 K), the thermal conductivity, electrical resistivity, thermopower measurements, and magnetization curves $M(\mu_0 H)$ were performed as explained in section 3.4.

4.3 Characterization

4.3.1 Crystal Structure Analysis

Rickardite mineral differs from other copper tellurides both in composition and appearance due to its characteristic purple color. Because of its uncertain composition and unknown crystal structure, rickardite was first recognized as weissite, $Cu_{2-x}Te$ [155]. Both minerals are massive with approximately the same hardness but differ in density and color, suggesting different electronic properties at room temperature. Following detailed studies of the binary Cu-Te system and rickardite phase [54, 68], the structural formula was reported as $Cu_{4-x}Te_2$, indicating Cu deficiency of approximately one atom per unit cell. Rickardite displays an unconventional defective structure with a large number of

vacant metal positions. These prior investigations have clearly confirmed that rickardite is distinct from the slightly Cu-deficient weissite phase, $Cu_{2-x}Te$[54, 68].

To determine the atomic arrangements, the search for analogous structures revealed that copper antimonide (Cu_2Sb), determined by Elander, Hägg and Westgren, is structurally similar to rickardite [71]. The crystal structures of both compounds were described in the space group *P*4/*nmm* with lattice parameters a = 3.97 Å, c = 6.11 Å and a = 3.992 Å, c = 6.091 Å for the rickardite and copper antimonide, respectively. Both compounds have a similar atomic arrangement (isostructural) and a layered crystal structure in which close-packed layers are weakly bound to Te atoms by half-filled Cu positions [68].

For $Cu_{3-x}Te_2$, both orthorhombic [54] and tetragonal [149] symmetries were reported. Herein, the crystal structure of this compound was investigated by single-crystal X-ray diffraction. From the obtained experimental data, the orthorhombic and tetragonal structures could not be unambiguously distinguished due to very close lattice parameters a and b, as well as very similar agreement of the refinement factors, that is R_{int} values, for Laue symmetries *mmm* and 4/*mmm*. However, clear splitting of the respective reflections was observed on the PXRD patterns indicating an orthorhombic lattice symmetry. A specific set of weak reflections, both on single-crystal and powder diffraction data, was also observed, suggesting that the crystal structure of $Cu_{3-x}Te_2$ is modulated (The detailed report about the investigation of the modulated model of the structure will be a subject of a separate publication). Moreover, single crystalline specimens show a tendency to form twinned agglomerates, which will require further investigation. Hereafter, a sub-cell in the orthorhombic space group *Pmmn* will be used for the description of the room-temperature crystal structure of $Cu_{3-x}Te_2$. Tellurium and copper atoms are distributed on one and two crystallographic sites, respectively (Figure 4.3). One copper position (Cu1 at the 2a site) is fully occupied, while the second (Cu2 at the 2b site) is partially occupied. The ordered part of the structure of $Cu_{3-x}Te_2$, the Te sub-cell and planar arrangements of Cu atoms, reproduce an atomic arrangement found in the tetragonal FeS (PbO) structure (space group *P*4/*nmm*). This structure type is typically observed for equiatomic phases described in the binary transition metal−Te (Se) systems, e.g., FeTe [156], FeSe [157], and mixed (Fe,Cu)Se [158]. Interestingly, in contrast, the CuTe phase exhibits a corrugated (not planar) Cu sublattice in the space group *Pmmn* [156].

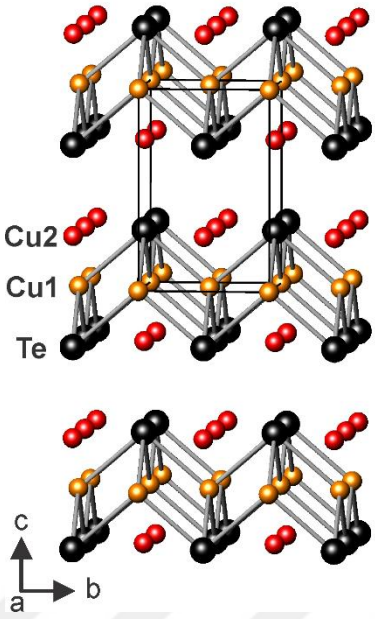

Figure 4.3 Crystal structure of $Cu_{2.8}Te_2$. The ordered part of the structure (Cu1 and Te atoms) is emphasized as the Cu−Te framework with *d*(Cu−Te) = 2.6313(9) and 2.6625(9) Å; the partially occupied Cu2 position [occupancy factor 0.406(1)] is represented as individual atoms.

The XRD results of the samples are shown in Figure 4.4, demonstrating that the target phase has been obtained successfully with a minute amount of CuTe as a secondary phase. With increasing nominal copper content (x = 0.1), the amount of CuTe is suppressed slightly. The lattice parameters of the two products were found to be a = 3.9933(1), b = 3.9635(1), c = 6.1159(3) Å for $Cu_{2.8}Te_2$ and a = 4.0067(2), b = 3.9793(2), c = 6.1120(3) Å for $Cu_{2.9}Te_2$. The slight increase in a and b and decrease in c lattice parameters for the latter case can be correlated with its fewer Cu vacancies (Cu2 occupancy: 0.422(9) and 0.446(7), respectively) (see Table 4.1 and Table 4.2 for $Cu_{2.9}Te_2$).

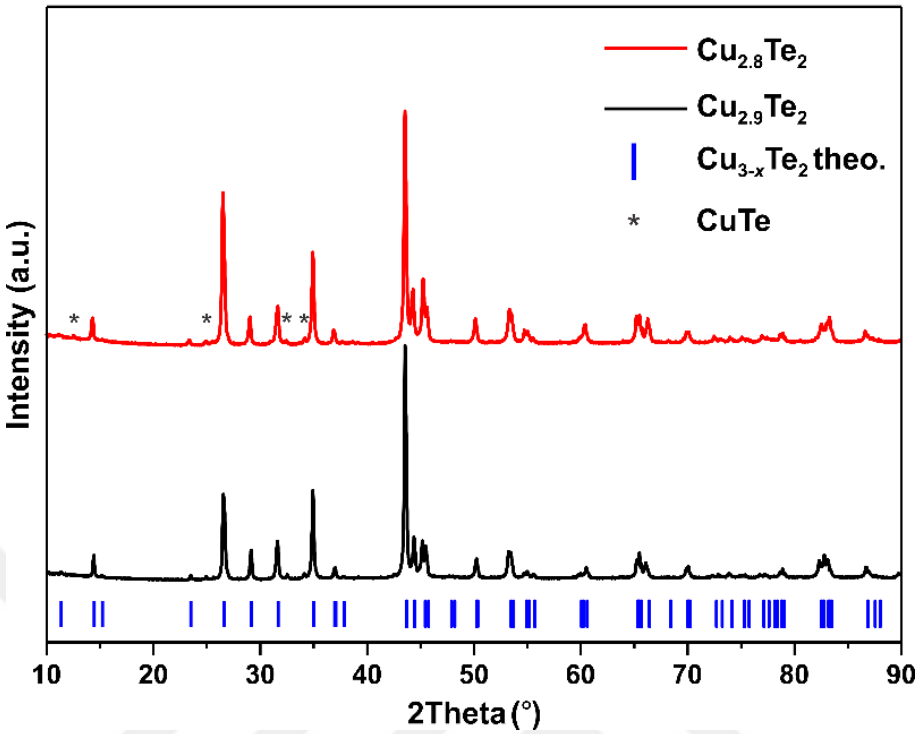

Figure 4.4 XRD patterns (Cu Kα) of experimental $Cu_{2.8}Te_2$ (red) and $Cu_{2.9}Te_2$ (black) after SPS. The ticks mark the theoretical peak positions of the low-temperature phase of $Cu_{3-x}Te_2$.

Table 4.1. Crystallographic data of $Cu_{2.9}Te_2$.

Composition	$Cu_{2.89(1)}Te_2$
Space group	*Pmmn*
Formula units per unit cell, *Z*	2
Lattice parameters*	
a / Å	4.0067(2)
a / Å	3.9793(2)
c / Å	6.1120(3)
V / Å^3	97.449(8)
Crystal form	irregular block
Crystal size / μm	25 × 40 × 60
Diffraction system	RIGAKU AFC7
Detector	Saturn 724+ CCD
Radiation, λ / Å	Mo$K\alpha$, 0.71073
Scan; step / degree; *N*(images)	φ, 0.6, 1200
Maximal 2θ / degree	64.05
Absorption correction	Multiscan
T(max)/*T*(min)	2.36
Absorption coeff. / mm^{-1}	30.1
Range in *h*, *k*, *l*	$-5 \le h \le 3$ $-5 \le k \le 4$ $-8 \le l \le 8$
N(*hkl*) measured	729
N(*hkl*) unique	204
R_{int}	0.029
N(*hkl*) observed	203
Observation criteria	$F(hkl) \ge 4\sigma(F)$
Refined parameters	14
*R*1	0.024
*wR*2	0.060
Residual peaks / e Å^{-3}	−1.44/1.53

*X-ray powder diffraction data (Huber Guinier G670 Camera, CuKα_1 radiation)

Table 4.2. Atomic coordinates, displacement parameters (in Å^2) and site occupancy factor (*SOF*) of $Cu_{2.9}Te_2$ in *Pmmn* (R1= 0.024; wR2 = 0.060). Standard deviations are provided in parentheses.

Atom	**Site**	***SOF***	***x***	***y***	***z***	U_{iso}
Cu1	2*a*	1	¼	¾	0.0000(1)	0.0233(3)
Cu2	2*b*	0.446(7)	¼	¼	0.7048(4)	0.0256(9)
Te1	2*b*	1	¼	¼	0.28462(7)	0.0197(2)

High-temperature XRD measurements were performed on a $Cu_{2.8}Te_2$ sample at 300 K, 473 K, and 673 K to investigate the phase transformations. The results, shown in Figure 4.5(a), indicate reversible phase transitions following the sequence orthorhombic ↔ tetragonal ↔ hexagonal phases (see XRD data in Figure 4.5(b) for 5-40 2theta range and in Figure 4.6 for the orthorhombic deformation of the tetragonal unit cell). The pattern obtained at 673 K could not be indexed with the cubic unit cell and lattice parameters reported by Stevels et al.[54]. However, the pattern was successfully indexed by considering a hexagonal unit cell with lattice parameters a = 7.2886 Å and c = 7.855 Å.

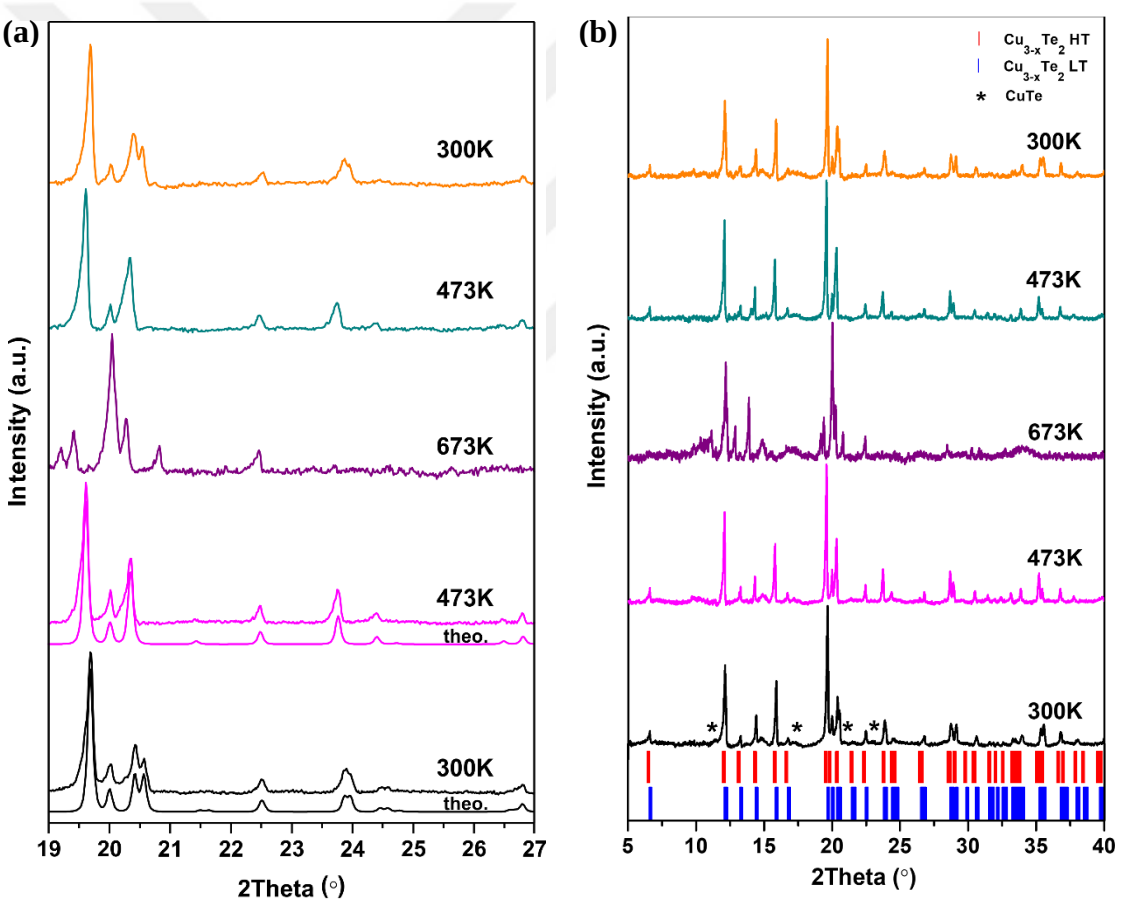

Figure 4.5 (a) HTXRD patterns (Mo Kα) of a $Cu_{2.8}Te_2$ sample at 300, 473, and 673 K upon heating and cooling [theoretical patterns for orthorhombic (black) and tetragonal (pink) phases are given below the experimental data], **(b)** HT-XRD patterns (Mo Kα) of a $Cu_{2.8}Te_2$ sample at 300 K, 473 K, and 673 K upon heating and cooling (tick marks represent theoretical peak positions; blue: LT, red: HT).

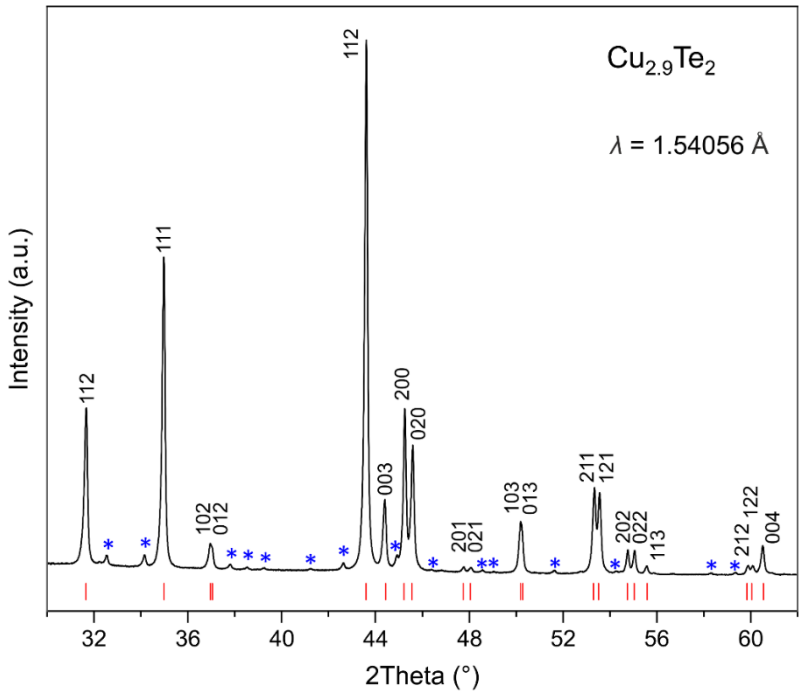

Figure 4.6. The selected region of the X-ray powder pattern of $Cu_{2.9}Te_2$ recorded at ambient conditions (Huber Guinier G670 camera, Cu Kα_1 radiation). The ticks mark theoretical peak positions of calculated sub cell (space group Pmmn, a = 4.0067 Å, b = 3.9793 Å, c = 6.1120 Å). The indices are displayed above the corresponding peaks. The observed splitting of the reflections is typical for the orthorhombic deformation of the tetragonal unit cell. The asterisks mark reflections that are compatible with the modulation vector q = [0 ~0.40 0].

The crystal structure analysis was challenging due to the high absorption of the sample for the weak modulated reflections for the low temperature and its reversible phase transition for the high temperatures. The analysis after quenching the sample is not possible as the structural transformations are reversible and the phase goes back to the orthorhombic modulated structure after cooling. The high-resolution powder diffraction by synchrotron measurements of $Cu_{2.9}Te_2$ (Figure 4.8) revealed that the patterns obtained between room-temperature and 420 °C support the HT-XRD measurements. While the room-temperature phase displays modulated orthorhombic phase, after 160 °C the phase is found to be tetragonal. The high-temperature crystal structure is a hexagonal phase showing enormous prefered orientation with the lattice parameters of a = 7.24 Å and c = 7.84 Å. As seen in the high-temperature kinetic study in Figure 4.7, the phase transformation starts around 340 °C, and the tetragonal phase completely transforms into hexagonal at around 370 °C where we actually observe the transition in DSC and the transport property measurements.

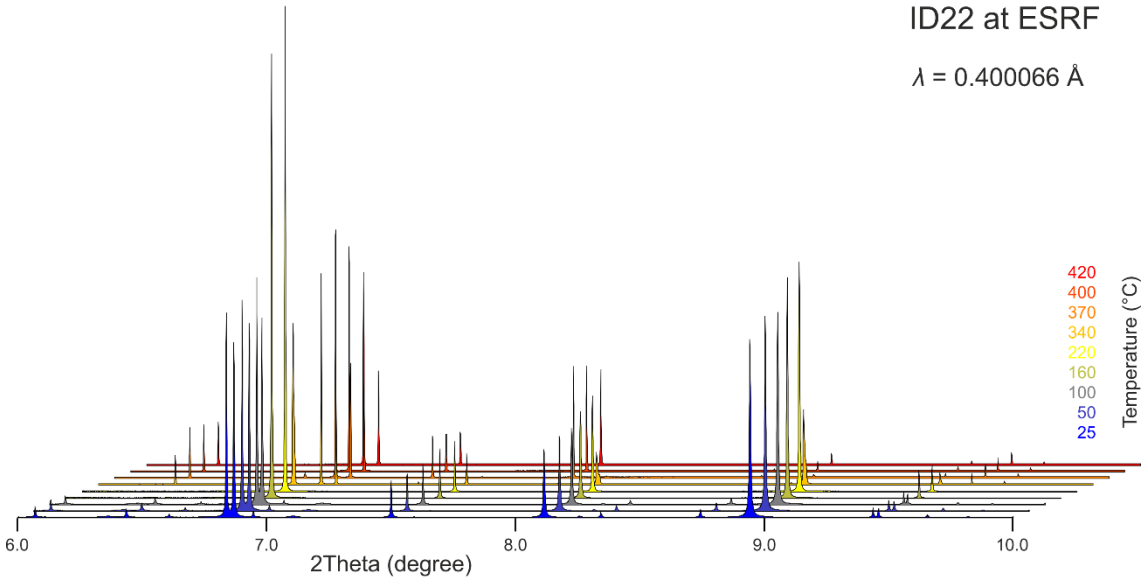

Figure 4.8 Temperature dependent high-resolution synchrotron x-ray powder diffraction pattern of $Cu_{2.9}Te_2$ between the range of 25 °C and 420 °C.

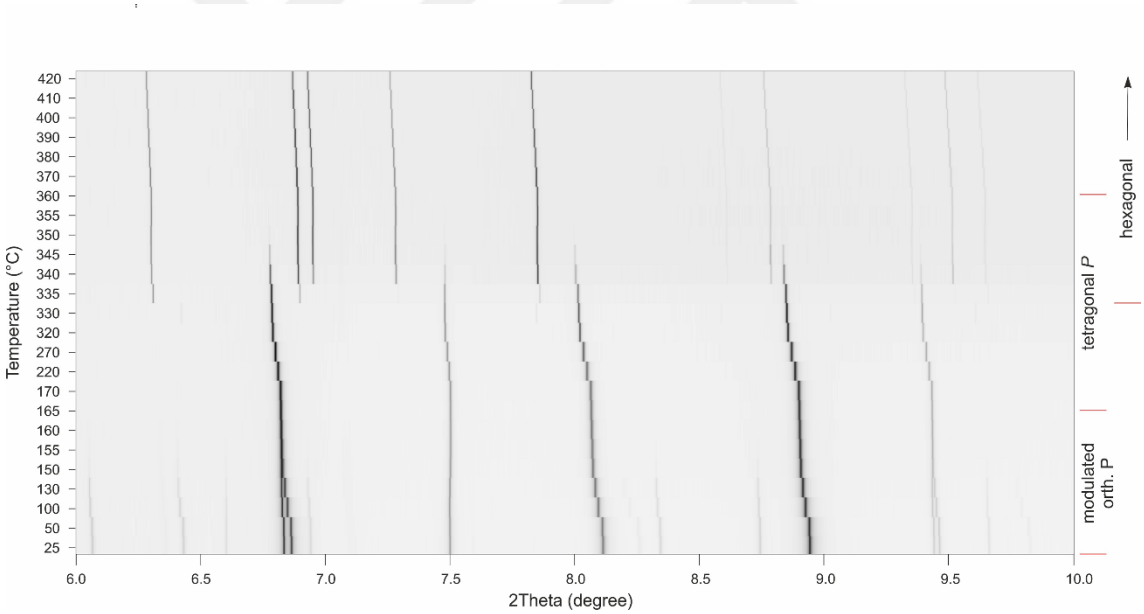

Figure 4.7 High-temperature kinetic study of high resolution x-ray powder diffraction data of $Cu_{2.9}Te_2$ showing phase transitions between the range of 25 °C and 420 °C.

The analysis of the modulated orthorombic structure by synchrotron measurement at room temperature (blue lines in Figure 4.9) shows that there are split reflections of the orthorhombic distortions structure and additional reflections belonging to the modulated structure. The observed splitting of the reflections is typical for the orthorhombic distortion of the tetragonal unit cell. After the first phase transition, the measurement at

425 K (red line in Figure 4.9) shows that the split reflections caused by distortions and the additional reflections caused by modulated structure disappear, leading to tetragonal structure, higher symmetry. A modulated structure refers to a crystal structure where the original translational symmetry is disrupted due to the introduction of periodic modulations. These modulations can occur in one or more directions and are characterized by modulation wavevectors, which describe the direction and period of the modulation. In this case, the modulation is along b-axis and more specifically, the modulated reflections are assigned to respective planes in the Figure A 2 with the modulation vector q = [0 0.39705(1) 0] by high-resolution synchrotron XRD analysis. The variation of the occupancy of Cu2 position and Cu-Te distances as a function of the fourth coordinate (x4) in the orthorhombic modulated structure is show in Figure A 3 displaying the direction and the periodicity of the modulation. The oscilation photo obtained by single crystal analysis along "b" axis with with q-vector = 0.397 shown in Figure A 4 confirms the synchrotron data. The set of weak modulated reflections with the q-vector are easily distinguishable from the strong reflections corresponding to the lattice parameter of 3.98 Å.

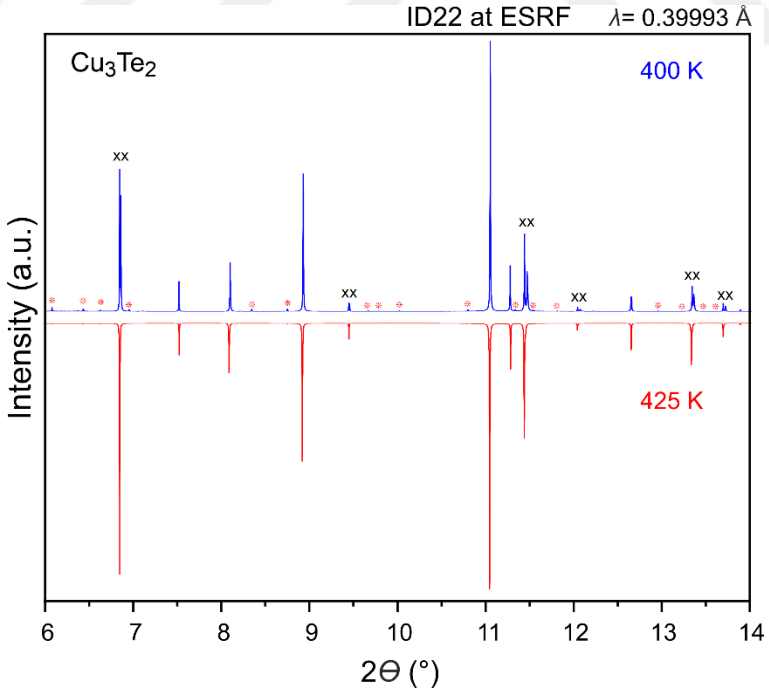

Figure 4.9 The XRD patterns of orthorombic modulated structure (blue) and tetragonal patterns (red) of $Cu_{2.9}Te_2$. "xx" marks correspond to split reflections in the orthorhombic structure, asterisks (*) indicate modulated reflections.

The high temperature crystal structure analysis successfully performed by Rietveld refinement when the best pattern was obtained by placing the capillary containing sample directly in the heat flow at 410 °C. The refinement result shows that the pattern matched well with the hexagonal structure. The hexagonal structure is described in *P*6/*mmm*, with 2Te and 7Cu positions and characterized by ordered Te sublattice and a completely disordered Cu sublattice ("liquid-solid") which shows the similar behavior with β-Cu_2Se [24]. The occupancies of the Cu positions vary between 0.123(1) and 0.678(1) (Figure 4.10 b).

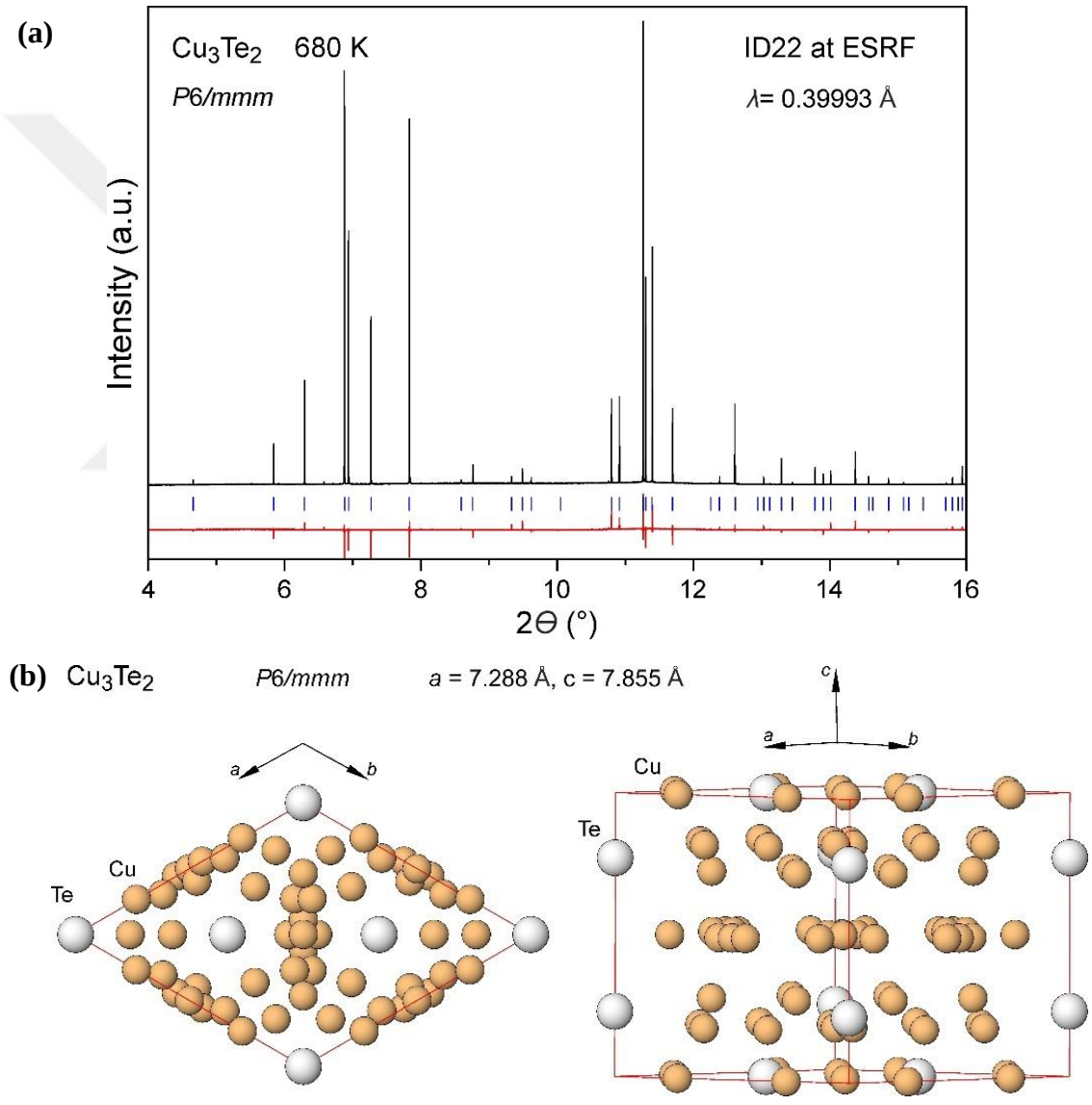

Figure 4.10 (a) High-resolution high-temperature synchrotron XRD pattern with the Rietveld refinement of $Cu_{2.9}Te_2$ at 680 K. The black line, the blue bars, and the red line represent the experimental pattern, calculated reflection positions, and the difference between the experimental and calculated intensities, respectively. (b) The representation of the hexagonal structure for high-temperature phase.

4.3.2 Phase Analysis

The EDX elemental mapping of $Cu_{2.8}Te_2$ indicates a homogenous distribution of Cu and Te throughout the microstructure (Figure 4.11). Further EDX measurements of the samples were carried out at 6 different randomly chosen spots. These analyses reveal that the actual chemical compositions of the samples match the nominal ones (Table 4.3). More accurate compositions were obtained from WDS analysis by averaging 10 measurement data points (Figure 4.12 and Table 4.4). The Cu content slightly increases with increasing the Cu content in the nominal composition; $Cu_{2.83(1)}Te_2$ (for $Cu_{2.8}Te_2$) and $Cu_{2.84(1)}Te_2$ (for $Cu_{2.9}Te_2$). These results are consistent with the existence of a small phase range for this material (Figure 4.1). Based on the reported binary phase diagram, the rickardite phase range was estimated to extend from $x = 0$ up to 0.18 in $Cu_{3-x}Te_2$[68].

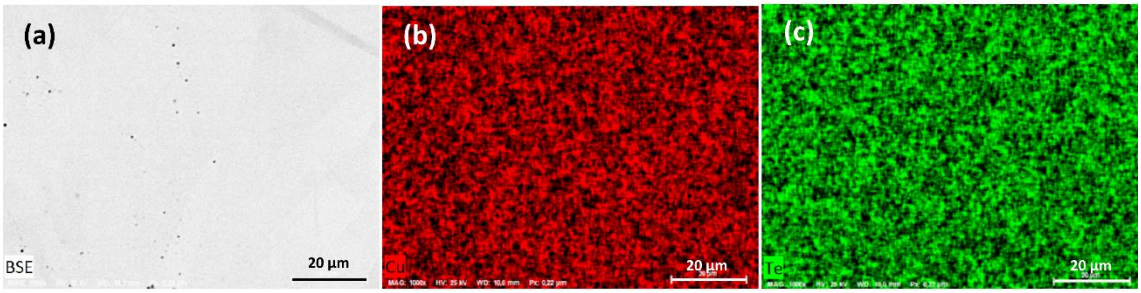

Figure 4.11. a) The back-scattered-electron image of $Cu_{2.8}Te_2$. Elemental mapping of the same sample showing the homogenous distribution of b) Cu and c) Te throughout the microstructure. Note that black spots on figure (a) belong to holes on the surface.

Table 4.3. The EDX analysis results of $Cu_{2.8}Te_2$ and $Cu_{2.9}Te_2$ (for the final composition, Te position is considered to be fully occupied).

Spot # / at%	$Cu_{2.8}Te_2$ **(nominal)**				$Cu_{2.9}Te_2$ **(nominal)**			
	Cu	**Te**	**Total**	**Composition**	**Cu**	**Te**	**Total**	**Composition**
1	58.4	41.6	100.0	$Cu_{2.80}Te_2$	59.1	40.9	100.0	$Cu_{2.89}Te_2$
2	58.5	41.5	100.0	$Cu_{2.82}Te_2$	59.4	40.6	100.0	$Cu_{2.92}Te_2$
3	58.2	41.8	100.0	$Cu_{2.78}Te_2$	59.1	40.9	100.0	$Cu_{2.89}Te_2$
4	58.4	41.6	100.0	$Cu_{2.80}Te_2$	59.6	40.4	100.0	$Cu_{2.95}Te_2$
5	58.4	41.6	100.0	$Cu_{2.80}Te_2$	59.5	40.5	100.0	$Cu_{2.93}Te_2$
6	58.2	41.8	100.0	$Cu_{2.78}Te_2$	58.7	41.3	100.0	$Cu_{2.84}Te_2$

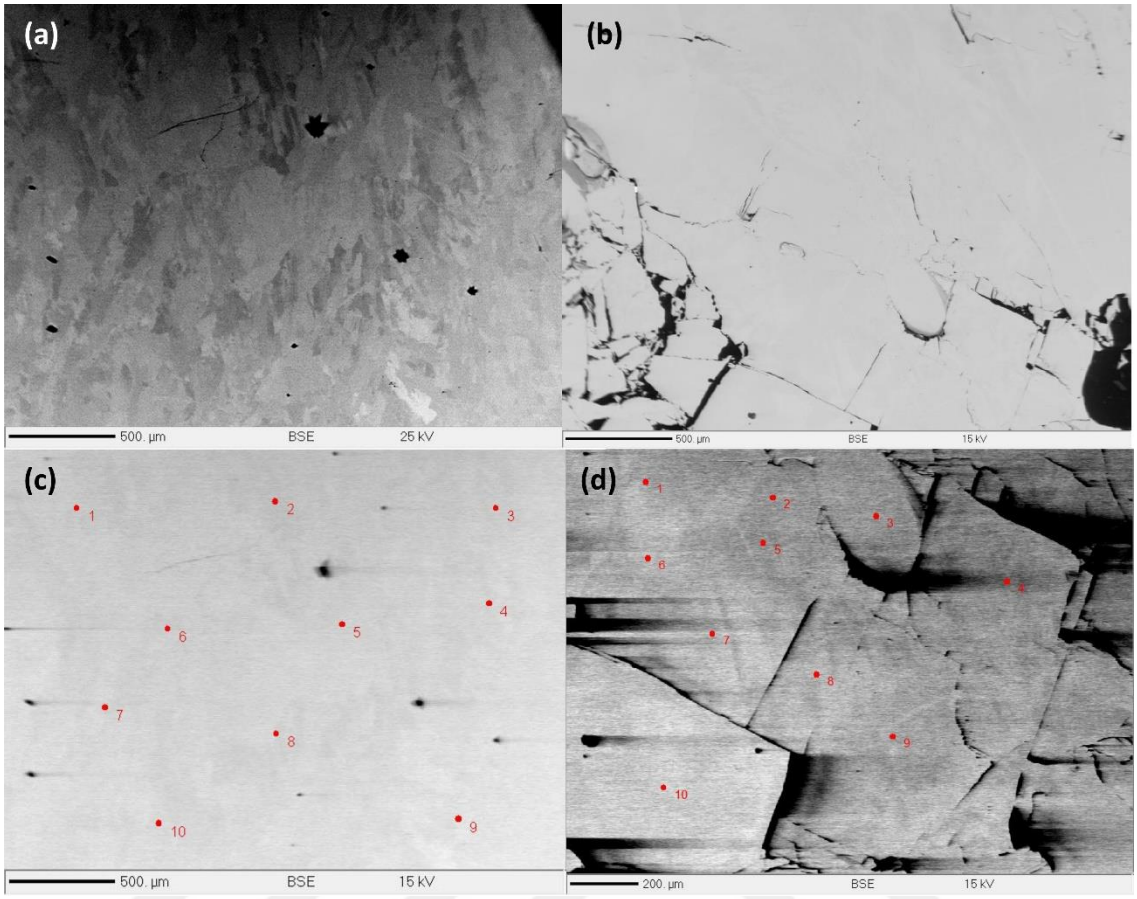

Figure 4.12. SEM images of a) $Cu_{2.8}Te_2$ and b) $Cu_{2.9}Te_2$ and with corresponding 10 different spots used for WDS analysis of c) $Cu_{2.8}Te_2$ and d) $Cu_{2.9}Te_2$.

Table 4.4. The WDS analysis results of $Cu_{2.8}Te_2$ and $Cu_{2.9}Te_2$.

	$Cu_{2.8}Te_2$ **(nominal)**			$Cu_{2.9}Te_2$ **(nominal)**		
	Atomic %	**Weight %**	**StdDev wt%**	**Atomic %**	**Weight %**	**StdDev wt%**
Cu	58.6	41.4	0.2	58.7	41.5	0.2
Te	41.4	58.6	0.2	41.3	58.5	0.2
Total	100.0	100.0		100.0	100.0	
	$Cu_{2.83(1)}Te_2$			**$Cu_{2.84(1)}Te_2$**		

Optical micrographs show strong orientation contrast of the target phase in polarized light (Figure 4.13). The microstructure is formed by primary grains of irregular shape that contain fine, lamellar domains. The shape and the very regular orientation of the domains strongly indicate a solid-state formation of the targeted phase during sample preparation. The very fine lamellae may originate from a polymorphic phase transformation from the primary high-temperature phase. Needle-like domains are generally consequences of a peritectoid decomposition of minor portions of the high-temperature phase. The grain size

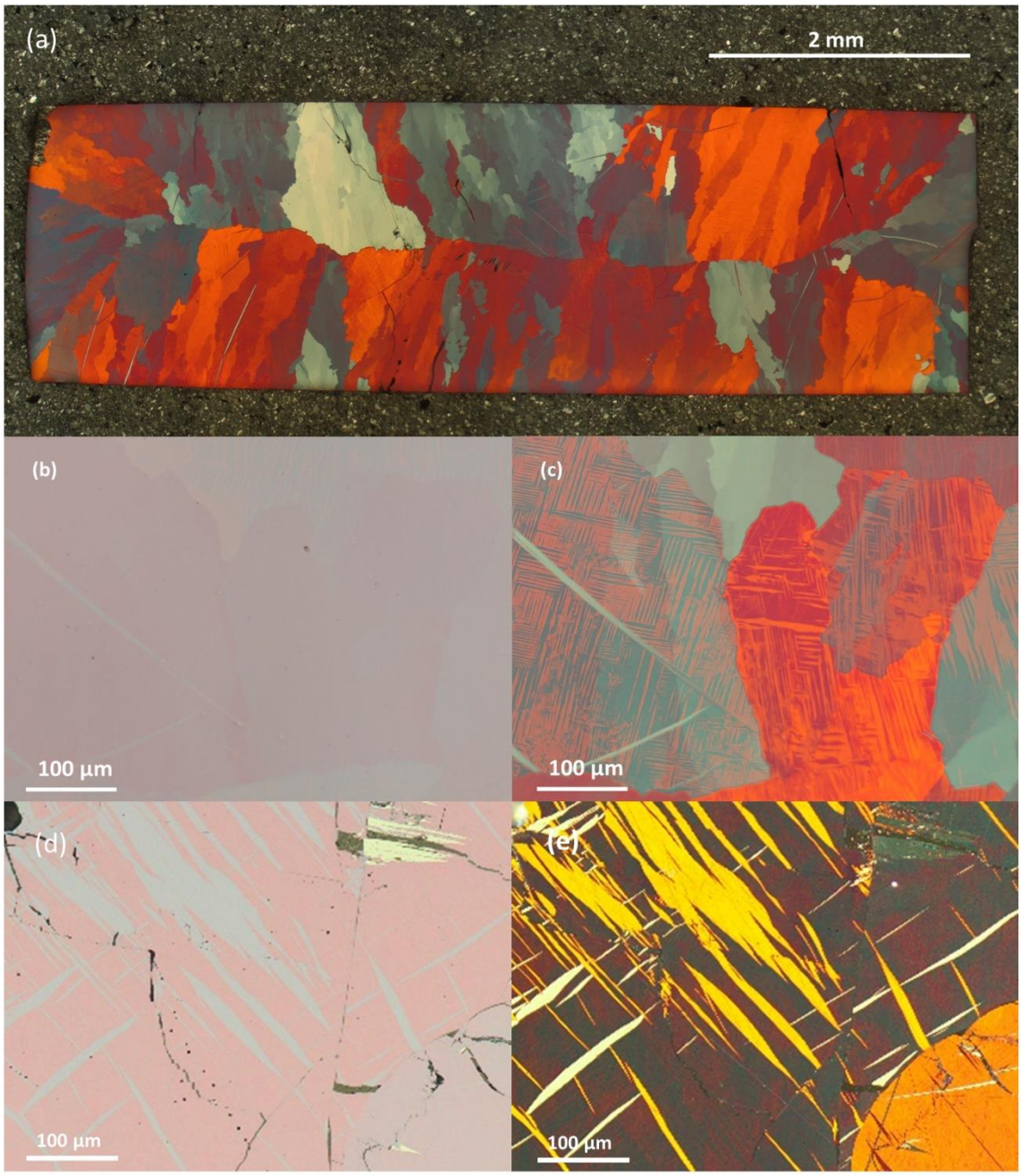

Figure 4.13 OM images of rickardite samples: (a) bulk piece under polarized light, (b) zoomed version of the bulk piece under a bright field, and (c) polarized light of $Cu_{2.8}Te_2$. (d) Bright field and (e) polarized light images of $Cu_{2.9}Te_2$.

of the samples varies between 10 and 200 ((m significantly. A network of needle-like grains is observed within much larger grains.

The DSC thermogram (Figure 4.14a) indicates that $Cu_{2.9}Te_2$ undergoes at least three phase transitions at around 458 K, 640 K, and 647 K. These transitions are similar to those reported by Stevels and Wiegers at slightly lower temperatures of 413 K, 623 K and 633 K[54]. The first transition was described as a second-order phase transition corresponding to a change in the lattice symmetry from orthorhombic to tetragonal. The shoulder observed at 640 K near the prominent endothermic peak at 647 K was discussed in the context of tetragonal-to-rhombohedral and rhombohedral-to-fcc phase transitions [54]. Our results do not support the presence of a high-temperature cubic phase up to 733 K. The exothermic peaks appearing in the cooling cycle indicate that the phase transitions are reversible. In the DSC diagram of $Cu_{2.8}Te_2$ (Figure 4.16 and Figure 4.15), four endothermic (at 460 K, 623 K, 650 K, and 691 K) and three exothermic peaks were observed on heating and cooling cycles, respectively. The first and third peaks are similar to the ones observed for $Cu_{2.9}Te_2$. The second endothermic peak is rather sharp and occurs at a distinctly lower temperature than the copper excess phase (623 K vs. 640 K). The additional endothermic peak at 691 K coincides with the incongruent melting temperature of CuTe by the reaction: CuTe $\rightarrow$ M (high T cubic phase) + L (Liquid).

The temperature dependence of the isobaric specific heat C_p of the $Cu_{2.9}Te_2$ sample is shown in Figure 4.14b. Only weak variations in the Cp values were observed between this sample and the stoichiometric sample $Cu_{2.8}Te_2$ (Figure 4.15). The low-temperature data of $Cu_{2.9}Te_2$ follows the free-electron formula $C_p/T = \gamma + \beta T^2$ below about 4.5 K. A fit of the data according to this relation yields an electron contribution γ of 10.3 mJ mol^{-1} K^{-2}, confirming a finite density of states at the Fermi level in the LT phase in agreement with the metallic behavior of this compound (see below). The β parameter of 2.85 mJ mol^{-1} K^{-4}, linked to the phonon contribution, corresponds to a Debye temperature of 200 K. At room temperature, C_p reaches a value of about 323 J mol^{-1} K^{-1}, which exceeds the Dulong-Petit limit of 300 J mol^{-1} K^{-1}. Upon further warming up to 733 K (Figure 4.14b), the two transitions evidenced by the XRD data give rise to two lambda-shaped anomalies at 458 and 647 K, in good agreement with the transport data. While the small amplitude of the first transition is in agreement with its weak fingerprints in the electronic data, the amplitude for the transition at 467 K is significantly larger, akin to that observed in SnSe [159, 160] near 800 K or in various argyrodite ionic conductors [161, 162].

Additional shoulder, close to the second phase transition temperature, is also visible at 640 K, which might correspond to the onset of the structural reordering.

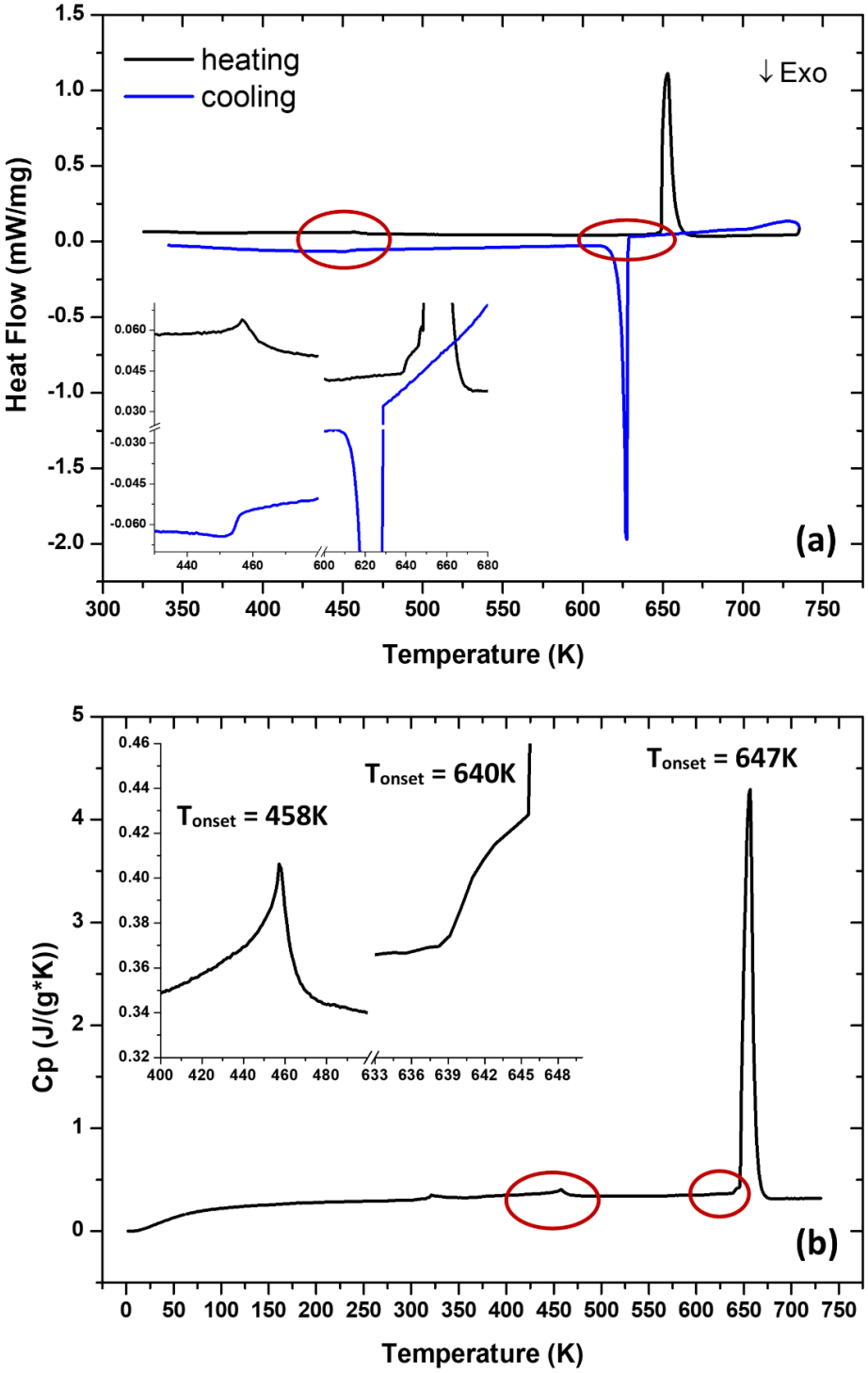

Figure 4.14 (a) DSC thermogram of $Cu_{2.9}Te_2$ (scanning rate 10 K min^{-1}) showing reversible phase transitions at 458, 640, and 647 K. (b) Cp data of $Cu_{2.9}Te_2$. The inset graphs show corresponding red marked phase-transition regions.

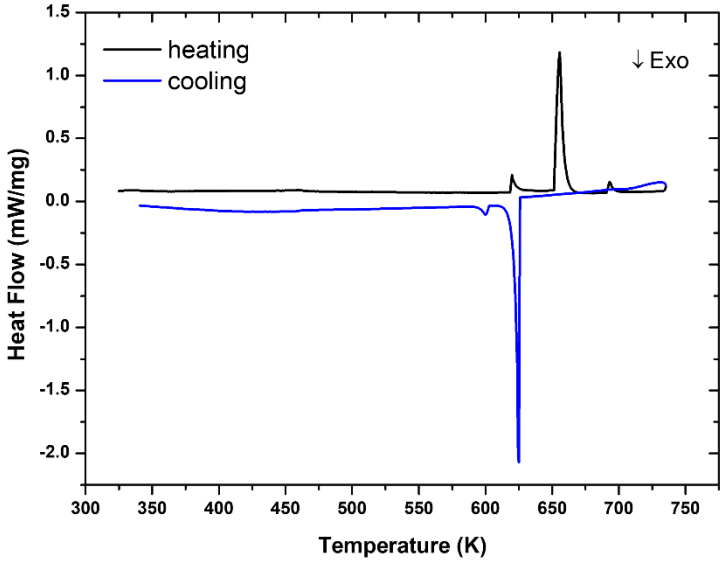

Figure 4.16. DSC thermogram of $Cu_{2.8}Te_2$ with heating and cooling rate of 10 K min^{-1}.

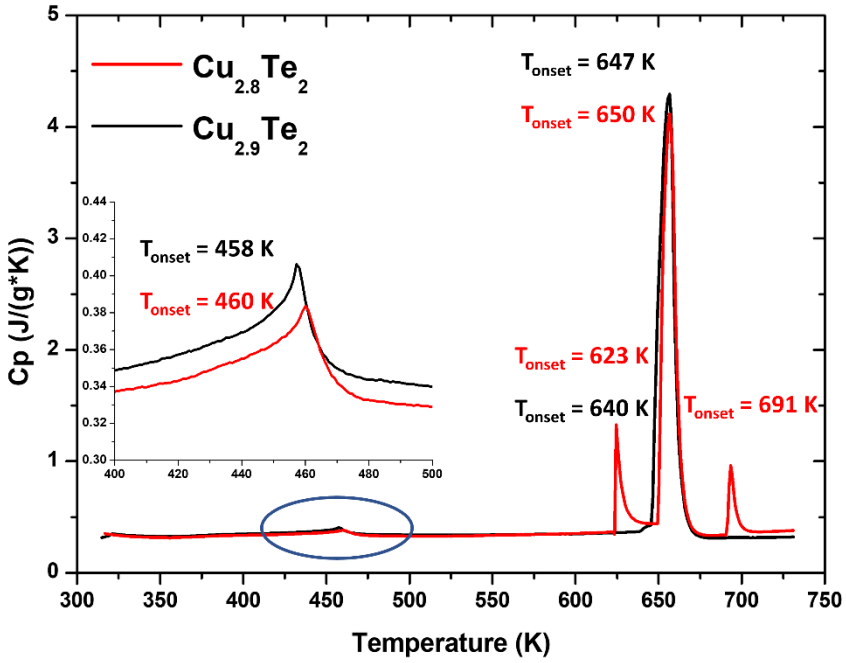

Figure 4.15. The Cp of $Cu_{2.8}Te_2$ and $Cu_{2.9}Te_2$, the inset graph shows corresponding blue marked phase transition region.

4.4 Transport Property Measurements

The temperature dependences of the electrical resistivity, ρ, and thermopower, α of $Cu_{2.9}Te_2$ sample are shown in Figure 4.17a and b, respectively. $Cu_{2.9}Te_2$ shows very low ρ values, indicative of a metallic behavior that weakly increases with increasing temperature up to 650 K. Consistent with this degenerate nature, the α values remain below 10 μV. K^{-1} up to about 600 K. The shallow dip observed near 450 K corresponds to the first structural transition, the influence of which on the electrical properties remains nevertheless weak. At low temperatures, α (T) shows a broad maximum reached near 50 K, likely due to a phonon drag contribution superimposed to the diffusive term that dominates above 100 K (Figure A 5 in Appendix A.). The positive α values over the entire temperature range are indicative of holes as the dominant charge carriers. In contrast to the smooth variations in ρ and α with temperature up to about 600 K, a sudden increase in both properties is observed above 650 K. This temperature closely corresponds to the HT structural transition evidenced by XRD and DSC. Additional measurements performed upon heating and cooling across this second high-temperature transition did not evidence any hysteretic behavior within experimental uncertainty (Figure 4.19, Figure A 6 and Figure A 7), in agreement with the reversible nature of this phase transition. All these traits remain similar in stoichiometric $Cu_{2.8}Te_2$, showing that both transitions are not sensitive to Cu stoichiometry (Figure A 8).

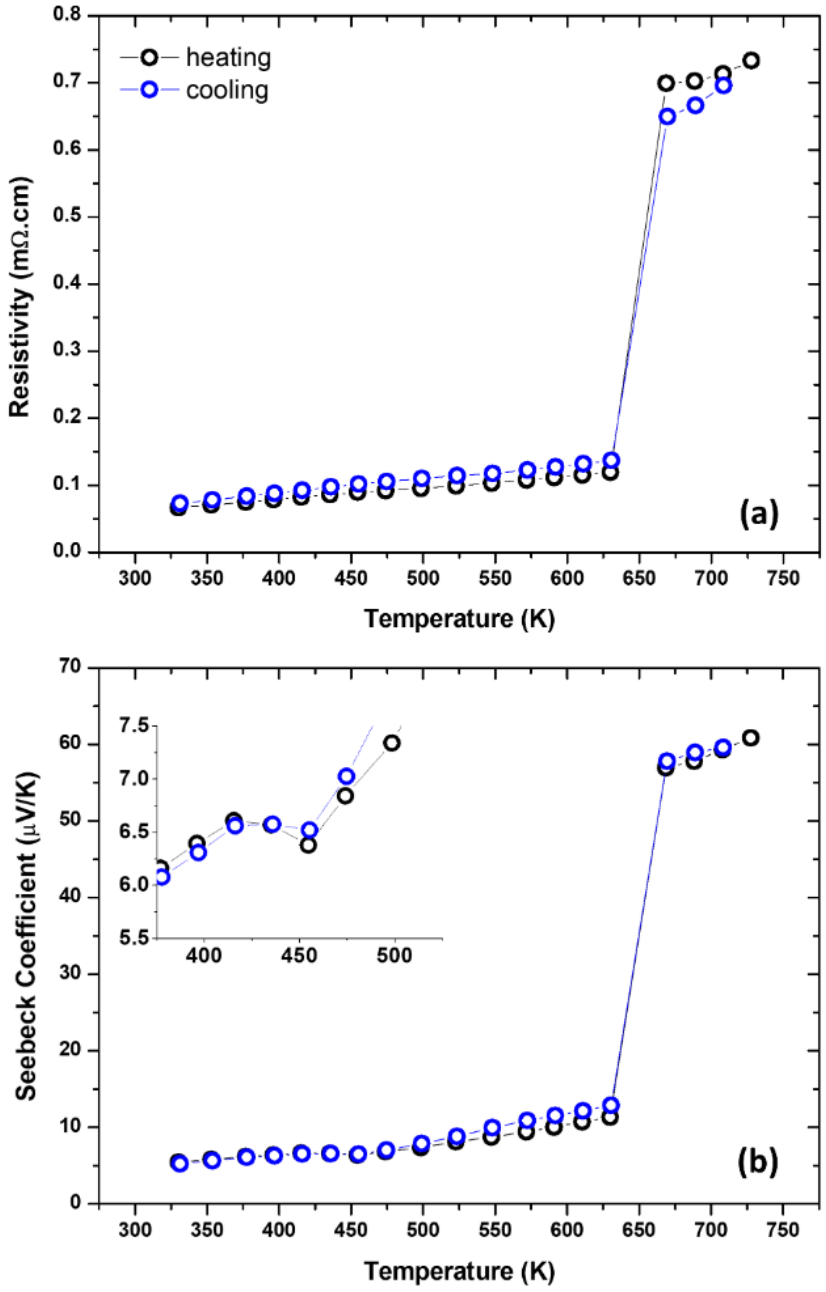

Figure 4.17 a) Electrical resistivity and b) Seebeck coefficient of $Cu_{2.9}Te_2$ as a function of temperature showing metallic behavior with a strong transition at 650 K and comparatively minor change at 450 K (see inset figure in (b)).

The nearly sevenfold and sixfold increase in ρ and α, respectively, observed above 650 K further suggests a metal-insulator-like transition. Removal of the density of states at the chemical potential induced by this transition, possibly leading to a full band gap opening, is supported by measurements of the magnetic susceptibility, χ (Figure 4.18). The negative χ values were measured below the transition temperature decrease at higher temperatures. This variation is consistent with a decrease in the Pauli contribution that originates from the free charge carriers and hence, with at least a partial removal of the electronic density of states. However, whether a complete band gap opens in the high-temperature phase will require electronic band structure calculations.

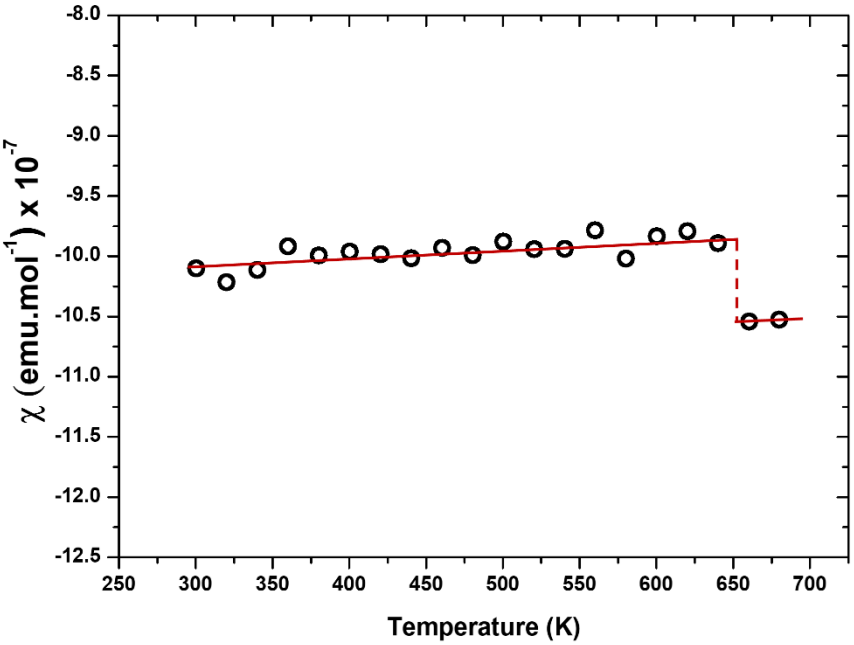

Figure 4.18 Temperature dependence of the magnetic susceptibility, χ of $Cu_{2.9}Te_2$ showing a small change at 650 K.

One interesting aspect of the transport in this compound is the negative sign of the Hall response, which is opposite to that of α. The magnitude of the Hall coefficients corresponds to a large concentration of electron-like carriers on the order of 3×10^{22} cm^{-3} at 300 K, which is consistent with the degenerate behavior of this compound. The opposite signs of α and the Hall coefficient R_H in this metallic compound bear strong resemblance with what is observed in the alkali metal Li and the noble metals Cu, Ag, and Au, for which the positive sign of α is a long-standing issue which is still yet to be fully understood [163].

Mainly three classes of scenarios have been advanced to reconcile both observations. A first-class relates this sign change to peculiarities in Fermi surface topology, the distortion of which close to the Brillouin zone boundaries yielding both electron-like and hole-like curvatures [164], with the extreme case of direction-dependent sign α in layered-like compounds dubbed as goniopolar materials [165]. The second class gathers models in which a strong energy dependence of electron-phonon interactions around the Fermi energy plays a central role [166]. A third possibility has been demonstrated in the specific case of Li, for which the positive sign of α originates from the energy dependence of the electron lifetime due to strong deviations in the electronic density of states around the Fermi energy from the free-electron model, with little influence of the electron-phonon coupling [167]. Determining which class $Cu_{2.9}Te_2$ falls will require detailed electronic band structure and Fermi surface calculations.

The temperature dependence of the total thermal conductivity κ at high-temperature is shown in Figure 4.19, while the low-temperature data are shown in Figure A 5c. Below 300 K, κ rapidly increases with increasing temperature, reaching a value of about 13 W m^{-1} K^{-1} at 150 K. Above this temperature, κ slowly decreases upon further warming to room temperature. The temperature dependence of κ is characteristic of crystalline solids with a dielectric maximum at low temperatures followed by a smooth decrease stemming

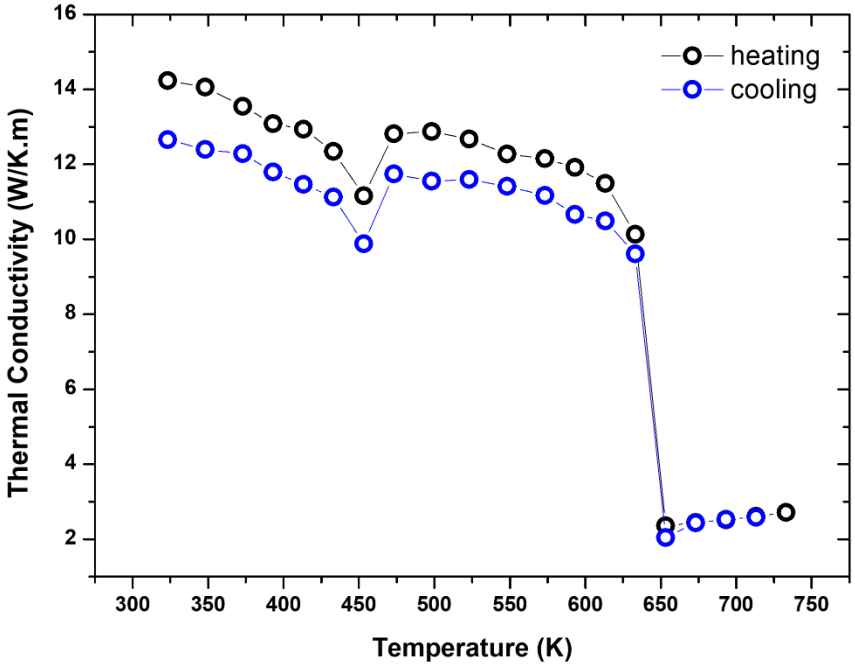

Figure 4.19 Thermal conductivity of $Cu_{2.9}Te_2$ showing effects of transitions at 450 and 650 K.

from Umklapp scattering processes (Figure A 5c). At higher temperatures, the first phase transition near 460 K is likely at the origin of the dip observed around this temperature. While the influence of this first transition on the thermal transport remains mild, the second phase transition observed in the Cp data gives rise to a sharp drop in the κ values. Upon crossing this structural transition at 647 K, κ drops from 10.0 W m^{-1} K^{-1} at 625 K to only 2.3 W m^{-1} K^{-1} above 650 K. Of note, unlike ρ and α, a weak hysteretic behavior was observed upon warming above the second phase transition temperature a second time (Figure A 7 b). These variations might be related to a change in the grain size or the microstructure.

The influence of structural phase transitions on the specific heat and thermal diffusivity has been discussed in prior studies on Zn_4Sb_3 at low temperatures and on binary Cu- and Ag-based chalcogenides that undergo transitions between 350 and 460 K [168, 169]. While the influence of structural phase transitions on C_p can be directly probed experimentally, how impacted the thermal diffusivity across such a transition remains a delicate problem that can have a significant impact on the estimation of the κ values and, hence, of the zT values. In particular, the usually observed dramatic decrease in the thermal diffusivity across the transition temperature may not reflect the intrinsic thermal transport of the material. In the case of $Cu_{2.8}Te_2$ and $Cu_{2.9}Te_2$, the possible gap opening induced by the structural transition near 650 K may also be at the origin of the substantial decrease in the diffusivity data. The C_p values that peak near this temperature have been estimated following the method widely used in prior studies, as shown in Figure 4.15. Most importantly, the enormously increasing C_p values reflecting the extra energy required to transit toward the high-temperature phase were not considered. As suggested in prior studies, the impact of such a transition on the thermal diffusivity data can be qualitatively investigated by determining the speed of the transition, reflected by the shift in the peak temperature in the C_p data upon varying the heating rate. While fast transitions will strongly lower the thermal diffusivity values, slower transitions will lead to smooth variations of the thermal transport across the transition. To determine into which category the present compounds fall, we have measured the C_p data of $Cu_{2.9}Te_2$ with a heating rate of 20 K min^{-1}, that is, twice as high as the measurements shown in Figure 6. The result evidence significant shifts in the peak temperature characterizing both transitions (6 and 10 K for the first and second transition, respectively), indicative of slow transitions (Figure A 9). This characteristic suggests that both transitions are smooth and hence, are

not expected to dramatically alter the thermal properties. The weak yet discernible fingerprint of the first phase transition at 450 K on the thermal transport data supports this conclusion. Hence, the strong drop observed in the κ values near 650 K can be mainly attributed to the electronic metal-insulator-like transition, which removes a large fraction of the electronic thermal conductivity, rather than to an artificial decrease in the thermal diffusivity due to the phase transition.

The strong metallic character of $Cu_{2.9}Te_2$ implies that a significant fraction of κ below 650 K is due to the electronic contribution κ_e. Thus, the significant reduction in κ is consistent with the metal-insulator transition observed in the electronic and magnetic properties. The substantial increase in ρ that accompanies this transition results in a drop in κ_e according to the Wiedemann-Franz (WF) law $\kappa_e = LT/\rho$ where L is the Lorenz number. Further disentangling the electronic and lattice contributions to κ is, however, challenging in the present case. Despite the strongly degenerate behavior of $Cu_{2.9}Te_2$, taking the corresponding degenerate limit for L, that is, $L_0 = 2.44\times10^{-8}$ V^2 K^{-2}, yields κ_e values that largely exceed κ above 35 K. The deviations of L from this universal limit suggest differing electrical and thermal relaxation times due to the presence of inelastic electron-phonon and electron-electron scattering processes that significantly lower L values. The large deviations from L_0 can be estimated by assuming that above the second phase transition κ_e is negligible compared to the lattice contribution κ_L due to the strong increase in ρ. If we further assume that κ_L is equivalent in both the LT and HT phases, the κ_L value measured at 650 K can be used to estimate κ_e at 600 K, and hence, L. This analysis yields a L value of 1.53×10^{-8} V^2 K^{-2}, which mirrors the low values usually determined in doped semiconductors above room temperature and unexpected results for such metallic material. The obtained low L value suggests that inelastic scattering events dominate the scattering mechanisms in this compound. Similar results were reported for some other complex metallic structures with unusually low Lorenz number [170], [87].

Figure 4.20 shows the temperature dependence of the dimensionless thermoelectric figure of merit, zT, of $Cu_{2.9}Te_2$ (see Figure A 8 for $Cu_{2.8}Te_2$). The strong metallic character of the transport properties below 650 K results in very small values. However, the metal-insulator transition undergone by $Cu_{2.9}Te_2$ results in a steep rise in the zT values above this temperature, with a peak value of around 0.14 achieved at 673 K, due to the concomitant increase in the power factor α^2/ρ and the drop in the thermal conductivity, κ.

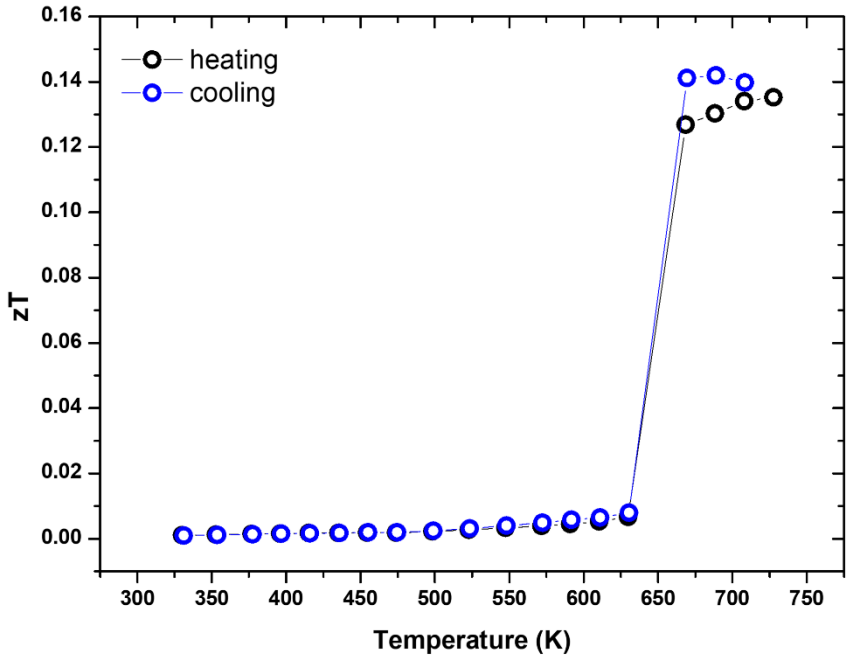

Figure 4.20 Temperature dependence of zT curves of $Cu_{2.9}Te_2$ upon heating and cooling showing rapid increase in zT above the transition at 650 K.

4.5 Conclusions

Synthetic polycrystalline rickardite samples with $Cu_{3-x}Te_2$ (x = 0.1 and 0.2) compositions were successfully synthesized by a direct solid-state reaction. These samples undergo several reversible phase transitions at 458 K, 640 K, and 647 K based on a combined analysis of high-temperature X-ray diffraction, differential scanning calorimetry, and specific heat measurements. The electronic and thermal transport properties measured over a broad range of temperatures (5 – 673 K) display signatures of these phase transitions with notably a crossover from metallic-like to semiconducting-like properties at around 650 K. A peak $zT \sim 0.14$ is obtained at 733 K thanks to moderate power factor and low thermal conductivity attained in the high-temperature phase. As a phase-changing material, the current study on rickardite minerals may provide insightful strategies for designing functional products, e.g., in waste-heat harvesting and photovoltaic systems.

CHAPTER 5

EFFECT OF SUBSTITUTON (Zn, Ag) ON PHASE TRANSITION TEMPERATURE AND THERMOELECTRIC TRANSPORT PROPERTIES OF $Cu_{2.9}Te_2$

5.1 Introduction

Many studies on suppressing phase transitions have been implemented to obtain more stable and highly efficient thermoelectric materials, such as in GeTe, by introducing high entropy via multiple doping to form $Ge_{0.84}In_{0.01}Pb_{0.1}Sb_{0.05}Te_{0.997}I_{0.003}$ [171]. Since the high-temperature phase has higher thermoelectric performance than the low-temperature phase, decreasing in the phase transition temperature improved the performance significantly over a wide temperature range while increasing the Seebeck coefficient and decreasing the thermal conductivity. The phase transition temperature of this compound decreased dramatically from 660 K in pristine GeTe to 523 K in $Ge_{0.84}In_{0.01}Pb_{0.1}Sb_{0.05}Te_{0.997}I_{0.003}$. Increasing the symmetry in the structure and having a large effective mass also helped to improve the efficiency, and optimizing entropy helped suppress the lattice's thermal conductivity [171]. In another study of GeTe, by Bi- and Mn-doping on Ge sites, the phase transition was successfully suppressed from 700 K to 300 K [172].

With the Ag_2Te incorporation into Cu_2Te, the high carrier concentration in Cu_2Te due to the migration of Cu is significantly reduced, leading to a substantial decrease in thermal conductivity and an enhancement in power factors within the working temperature range. Moreover, the phase transition temperature was significantly suppressed with increasing Ag incorporation by sustaining improved TE properties of the cubic phase at low temperatures [64].

In the light of all these studies, to optimize the carrier concentration and examine the effect of substitution on phase transition temperatures, an extensive investigation was conducted on $Cu_{2.9}Te_2$ with Zn- and Ag-substitution of $M_xCu_{2.9-x}Te_2$ ($M = Zn, Ag$, x = 0.05, 0.10 for Zn, x = 0.05, 0.10, 0.20 for Ag). Consequently, the study focused on exploring the influence of substitution on the transport properties during the phase transitions and the corresponding transition temperatures.

5.2 Experimental Methods

The pristine and the doped samples were prepared the same way as discussed in section 4.2. The Zn and Ag substituted $Cu_{2.9}Te_2$ samples were synthesized by reacting cleaned copper, tellurium, and the dopant element (Zn or Ag) in the stoichiometric ratio by a solid-state synthesis method. Raw materials were sealed into a carbon-coated silica tube under a vacuum. The sealed tube was placed into a muffle furnace and kept at 1223 K for 12 h. After quenching in water at room temperature, the tube was put into a preheated furnace for further annealing at 623 K for 96 h. For chemical characterization and transport property measurements, dense cylindrical pellets were obtained by SPS in a graphite die at 623 K for 10 min under a pressure of 65 MPa.

5.3 Characterization

The characterization of the samples were done using XRD, SEM, and EDX methods for compositional and microstructural analysis as well as DSC measurements for the determination of thermal behavior and phase change temperature. The crystal structure analysis of pristine $Cu_{2.9}Te_2$ sample was discussed in section 4.3.1 in details.

The XRD results of the samples are shown in Figure 5.1, showing that the targeted phase is obtained successfully with a small amount of CuTe as a secondary phase as it was reported in the previous section. If we discuss the results one by one, with Zn-substitution (0.05 and 0.1), in both composition, there is $Cu_{1.5}Zn_{0.4}Te$ phase observed as an impurity phase beside CuTe phase occurs in all of the samples.

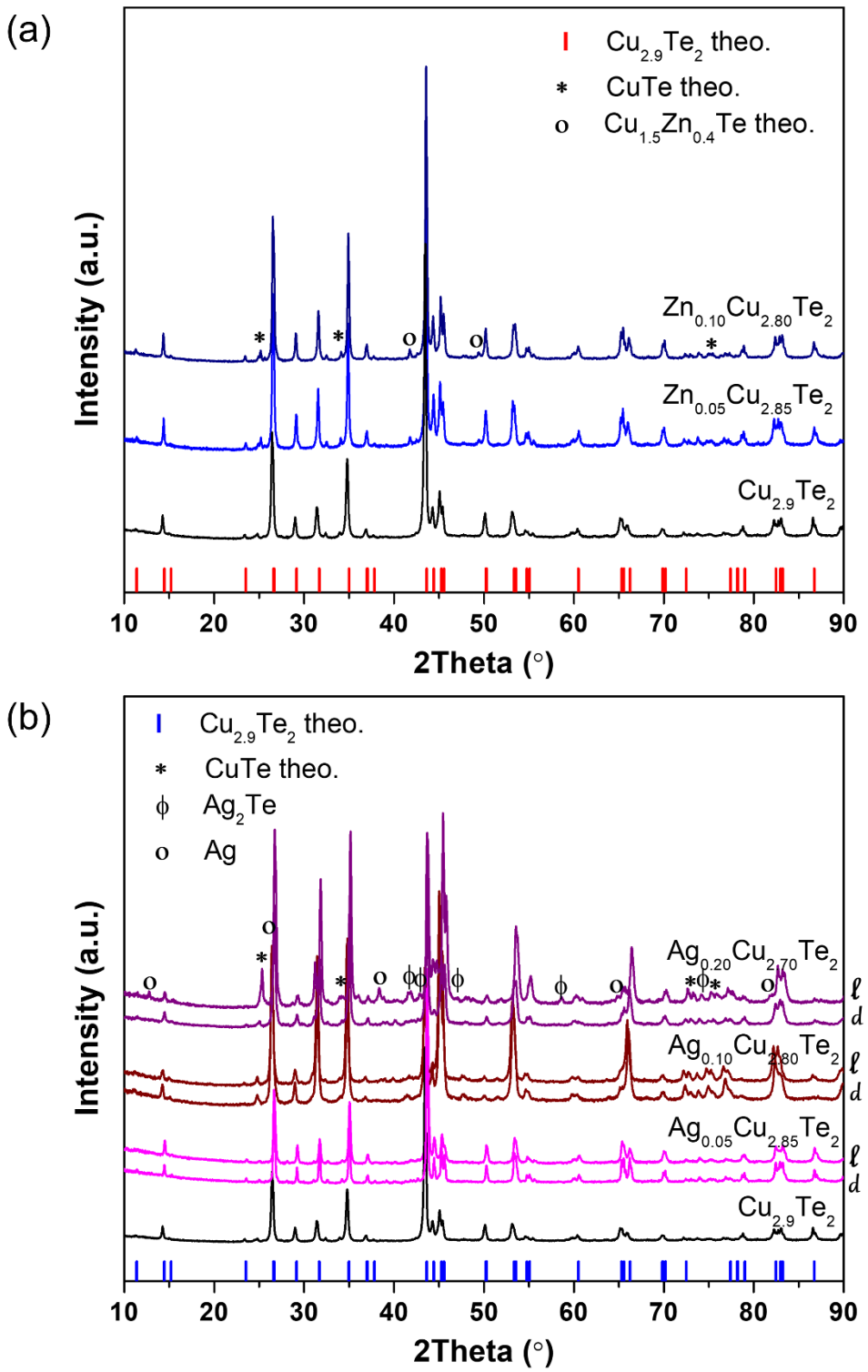

Figure 5.1 XRD patterns (Cu Kα) of experimental a) Zn- and b) Ag-substituted $Cu_{2.9}Te_2$ samples after SPS. The ticks mark the theoretical peak positions of the low-temperature phase of $Cu_{3-x}Te_2$.

The color of $Cu_{3-x}Te_2$ samples are a bir different; $Cu_{2.8}Te_2$ is a bit lighter, reddish purple, while $Cu_{2.9}Te_2$ is darker, bluish purple as discussed in chapter 4. With inctrasing Zn-substitution, although the color distribution is homogenous, the pellets gets lighter purple color and it is easily recognizable as seen in Figure 5.2 a. The left one is $Zn_{0.05}Cu_{2.85}Te_2$ and the right pellet is $Zn_{0.10}Cu_{2.80}Te_2$ sample. With the Ag-substitution in $Ag_{0.05}Cu_{2.85}Te_2$, $Ag_{0.10}Cu_{2.80}Te_2$, $Ag_{0.20}Cu_{2.70}Te_2$ samples, the samples after SPS show inhomogenous color distribution over the densified pellets. While one side of the pellets has the light reddish purple color (similar to $Cu_{2.8}Te_2$ composition), the other side of the pellet has dark blueish purple color (similar to $Cu_{2.9}Te_2$ composition). There is a clear composition difference within along the height of the pellet. The color difference is not that notacable with the $Ag_{0.05}Cu_{2.85}Te_2$, however, it is visible on $Ag_{0.10}Cu_{2.80}Te_2$ and visually more clear on $Ag_{0.20}Cu_{2.70}Te_2$ as seen in Figure 5.2 b for visualization. The X-ray diffraction measurements were done on both sides to understand the phase difference if there is any and the patterns are abbreviated as "*l"* and "*d"* next to the patterns for light and dark sides, respectively.

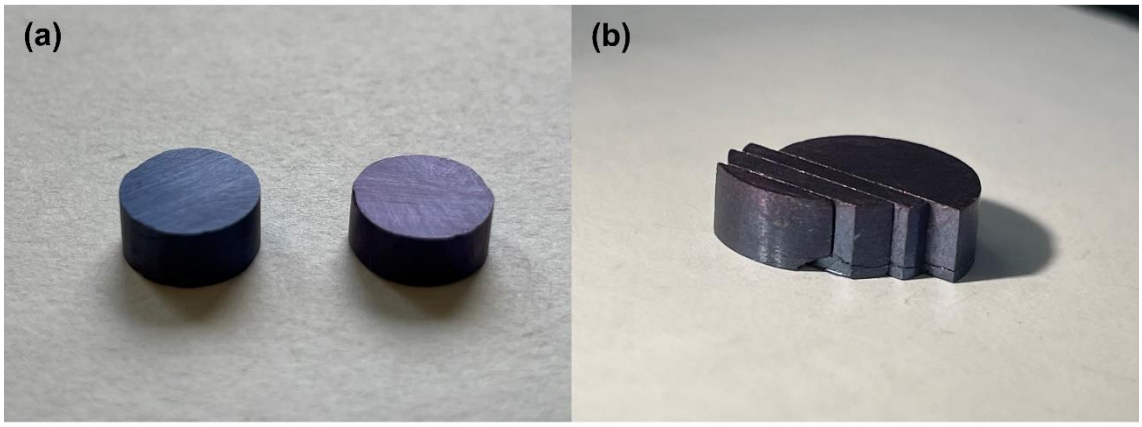

Figure 5.2 Pellets of a) $Zn_{0.05}Cu_{2.85}Te_2$ and $Zn_{0.10}Cu_{2.80}Te_2$, and b) $Ag_{0.20}Cu_{2.70}Te_2$ after SPS.

Scanning electron microscopy (SEM) images of all the samples have secondary phases homogenously distributed all over the sample. Figure 5.3 shows that $Ag_{0.10}Cu_{2.80}Te_2$ sample has brighter regions distributed homogenously along the sample which is a phase of Ag rich region where it is confirmed as Ag_2Te by XRD analysis. Even though the grains of $Cu_{2.9}Te_2$ samples in general is not visible with SEM imaging, the secondary phases are located in the Zn- and Ag-substituted samples at the grain boundaries.

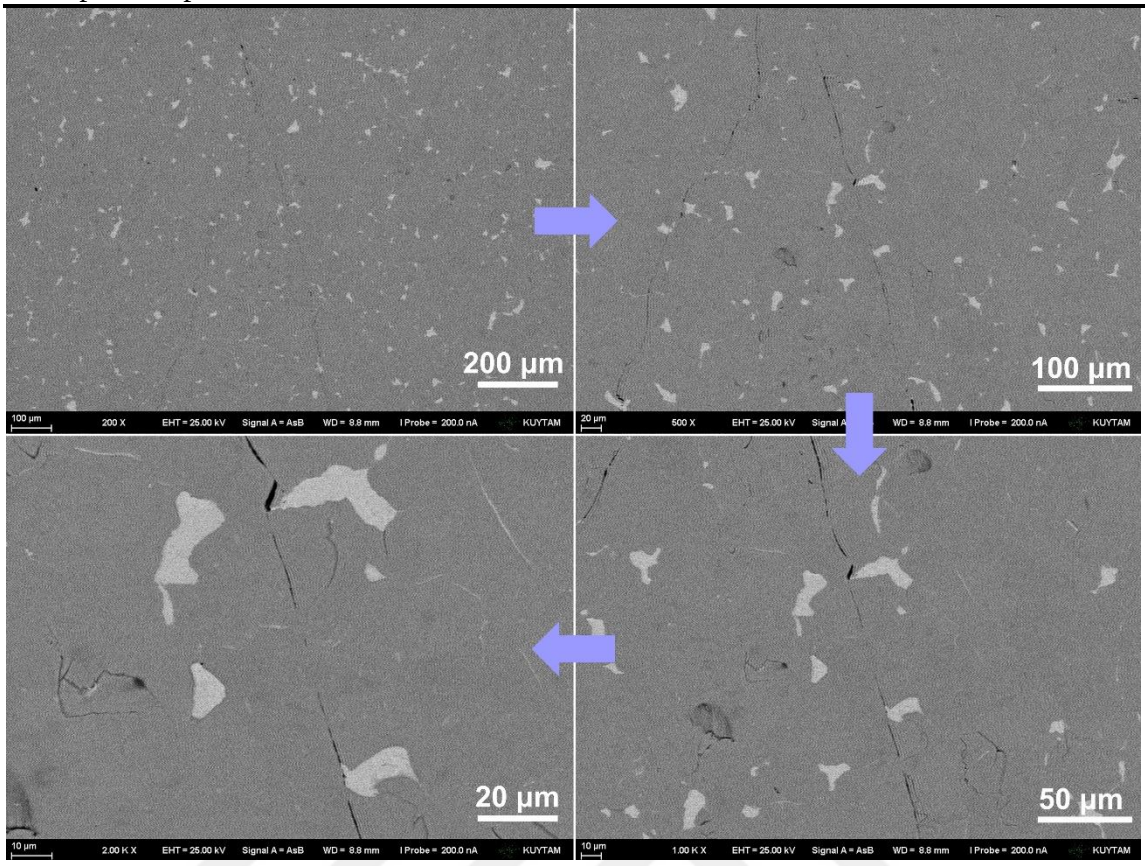

Figure 5.3 SEM images of $Ag_{0.10}Cu_{2.80}Te_2$ after SPS with different magnifications.

The EDX elemental mapping of Zn- and Ag-substituted $Cu_{2.9}Te_2$ samples confirms the homogenous distribution of the main phase as well as the binaries (Figure 5.4 for $Ag_{0.10}Cu_{2.80}Te_2$, Figure B 1 for $Ag_{0.05}Cu_{2.85}Te_2$, Figure B 2 for $Zn_{0.10}Cu_{2.80}Te_2$, and Figure B 3 for $Zn_{0.05}Cu_{2.85}Te_2$). The elemental mappings show that Zn or Ag is replaced Cu regions in the lighter regions in the SEM (Figure 5.4). The Zn or Ag rich regions are slightly deficient on Cu, almost none. The secondary phases of Ag_2Te is distributed as a relatively large grains as well as along the grain boundaries. The compositional analysis done by EDX system is listed in . The analysis were made on the first SEM images of each EDX analysis images of Figure 5.4, Figure B 1, Figure B 2, and Figure B 3. The compositions are close to the nominal compositions.

Table 5.1 The EDX analysis results of the samples (for the final composition, Te position is considered to be fully occupied)

Nominal Comp.	Zn/Ag (at %)	Cu (*at* %)	Te (at %)	calculated comp.
$Zn_{0.10}Cu_{2.80}Te_2$	2.36	56.64	41.00	$Zn_{0.11}Cu_{2.76}Te_2$
$Ag_{0.05}Cu_{2.85}Te_2$	1.18	58.68	40.14	$Ag_{0.05}Cu_{2.92}Te_2$
$Ag_{0.10}Cu_{2.80}Te_2$	2.33	56.39	41.27	$Ag_{0.11}Cu_{2.73}Te_2$

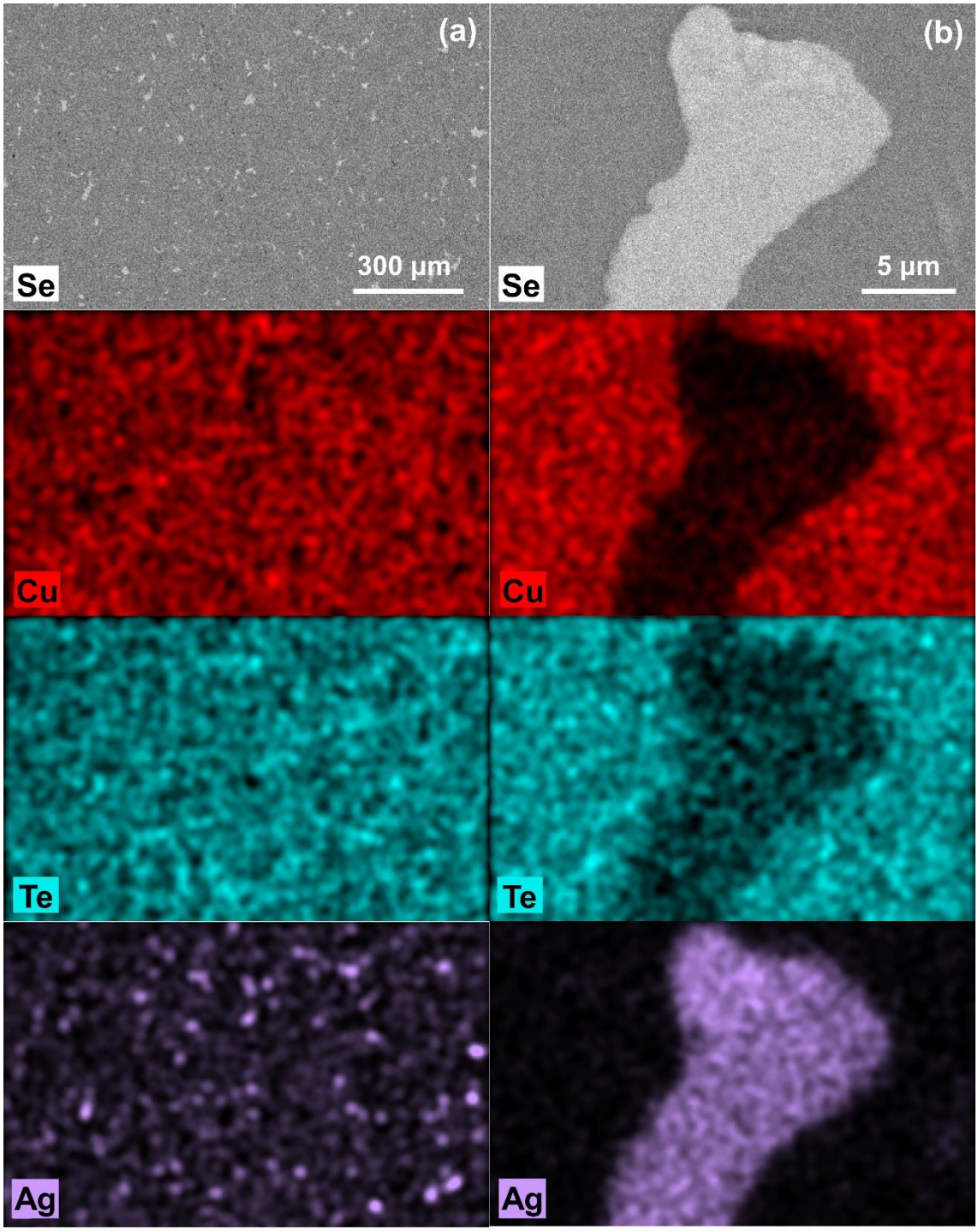

Figure 5.4 a) and b) SEM images of $Ag_{0.10}Cu_{2.80}Te_2$ with different magnifications, and the elemental mapping analysis (EDX) of the same SEM images showing the distribution of Cu, Te, and Ag distributions.

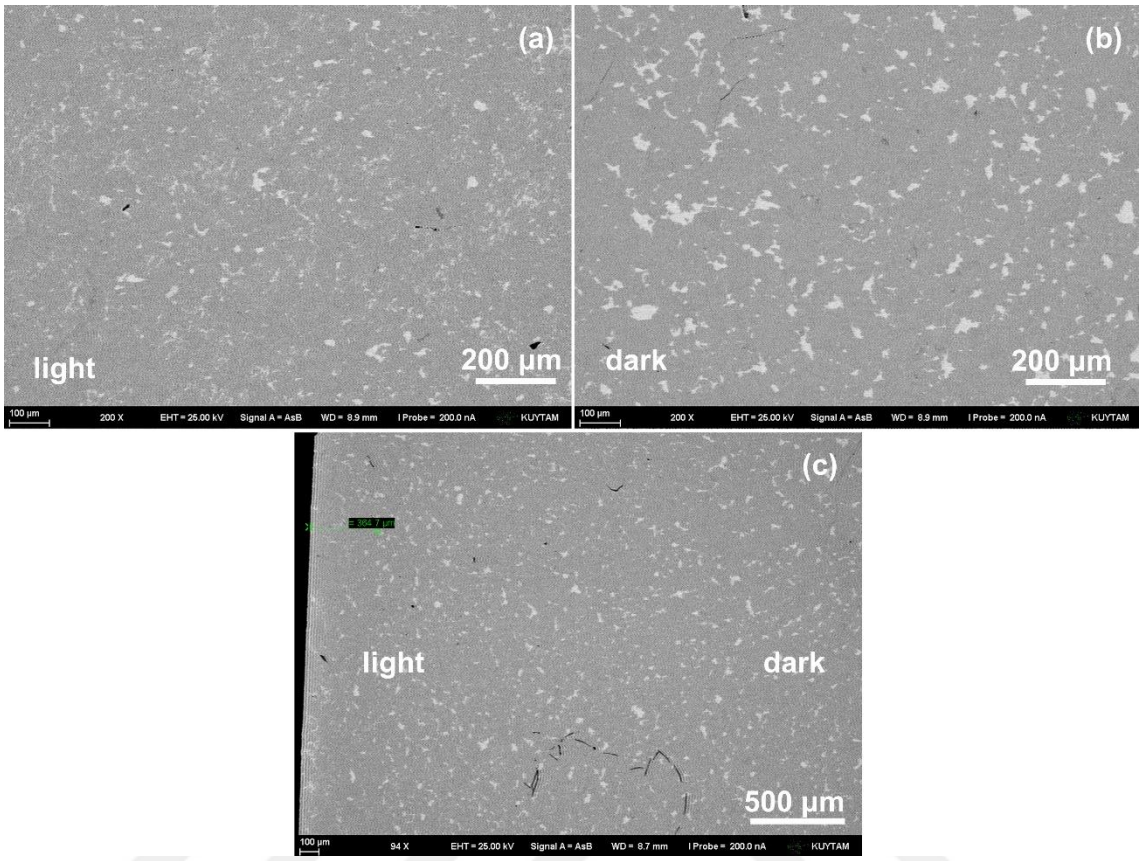

Figure 5.5 SEM images of $Ag_{0.20}Cu_{2.70}Te_2$ after SPS a) light side, b) dark side of the pellet, and the cross-section of the same sample.

The SEM images of $Ag_{0.20}Cu_{2.70}Te_2$ is shown in Figure 5.5. The pellet of the sample has different color on each side and the SEM images are showing that the distribution and the size of Ag-rich composition is different on each side. The light purple side has smaller and more spreaded distribution of this phase while the dark purple side of the pellet has larger grains of this phase. The crossection of the same pellet is shown in Figure 5.5 c displaying the same behavior and the smaller grain region is assigned to the left side with only small percentage of the whole pellet.

Optical micrographs show strong orientation contrast of the target phase in polarized light in Figure 5.6 and Figure 5.7 for Zn- and Ag-substituted samples, respectively. Based on optical microscopy images, Zn-substituted samples show unhomogenous distribution of grains when we compare the samples with pristine ones discussed in chapter 4 section 4.3.2 or Ag-sustituted samples. The microstructure forms of primary grains of irregular shapes and lamellar domains visible inside bigger grains and the needle-like domains are generally consequences of a peritectoid compositions as stated earlier and all of the samples, Zn- and Ag-substituted samples as well as pristine ones, have these needle-like domains. The grain size distribution of Zn-substituted samples are not homogenous whereas Ag-substituted samples have larger and more homogenous grains that contain needle-like grains within much larger grains. To have an idea about the grain size distribution, the images taken with 5x and 10x under polarized light can be found in Appendix B shown in Figure B 4 and Figure B 5.

Moreover, the orientation difference of the grains are more predominant in Zn-sunbstituted samples that allow us to see the grains distinctively while the neighbouring grains of Ag-substituted samples show little difference in the orientation leading us to see in the same color with slightly different shade. Although they are seen as a large grains, they are not and within the larger grains they still have needle-like grains as can be seen in Figure B 7 with larger magnifications as an example. In order to see if the color difference through the sample shows any variation in polarized light, it was labelled and checked throughout sample (Figure 5.8). In the bright light images, there is a color variations and it is more red on the sides labelled as light color which is reddish-purple in sample, and more bluish in side labelled as dark which is blueish-purple in the sample. In Figure 5.8 a, it is clearly seen that upper part of the sample is more red compared to the other side, however, there is no variation in the grain sizde distribution and color in the images taken under polarized light. There is also close up images of the upper and lower part of the samples showing the invariation in bright light images but not in polarized light images (Figure 5.8 (c) & (d) upper (light) part and (e) & (f) lower (dark) part).

Since the unhomogenouty is relatively more in $Ag_{0.20}Cu_{2.70}Te_2$ sample compared to other two samples with lesser Ag content, all the thermal analysis and transport measurements were carried out with only on $Ag_{0.05}Cu_{2.85}Te_2$ and $Ag_{0.10}Cu_{2.80}Te_2$ as well as Zn-substituted samples.

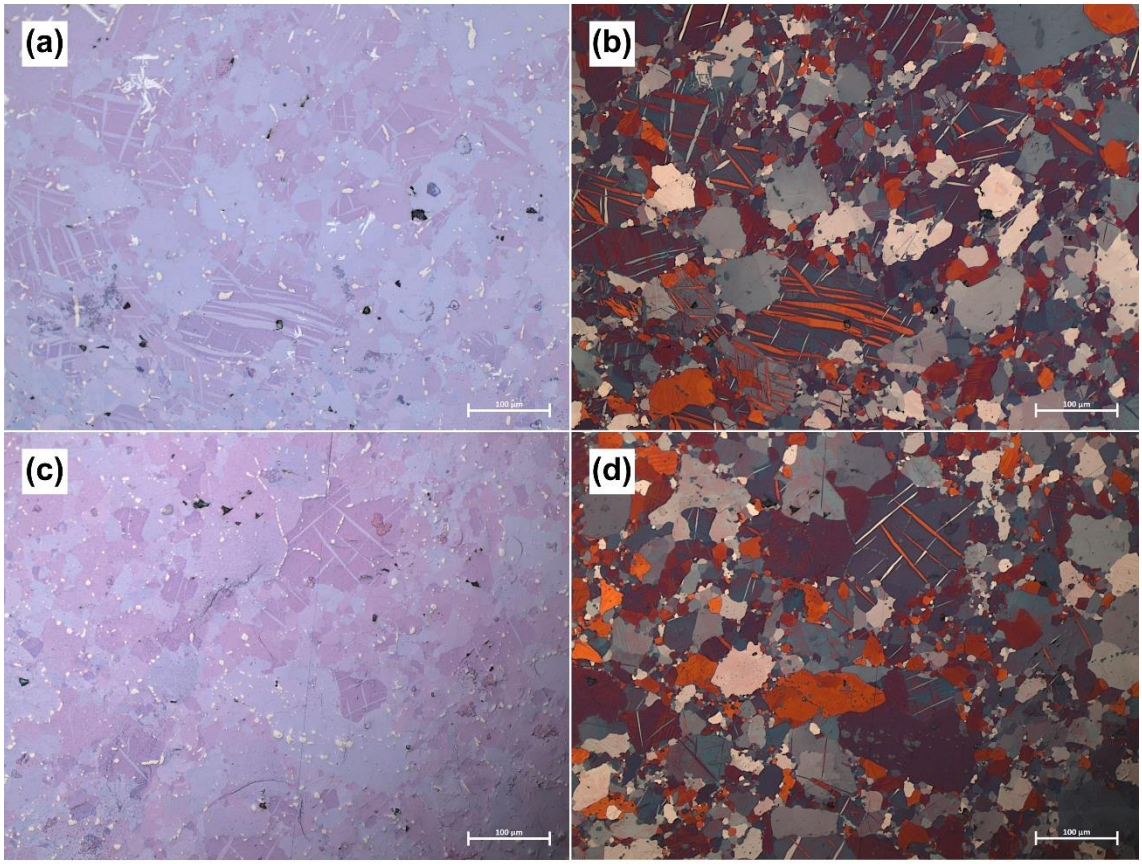

Figure 5.6. OM images of Zn-substituted $Cu_{2.9}Te_2$.samples: (a) $Zn_{0.05}Cu_{2.85}Te_2$.sps piece under bright field & (b) under a bright field. and (c) $Zn_{0.10}Cu_{2.80}Te_2$.sps piece under bright field & (d) under polarized light with 20x magnification and 100µm scale bar.

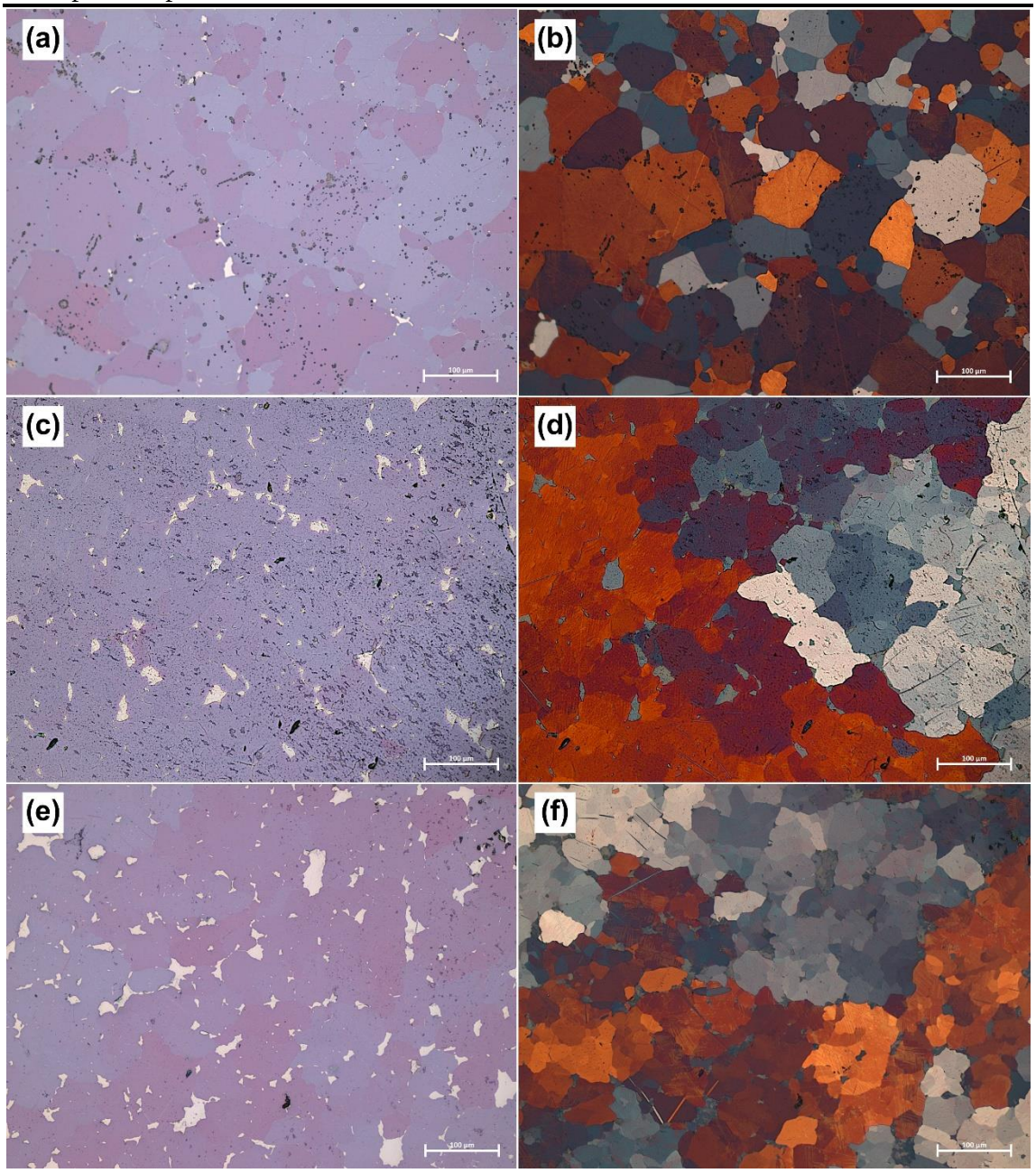

Figure 5.7. OM images of Ag-substituted $Cu_{2.9}Te_2$.samples: (a) **$Ag_{0.05}Cu_{2.85}Te_2$**.sps piece under bright field & (b) under polarized light, **$Ag_{0.10}Cu_{2.80}Te$** sps piece under (c) bright field & (d) under polarized light, and **$Ag_{0.20}Cu_{2.70}Te_2$** sps piece under (e) bright field & (f) polarized light with 20x magnification and 100μm scale bar.

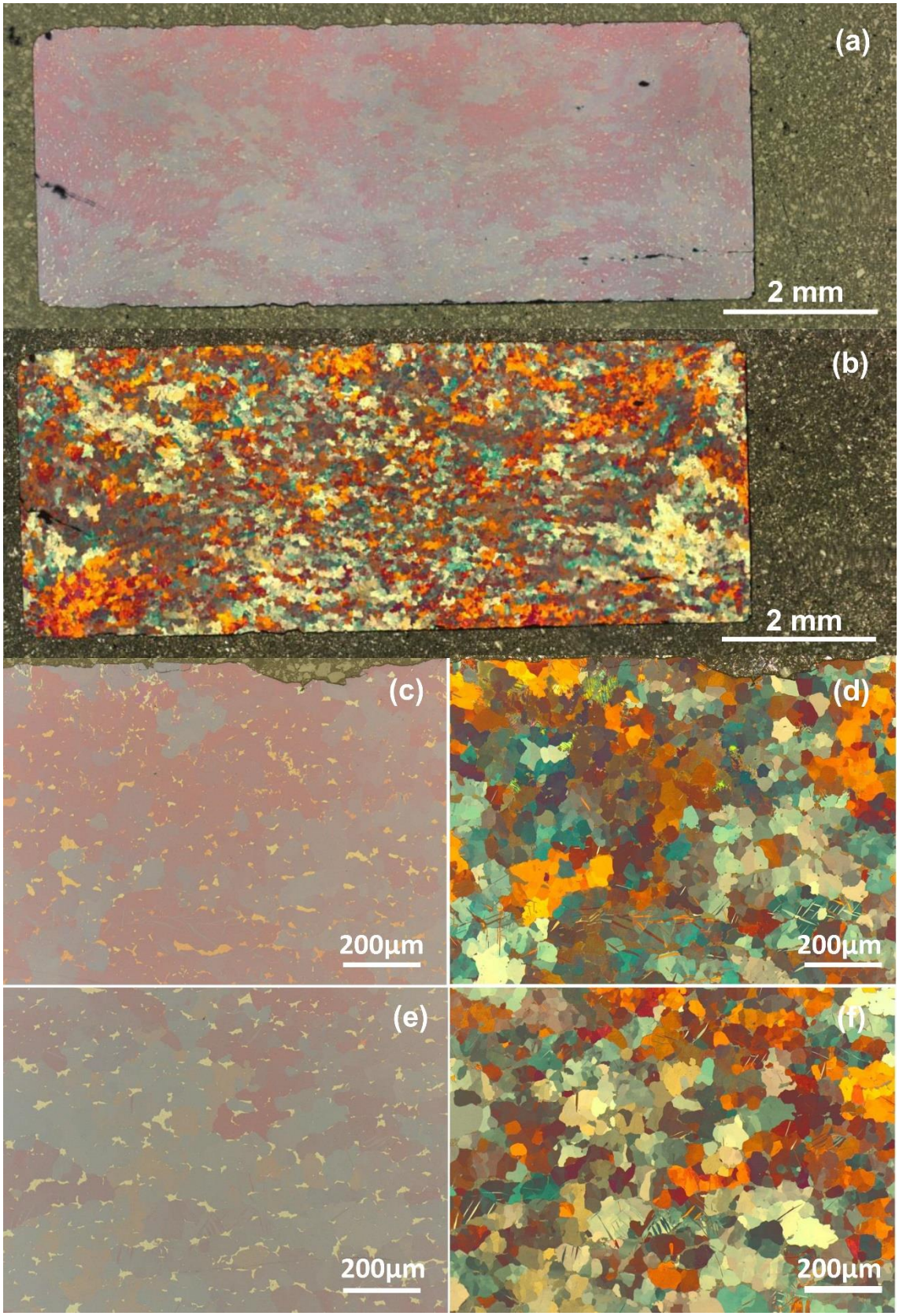

Figure 5.8. OM images of vertical cut of sps'ed $Ag_{0.20}Cu_{2.70}Te_2$.sample, (a) bright field & (b) under polarized light of vertically cut sample. (c) bright field & (d) under polarized light of upper side of the sample, and (e) bright field & (f) polarized light of lower side of the sample shown in (a).

The DSC thermogram (Figure 5.9) indicates that Zn- and Ag- substituted $Cu_{2.9}Te_2$ undergoes several phase transitions as the pristine sample that is reported in section 4.3.2 at around 458 K, 640 K, and 647 K. The first phase transition in all the samples was described as a second-order phase transition previously and it correspons to a change in the lattice symmetry from orthorhombic to tetragonal between 450 - 460 K as seen in inset figure in Figure 5.9. The T_{onset} peaks are at 450 K, 457 K, 457 K, and 453 K for $Zn_{0.05}Cu_{2.85}Te_2$, $Zn_{0.10}Cu_{2.80}Te_2$, $Ag_{0.05}Cu_{2.85}Te_2$, and $Ag_{0.10}Cu_{2.80}Te_2$, respectively. There was also one more endothermic peak observed only in $Ag_{0.10}Cu_{2.80}Te_2$ sample with T_{onset} 373 K and T_{peak} at 378 K and none in cooling which correspons to Ag_2Te phase transition. The endothermic peaks observed right before the main HT phase transitions with T_{onset} peaks of 613 K and 593 K of $Zn_{0.10}Cu_{2.80}Te_2$ and $Ag_{0.05}Cu_{2.85}Te_2$ samples belong most probably to phase transitions of CuTe that was observed in $Cu_{2.8}Te_2$ sample shown in

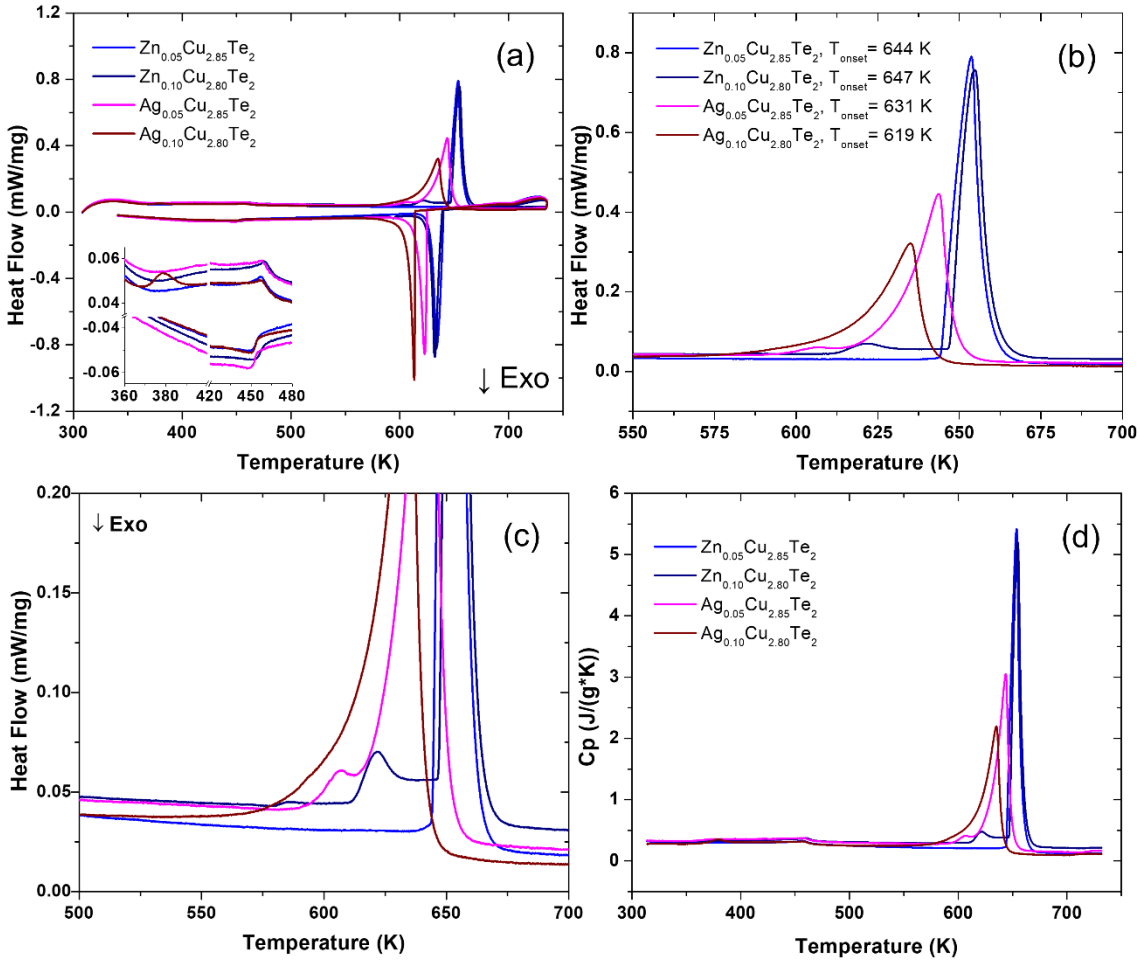

Figure 5.9. (a) DSC thermogram of Zn and Ag substituted $Cu_{2.9}Te_2$ (scanning rate 10 K min^{-1}) showing reversible phase transitions at multiple temperatures, the inset graph in a) shows corresponding zoomed on the first phase-transition region (b) & (c) zoomed on the main phase transition region around 650 K, (d) Heat capacity, C_p of the samples.

Figure 4.15 in chapter 4. Substitition of Zn and Ag might enhance the formation of CuTe in some of the samples. The effect of the substitution is prominent on the HT phase transition temperatures, from tetragonal to hexagonal phase transition as there is shift in the transition temperatures. The T_{onset} peaks for HT transition temperaures are at 644 K, 647 K, 631 K, and 619 K for $Zn_{0.05}Cu_{2.85}Te_2$, $Zn_{0.10}Cu_{2.80}Te_2$, $Ag_{0.05}Cu_{2.85}Te_2$, and $Ag_{0.10}Cu_{2.80}Te_2$, respectively. While Zn-substitution has little influence on the high temperature phase transition temperature, Ag-substitution has more prominent effect by decreasing the transition temperature. The exothermic peaks appearing in the cooling cycle are the evidence of the phase transitions are reversible in all the samples.

5.4 Transport Property Measurements

Transport property measurements were done as explained in section 3.4. The temperature dependences of the electrical resistivity, ρ, and Seebeck coefficient values, *S* of of Zn- or Ag- substituted $Cu_{2.9}Te_2$ sample are shown in Figure 5.10 a and b, respectively. All the samples show very low resistivity values less than 0.1 from room temperature up to 550 K and there is a six- or seven-fold increase in resistivity values as the samples go into phase transition after 600 K. The phase transition in the resistivity values show that the samples are having from metallic-like to semiconductor-like transtition. All the samples have Seebeck coeffient values below 10 μV/K up to 650 K and a six-fold increase was observed for all of the samples with the phase change. The similar behaviors in the transport properties with the pristine sample were explained in detail in section 4.4. The shallow dips on Seebeck measurements were observed in all of the samples while there is no significant effect on the resistivity data. All of these sudden changes in the data were also in align with DSC measurements showing all phase transitions. The positive Seebeck values over the entire working temperature mean that the dominant carriers are the holes. The sudden changes around 650 K correspond to high-temperature phase transitin evidenced by DSC. The effect of substitution on phase change, therefore on resistivity and the Seebeck coefficient measurements are consistent around the main phase transition. The phase transition shift observed in DSC thermograms are in consistent with these data and the trend between samples.

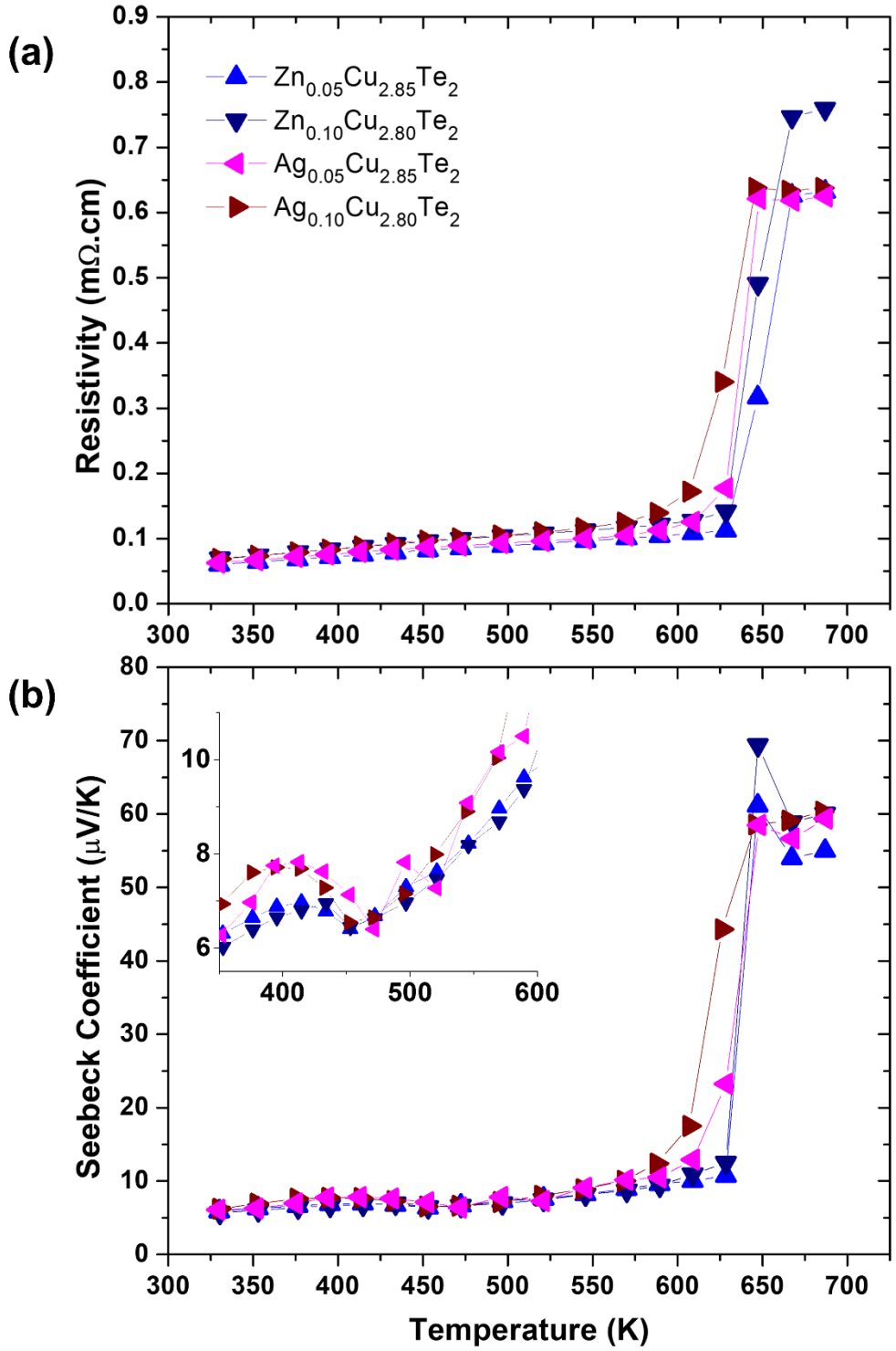

Figure 5.10 Temperature dependences of a) electrical resistivity and b) Seebeck coefficient data of Zn- and Ag-substituted $Cu_{2.9}Te_2$ samples.

The total thermal conductivity, κ data is shown in Figure 5.11 a. The valus are slightly decreasing as the temperature increases till the first phase transition at around 450 K. The effect of the first phase transition on thermal conductivity is mild as a small dip is observed in the values while the effect of the second phase transition is more dominant. The slight decrease in the values is observed till the second phase transition. When the sample experience the main HT phase transition, κ values drops to between 2 - 3 W m^{-1} K^{-1} above 650 K. The effect of the substitution on phase change observed on DSC thermograms and the values of thermal conductivity around the phase change are in consistent. Zn-substituted samples are displaying the similar behavior as the pristine sample has the sharp drop in thermal conductivity values while Ag-substituted samples have more smooth transition as the values slightly decreases even before 550 K. As Ag amont increases, this transition is getting less sharp and the shift of this transition is more prominent to the lower temperatures.

The temperature dependence of the dimensionless thermoelectric figure of merit, *zT*, of Zn- and Ag-substituted $Cu_{2.9}Te_2$ samples is shown in Figure 5.11 b. As in the pristine sample shown in chapter 4 section 4.4, the *zT* values are very low below 650 K due to the strong metallic behavior of the transport properties. However, the HT transition experienced by the Zn- and Ag-substituted samples resulted in rise in the *zT* values above this temperature with different rate and a shift to the lower temperatures evidenced by the transition shift. The hightes *zT* values observed for the samples is between 0.10 – 0.15 roughly.

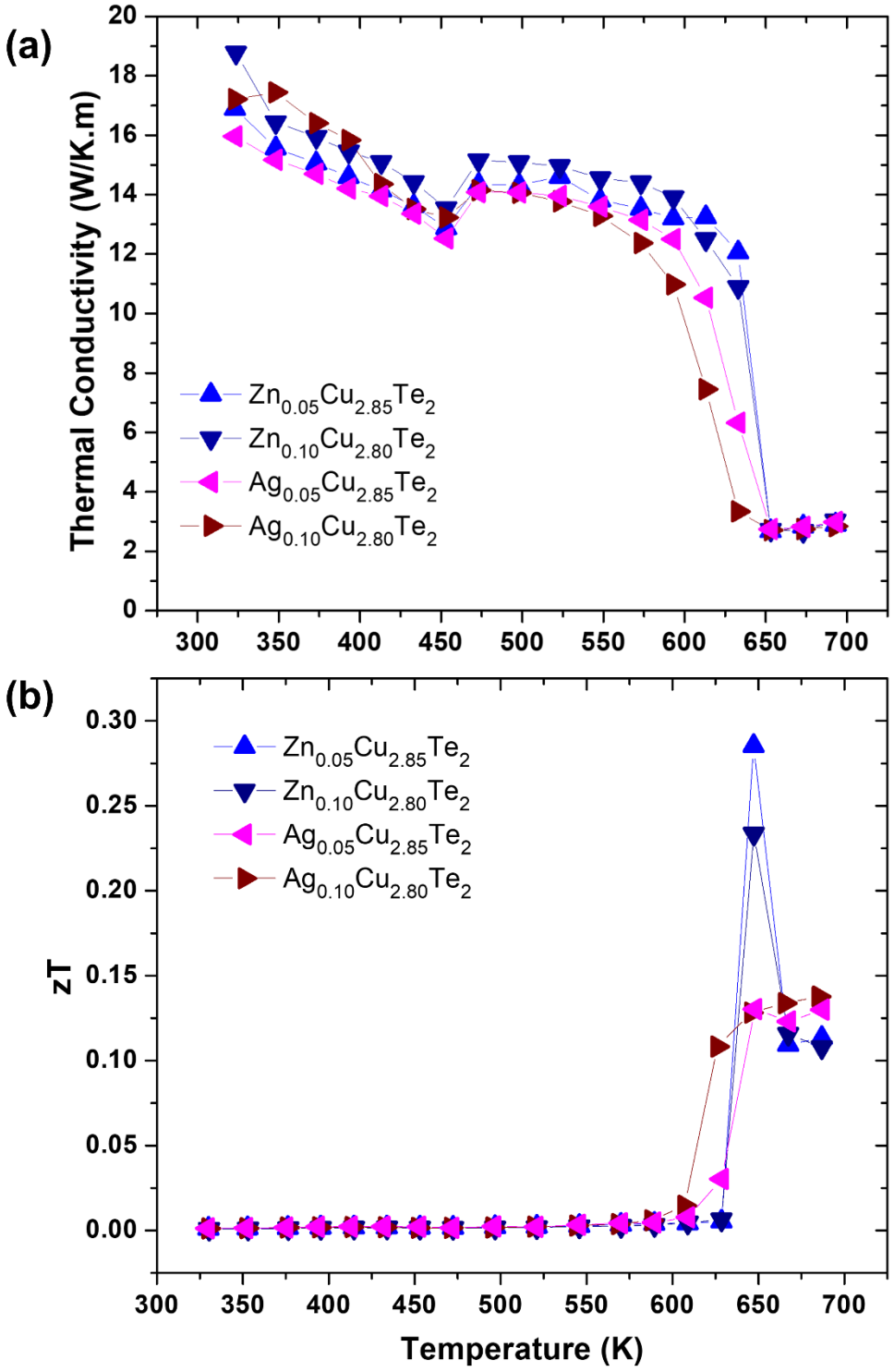

Figure 5.11 Temperature dependences of a) total thermal conductivity and b) and *zT* data of Zn- and Ag-substituted $Cu_{2.9}Te_2$ samples.

5.5 Conclusions

To optimize the carrier concentration and investigate the impact of substitution on phase transition temperatures, a comprehensive study was conducted on $Cu_{2.9}Te_2$ with Zn- and Ag-substitutions, resulting in the compositions $M_xCu_{2.9-x}Te_2$ (*M = Zn, Ag, x =* 0.05, 0.10 for Zn, *x* = 0.05, 0.10, 0.20 for Ag). The samples were synthesized using the same method as pristine $Cu_{2.9}Te_2$, and the X-ray diffraction (XRD) analysis confirmed the attainment of the targeted phases with minute impurities as the substitution amount increased. Under polarized light, all the samples display strong orientation contrast. Zn-substitution results in a more inhomogeneous grain size distribution, whereas Ag-substitution leads to a more homogenous distribution. The differential scanning calorimetry (DSC) data shows that all compositions, including $Zn_{0.05}Cu_{2.85}Te_2$, $Zn_{0.10}Cu_{2.80}Te_2$, $Ag_{0.05}Cu_{2.85}Te_2$, and $Ag_{0.10}Cu_{2.80}Te_2$, exhibit the same phase transitions, but with shifted transition temperatures. Zn-substitution in the high-temperature phase has minimal impact on the phase transition temperature, with the T_{onset} for the high-temperature transition at 644 K and 647 K for $Zn_{0.05}Cu_{2.85}Te_2$ and $Zn_{0.10}Cu_{2.80}Te_2$, respectively. In contrast, the substitution of Ag in the same compound exhibits a more pronounced effect, causing a decrease in the transition temperature as the substitution amount increases. The T_{onset} for the high-temperature transition is 631 K and 619 K for $Ag_{0.05}Cu_{2.85}Te_2$ and $Ag_{0.10}Cu_{2.80}Te_2$, respectively. As a result, the transport properties during the phase transitions and the transition temperature are influenced by the shifts in transition temperature caused by Zn- and Ag-substitution and their respective amounts.

CHAPTER 6

SYNTHESIS, CHARACTERIZATION, AND TRANSPORT PROPERTIES OF Cu_2Se

6.1 Introduction

Among all the Cu-based TE materials, Cu_2Se is the most studied Cu-chalcogenides, as it has good thermoelectric performance. Cu_2Se is an intrinsic p-type semiconductor with a bandgap of 1.23 eV. A half-decade ago, the transport property of Cu_2Se was studied, and the *zT* value was found to be 1.2 [23]. To date, the electronic structures and thermal conductivity of Cu_2Se have been modified and the TE performance has been enhanced by solid solution alloying, element doping or highly dispersed nanoparticle inclusion, and nanostructure engineering. In this chapter, the effect of using the light weighted, non-toxic boron in the Cu_2Se on thermoelectric performance was investigated.

6.2 Experimental Methods

Cu_2Se and nano-B or C-coated nano-B incorporated Cu_2Se samples were synthesized with two different methods: hydrothermal and solid-state synthesis methods.

6.2.1 Hydrothermal Synthesis

All Cu_2Se samples via HT method were prepared by using $CuSO_4.5H_2O$ (98%, Sigma Aldrich) and Se (Se, 99.999%, Alfa Aesar) powder or SeO_2 (SeO_2, 98%, Alfa Aesar), hydrazine hydrate ($N_2H_4.H_2O$, 100%, Alfa Aesar) as reducing agent and nano-B or C-coated nano-B as dopants for doping studies. First, an appropriate amount of $CuSO_4.5H_2O$ was dissolved inside deionized water. After 15 minutes of stirring inside a beaker with a magnetic stirrer, a clear blue $CuSO_4.5H_2O$ solution was obtained. A stoichiometric amount of Se or SeO_2 powder is then added to the $CuSO_4.5H_2O$ solution and mixed for about 30 minutes. A stoichiometric amount of dopant was added in this step before adding reducing agent for incorporated samples. The amounts were 0.15, 0.30, 0.45, 0.90, 1.80 wt % nano-B. After all the reactants were dissolved and mixed well, $N_2H_4.H_2O$ was added drop by drop by using Pasteur pipettes and mixed for another 15 minutes. After an exothermic reaction with gas evolution (N_2 gas formation), the mixture turned dark brown/black. The total solution, around 40 ml, was transferred into a PPL-lined autoclave, and deionized water was added to fill up to 80 % of the 100 ml PPL container. The autoclave is put inside a muffle furnace at 473 K for 24 hours. When the furnace was cooled down neutrally to room temperature, the product was collected by gravitational filtration method and centrifuge, washed with DI water and ethanol several times, then dried in a drying oven. The chemical reactions take place are given below;

$$SeO_2 + H_2O \rightarrow H_2SeO_3$$
$$H_2SeO_3 + N_2H_4.H_2O \rightarrow Se + N_2 + 4H_2O$$
$$2CuSO_4.5H_2O + N_2H_4.H_2O \rightarrow 2Cu + 2H_2SO_4 + N_2 + 6H_2O$$
$$2Cu + Se \rightarrow Cu_2Se$$

The pristine/undoped Cu_2Se samples were black while the incorporated ones were all brown/black. For the thermoelectric measurements, dense pellets of pristine and incorporated Cu_2Se samples were obtained by spark plasma sintering in a graphite die at 673 K for 10 min under a pressure of 65 MPa. Thermal transport measurements were conducted on these pellets. After the measurements of the thermal diffusivity, the thermal conductivity of the samples was calculated. The other part of the samples were then cut into a rectangular bar for electrical transport measurements, electrical resistivity and Seebeck coefficient measurements.

6.2.2 Solid-state Synthesis

Elemental copper (Cu, beads, 99.9999%, Chempur) and selenium (Se, pieces, 99.999%, Alfa Aesar) were used as starting materials to synthesize Cu_2Se samples. All the reactants were sealed into a C-coated silica tube under vacuum (Figure 6.1). Then the sealed tube was annealed at 1443K for 12 hours. After the furnace was cooled down to room temperature naturally, the sample was obtained as one-piece ingot out from the silica tube. nano-B or C-coated nano-B incorporated Cu_2Se samples were prepared by using a high energy ball mill (SPEX 8000M Mixer/Mill, 1425 rpm). Powder Cu_2Se and dopants (0.15, 0.30, and 0.45 wt % nano-B or C-coated nano-B) were added into stainless steel vials with half-inch stainless steel balls under argon atmosphere inside the glove box to prevent any oxidation and milled for 30 minutes. Dense pellets of pristine and incorporated Cu_2Se samples were obtained by spark plasma sintering (SPS) in a graphite die at 873 K for 5 min under a pressure of 65 MPa for characterization and transport property measurements. For the incorporation studies, the samples with the same dopant type were made from the same ingot to eliminate the compositional variation.

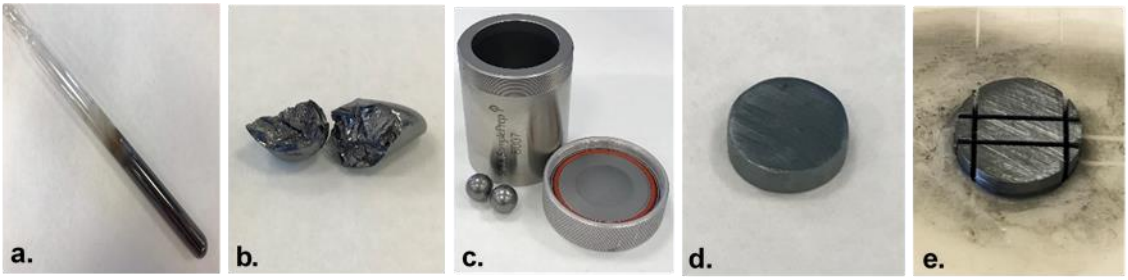

Figure 6.1 Synthesis and sample preparation procedures of Cu_2Se; a) C-coated silica tube used for annealing, b) synthesized Cu_2Se ingot, c) SPEX used for ball milling for nano-B or (c)nano-B doping, d) dense pellets obtained after SPS for thermal transport measurements, e) cut samples for electrical transport measurements.

6.3 Characterization

6.3.1 Hydrothermal Synthesis Method

Figure 6.2 presents powder XRD patterns of experimental Cu_2Se and nano-B incorporated Cu_2Se samples prepared by using two different selenium precursors. Both samples prepared by using Se and SeO_2 have high purity, single phase of cubic $Cu_{2-x}Se$. As the dopant (nano-B) amount increases, powder XRD patterns of the samples prepared using SeO_2 are single-phase as pristine sample. However, samples prepared using Se contain many phases including monoclinic Cu_2Se, orthorhombic $CuSe_2$ and cubic Cu beside cubic $Cu_{2-x}Se$. After these results, we wanted to proceed with the samples synthesized using SeO_2.

In Figure 6.3, SEM images show that Cu_2Se samples synthesized with different selenium precursors have different morphologies. Cu_2Se sample synthesized using SeO_2 has smaller grain size compared to Cu_2Se sample synthesized using Se powder.

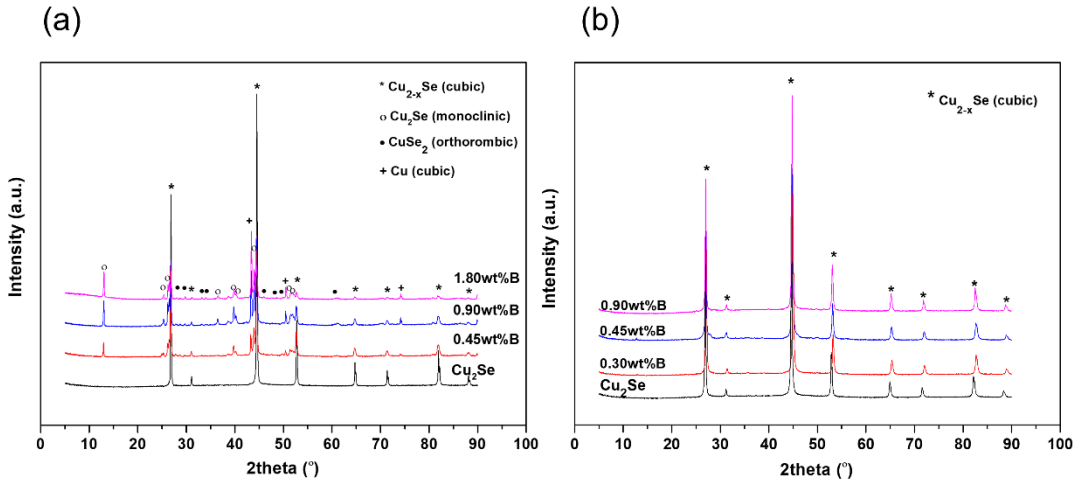

Figure 6.2 Experimental XRD patterns (Cu Kα) of Cu_2Se and nano-B incorporated Cu_2Se samples prepared by using two different Se precursors; a) Se and b) SeO_2.

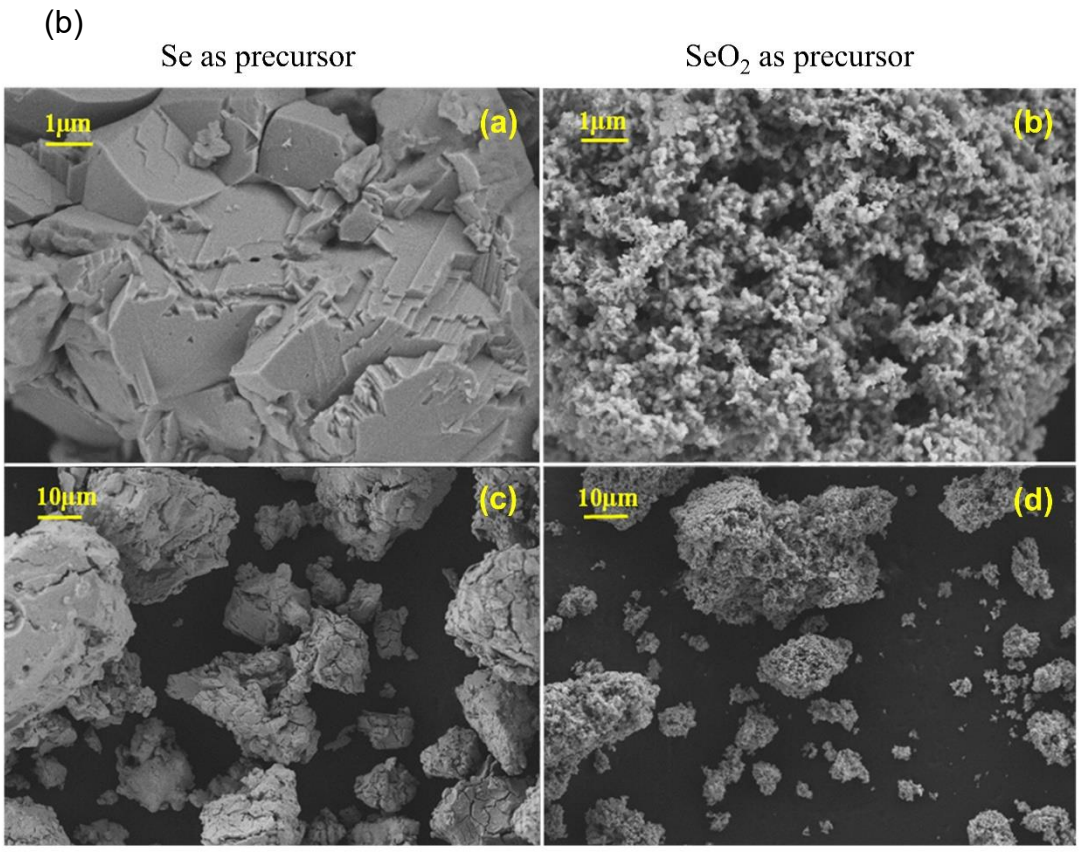

Figure 6.3 SEM images of Cu_2Se samples with different magnifications, a) & c) Se as precursor and b) & d) SeO_2 as precursor

EDX analysis shows that the sample contains sulphur as impurity that might be coming from side reaction impurities. Chemical composition analysis also gives information about Cu/Te ratio and it is very low compared to the nominal composition.

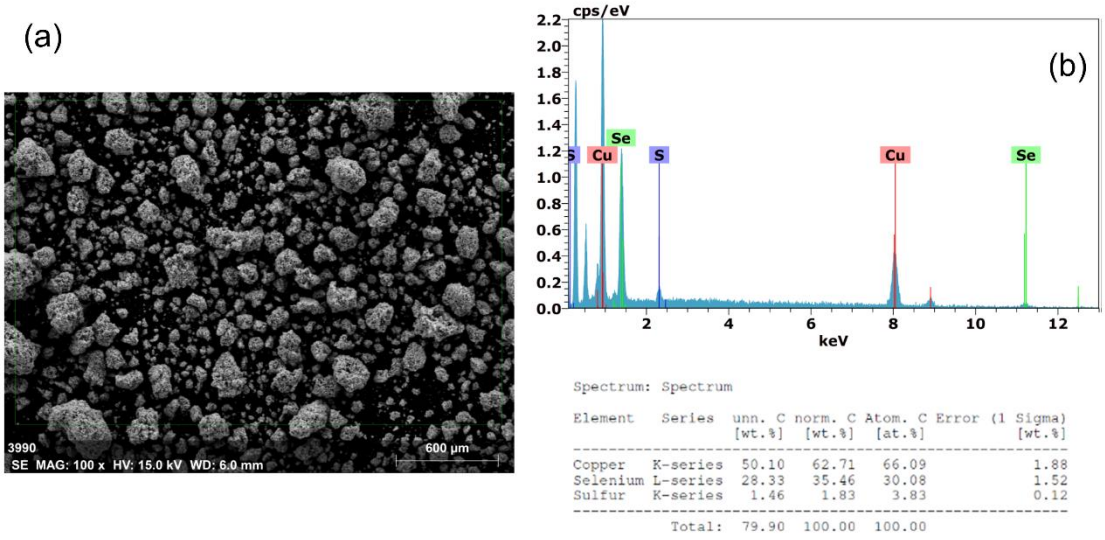

Figure 6.4 (a) SEM image of Cu_2Se sample produced with SeO_2 precursor and (b) elemental spectrum by EDX.

To have an idea and get a trial measurement of transport data of hydrothermally synthesized samples, an pristine Cu_2Se sample produced with SeO_2 precursor was densified by SPS and transport property of this sample was measured by LFA and Zem-3 devices.

6.3.2 Solid-State Synthesis Method

Pristine Cu_2Se synthesis

When pristine ingot of Cu_2Se produced by solid-state synthesis method was obtained on the first trial, there were shiny elemental copper parts on the surface of the ingot as seen in Figure 6.5 b which might mean that the experimental composition of Cu_2Se sample was not exactly the same with the nominal intended composition. The synthesized ingot will be copper deficient as $Cu_{2-x}Se$. Most probably the sample composition will be affected by the temperature profile (fluctuations maybe) followed during synthesis. Another Cu_2Se synthesis was done with the same procedure in which there was no elemental Cu aside.

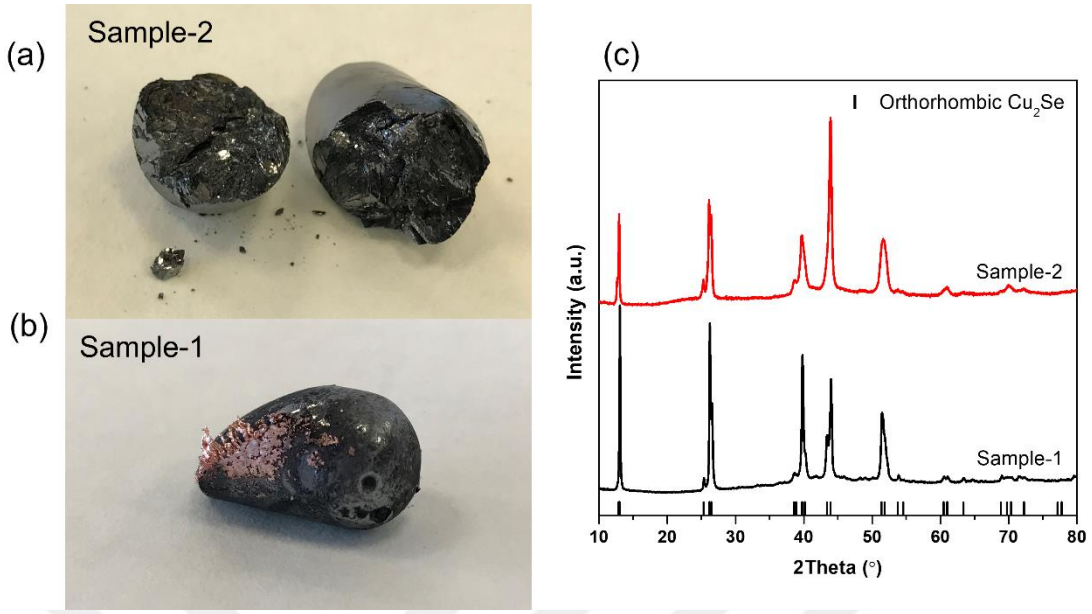

Figure 6.5 Cu_2Se ingots synthesized by solid-state synthesis method (a) sample-2 & (b) sample-1, and (b) experimental XRD patterns of pristine Cu_2Se samples corresponding sample 1 and 2 (reference code # 047-1448).

The XRD patterns of two pristine samples are in single monoclinic phase as room temperature phase and expected from the solid-state synthesis method after long annealing. The transport property measurements were completed on these samples. However, even though the nominal compositions of these two samples were exactly the same, copper amount that was aside the ingot was different. The chemical composition variation will expect to affect all the transport properties because of Cu vacancies affecting carrier concentration. To see the difference and the effect on transport properties, LFA and zem-3 measurements were done on both samples after they were densified by SPS.

For compositional analysis, the piece of densified samples were mounted and well polished. More accurate compositions were determined from WDX analysis by averaging 10 measurement data points. The Cu content of these sample with the same nominal intended composition is slightly different. When 10 data point determined by WDX are averaged, the compositions are calculated as $Cu_{1.9824}Se$ and $Cu_{1.9967}Se$ for sample-1 and sample-2, respectively. An example of an EDX mapping of Cu_2Se samle-1 can be seen in Figure C 1 showing the elemental distribution of Cu and Se are homogenously distributed.

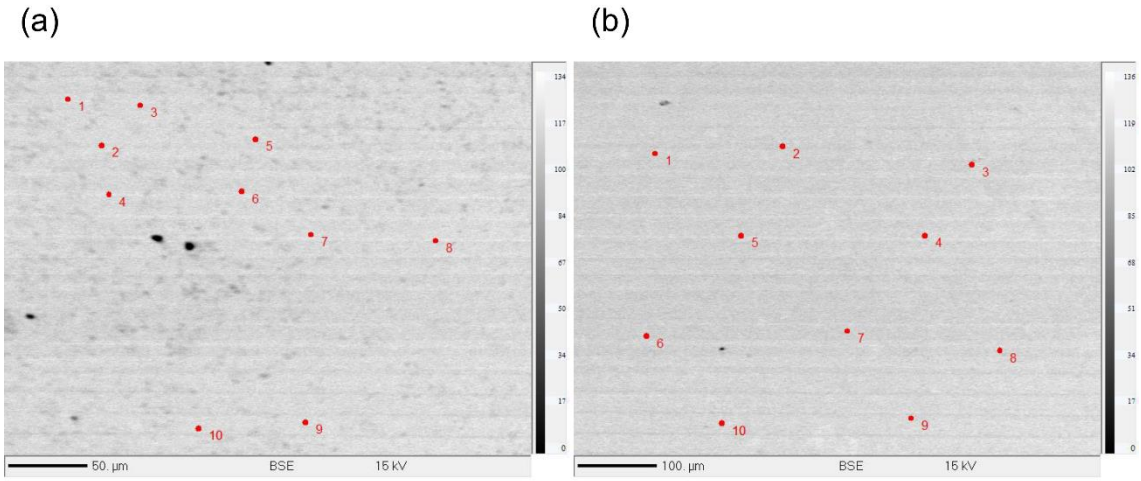

Figure 6.6 SEM images of Cu_2Se a) sample-1 and b) sample-2 with corresponding 10 different spots used for WDX analysis.

The Cu content difference of these two samples lead to display different transport properties as expected. The Cu ions that gives the liquid like behavior of the material is responsible for the transport data variations.

Incorporated Cu_2Se studies

For the doping studies, big 12 grams of ingots were synthesized and all the doping studies from the same dopant were made from the same ingot to eliminate effect of compositional changes.

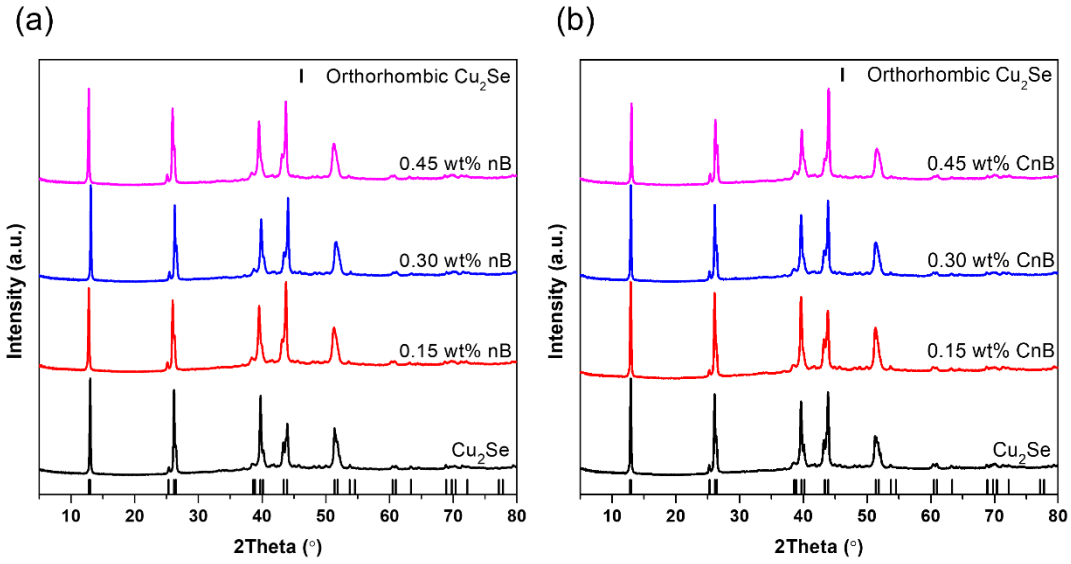

Figure 6.7 Experimental XRD patterns of a) nano-B incorporated and b) C-coated nano-B samples Cu_2Se (reference code # 047-1448).

The X-ray diffraction (XRD) patterns (Figure 6.7) shows that the nano-B and C-coated nano-B incorporated samples at room temperature are always referred as α-phase which is mentioned as orthorhombic or monoclinic in the previous studies [24, 28, 29]. In this study, the XRD analysis shows that the room temperature α-phase is orthorhombic Cu_2Se.

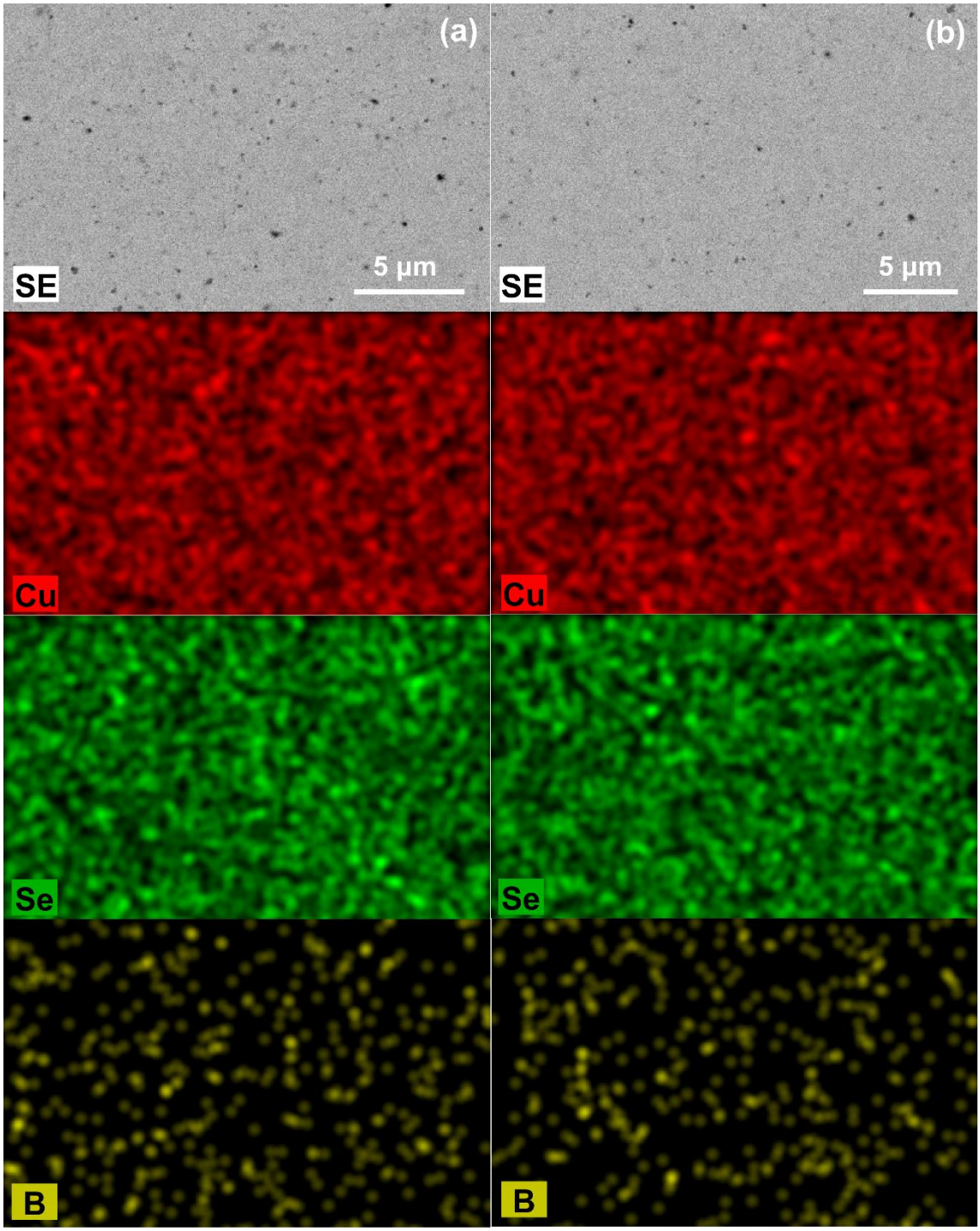

Figure 6.8 SEM images of a) 0.15 wt % nano-B and b) 0.15 wt % C-coated nano-B incorporated Cu_2Se the elemental mapping analysis (EDX) of the same SEM images showing the distribution of Cu, Se, and B distributions

The elemental mapping (EDX) analysis of the pristine samples were shown in Figure C 3 and Figure 6.8 for pristine samples and the lowest amount doped samples to check the presence of boron. The EDX analysis on the lowest nano-B and C-coated nano-B incorporated samples were shown in Figure 6.8, showing homogenous distribution of the elements and the incorporated B. The dark spots on the SEM images are where the B are located as proved on the distribution of elemental mapping of B.

6.4 Transport Property Measurements

6.4.1 Hydrothermal Synthesis Method

An example of transport data of the pristine sample is shown in Figure 6.9**.** Cu_2Se shows very low resistivity (ρ) values, indicative of good metallic behavior, that weakly increases with increasing temperature (Figure 6.9a). The positive Seebeck coefficient (α) values over the entire temperature range are indicative of holes as the dominant charge carriers (Figure 6.9b). Relatively low Seebeck coefficient values are showing that p-type

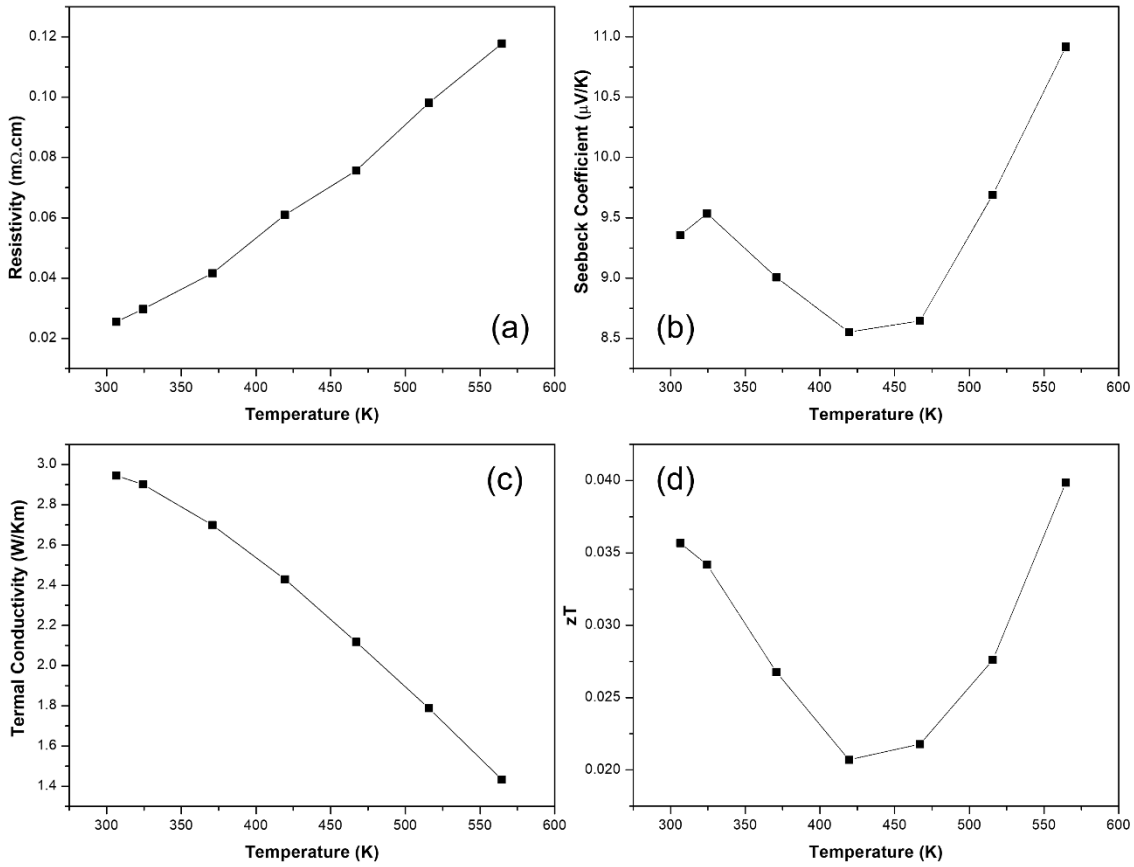

Figure 6.9 a) Electrical resistivity, b) Seebeck coefficient, c) thermal conductivity and d) thermoelectric efficiency, zT data of pristine Cu_2Se sample.

carries are much less than expected. These values are not even comparable with the values from the literature that is obtained by solution synthesis method. Thermal conductivity of the sample decreases as the temperature increases because of phonon scattering at high temperatures (Figure 6.9c). Thermoelectric efficiency, zT values (Figure 6.9d) are much smaller than the literature values. There are series of problems that needed to be solved in this method such as acidity, synthesis procedure and having control over chemical composition of the samples. There were also deformation of the samples after each measurements, thermal diffisuvity and zem-3 measurements.

After thermal diffusivity measurements, there was black remaining on the glass part where the laser comes and hit the samples which will affect the diffusivity results. This is also showing us there is an evaporation from the samples as they are heated. There were also deformations on the sample in which the thickness had changed significantly and they were unfolded layer by layer (Figure 6.10).

After taking consideration of all these problems that needed to be solved and complications of having control over the reaction through hydrothermal method, moving forward with solid-state synthesis method was a better option to pursue.

Figure 6.10 Deformation of the samples after thermal diffusivity measurements.

6.4.2 Solid-State Synthesis Method

Transport property measurements were done as explained in section 3.4.

Pristine Cu_2Se synthesis

Figure 6.11 shows the transport data of two of pristine Cu_2Se samples from different ingots within the β-phase temperature range of Cu_2Se after phase change. Since sample-1 has slighltly less Cu than the sample-2, the transport ptoperties were affected by this compositional change. Both of the samples have low resistivity values and high Seebeck coefficient values (Figure 6.11 a and b) in the whole temperature range and they are comparable to the other state-of-the-art thermoelectric materials [4]. The Seebeck coefficient values are between 100 -~ 300 μV/K at temperatures of 423 – 973 K. The values are attainable in extrinsically doped materials like Cu_2Se with a large band gap.

The total thermal conductivity values of both samples (Figure 6.11 c) are very low, below 1 W/m.K. The lattice thermal conductivity, κ_L values (Figure C 2) are calculated for all samples by subtracting the electronic thermal conductivity from the total thermal conductivity ($\kappa_L = \kappa_T - \kappa_e$). The κ_e is calculated based on the Wiedemann-Franz law, $\kappa_e = L\sigma T$, where L is the Lorenz number and calculated by $L=1.5+ \exp[-\frac{|S|}{116}]$ [14]. The lattice thermal conductivity values are very low, below 0.5 – 0.6 W/m.K for both samples compared to other TE materials which requires complex chemical formula and many atoms in a unit cell to have this low values. The *zT* values of both samples are shown in Figure 6.11 d. The values are high and the comparable with the reported studies with pristine samples [4, 24]. The highest values reached right above 1.2 after 800 K for sample-2. It could be even higher if a bit higher measuring temperature was covered. The values could reach up to 1.5 at 1000 K in the study of Liu et al. [24].

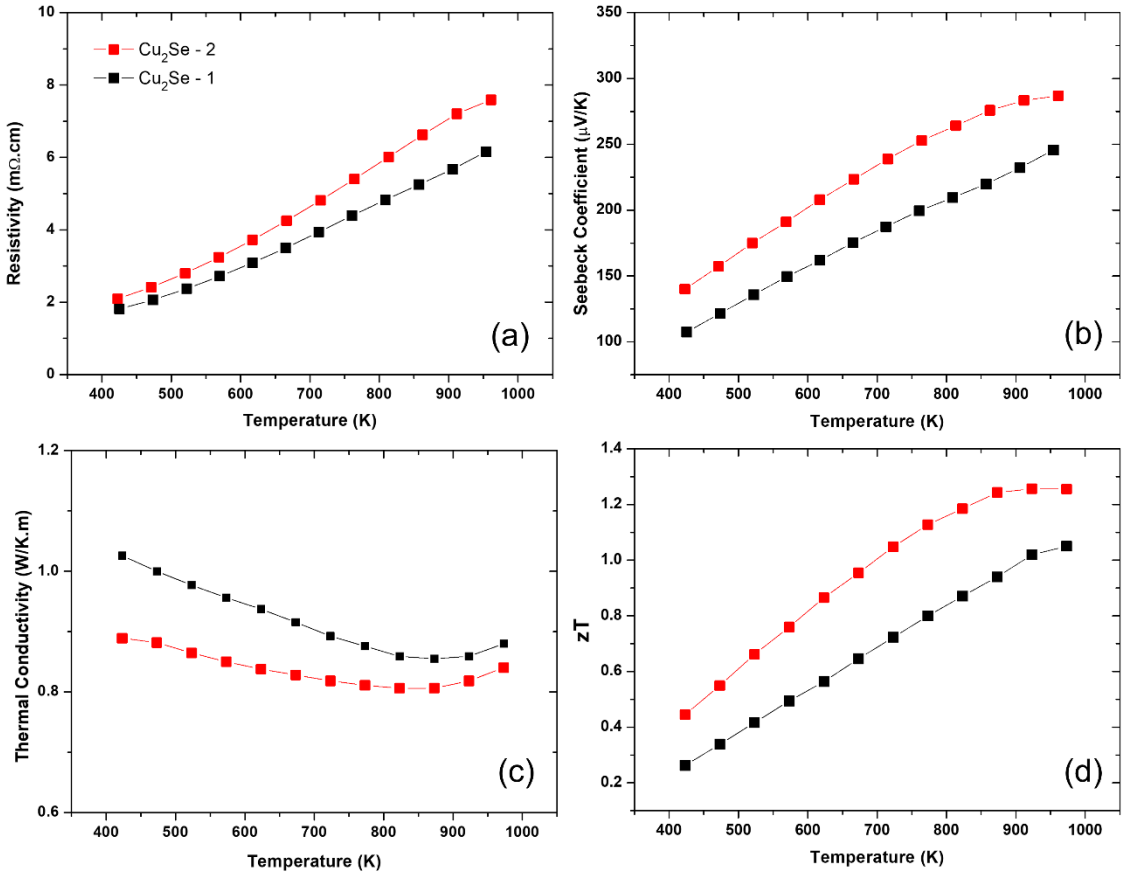

Figure 6.11 a) Electrical resistivity, b) Seebeck coefficient, c) thermal conductivity and d) thermoelectric efficiency, zT data of two pristine Cu_2Se samples.

In the study of Liu et al. [24], they studied TE transport properties of Cu_2Se and $Cu_{1.98}Se$ and they have almost similar results with this study. The Cu deficient sample was intended specifically with the stated composition, $Cu_{1.98}Se$ and the trends between two samples are almost the same. The resistivity values of the samples are reaching up to 3 and 8 mΩ.cm at 1000K for $Cu_{1.98}Se$ and Cu_2Se, respectively. The maximum Seebeck values of Cu_2Se are the same with Sample-2 which is 300 μV/K. The sample-2 has a plateu region between 850 – 973 K and the values are at maximum whereas Cu_2Se sample in the study of Liu et al. has values between 250 – 300 μV/K between the temperatures of 800 – 1000 K.

The total thermal conductivity values of $Cu_{1.98}Se$ are much higher than Cu_2Se and chang between 1.8 – 1 W/m.K between 400 – 1000 K. However, thermal conductivity values of Cu_2Se are more or less the same with the values of Sample-2. Overall, *zT* values of the samples studied in this section are comparable the study reported. The values in this study start a little higher around 400 K and reach to a little less than 1.3 around 973 K.

Incorporated Cu_2Se studies

For more reliable comparison the second set doping studies made from the same ingot synthesized as 12 grams for pristine and incorporated measurements. The first 12 gram ingot was used for an pristine/undoped and 3 nano-B incorporated samples with 0.15, 0.30, and 0.45 wt %. The second 12 gram ingot was used for a pristine/undoped and 3 C-coated nano-B incorporated samples with 0.15, 0.30, and 0.45 wt %. The thermoelectric transport property measurements were done on all these samples and they are shown in Figure 6.12 and Figure 6.13.

The resistivity and the Seebeck coefficient data of nano-B and C-coated nano-B incorporated samples are shown in Figure 6.12. The pristine samples for both set have almost the same resistivity values with small variations and the values are increasing wth increasing temperature. Overall, as the dopant is added in any amount the values are increased for both α- (orthorombic) and β-phases (cubic) when they are compared to the pristine samples within the batch. The the incorporated samples with different level of dopant gave almost the same results overall for the resistivity values. The increase in the resistivity values were also seen in previous reported studies done with nano-B and C-coated nano-B samples and the results were explained by the decrease in the samples' carrier concentration measured by hall [28, 29].This decrease in electrical conductivity resulted by decreased carrier concentration the interfaces of the dopants located in the grain boundaries as an extra surface to act as scattering centers. However, the increase in the resistivity values is not desired for an improved TE efficiency, *zT* values. Nano-B or C-coated nano-B incorporation does not improve the conductivity values.

The Seebeck coeffiecient values are shown in Figure 6.12 c for nano-B incorporated samples and Figure 6.12 d for C-coated nano-B incorporated samples. The pristine samples in both sets of study have high Seebeck values without any optimization compared to the other studies over the working temperature range [28, 29, 173, 174]. The synthesis method and the route is affecting the Cu content in the composition and the microstructure of the material that affect the transport properties significantly [173]. The enhancement in Seebeck coefficient values for both incorporated sets of Cu_2Se samples were observed for both α- and β-phases. The enhancement is more notable in nano-B incorporated Cu_2Se samples Figure 6.12c compared to C-coated nano-B Cu_2Se samples (Figure 6.12d). Since the pristine samples already have high Seebeck values over the temperature range and the highest above 250 μV/K at above 500 K, the overall improvement is not big. Since the Seebeck coefficient is related to the composition of the

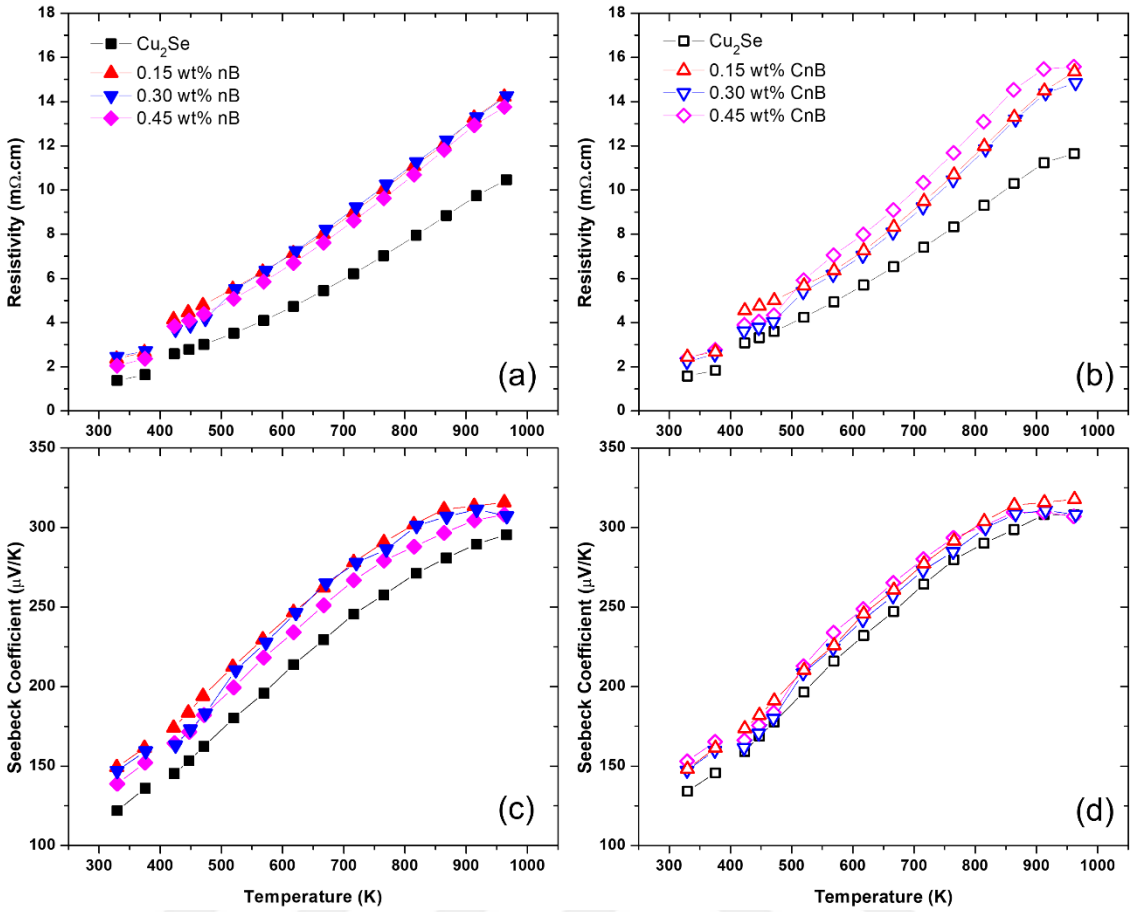

Figure 6.12. Thermoelectric properties of the low-temperature and high-temperature phases in pristine, nano-B and C-coated nano-B incorporated Cu_2Se samples. Temperature dependences of electrical resistivity (a and b) and Seebeck coefficient (c and d) data.

materials and the values for all incorporated samples are almost the same, it can be concluded that the samples reached the highest B-doping efficiency even with the smallest amount added The highest value reached with nano-B doping is 316 μV/K with 0.15 wt% inclusion while 318 μV/K with 0.15 wt% C-coated nano-B doping. For the both set of study, after doping the values have reached to a plateu above 300 μV/K 800 K.

The temperature dependence of the total thermal conductivity (κ) and the calculated lattice thermal conductivity, κ_L) are presented in Figure 6.13 a &b and Figure C 6, respectively. The total thermal conductivity values of the pristine samples from both sets are low, below 0.7 W/K.m which is very low compared to the ones reported previously [173]. As the samples are incorporated with nano-B, the thermal conductivity values decreases while there is significant increase in the values as C-coated nano-B is incorporated in the samples. This increase could be the effect of carbon on the surface layers of nano-B particles being incorporated. The lattice thermal conductivity is the

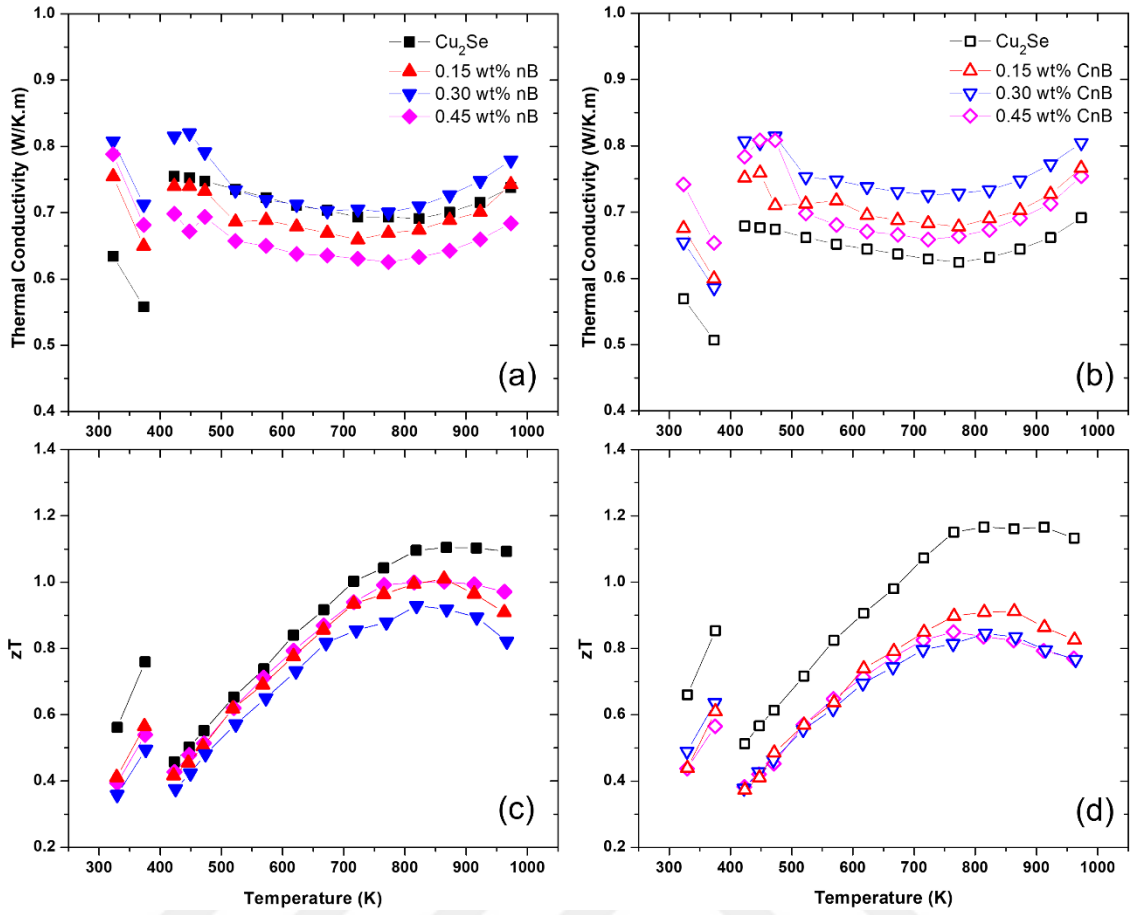

Figure 6.13. Thermoelectric properties of the low-temperature and high-temperature phases in pristine, nano-B and C-coated nano-B incorporated Cu_2Se samples. Temperature dependences of total thermal conductivity (a and b) and *zT* (c and d) data.

dominant portion of the total thermal conductivity of the samples and the values are very low.

When thermoelectric figure of merit, *zT* values are calculated, as the samples incorporated even though high resistivity values were unfavorable, high Seebeck coefficient values were making the overall efficiency high. The efficiency of Cu_2Se could not be improved by incorporation of nano-B or C-coated nano-B when we compare the pristine samples with high Seebeck values and low total thermal conductivity values. The heating curves together with the cooling curves of the transport data of all the samples were shown in Figure C 4 and Figure C 5 in Appendix C showing almost no hysterises.

6.5 Conclusions

In summary, there were two different synthesis method were employed to obtain Cu_2Se samples; hydrothermal and solid-state synthesis method. The main part of this work was with the solid-state synthesis method over hydrothermal synthesis method because of its easy to handle synthesis procedure and not having side reactions. The Cu_2Se samples were prepared by melting the elemental precursors in a C-coated quartz tube at elevated temperatures following with long annealings. The effect of nano-B and C-coated nano-B nanoparticles incorporation on thermoelectric properties of the samples within room-temperature and 1000 K temperature range were discussed.

CHAPTER 7

STRESS/PRESSURE-STABILIZED CUBIC POLYMORPH OF Li_3Sb WITH IMPROVED THERMOELECTRIC PERFORMANCE

*This chapter has been published in *Journal of Materials Chemistry A, 2021, 9.44: 25024-25031* [175]. The original manuscript has been rearranged to conform to the format requirements of the dissertation.

7.1 Introduction

In this study, we experimentally assess the thermoelectric potential of c-Li_3Sb through a detailed investigation of its high-temperature thermoelectric properties measured on polycrystalline specimens prepared by high energy ball milling. We revealed that Li_3Sb undergoes a phase change from h-Li_3Sb to c-Li_3Sb either by ball milling or applying low pressures (as low as 60 MPa at room temperature), which is quite unusual for thermoelectric materials. The results are further discussed in light of the recent study on h-Li_3Sb [176].

7.2 Experimental Methods

Li_3Sb samples were synthesized from high-purity elemental lithium (Li, 99.9%, Sigma Aldrich) and antimony shots (Sb, 99.999%, Sigma Aldrich). First, Li was cut into very tiny pieces in an argon-filled glovebox. Stoichiometric mixtures of the starting elements were then loaded into stainless steel vials with two half-inch stainless-steel balls and sealed inside a glovebox. Li_3Sb powder samples were obtained using SPEX 8000M Series MixerMill in 90 minutes (6 cycles of 15 min on/off). Dense pellets of as-obtained powders were prepared with both spark plasma sintering (SPS; at 673 K, 60 MPa, 10 minutes) and rapid hot pressing to compare the phase formation.[177] For transport property measurements, the powder samples were loaded into half-inch diameter high-density graphite dies (POCO) and compacted into dense pellets by using a direct current-induced hot press at 773 K for 1 h under 60 MPa pressure in an Ar atmosphere. Phase purity and the samples' oxidation behavior on air were analyzed by X-ray diffraction (XRD) using a Phillips X'Pert diffractometer. The phase stability of the c-Li_3Sb sample was determined by DSC/TG (NETZSCH STA 449 F3 Jupiter) measurement in a closed Nb ampoule. Electrical and thermal transport properties were measured from 325 to 675 K. The electrical resistivity (r) and Hall effect measurements were carried out by using the van der Pauw technique under a magnetic field of 2 T using pressure-assisted tungsten electrodes.[178] The Seebeck coefficients (a) of the materials were measured by using chromel-Nb thermocouples.[179] Thermal diffusivity, D, measurements were performed with a Netzsch LFA 457 laser flash apparatus. Thermal conductivity (κ) of the samples was calculated using the relation $\kappa = D\ C_P\ d$, where C_p is the isobaric heat capacity estimated using the Dulong–Petit law and d is the experimental geometric density.

7.3 Characterization

Li_3Sb is an extremely air- and moisture-sensitive material that needs special care in storing and handling. Therefore, all the XRD samples were prepared in the glove box using Polyimide (Kapton) films. The XRD patterns of as-synthesized powder (**Figure 7.1** and Figure D 1 in Appendix D) show that the target cubic phase was successfully obtained after ball milling.

Li_3Sb crystallizes with two polymorphic forms: in a face-centered cubic cell (BiF_3 structure type; space group $Fm\overline{3}m$ (No. 225)) and in a hexagonal unit cell (Na_3As structure type; space group $P6_3/mmc$ (No.194)). In the structure of Li_3Sb, there are twelve atoms per cubic (Z = 4; Li1 at 4*b* (½, ½, ½), Li2 at 8*c* (¼, ¼, ¼), and Sb at 4*a* (0,0,0) sites) and eight atoms per hexagonal (Z = 2; Li1 at 2*b* (0, 0, ¼), Li2 at 4*f* (1/3, 2/3, 0.583), and Sb at 2*c* (1/3, 2/3, 1/4) sites) unit cells with experimental lattice parameters of a=6.576 (1) Å, and a = 4.689 (1) Å, c = 8.328 (1) Å, respectively (see Figure 7.2).[180, 181] Early phase diagrams and battery studies about the stability of these phases with temperature yielded contradictory reports.[114, 180, 182-186] Some studies reported c-Li_3Sb as the stable low-temperature phase, while some others considered h-Li_3Sb as the stable one under ambient conditions. After high-energy ball milling, our samples were all single-phase crystallizing in the c-Li_3Sb form. After annealing the as-synthesized c-Li_3Sb sample at 650 K for four days, the sample has transformed to h-Li_3Sb with a minor c-Li_3Sb (Figure 7.1), which may indicate that the c-Li_3Sb is a metastable phase at ambient conditions. Beutl et al. correlated this behavior with the pressure effect, claiming that moderate pressure/stress stabilizes the c-Li_3Sb, while stress-releasing processes such as thermal treatment lead to the formation of the h-Li_3Sb.[180] In similar systems of Li_3P, Na_3Sb, and Na_3Bi, only the hexagonal phase forms under ambient conditions,56 whereas the cubic phase of Li_3P and Na_3Sb emerge only at higher pressures of around 1.3 – 3.3 GPa and 13 GPa, respectively.[183, 187] This correlates well with the total energy calculations indicating a slight energy difference between the hexagonal and cubic phase of Li_3Sb (7 meV), whereas a larger one (131 meV) for the Na_3Sb.[188] Notably, Li_3Bi, Cs_3Bi, and Cs_3Sb crystallize only in the cubic structure.[189] With higher packing density, the cubic phase of Li_3Sb might be stabilized under pressure, which was tested by pressing a sample consisting of mostly h-Li_3Sb by a hydraulic press at room temperature (Figure 7.1). Applying 60 MPa pressure in a stainless-steel die (Ø = 10 mm), a small amount of h-Li_3Sb was transformed to the c-Li_3Sb after 20 s. Almost the same amount

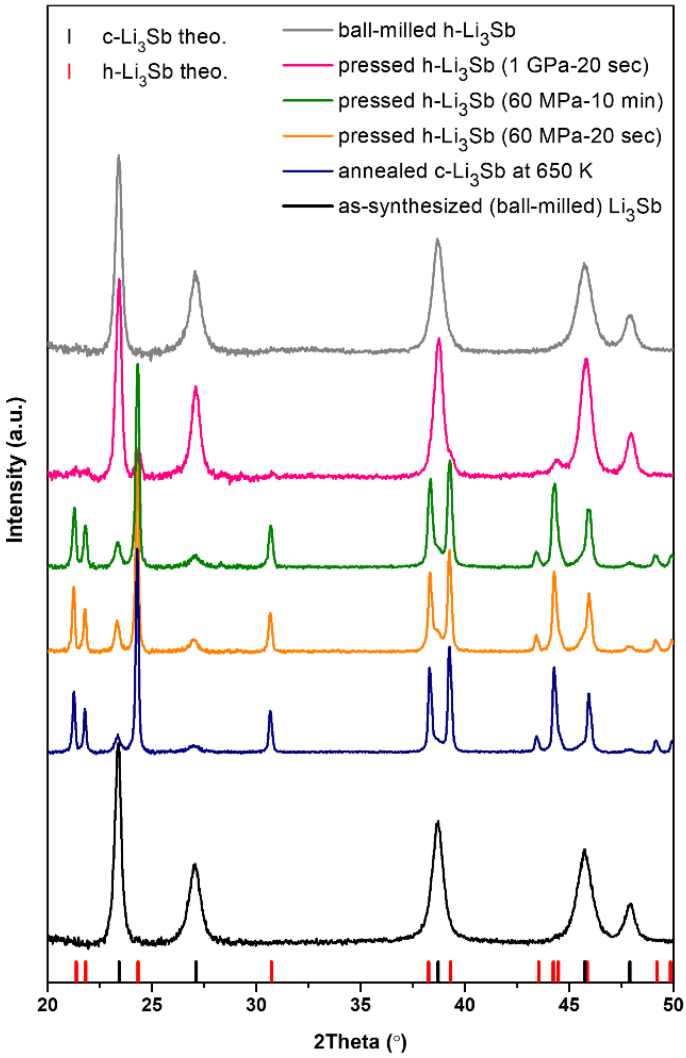

Figure 7.1 Experimental XRD patterns (Cu Kα) of as-synthesized Li_3Sb powder by high energy ball mill (black), c-Li_3Sb annealed at 650 K (blue), h-Li_3Sb hydraulic-pressed (orange: 60 MPa – 20 s, green: 60 MPa – 10 min, pink: 1 GPa – 20 s), and h-Li_3Sb ball milled for 30 min (grey) samples. Black and red ticks mark the calculated reflection positions of the c-Li_3Sb and h-Li_3Sb, respectively.

was transformed at the same pressure after 10 min, signifying the transformation is time-independent and governed by the applied pressure. Almost complete phase transition occurred under 1 GPa pressure in a stainless-steel die (Ø = 4 mm) after 20 s. This explains well the existence of only the c-Li_3Sb after mechanochemical synthesis with ball milling. When a sample of h-Li_3Sb was ball milled for 30 min, a complete phase transformation to c-Li_3Sb was observed verifying that stress induced during high-energy ball milling stabilizes the c-Li_3Sb polymorph. The solid-state synthesis in Nb ampoules led to the formation of only h-Li_3Sb based on Peng et al.,[176] which is expected for a stable low-temperature phase.

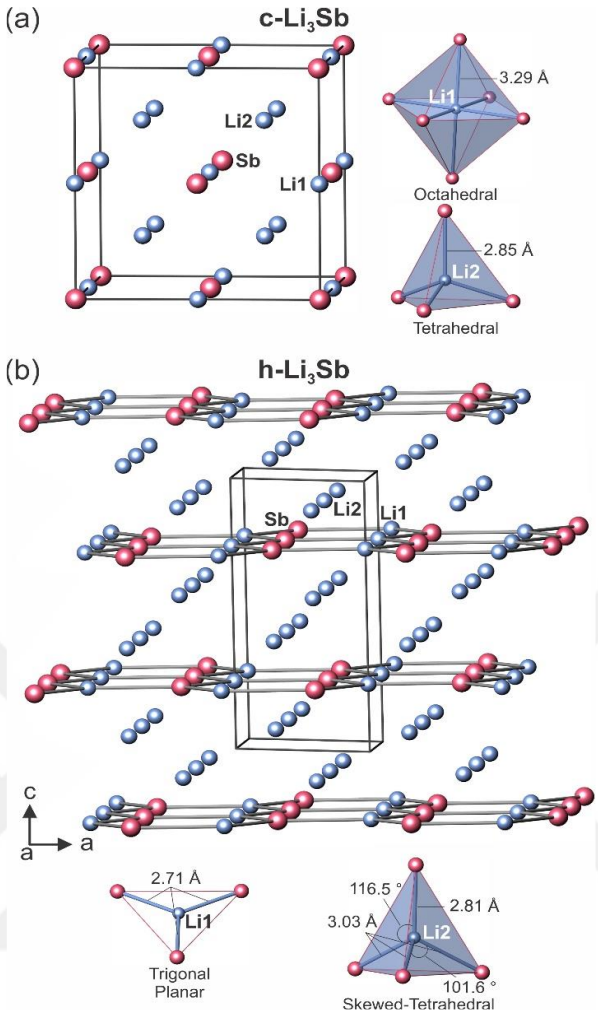

Figure 7.2 The crystal structure of Li_3Sb. (a) The cubic c-Li_3Sb phase has Face Centered Cubic (FCC) Sb with Li in both octahedral (Li1) and tetrahedral (Li2) interstices. (b) The hexagonal h-Li_3Sb Hexagonal Close Packed (HCP) Sb with Li in trigonal (Li1) and skewed tetrahedral (Li2; one shorter, three longer bonds) interstices. Alternatively, the structure can be described as alternating planar Li1Sb layers stacking in ABAB sequence along the c-axis in which two layers of Li2 atoms are intercalated.

Regarding the thermal stability of c-Li_3Sb, the DSC/TG thermogram in Figure 7.4 indicates one endothermic (at T_{onset} = 450 K) and one exothermic effect (T_{onset} = 620 K and T_{peak} = 633 K) up to 673 K. No weight loss was observed based on the TG data. The peak at 450 K can be attributed to either the melting point of pure Li (454 K) [190] or the eutectic temperature of the Li-rich phase (>75 at% Li), as reported by Beutl et al. [180] The exothermic peak at T = 620 – 633 K is ascribed to transforming metastable c-Li_3Sb to stable h-Li_3Sb phase. These predictions were further verified with XRD analysis performed on the sample after the DSC/TG measurement (Figure 7.3). The XRD data show that the starting cubic phase was primarily transformed into the hexagonal one.

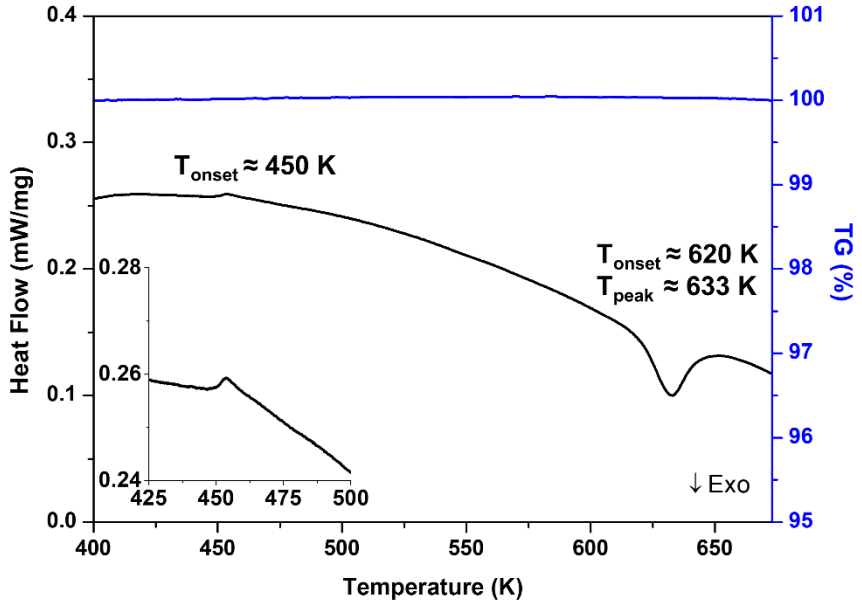

Figure 7.4 DSC/TG diagrams of c-Li_3Sb (scanning rate 10 K min^{-1}) showing an endothermic peak at $T_{onset} \approx 450$ K and an exothermic peak at $T_{onset} \approx 620$ K and $T_{peak} \approx 633$ K.

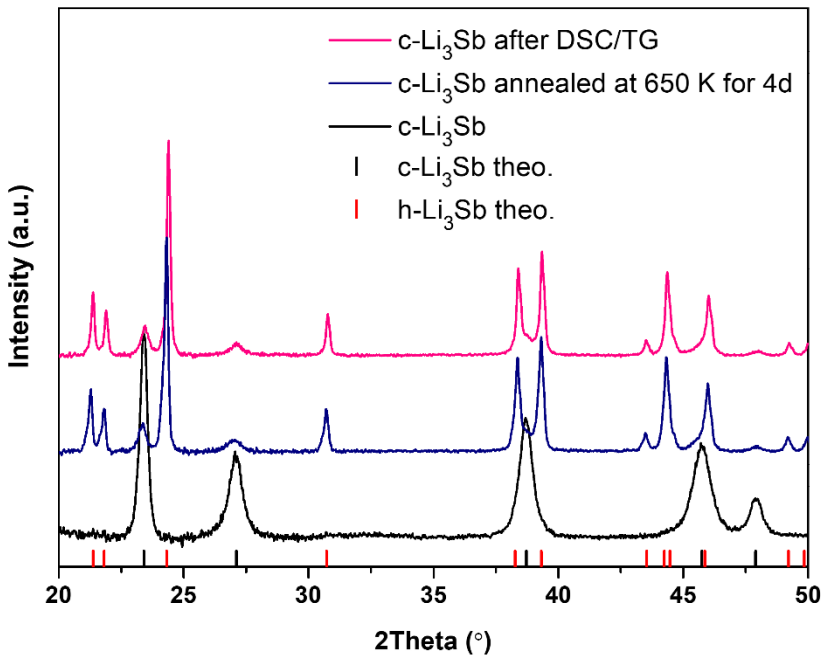

Figure 7.3 Experimental XRD patterns (Cu Kα) of as synthesized powder c-Li_3Sb (black), annealed c-Li_3Sb at 650 K for XRD (blue), and c-Li3Sb after DSC/TG measurement. Black and red ticks mark the calculated reflection positions of the c-Li_3Sb and h-Li_3Sb, respectively.

From a local structure analysis, it is apparent that very different Li environments exist for the two polymorphs of Li_3Sb (Figure 7.2). Li atoms in c-Li_3Sb have octahedral and tetrahedral coordination with Sb atoms, whereas they are coordinated in skewed tetrahedral and trigonal planar geometries in the h-Li_3Sb. Considering a very small ionic radius of Li^+ (0.76 Å; 6-fold coordination), [191] an octahedral hole could be too large to be positioned, which could be tested with Pauling's rules on different coordination polyhedra.[192] For an octahedral environment, a r_{cation}/r_{anion} should be between 0.414 and 0.732. Taking the anionic radius of Sb^{3-} to be 2.23 Å,[193] a r_{cation}/r_{anion} of 0.34 is obtained, which is much lower than the stability limit. Therefore, Li+ should be highly unstable in an octahedral environment in c-Li_3Sb and may distort to tetrahedral and trigonal planar sites in the h-Li_3Sb at ambient conditions, which can lead to low thermal conductivity by a rattling-like mechanism (soft mode with high anharmonicity). [194] By applying low or moderate pressures, Li^+ in octahedral coordination might be restored with a metastable character.

After hot pressing, additional peaks of Li_2Sb and Sb are observed besides c-Li_3Sb, indicating Li loss during processing, which leaves Li-deficient phases Li_2Sb and elemental Sb in the samples (Figure D 1). In this case, the phase composition shifts towards the Li-deficient region in the phase diagram.[180] Similar decomposition behavior was observed in other experimental phase diagram studies for annealed samples [180] in which an extremely high Li mobility may also contribute to this issue.[115, 195] The lattice parameter of Li_3Sb after ball milling, hot-pressing, and transport property measurements was found to be a = 6.59448 °A, 6.5833(2) °A, and 6.5777(1) °A, respectively, indicating partial Li loss and/or phase decomposition as well. The XRD pattern for the SPS-sintered sample reveals a mixed-phase nature composed of h-Li_3Sb as the primary phase and the c-Li_3Sb as the minor one (Figure D 2 in Appendix D). Considering the same pressure applied, the lower sintering temperature, current effect, and/or concise sintering time might result in a different phase formation behavior than hot-pressed samples. In this study, all the transport properties were reported for the hot-pressed sample with the c-Li_3Sb as the only phase form of this system.

Since Li_3Sb is an extremely air- and moisture-sensitive material after air-protective XRD measurement was done, Kapton foil was taken out from the sample holder, and several 15-minute scans were performed to investigate the oxidation behavior of the Li_3Sb powder in the air under ambient conditions. The XRD pattern obtained during the first 15

minutes scan reveals severe decomposition of Li_3Sb. As the exposure time increases, further deterioration is observed until the sample is almost fully oxidized and decomposed into Sb, $LiOH.H_2O$, and $LiSbO_3$ (Figure D 3 in Appendix D). Right before the transport measurements, the surfaces of the bulk pieces were slightly polished; however, partial surface oxidation could not be avoided.

7.4 Transport Property Measurements

The transport properties of the two identically prepared Li_3Sb samples were measured between 325 and 675 K. The temperature dependence of the electrical resistivity and Seebeck coefficients are presented in Figure 7.5 (a) and (b), respectively. The ρ values were found to be constant up to 625 K for both samples. Above this temperature, the faster rise is probably due to either phase transition from c- to h-Li_3Sb or partial decomposition of Li_3Sb into Li_2Sb and Sb.[196] XRD analysis performed after measurement confirms the formation of secondary phases (see Figure D 1 in Appendix

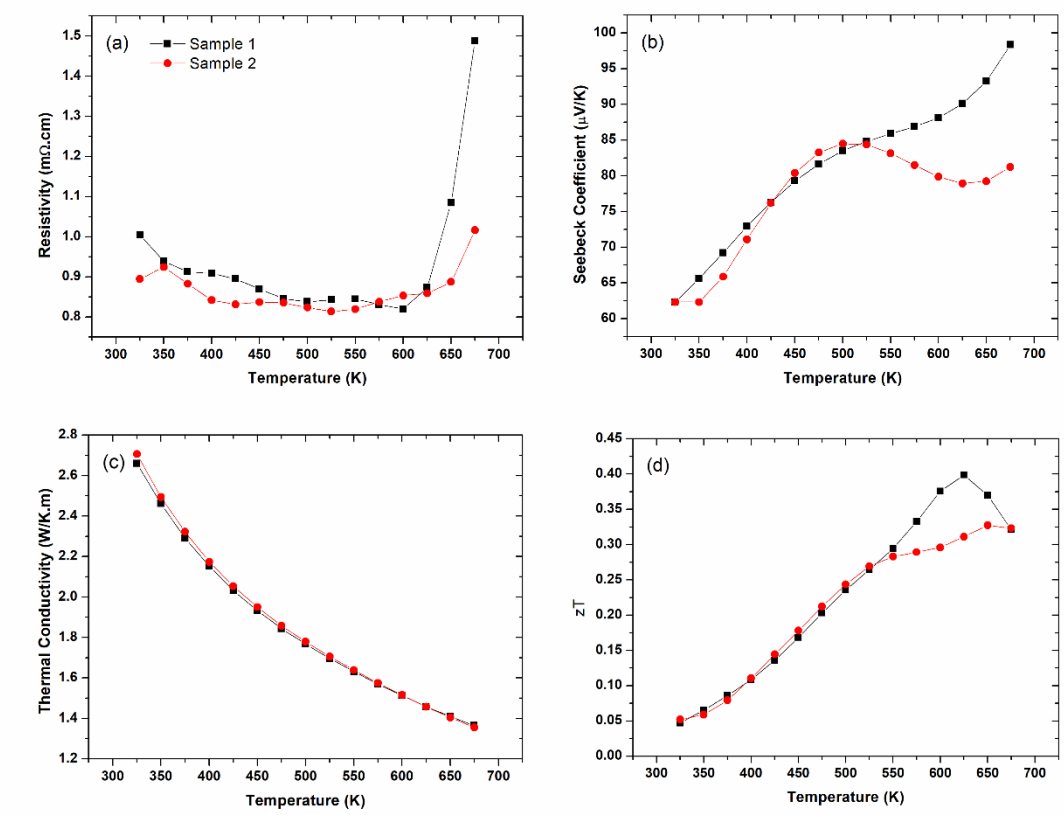

Figure 7.5 Temperature dependence of the (a) electrical resistivity, (b) Seebeck coefficient, (c) total thermal conductivity, and (d) thermoelectric figure of merit (zT) for the two Li_3Sb samples prepared.

D). Below 625 K, both samples display low ρ values between 0.8 and 1.0 mΩ cm over the entire temperature range. The low values measured indicate a degenerate behavior, suggesting the presence of native defects. This finding is consistent with defect calculations indicating that acceptor-like Li vacancies acting as shallow acceptors are the most favorable defects due to their very low formation energy and the absence of competing electron-like defects.[115]

In agreement with the degenerate character, the values of the Seebeck coefficients (Figure 7.5b) remain moderate, increasing upon warming to ~ 85 μV K^{-1} at 500 K. The positive α values indicate that holes are the main charge carriers, as observed in the hexagonal polymorph.

Figure 7.6a shows the hole concentration from the Hall effect of the two Li_3Sb samples as a function of temperature. The data measured on the two samples (low-temperature data for sample 1 and high-temperature data for sample 2) were combined to avoid inconsistent data points stemming from the difficulties in Hall-effect measurements for such an air-sensitive material. At room temperature, Li_3Sb has a relatively high hole concentration ($p \approx 0.5 \times 10^{20}$ h^+ cm^{-3}), in agreement with its degenerate character.

The weighted mobilities μ_w were calculated from the measured α and ρ values (Figure 7.6b). μ_w has been shown to be proportional to drift mobility, which helps identify the dominant electron scattering mechanism in semiconductors.[197] In the case of Li_3Sb, the decreasing trend of μ_w with temperature indicates that electron–phonon scattering dominates. Grain boundary effects are likely not significant at high temperatures but may contribute to flattening the curve near room temperature.

The density of state effective mass can be estimated from the measured Seebeck and Hall coefficients using an "effective mass" or often called "SPB" model [198]. The experimental Seebeck effective mass m^*_S is found to be 1.4 m_e. This is higher than the value determined by density functional theory calculations (0.5 me).[115, 177]

In comparison to the experimental Seebeck values, the α value at 500 K (85 μV K^{-1}) was lower than the calculated value (170 μV K^{-1}) predicted for p-type c-Li_3Sb at the same hole concentration (3 x 10^{20} h^+ cm^{-3}).[109]

The mobility parameter μ_0 was extracted from:

$$\mu_w = \mu_0 \left(\frac{m_S^*}{m_e}\right)^{3/2} \qquad (7.1)$$

The μ_0 value of 38 $cm^2\ V^{-1}\ s^{-1}$ at 400 K, calculated from the experimental hole concentration, Seebeck coefficients, and electrical resistivity, compares very well with that determined by Ha et al. (40 $cm^2\ V^{-1}\ s^{-1}$ at 400 K).[115]

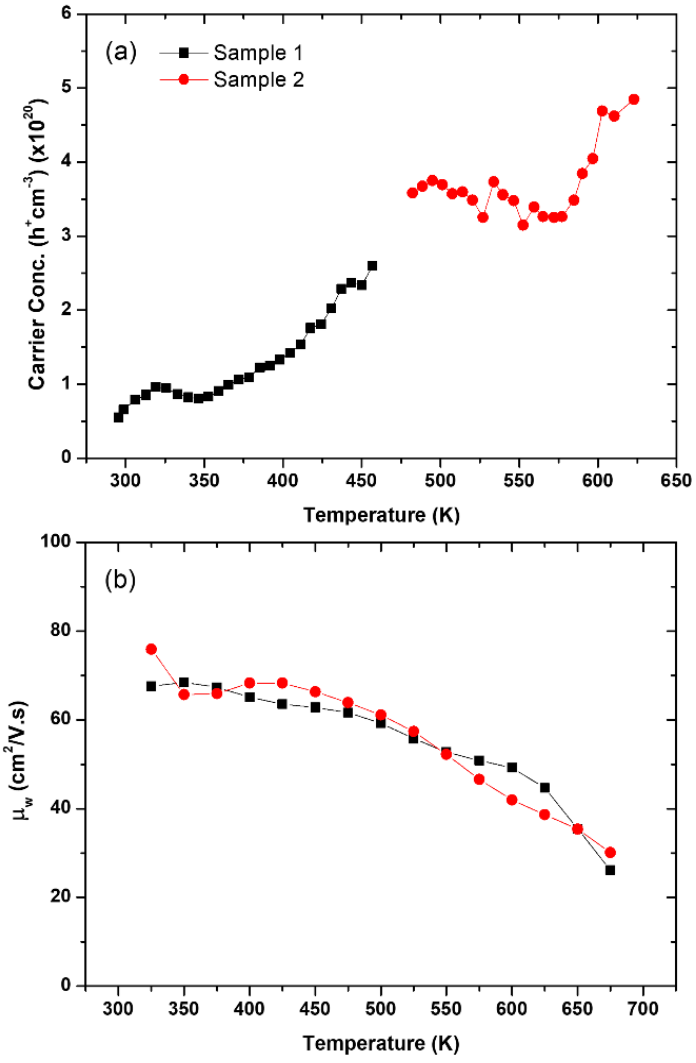

Figure 7.6 (a) Carrier concentration and (b) weighted mobility of Li_3Sb samples (sample 1: black, sample 2: red).

The total thermal conductivities κ of the samples, with densities over 98 % of the theoretical density, are shown in Figure 7.5c and Figure D 4. For all samples, κ decreases with increasing temperature following a T^{-1} law indicative of dominant phonon–phonon Umklapp scattering. The SPS-treated sample has somewhat lower thermal conductivity values which could be due to the sample having both c- and h-Li_3Sb phases. The lattice thermal conductivity κ_L values were calculated by subtracting the electronic thermal conductivity from κ. κ_e was calculated using the Wiedemann–Franz law $\kappa_e = L\ \sigma\ T$ where

L is the Lorenz number, calculated from the SPB model to vary between 1.9 and 2.1 x 10^{-8} W Ω K^{-2} in the temperature range measured [199]. At 300 K, the κ_L values of around 2 W m^{-1} K^{-1} are consistent with lattice dynamics calculations for c-Li_3Sb[109] and with the experimental results obtained by Peng et al. on hexagonal Li_3Sb [176]. These low values mainly originate from the significant mass contrast between Li and Sb that contributes to low group velocities of the optical phonons, as evidenced by the phonon calculations [176, 194]. Upon heating, κ_L rapidly decreases, following a trend similar to that calculated [109]. However, this model yields unphysical values above 625 K. We note that the phase decomposition, which is known to directly affect thermal diffusivity and specific heat measurements [169, 200] occurs above these temperatures. Thus, the unphysical values reached near 625 K is not due to a problem in the measurement of the thermal diffusivity. This could be a consequence of a phase transition enthalpy and hence an overestimation of κ [169].

Combined with the lattice thermal conductivity κ_L, μ_w determines the dimensionless material quality factor ($B \propto \mu_w/\kappa_L$), which provides an estimate for the peak zT achievable upon proper optimization of the carrier concentration. The experimental μ_w values inferred for Li_3Sb are relatively high compared to most p-type Zintl thermoelectrics [106, 201-203]. Figure 7.5 d shows the zT values of the Li_3Sb samples as a function of temperature. The highest zT of 0.4 was achieved for sample 1 at 625 K, which is higher than that achieved for hexagonal Li_3Sb (0.3 at 760 K). However, as sample 2 shows a little lower zT at this temperature and the phase transition from c-Li_3Sb to h-Li_3Sb happens at 620–633 K, we prefer to report a zT value of around 0.3 at 550 K for the sake of consistency. In addition, the hole concentration dependence of the zT calculated at 500 K by the SPB model (Figure 7.7b), shows that the experimental zT is consistent with these predictions. However, a peak zT of 0.7 is predicted for a hole concentration of 3.7 x 10^{19} cm^{-3}, that is, an order of magnitude lower than the experimental hole density achieved herein. Compared to the theoretical assumption of Yang et al., this predicted zT value at 500 K is significantly lower by 38 % [109].

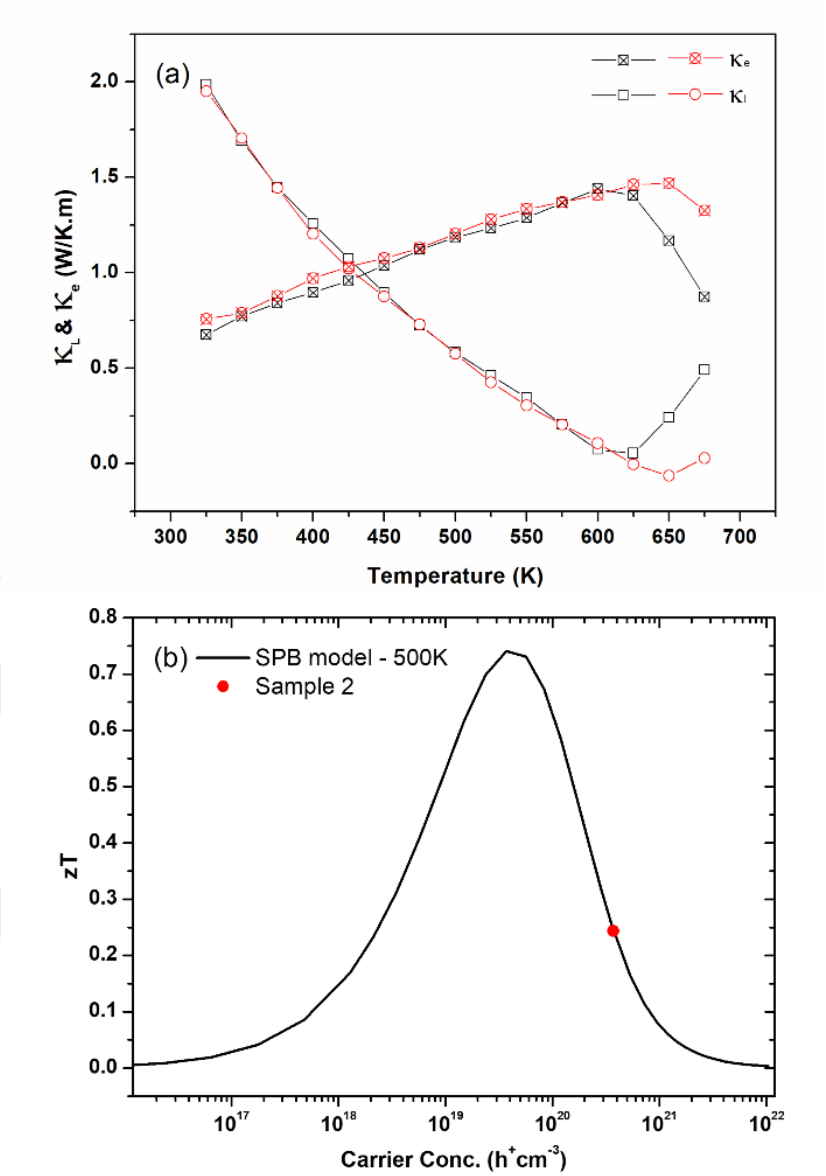

Figure 7.7 (a) Lattice and electronic thermal conductivity as a function of temperature (sample 1: black, sample 2: red) and (b) model of zT showing that the carrier concentration is much higher than the optimum value (m^*_{SPB} = 1.4 m_e, μ_0 = 38 $cm^2\ V^{-1}\ s^{-1}$).

7.5 Conclusions

Li_3Sb has been successfully prepared in the face-centered cubic structure with a mechanochemical route. A stress/pressure induced phase transition was uncovered for this system, stabilizing the c-Li_3Sb metastable phase at low temperatures. The stability of c-Li_3Sb may be further improved by partially substituting Cs for Li and Bi for Sb as Li_3Bi, Cs_3Bi, and Cs_3Sb crystallize only in the cubic structure. Electrical resistivity measurements reveal a degenerate semiconducting behavior with relatively low resistivity values (0.8 and 1.5 mΩ cm) and moderate Seebeck coefficients (60 – 100 μV K^{-1}). The total thermal conductivity drops down to 1.35 W m^{-1} K^{-1} at 673 K, which is a relatively low value for such a lightweight material. A zT of 0.3 was realized at 550 K, which is lower than the peak zT of 0.7 predicted by an SPB model for a hole concentration of 4 x 10^{19} h^+ cm^{-3}. Higher *zT* values may be achieved in c-Li_3Sb upon further optimizing the hole concentration through doping studies. To be implemented in thermoelectric energy harvesting applications, airtight systems should be designed due to the highly air-sensitive nature of this material.

CHAPTER 8

REALIZING THERMOELECTRIC TRANSPORT PROPERTIES OF P-TYPE NbCoSn

8.1 Introduction

Among the n-type half-Heusler materials, NbCoSn is a promising n-type thermoelectric material due to promising electronic properties while the desired p-type NbCoSn shows poor thermoelectric performance. In this work, a systematic study of Co-deficiency and Zr-substitution on Nb site were implemented to obtain p-type NbCoSn samples through a simple one-step arc-melting synthesis along with annealing methods and their transport properties were investigated.

8.2 Experimental Methods

NbCoSn and Zr-substituted NbCoSn samples were prepared by using powders of niobium (Nb, Chempur 99.8 %), cobalt (Co, Alfa Aesar 99.5 %), tin (Sn, Chempur 99.9999 % metal basis), and zirconium (Zr, Nanografi 99.9 %). Zr-doped samples were prepared by the compositions of $Zr_xNb_{1-x}CoSn$ with x = 0 – 0.3, Co-deficient samples $NbCo_{1-y}Sn$ with y = 0.05, 0.10, and Zr-doped Co-deficient samples with $Zr_{0.2}NbCo_{1-y}Sn$ compositions. All the powders were mixed well in a mortar, pressed into pellets using cold press. The pellets obtained by mixing the powder homogenously were arc melted two times each sides to ensure homogeneity. All the steps of sample preparation including arc-melting process were carried out in Ar-filled glove box to avoid any oxidation in any steps. The samples were prepared as couples, two for each compositions to keep one for further annealing process at this point for 7-days at 1223 K. The obtained ingots and the other pairs after annealing process were ball-milled only five minutes to obtain fine powders for the SPS process. To obtain powder samples, the ingots were put inside stainless-steel spex jars with two half inch stainless-steel balls and sealed inside the Ar-filled glove box to avoid oxidation.

For chemical characterizations and transport property measurements, dense cylindrical pellets were obtained by SPS in a graphite die at 1173 K for 10 min under a pressure of 65 MPa. All the experimental characterization methods were used as explained in chapter 3. Electrical resistivity and Seebeck coefficient (thermopower) measurements were performed using a ZEM-3 measurement system (ULVAC-Riko, Japan) on a bar-shaped sample. Thermal diffusivity, D, measurements were performed with a NETZSCH LFA HT467 laser flash apparatus. Thermal conductivity (K) of the samples was calculated using the relation $\kappa = DC_Pd$, where C_P is the isobaric heat capacity

estimated using the Dulong-Petit law and d is the experimental geometric density. All the measurements were done with 50 K interval on heating and 100 K of cooling.

8.3 Characterization

In the literature, transport properties of NbCoSn and Zr-doping studies were already reported. Synthesis method of the material involves multiple steps with long annealing processes. Reported transport property results of the material seems not good enough to have high thermoelectric efficiency. Therefore, we propose different synthesis method with high doping efficiency for NbCoSn compound: arc melting.

8.3.1 $Zr_xNb_{1-x}CoSn$ ($x = 0 - 0.3$)

The crystal structure of NbCoSn is shown in Figure 8.1 [204]. The Nb atoms occupy the 4a site, while the Co atoms occupy the 4b site, and together they form a NaCl structure with octahedral coordination. Then, the Sn elements occupy half of the 4c sites, central tetrahedral central sites that gives the name for half-Heusler to this compound. Considering Zintl chemistry concept on this compound, the crystal structure is composed of an anionic framework of $[CoSn]^{5-}$ by the tetrahedral coordinations of Co and Sn, and Nb^{5+} cations in the octahedral voids that is formed by the tetrahedral frameworks.

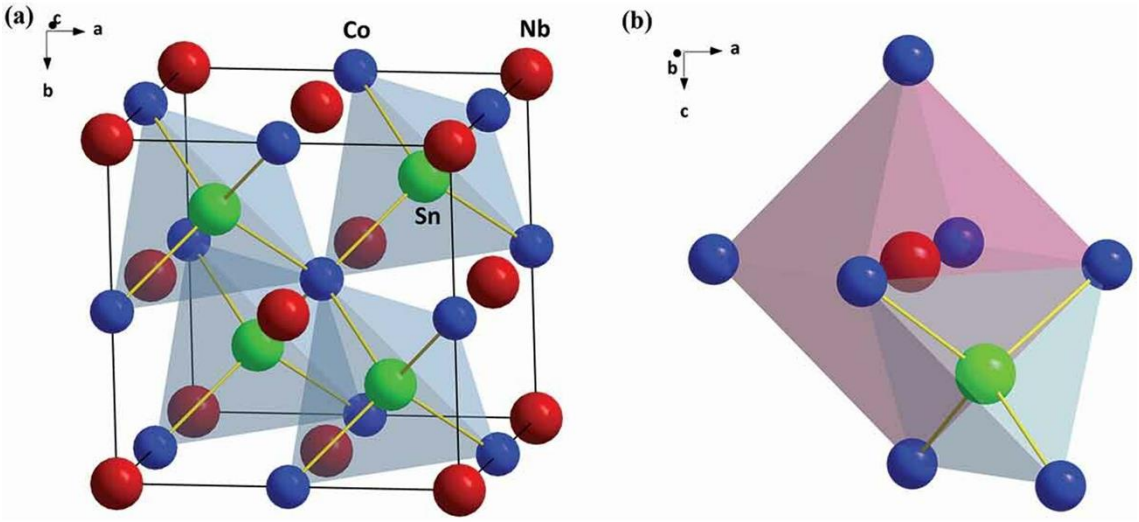

Figure 8.1 a) The crystal structure of NbCoSn and b) Nb and Sn coordinations in the structure [204].

XRD powder patterns of the synthesized samples are present in Figure 8.2 and Figure 8.3. The samples were synthesized successfully and the peaks could be indexed to MgAgAs cubic phase. XRD patterns of pristine only arc-melted NbCoSn sample before and after SPS process is given in Figure 8.2 as an example for an SPS effect. The black XRD pattern in Figure 8.2 is the pattern of powder sample after arc-melting reaction and 5-minute ball milling while the red one is the pattern of densified pellet of the same powder right after SPS process. The XRD investigation reveals cubic NbCoSn with small amount of binary impurities is almost gone after SPS process.

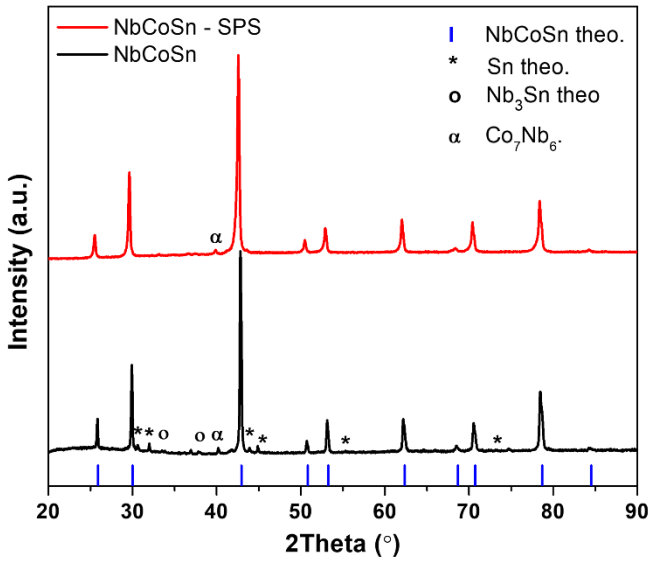

Figure 8.2 Experimental XRD patterns (Cu Kα) of NbCoSn samples before (black) and after (red) SPS process.

The XRD patterns of Zr-doped samples are shown in Figure 8.3. The pairs of same colors represent the same composition samples, and the upper one of each pair is the samples synthesized with an additional step of annealing. When we compare the patterns of pairs, same compositions synthesized by only arc-melting (below) and by arc-melting and annealing (above), there is a slight improvement in the purity of the samples. As the Zr-doping amount increases and *x* is more than 0.1, the secondary phases are observed and slightly increase as the Zr amount increases. We can clearly see the 2theta shifts of the peak positions to the higher 2theta with Zr-substitution. As the Zr-substitution amount increases, the peak positions shifts to the lower 2theta angles in a trend, meaning the lattice parameters of the cubic phase increases as the radius of Zr is larger than the radius of Nb in the covalent bond.

The synthesis method itself as a single step method by arc-melting is successful when the XRD patterns were compared with previous studies that used different synthesis methods with multiple steps and annealing processes [135, 204]. The pristine NbCoSn sample has almost no impurity. The Zr-substitution on transport data were investigated systematically by measuring physical properties of all the samples. The Seebeck coefficient data will give more information about the samples carrier type.

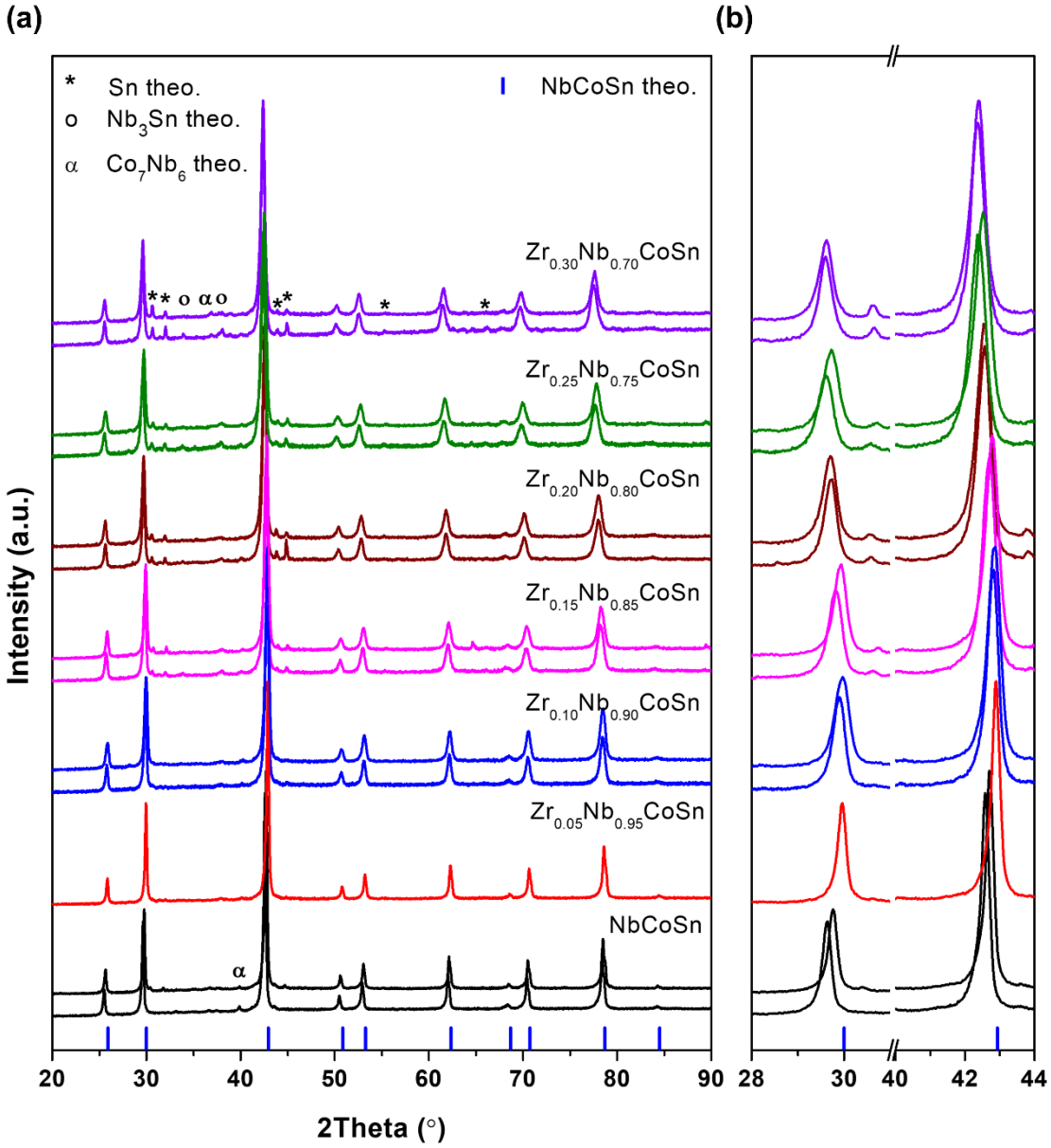

Figure 8.3 Experimental XRD patterns (Cu Kα) of Zr-substituted NbCoSn samples after SPS.

8.3.2 $Nb_{1+x}Co_{1-y}Sn$ (x = 0.05 & 0.10), (y = 0, 0.05 & 0.10)

The XRD patterns of pristine NbCoSn and Co/Sn deficient samples are shown in Figure 8.4. The pairs of same colors represent the same composition-samples, and the upper one of each pair is the samples synthesized with an additional step of annealing. When we compare the patterns of pairs with the same compositions, the samples synthesized by only arc-melting (below) and by arc-melting and annealing (above), there is a slight improvement in the compositions by removing the secondary phases. As expected, the Co-deficieny, and the Co and Sn deficiency together increases, the peak intensities of binary phases increase. The deficiency effect of nominal compositions on transport data were investigated systematically by measuring physical properties of all the samples. In general, Co-deficiency or Co- and Sn-deficiency lead to a shift on the

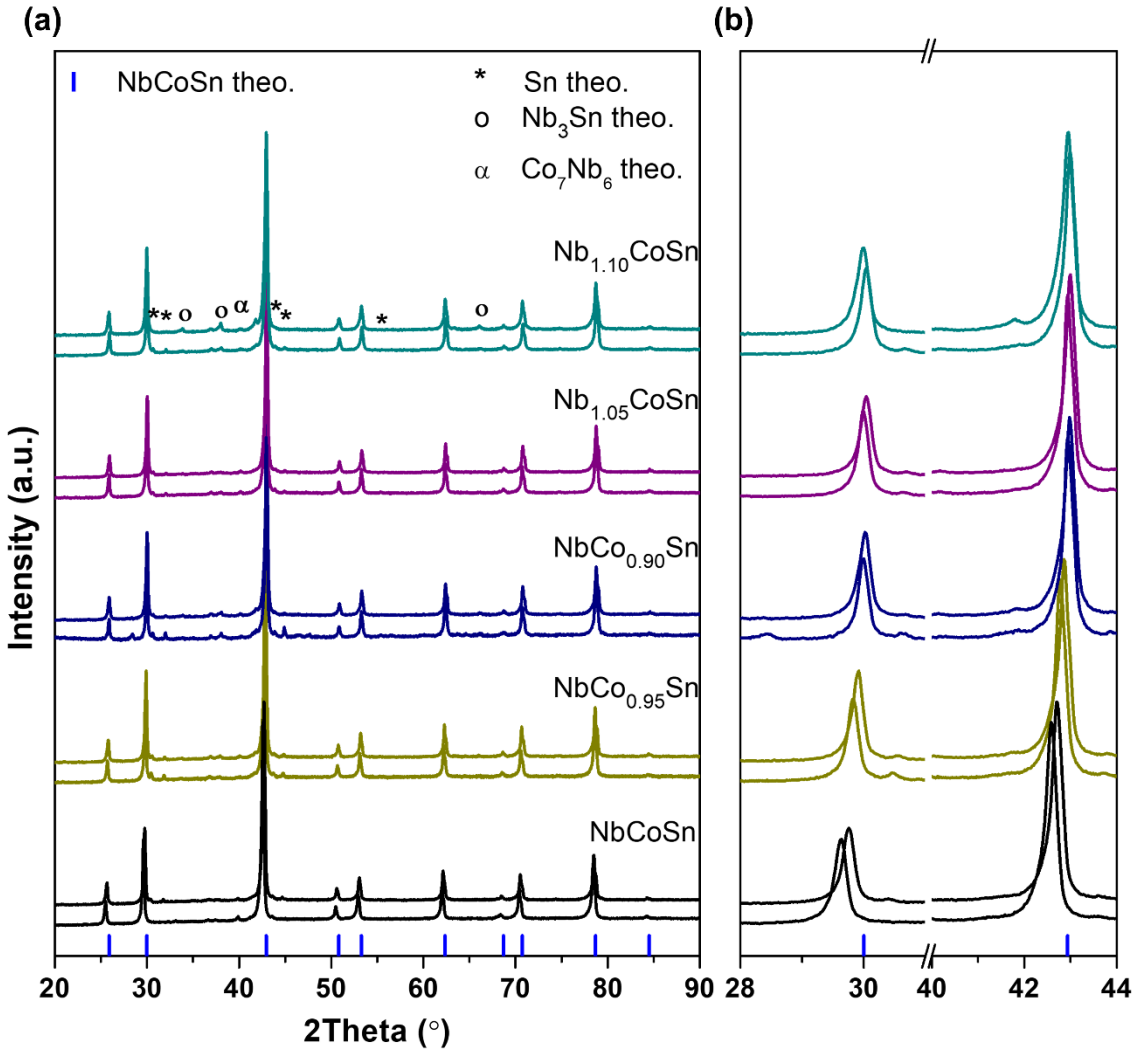

Figure 8.4 Experimental XRD patterns (Cu Kα) of NbCoSn samples with Co- and Co/Sn-deficiency after SPS.

peaks to the higher 2theta angles compared to the pristine NbCoSn sample meaning decrease in the lattice parameters. The decrease in the 4b occupancy of Co shrinks the unit cell.

8.3.3 $Zr_{0.2}Nb_{0.8}Co_{1-y}Sn$ (y = 0.05 & 0.10)

In order to have p-type NbCoSn, combination of Co-deficiency and the best p-type Zr-substitution amount were implemented on the samples and they were analyzed by X-ray diffraction method (Figure 8.5). By decreasing the Co nominal composition while adding the p-type dopant to the structure on Nb sites, the purpose of the study was obtain p-type carrier in the samples.

The XRD patterns of the samples show that with the same amount of Zr-dopant and different Co-deficiency the samples after SPS produced by arc-melting method is showing that there is a significant amount of Sn in the 5 % Co-deficient sample compared to 10 % Co-deficient sample.

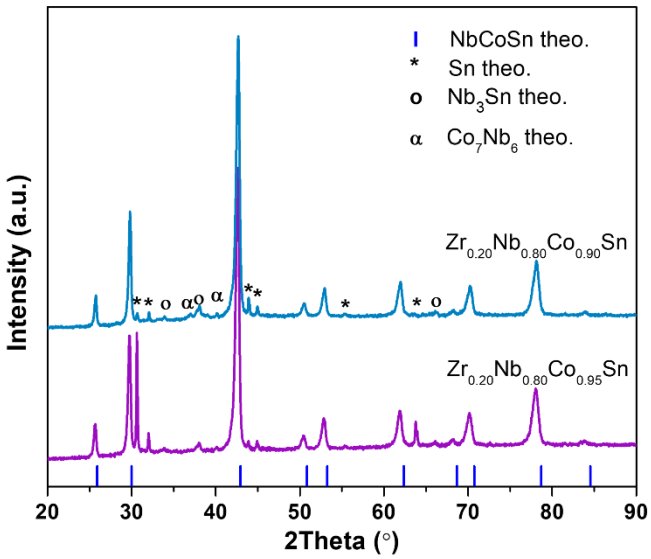

Figure 8.5 Experimental XRD patterns (Cu Kα) of Zr-substituted and Co-deficient NbCoSn samples after SPS.

8.4 Transport Property Measurements

The transport property measurements were done on desified pellets after SPS. Thermal diffisuvity measurements were done on the pellets and the electrical resistivity and the Seebeck coefficient measurements were performed on a bar shaped sample that was cut using diamond wire saw.

8.4.1 $Zr_xNb_{1-x}CoSn$ (x = 0 – 0.3)

The temperature dependences of the electrical resistivity, ρ, Seebeck coefficient data, *S*, power factor S^2/ρ, total thermal conductivity κ, and *zT* of NbCoSn samples are shown in Figure 8.6 a), b), c), d), and e) & f), respectively. The resistiviy values of pristine NbCoSn sample is low, below 5mΩ.cm and are decreasing with increasing temperature. As the Zr is introduced on Nb sites, the resistivity values increases substantially with Zr-substitution of 0.05 and 0.10. The resistivity values are at the maximum with 0.10 Zr-substitution and the values decreases with further Zr-substitution. When the values are compared with the same compositions of pristine NbCoSn and $Zr_{0.2}Nb_{0.80}CoSn$ synthesized via long annealings in an earlier study with an afford to obtain a p-type NbCoSn sample, the resistivity values are above 7 mΩ.cm and 27 mΩ.cm at room temperature, respectively. The values for $Zr_{0.2}Nb_{0.80}CoSn$ sample are above 25 mΩ.cm till 600 K and drops down to ~20 mΩ.cm around 800 K. In this study, the resistivity value of NbCoSn is 5 mΩ.cm at room temperature and stays below 5 mΩ.cm throught the working temperature range while te values of $Zr_{0.2}Nb_{0.80}CoSn$ vary between 5 - 7 mΩ.cm between room temperature and 873 K. With 0.25 and 0.30 Zr-substitutions, the values are below the values of pristine sample which varies between 2.5 - 4 mΩ.cm.

The Seebeck values (Figure 8.5 b) of pristine sample is showing negative values indicating the n-type behavior with the electrons as the main charge carriers. With Zr-substitution, the electrons were suppressed and the samples gets more p-type behavior. With 0.10 and more Zr-substitution, the Seebeck values are positive, indicating the p-type characteristics with the holes as the main charge carriers. The Seebeck values increases with increasing temperature and they are low till 500 K. The peak Seebeck value reaches ~150 μV/K at 873 K for the $Zr_{0.2}Nb_{0.80}CoSn$ sample and it supports the values from the previous study [135]. However, because of high resistivity values of this sample in the same study, the power factor (PF, S^2/ρ) remains very low, around 0.1 mW/mK^2 for the $Zr_{0.2}Nb_{0.80}CoSn$ samples while it is 0.4 mW/mK^2 around the same temperature (at around

800 K) and reaches up to 0.6 at 873 K. $Zr_{0.2}Nb_{0.80}CoSn$ sample is the best p-type sample with the highes p-type carrier concentration among all the other samples.

The total thermal conductivity values decrease with increasing temperature and also as the Zr amount increases as expected. The values decrease down to ~4 W/mK with the doping and remains almost constant within the working temperature range. When we combine all these three variables to calculate *zT*, thermoelectric figure of merit of p-type samples, the sample with the highest zT value of 0.11 at 873 K is $Zr_{0.2}Nb_{0.80}CoSn$ due to the highest power factor and one of the lowest total thermal conductivity values. This sample has double *zT* value of ~ 0.06 at around 773 K compared to the reported *zT* value below 0.03 reported in the same study [135] for the same compositions of $Zr_{0.2}Nb_{0.80}CoSn$.

When the transport data of annealed samples (Figure 8.7) were compared to the samples haven't experienced further annealing step (Figure 8.6), there is only minor changes in the values. Only significant difference between the samples is between the pristine samples. Although the resistivity values of pristine sample decreases over a wide temperature range, the Seebeck values and the theral conductivity also decrease, resulting in low *zT* values in general. Since the absolute Seebeck coefficient values decrease significantly, we can say that the composition changes slightly. Increase in the thermal conductivity values could be result of increase in the grains.

Theresistivity values of all the samples stay almost the same after long and high temperature annealing treatment. The Seebeck coefficient of the Zr-substituted samples enhanced at the higher temperatures reaching above 100 μV/K. The power factor of all the samples, except $Zr_{0.10}Nb_{0.90}CoSn$, increases and reaching to the values of $Zr_{0.20}Nb_{0.80}CoSn$. The zT values increased between 0.10 and 0.12 for most of the samples. Overall, the long and high temperature annealing steps for pristine NbCoSn sample did not improve the transport properties while the values and the efficiency of Zr-substituted samples have enhanced slightly.

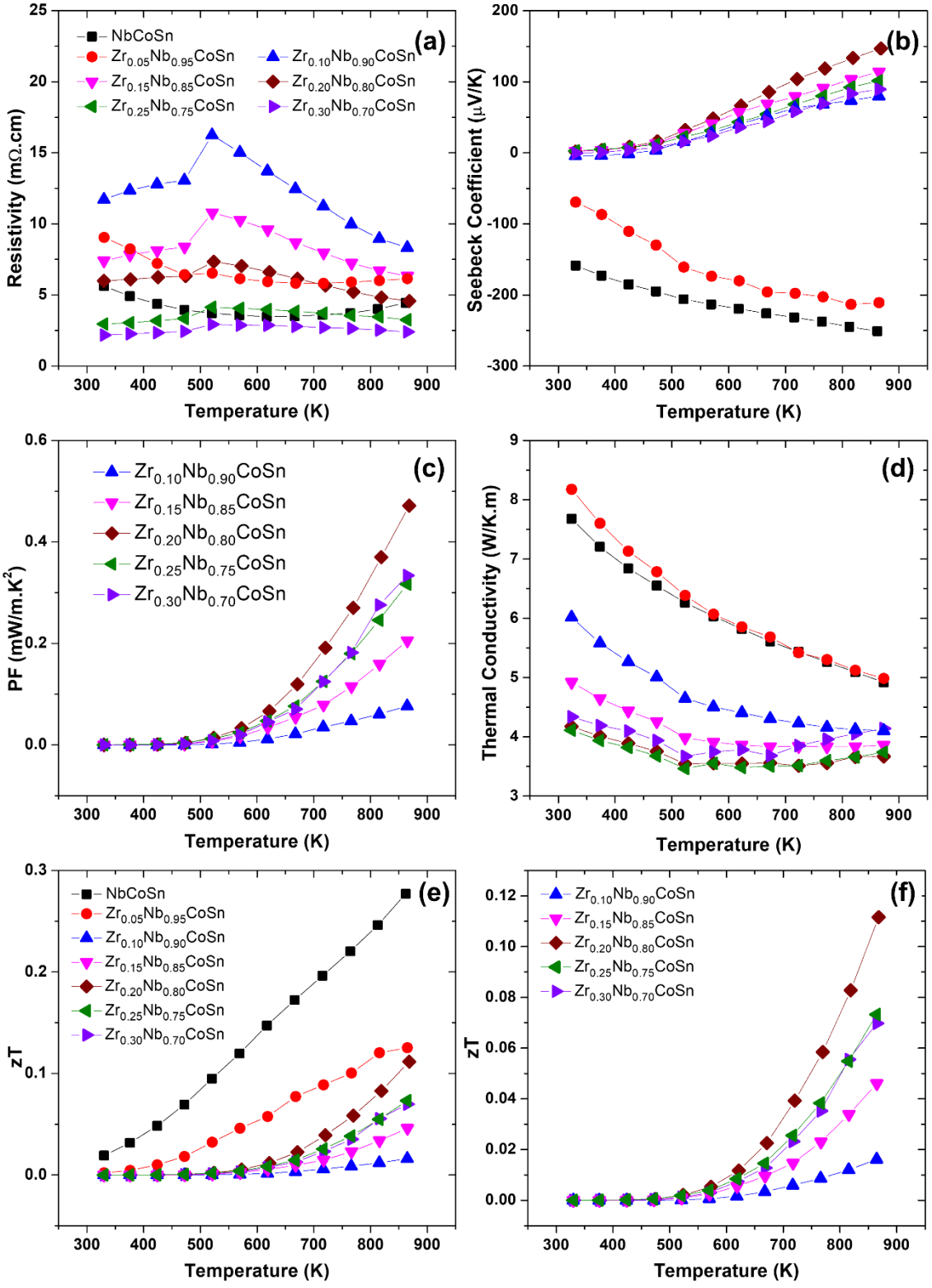

Figure 8.6 Temperature dependence of the (a) electrical resistivity, (b) Seebeck coefficient, (c) power factor (of only p-type samples), (d) total thermal conductivity, (e) *zT* of pristine and Zr-substituted NbCoSn samples, and (f) zT of p-type samples (zoom in region of (e).

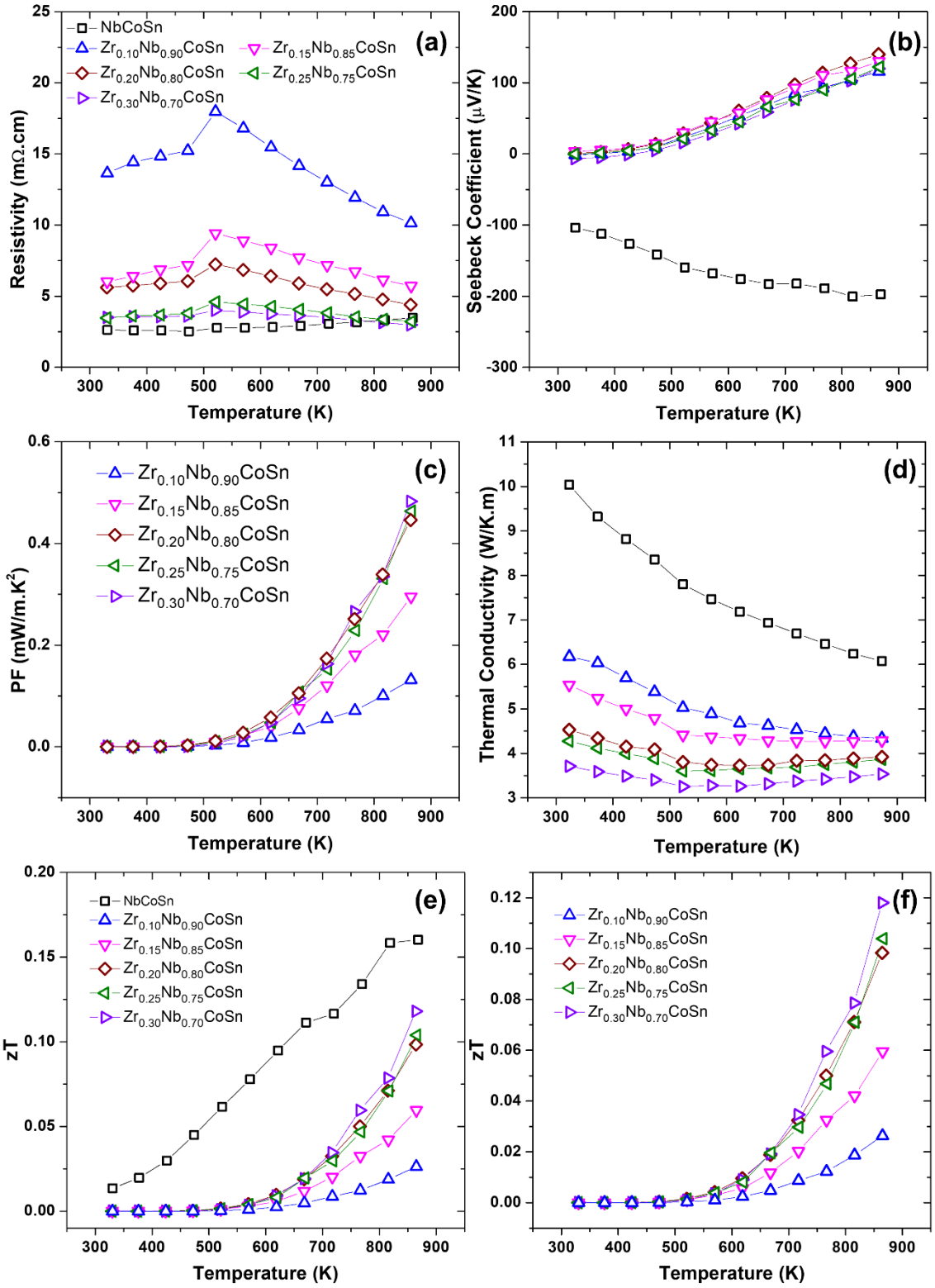

Figure 8.7 Temperature dependence of the (a) electrical resistivity, (b) Seebeck coefficient, (c) power factor (of only p-type samples), (d) total thermal conductivity, (e) *zT* of pristine and Zr-substituted NbCoSn annealed samples, and (f) zT of p-type samples (zoom in region of (e).

8.4.2 $Nb_{1+x}Co_{1-y}Sn$ (x = 0.05 & 0.10), (y = 0, 0.05 & 0.10)

The temperature dependences of the electrical resistivity, ρ, Seebeck coefficient data, *S*, total thermal conductivity κ, and *zT* of NbCoSn samples are shown in Figure 8.8 a), b), c), and d), respectively. The samples were produced in pairs as one of them was only by arc-melting method and the other one was subjected to the further annealing for a week at 1223 K. The electrical resistivity values of Co-deficient samples decreases substantially and stays below 5 mΩ.cm when we compare the pristine NbCoSn sample. The values decreases more with the increasing Co-deficiency when we compare the values between NbCoSn, $NbCo_{0.95}Sn$, and $NbCo_{0.90}Sn$. The samples with both Co- and Sn-deficiencies, $Nb_{1.05}CoSn$ and $Nb_{1.10}CoSn$ have also lower resistivity values compared to the pristine sample NbCoSn but slightly higher than the values of the samples with only Co-deficiency. Samples with the further annealing, the resistivity values increases slightly on the samples with the slight deficiencies; $NbCo_{0.95}Sn$ and $Nb_{1.05}CoSn$. However, there is substantial increase in resistivity values of $NbCo_{0.90}Sn$ and $Nb_{1.10}CoSn$ samples, especially at low temperatures. The reason could be the different binary phases form in the structure causing for the scattering in the sample. In general the annealing process was expected to decrease the resistivity values by causing to samples to have larger grains which was only seen in the pristine sample NbCoSn. While the values are almost the same in $Nb_{1.05}CoSn$ sample after annealing, the rest of the samples have higher resistivity values after annealing procedure.

The Seebeck coefficient values of all the samples are still in negative values meaning the main charge carriers are the electrons as the pristine NbCoSn sample. The Co- and Sn-deficiency help to decrease the n-type character and the samples are having lower Seebeck values. With increasing amount of Co-deficiency or combined effect of Co- and Sn-deficieny, the Seebeck values decreases compared to pristine NbCoSn samples, having less n-type behavior. With the further annealing, there should be a slight change in the composition of the samples causing this change in the Seebeck values. The effect of this change is more dominant on the highest amount of deciciencies; on the samples $NbCo_{0.90}Sn$ and $Nb_{1.10}CoSn$ while the change in the values is less in $NbCo_{0.95}Sn$ and $Nb_{1.05}CoSn$ samples.

Unlike the trend observed in Zr-substitution study in section 8.4.3, the total thermal conductivity values increases (almost 25 %), with the deficiency in the nominal composition when we compare the total thermal conductivity values of NbCoSn. The

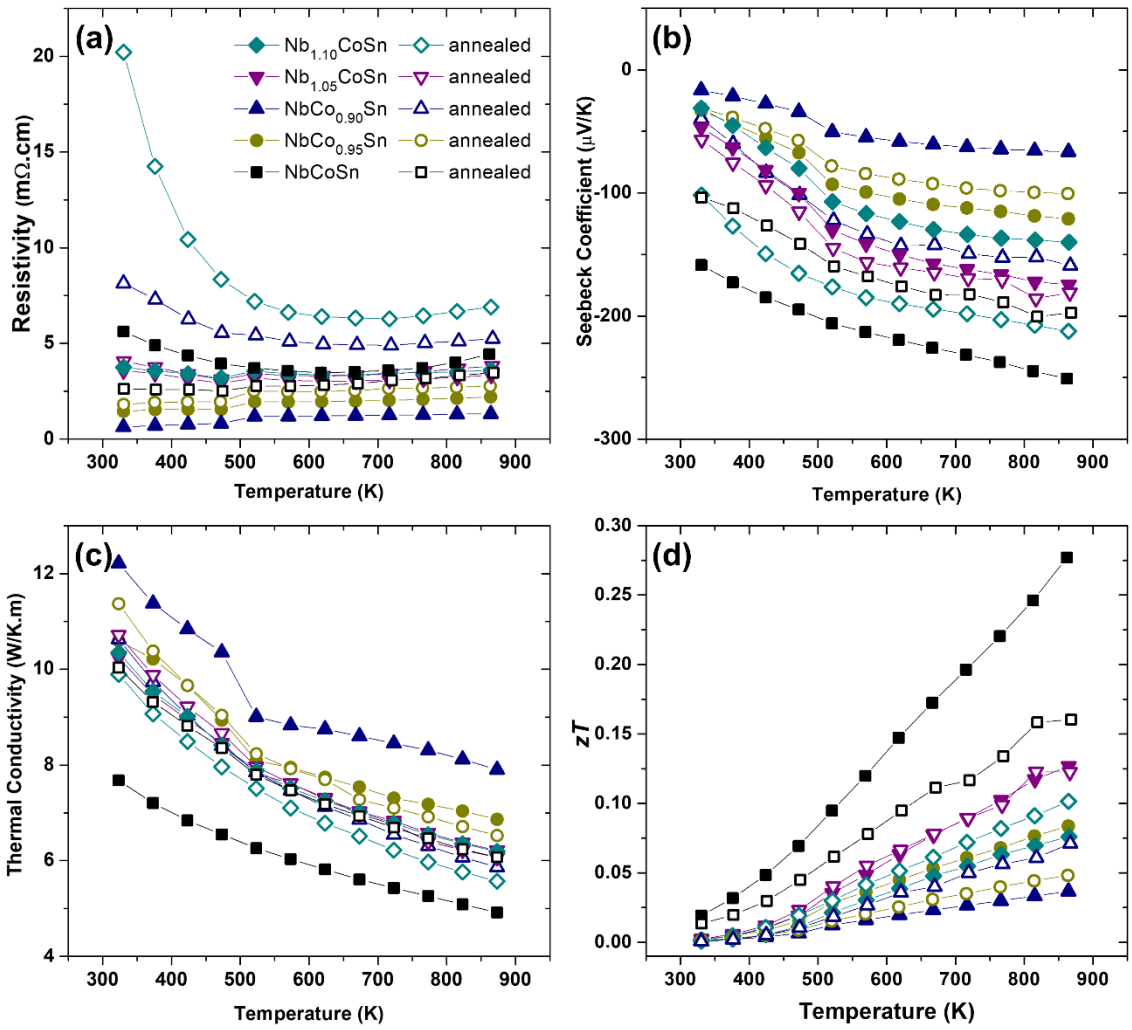

Figure 8.8 Temperature dependence of the (a) electrical resistivity, (b) Seebeck coefficient, (c) total thermal conductivity, and (d) thermoelectric figure of merit (zT) of pristine and Co/Sn-deficient NbCoSn samples.

values decreases slightly after annealing for the same compositions as expected that the samples will have larger grains and less binaries to act as scattering in the grains.

When the electrical resistivity, Seebeck coefficient, and the total thermal conductivity values are combined to obtain the *zT* values, as expected all the values decreases. The purpose of this section is to obtain less n-type sample with creating deficiencies in Co and Sn sites not to obtain samples with the high *zT* values. We can say that the samples without annealing steps seem more promising than the samples with multiple step synthesis; long annealings for the further investigation of p-type NbCoSn. We wanted to move on with Zr-substitution on samples with only Co-deficiency; $NbCo_{0.95}Sn$ and $NbCo_{0.90}Sn$ to see the combined effect of Zr-substitution and the Co-deficiency.

8.4.3 $Zr_{0.2}Nb_{0.8}Co_{1-y}Sn$ (y = 0.05 & 0.10)

The temperature dependences of the electrical resistivity ρ, Seebeck coefficient data S, power factor S^2/ρ, total thermal conductivity κ, and zT of Zr-substituted and Co-deficient NbCoSn samples are shown in Figure 8.9 a), b), c), d), e) and f), respectively. The compositions studied in this section were determined after evaluating the effect of Zr-substitution and the Co- and Sn-deficiency studies in section 8.4.1 and 8.4.2, separetly, and the samples were produced only via arc-melting. The compositions of interest is $Zr_{0.2}Nb_{0.80}Co_{0.95}Sn$ and $Zr_{0.2}Nb_{0.80}Co_{0.90}Sn$ to have a p-type NbCoSn samples, as the best p-type sample in Zr-substitution was $Zr_{0.2}Nb_{0.80}CoSn$ and the least n-type character samples were $NbCo_{0.95}Sn$ and $NbCo_{0.95}Sn$.

The electrical resistivity (ρ) values of Zr-substituted and Co-deficient samples are around 3 mΩ.cm between room temperature and 500 K, and there is a slight increase in the values around the same temperature. The values of $Zr_{0.2}Nb_{0.80}Co_{0.95}Sn$ increase up to 4 mΩ.cm and decreases slightly as the temperature increases. The jump in the values around 500 K is very small in $Zr_{0.2}Nb_{0.80}Co_{0.90}Sn$ compared the values in $Zr_{0.2}Nb_{0.80}Co_{0.95}Sn$. The values of $Zr_{0.2}Nb_{0.80}Co_{0.95}Sn$ and $Zr_{0.2}Nb_{0.80}Co_{0.90}Sn$. are much smaller than the values of $Zr_{0.2}Nb_{0.80}CoSn$ sample and almost similar to the samples with the lowest resistivity values of the highest doped ones as shown in Figure 8.6 a. The compositions studied with the Zr-substitution and the Co-deficiency is effective for the resistivity values.

The Seebeck coefficient values (Figure 8.9 b) are almost the same for both compositions of $Zr_{0.2}Nb_{0.80}Co_{0.95}Sn$ and $Zr_{0.2}Nb_{0.80}Co_{0.90}Sn$ and the values remain below the values of $Zr_{0.2}Nb_{0.80}CoSn$ shown in Figure 8.6. The values are relatively low between the room temperature and 600 K, and increase with a higher rate till 873 K, reaching up to ~100 μV/K and 92 μV/K for $Zr_{0.2}Nb_{0.80}Co_{0.95}Sn$ and $Zr_{0.2}Nb_{0.80}Co_{0.90}Sn$, respectively. The highest values obtained is almost 1/3 less than the Seebeck value of $Zr_{0.2}Nb_{0.80}CoSn$ sample. Since the power factor, thus the zT is more affected by the Seebeck coefficient than the resistivity values, the power factor is reaching to 0.35 mW/mK^2 with both of the compositions of $Zr_{0.2}Nb_{0.80}Co_{0.95}Sn$ and $Zr_{0.2}Nb_{0.80}Co_{0.90}Sn$ (Figure 8.9 c) while it was 0.47 mW/mK^2 for $Zr_{0.2}Nb_{0.80}CoSn$ (Figure 8.6 c).

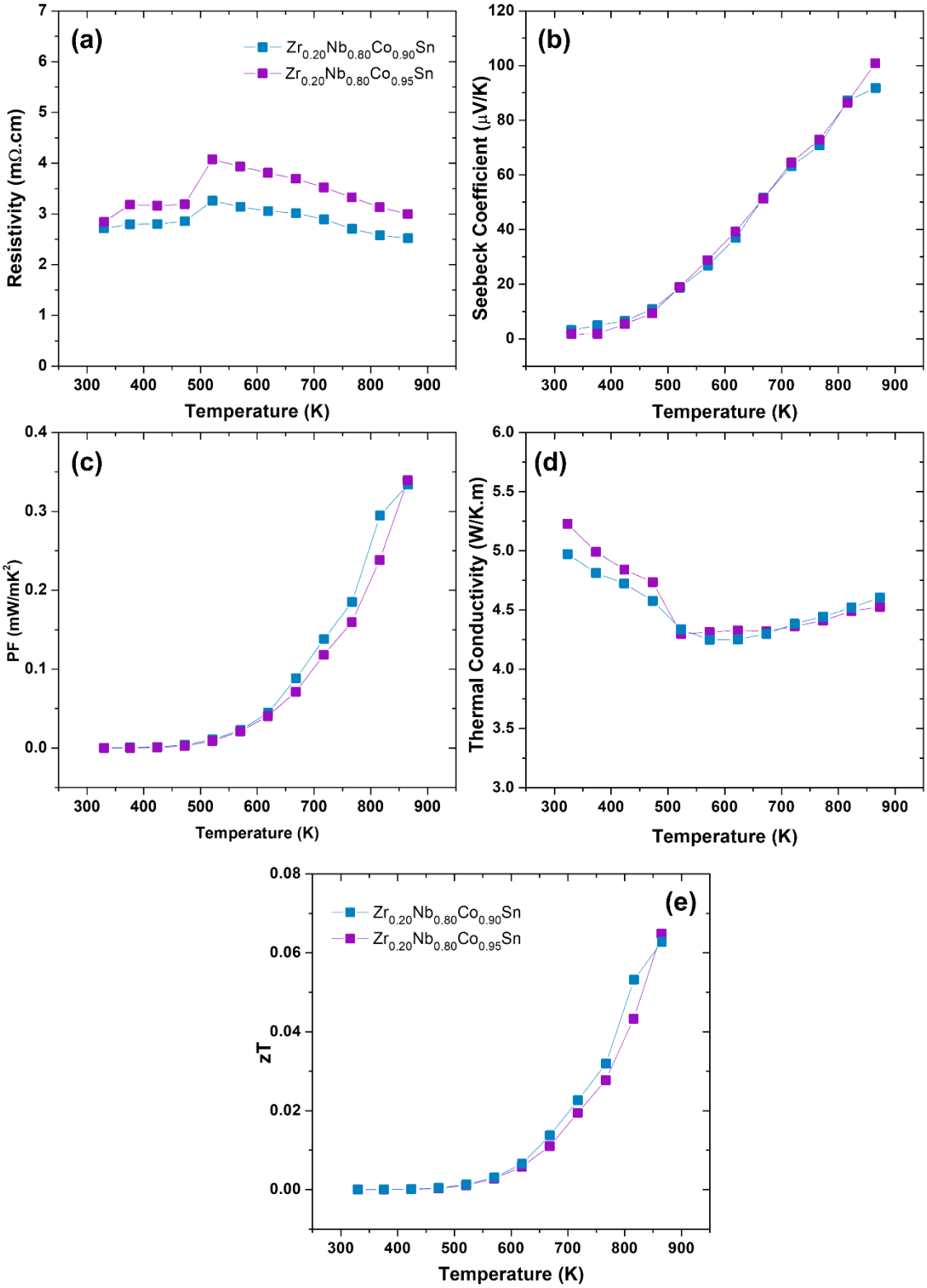

Figure 8.9 Temperature dependence of the (a) electrical resistivity, (b) Seebeck coefficient, (c) power factor, (d) total thermal conductivity and, (e) thermoelectric figure of merit (zT) of Zr-substituted Co-deficient NbCoSn samples.

The total thermal conductivity data of $Zr_{0.2}Nb_{0.80}Co_{0.95}Sn$ and $Zr_{0.2}Nb_{0.80}Co_{0.90}Sn$ samples are shown in Figure 8.9 d. The values are ~ 5.25 and 5.00 W/K.m and decreases with increasing temperature till 500 K, then increase slightly up to 873 K. These values are much smaller than the pristine NbCoSn sample, however; higher than the values of $Zr_{0.2}Nb_{0.80}CoSn$ sample. The *zT* values of the samples were shown in Figure 8.9 e, and they are below 0.01 between room temperature - 600 K and experience increase with increasing temperature reaching to maximum value of 0.065 and 0.063 for $Zr_{0.2}Nb_{0.80}Co_{0.95}Sn$ and $Zr_{0.2}Nb_{0.80}Co_{0.90}Sn$ at 873 K, respectively. Overall, $Zr_{0.2}Nb_{0.80}Co_{0.95}Sn$ and $Zr_{0.2}Nb_{0.80}Co_{0.90}Sn$ samples are affected more of Zr-substitution than the Co-deficiency. Even though the electrical resistivity values and the thermal conductivity values of both samples are less than the $Zr_{0.2}Nb_{0.80}CoSn$ sample, the Seebeck values are smaller leading to have smaller power factor values, thus smaller *zT* values.

8.5 Conclusions

In this study, different compositions of NbCoSn and Zr-substituted NbCoSn compounds were synthesized by a fast and single step synthesis method; an arc-melting. To investigate the further annealing effect, the samples were prepared as couples and one of them were annealed at elevated temperature for a week. The purpose of the study is to study p-type behavior of NbCoSn samples with Co or Co/Sn deficiency and Zr-substitution on Nb site. With the study on the effect of the Zr-substitution amount and the Co-deficiency alone or with Sn-deficiency, a systematic study was implemented to obtain a p-type NbCoSn samples. To combine the best, promising samples of $Zr_{0.2}Nb_{0.80}CoSn$ and $NbCo_{0.95}Sn$ & $NbCo_{0.90}Sn$, the transport properties of $Zr_{0.2}Nb_{0.80}Co_{0.95}Sn$ and $Zr_{0.2}Nb_{0.80}Co_{0.95}Sn$ compositions were investigated. As a result, Zr-substitution has more effective than the Co-deficiency without changing the composition of the main phase. Overall, $Zr_{0.2}Nb_{0.80}CoSn$ is the most promising p-type sample among the studied compositions with the highest Seebeck coefficient of ~150 μV/K at 873 K.

CHAPTER 9

CONCLUSION

This dissertation present a comprehensive study on the synthesis, characterization, and thermoelectric transport properties of phase-changing binary copper chalcogenides ($Cu_{3-x}Te_2$ and Cu_2Se) and Li_3Sb, along with a study on the p-type half-Heusler compound, NbCoSn.

Two compositions of synthetic rickardite mineral, $Cu_{3-x}Te_2$ with $x = 0.2$ and 0.1, were successfully synthesized by solid-state synthesis method with lattice parameters of a = 3.9933(1), b = 3.9635(1), c = 6.1159(3) Å and a = 4.0067(2), b = 3.9793(2), c = 6.1120(3) Å for $Cu_{2.8}Te_2$ and $Cu_{2.9}Te_2$, respectively at room temperature. Specific weak "satellite" reflections were observed on both powder diffraction and single-crystal data, indicating that the crystal structure of $Cu_{3-x}Te_2$ has modulated type of ordering. Differential Scanning Calorimetry (DSC) analysis revealed that both compositions undergo several reversible phase transitions. $Cu_{2.9}Te_2$ exhibits two main phase transitions at approximately 458 K and 647 K. The first transition, a second-order phase transition, corresponds to the crystal structure change from orthorhombic to tetragonal. In contrast, the second phase transition, which is more prominent, fits to the transition from tetragonal to hexagonal structure, unlike the previously reported cubic or rhombohedral structures. The crystal structure transitions were studied by high-temperature XRD measurements done at 300, 473, and 673 K, and the transitions were confirmed as the following order orthorhombic ↔ tetragonal ↔ hexagonal phases. The effect of these phase transitions was investigated on the electronic and thermal transport properties, showing that while the first transition has minimal influence on the transport data, the second phase transition occurred at around 650 K leading to a metallic-like to semiconducting-like properties by a sharp increase in the electrical resistivity and thermopower values with a significant decrease in the thermal conductivity values. When these parameters are combined, the higher temperature phase has improved thermoelectric performance with a zT value of 0.14 at around 733 K.

In order to optimize the carrier concentration and study the effect of substitution on phase transition temperatures, a detailed study was performed on Zn- and Ag-substitution

on $Cu_{2.9}Te_2$ with the compositions of $M_xCu_{2.9-x}Te_2$ (*M = Zn, Ag*, x = 0.05, 0.10 for Zn, x = 0.05, 0.10, 0.20 for Ag). The samples were synthesized with the same method as the pristine $Cu_{2.9}Te_2$, and the XRD analysis shows that the targeted phases were obtained with increased impurities with increasing substitution amount. Microstructure analysis revealed that all the $Cu_{2.9}Te_2$ samples show strong orientation contrast under the polarized light. A more inhomogeneous grain size distribution is observed for Zn-substituted samples while more homogenous grain size distribution is revealed for Ag-substituted samples. The DSC data shows that all the compositions of $Zn_{0.05}Cu_{2.85}Te_2$, $Zn_{0.10}Cu_{2.80}Te_2$, $Ag_{0.05}Cu_{2.85}Te_2$, and $Ag_{0.10}Cu_{2.80}Te_2$ display the same phase transitions with shifts in their phase transition temperatures. Zn-substitution in the high-temperature phase has minimal influence on the phase transition temperature, with the T_{onset} for HT transition temperatures at 644 K and 647 K for $Zn_{0.05}Cu_{2.85}Te_2$ and $Zn_{0.10}Cu_{2.80}Te_2$, respectively. However, the substitution of Ag in the same compound has a more noticeable effect, resulting in a decrease in the transition temperature with increasing substitution amount, with T_{onset} for HT transition temperatures at 631 K and 619 for $Ag_{0.05}Cu_{2.85}Te_2$, and $Ag_{0.10}Cu_{2.80}Te_2$, respectively. Consequently, the transport properties around the phase transitions and the transition temperature are affected by the shifts in the transition temperature via Zn- and Ag-substitution and the amount.

Cu_2Se is a widely studied binary copper chalcogenide material in thermoelectrics due to its promising thermoelectric performance at mid-temperatures. Herein, two different synthesis approaches have been applied to produce Cu_2Se, hydrothermal and solid-state synthesis methods. After facing difficulties in hydrothermal synthesis, such as impurities on the surface of nanoparticles, acidity, etc., most of the results are reported on the Cu_2Se samples synthesized via the solid-state synthesis method. The aim of this study is to investigate the effect of nano-B or C-coated nano-B incorporation as a light and non-toxic element, into the Cu_2Se compound. Nano-B or C-coated nano-B incorporation was implied via high energy ball milling with 0.15, 0.30, and 0.45 wt % additions. However, nano-B or C-coated nano-B incorporation leads to an increase in the resistivity values over the entire temperature range. A small increase in the Seebeck values via nano-B incorporation is observed, while the values are almost the same for C-coated nano-B case. Overall, the thermoelectric efficiency could not be improved due to the higher resistivity values.

The study on Li_3Sb focuses on evaluating the thermoelectric potential of c-Li_3Sb synthesized via the high-energy ball milling method. Interestingly, a stress/pressure-

induced phase transition has been observed in this system, stabilizing the metastable c-Li_3Sb phase at low temperatures. Moderate pressure/stress like cold press or high energy ball-mill stabilizes the cubic phase while stress releasing process such as thermal treatment solid state synthesis leads formation of hexagonal phase. Transport property measurements of Li_3Sb indicate a degenerate semiconducting behavior characterized by relatively low resistivity values and moderate Seebeck coefficients. Additionally, the total thermal conductivity of Li_3Sb decreases to a relatively low value of 1.35 W m^{-1} K^{-1} at 673 K. A *zT* value of 0.3 was obtained with a hole concentration of 4 x 10^{19} h^+ cm^{-3} at 550 K. Considering its lightweight nature, Li_3Sb is a promising thermoelectric material with favorable electrical and thermal properties. However, the air-sensitive nature of this material hinders its thermoelectric energy harvesting applications unless an airtight system is designed.

A systematic study on synthesizing and addressing the poor thermoelectric performance of the desired p-type NbCoSn material was also performed. Specifically, the p-type behavior of NbCoSn was enhanced by exploring the effects of Co-deficiency and Zr-substitution on the Nb site. Samples were synthesized by a one-step arc-melting synthesis method. The samples were synthesized as pairs to see the effect of further annealing steps. By carefully controlling the Co-deficiency and introducing Zr-substitution, the aim was to optimize the electronic and structural properties of the NbCoSn material, ultimately leading to an improved thermoelectric performance in the p-type regime. As a result, Zr-substitution is found to be more effective than the Co-deficiency without changing the composition of the main phase. Overall, $Zr_{0.2}Nb_{0.80}CoSn$ is revealed to be the most promising p-type sample among the studied compositions, with the highest Seebeck coefficient of ~150 μV/K at 873 K.

BIBLIOGRAPHY

1. Forman, C., et al., *Estimating the global waste heat potential.* Renewable and Sustainable Energy Reviews, 2016. **57**: p. 1568-1579.
2. Tritt, T.M., *Thermoelectric phenomena, materials, and applications.* Annual review of materials research, 2011. **41**: p. 433-448.
3. Fleurial, J.-P., *Thermoelectric power generation materials: Technology and application opportunities.* Jom, 2009. **61**(4): p. 79-85.
4. Snyder, G.J. and E.S. Toberer, *Complex thermoelectric materials.* Nature materials, 2008. **7**(2): p. 105-114.
5. Papapetrou, M., et al., *Industrial waste heat: Estimation of the technically available resource in the EU per industrial sector, temperature level and country.* Applied Thermal Engineering, 2018. **138**: p. 207-216.
6. Yang, J. and T. Caillat, *Thermoelectric materials for space and automotive power generation.* MRS bulletin, 2006. **31**(3): p. 224-229.
7. Mao, J., G. Chen, and Z. Ren, *Thermoelectric cooling materials.* Nature Materials, 2021. **20**(4): p. 454-461.
8. Wang, Y., et al., *Wearable thermoelectric generator for harvesting heat on the curved human wrist.* Applied Energy, 2017. **205**: p. 710-719.
9. Nolas, G.S., J. Sharp, and J. Goldsmid, *Thermoelectrics: basic principles and new materials developments*. Vol. 45. 2001: Springer Science & Business Media.
10. Li, J.-F., et al., *High-performance nanostructured thermoelectric materials.* NPG Asia Materials, 2010. **2**(4): p. 152-158.
11. Pei, Y., et al., *Convergence of electronic bands for high performance bulk thermoelectrics.* Nature, 2011. **473**(7345): p. 66-69.
12. Pei, Y., et al., *High thermoelectric performance in PbTe due to large nanoscale Ag2Te precipitates and La doping.* Advanced Functional Materials, 2011. **21**(2): p. 241-249.
13. Toberer, E.S., et al., *Traversing the metal-insulator transition in a Zintl phase: rational enhancement of thermoelectric efficiency in Yb14Mn1− xAlxSb11.* Advanced Functional Materials, 2008. **18**(18): p. 2795-2800.
14. Kim, H.-S., et al., *Characterization of Lorenz number with Seebeck coefficient measurement.* APL materials, 2015. **3**(4): p. 041506.
15. Lee, K.H. and S.W. Kim, *Design and preparation of high-performance bulk thermoelectric materials with defect structures.* Journal of the Korean Ceramic Society, 2017. **54**(2): p. 75-85.
16. Pei, Y., H. Wang, and G. Snyder, *Thermoelectric materials: band engineering of thermoelectric materials (Adv. Mater. 46/2012).* Advanced Materials, 2012. **24**(46): p. 6124-6124.
17. Shuai, J., et al., *Tuning the carrier scattering mechanism to effectively improve the thermoelectric properties.* Energy & Environmental Science, 2017. **10**(3): p. 799-807.
18. He, J., M.G. Kanatzidis, and V.P. Dravid, *High performance bulk thermoelectrics via a panoscopic approach.* Materials Today, 2013. **16**(5): p. 166-176.
19. Zong, P.-a., et al., *Skutterudite with graphene-modified grain-boundary complexion enhances zT enabling high-efficiency thermoelectric device.* Energy & Environmental Science, 2017. **10**(1): p. 183-191.
20. Biswas, K., et al., *High-performance bulk thermoelectrics with all-scale hierarchical architectures.* Nature, 2012. **489**(7416): p. 414-418.

21. Slack, G.A., *New Materials and Performance Limits for Thermoelectric Cooling. In: Rowe D M (eds.).* CRC Handbook of Thermoelectrics 1995: p. 407-440.
22. Qiu, P., X. Shi, and L. Chen, *Cu-based thermoelectric materials.* Energy Storage Materials, 2016. **3**: p. 85-97.
23. Wei, T.-R., et al., *Copper chalcogenide thermoelectric materials.* Science China Materials, 2019. **62**(1): p. 8-24.
24. Liu, H., et al., *Copper ion liquid-like thermoelectrics.* Nature materials, 2012. **11**(5): p. 422-425.
25. He, Y., et al., *High thermoelectric performance in non-toxic earth-abundant copper sulfide.* Advanced Materials, 2014. **26**(23): p. 3974-3978.
26. He, Y., et al., *Ultrahigh thermoelectric performance in mosaic crystals.* Advanced Materials, 2015. **27**(24): p. 3639-3644.
27. Zhao, L., et al., *High thermoelectric and mechanical performance in highly dense Cu 2− x S bulks prepared by a melt-solidification technique.* Journal of Materials Chemistry A, 2015. **3**(18): p. 9432-9437.
28. Islam, S.M.K.N., et al., *Giant enhancement of the figure-of-merit over a broad temperature range in nano-boron incorporated Cu 2 Se.* Journal of Materials Chemistry A, 2018. **6**(38): p. 18409-18416.
29. Li, M., et al., *Ultrahigh figure-of-merit of Cu2Se incorporated with carbon coated boron nanoparticles.* InfoMat, 2019. **1**(1): p. 108-115.
30. Zhao, K., et al., *Enhanced Thermoelectric Performance through Tuning Bonding Energy in Cu2Se1–x S x Liquid-like Materials.* Chemistry of Materials, 2017. **29**(15): p. 6367-6377.
31. Gahtori, B., et al., *Giant enhancement in thermoelectric performance of copper selenide by incorporation of different nanoscale dimensional defect features.* Nano Energy, 2015. **13**: p. 36-46.
32. Olvera, A., et al., *Partial indium solubility induces chemical stability and colossal thermoelectric figure of merit in Cu 2 Se.* Energy & Environmental Science, 2017. **10**(7): p. 1668-1676.
33. Ge, Z.H., et al., *High-Performance Thermoelectricity in Nanostructured Earth-Abundant Copper Sulfides Bulk Materials.* Advanced Energy Materials, 2016. **6**(16): p. 1600607.
34. Jiang, B., et al., *Cu 8 GeSe 6-based thermoelectric materials with an argyrodite structure.* Journal of Materials Chemistry C, 2017. **5**(4): p. 943-952.
35. Qiu, P., et al., *Sulfide bornite thermoelectric material: a natural mineral with ultralow thermal conductivity.* Energy & Environmental Science, 2014. **7**(12): p. 4000-4006.
36. Ishiwata, S., et al., *Extremely high electron mobility in a phonon-glass semimetal.* Nature materials, 2013. **12**(6): p. 512-517.
37. Han, C.-G., et al., *Thermoelectric properties of p-type semiconductors copper chromium disulfide CuCrS 2+ x.* Journal of Materials Science, 2013. **48**(11): p. 4081-4087.
38. Plirdpring, T., et al., *Chalcopyrite CuGaTe2: A High-Efficiency Bulk Thermoelectric Material.* Advanced Materials, 2012. **24**(27): p. 3622-3626.
39. Liu, R., et al., *Ternary compound CuInTe 2: a promising thermoelectric material with diamond-like structure.* Chemical Communications, 2012. **48**(32): p. 3818-3820.
40. Liu, Y., et al., *Solution-based synthesis and processing of Sn-and Bi-doped Cu 3 SbSe 4 nanocrystals, nanomaterials and ring-shaped thermoelectric generators.* Journal of materials chemistry A, 2017. **5**(6): p. 2592-2602.

41. Skoug, E.J., J.D. Cain, and D.T. Morelli, *High thermoelectric figure of merit in the Cu3SbSe4-Cu3SbS4 solid solution.* Applied Physics Letters, 2011. **98**(26): p. 261911.
42. Shi, X., et al., *Cu− Se bond network and thermoelectric compounds with complex diamondlike structure.* Chemistry of Materials, 2010. **22**(22): p. 6029-6031.
43. Lin, H., et al., *Chemical modification and energetically favorable atomic disorder of a layered thermoelectric material TmCuTe2 leading to high performance.* Chemistry–A European Journal, 2014. **20**(47): p. 15401-15408.
44. Gulay, L., M. Daszkiewicz, and V.Y. Shemet, *Crystal structure of∼ RCu3S3 and∼ RCuTe2 (R= Gd–Lu) compounds.* Journal of Solid State Chemistry, 2012. **186**: p. 142-148.
45. Oudah, M., K.M. Kleinke, and H. Kleinke, *Thermoelectric properties of the quaternary chalcogenides BaCu5. 9STe6 and BaCu5. 9SeTe6.* Inorganic chemistry, 2015. **54**(3): p. 845-849.
46. Zhao, L.-D., et al., *BiCuSeO oxyselenides: new promising thermoelectric materials.* Energy & Environmental Science, 2014. **7**(9): p. 2900-2924.
47. Lan, J.L., et al., *Enhanced thermoelectric properties of Pb-doped BiCuSeO ceramics.* Advanced Materials, 2013. **25**(36): p. 5086-5090.
48. Li, F., et al., *Enhanced thermoelectric performance of Ca-doped BiCuSeO in a wide temperature range.* Journal of Materials Chemistry A, 2013. **1**(38): p. 11942-11949.
49. Aydemir, U., et al., *YCuTe 2: a member of a new class of thermoelectric materials with CuTe 4-based layered structure.* Journal of Materials Chemistry A, 2016. **4**(7): p. 2461-2472.
50. He, Y., et al., *High thermoelectric performance in copper telluride.* NPG Asia Materials, 2015. **7**(8): p. e210-e210.
51. Nunna, R., et al., *Ultrahigh thermoelectric performance in Cu 2 Se-based hybrid materials with highly dispersed molecular CNTs.* Energy & Environmental Science, 2017. **10**(9): p. 1928-1935.
52. Weldert, K.S., et al., *Thermoelectric transport in Cu7PSe6 with high copper ionic mobility.* Journal of the American Chemical Society, 2014. **136**(34): p. 12035-12040.
53. Bhattacharya, S., et al., *CuCrSe 2: a high performance phonon glass and electron crystal thermoelectric material.* Journal of Materials Chemistry A, 2013. **1**(37): p. 11289-11294.
54. Stevels, A. and G. Wiegers, *Phase transitions in copper chalcogenides II. The tellurides Cu3-x Te2 and CuTe.* Recueil des Travaux Chimiques des Pays-Bas, 1971. **90**(4): p. 352-359.
55. Mizota, T., K. Koto, and N. Morimoto, *Crystallography and composition of synthetic rickardite.* Mineralogical Journal, 1973. **7**(3): p. 252-261.
56. Ferizović, D. and M. Muñoz, *Optical, electrical and structural properties of Cu2Te thin films deposited by magnetron sputtering.* Thin Solid Films, 2011. **519**(18): p. 6115-6119.
57. Yun, J.H., et al., *Back contact formation using Cu2Te as a Cu-doping source and as an electrode in CdTe solar cells.* Solar Energy Materials and Solar Cells, 2003. **75**(1-2): p. 203-210.
58. Wu, X., et al., *Phase control of CuxTe film and its effects on CdS/CdTe solar cell.* Thin Solid Films, 2007. **515**(15): p. 5798-5803.
59. Lv, B., et al., *Preparation of Cu2Te thin films and back-contact formation of CdTe solar cells.* Japanese Journal of Applied Physics, 2009. **48**(8R): p. 085501.

60. Alfonso-González, E., et al., *A tandem photoelectrochemical cell based on Cu2-xTe nanocrystals for solar energy conversion to hydrogen.* Solar Energy Materials and Solar Cells, 2023. **250**: p. 112050.
61. Wu, Y., et al., *Enhanced photovoltaic performance of perovskite solar cells modified with plasmonic Cu1. 44Te nanocrystals.* Optik, 2022. **271**: p. 170229.
62. Nguyen, M.C., et al., *New layered structures of cuprous chalcogenides as thin film solar cell materials: Cu 2 Te and Cu 2 Se.* Physical review letters, 2013. **111**(16): p. 165502.
63. Mukherjee, S., et al., *Investigation on the structure and thermoelectric properties of Cu x Te binary compounds.* Dalton Transactions, 2019. **48**(3): p. 1040-1050.
64. Zhao, K., et al., *Are Cu2Te-Based Compounds Excellent Thermoelectric Materials?* Advanced Materials, 2019. **31**(49): p. 1903480.
65. Pandey, J., et al., *Raman Spectroscopy Study of Phonon Liquid Electron Crystal in Copper Deficient Superionic Thermoelectric Cu2–xTe.* ACS Applied Energy Materials, 2020. **3**(3): p. 2175-2181.
66. Pashinkin, A. and V. Fedorov, *Phase equilibria in the Cu–Te system.* Inorganic Materials, 2003. **39**(6): p. 539-554.
67. Schutte, W. and J. De Boer, *Determination of the incommensurately modulated structure of Cu3− xTe2.* Acta Crystallographica Section B: Structural Science, 1993. **49**(3): p. 398-403.
68. Forman, S.A. and M. Peacock, *Crystal structure of rickardite, Cu4–Te2.* American Mineralogist: Journal of Earth and Planetary Materials, 1949. **34**(5-6): p. 441-451.
69. Colaitis, D., et al., *High-resolution electron microscopic and electron diffraction study of non-stoichiometric phases in Cu3—xTe2.* physica status solidi (a), 1980. **58**(1): p. 271-288.
70. Huang, D., et al., *The Cu–Te system: phase relations determination and thermodynamic assessment.* Journal of Alloys and Compounds, 2021. **855**: p. 157373.
71. Elander, M., G. Hägg, and A. Westgren, *The Crystal Structure of Cu2Sb and Fe2As*. 1935: Almqvist & Wiksell.
72. De Medicis, R., *Etude de quelques sulfures, séléniures et tellurures de métaux de transition*. 1967, UCL-Université Catholique de Louvain.
73. Suzumura, A., et al., *Improvement in Thermoelectric Properties of Se-Free Cu 3 SbS 4 Compound.* Journal of electronic materials, 2014. **43**(6): p. 2356-2361.
74. Zhong, B., et al., *High superionic conduction arising from aligned large lamellae and large figure of merit in bulk Cu1. 94Al0. 02Se.* Applied Physics Letters, 2014. **105**(12): p. 123902.
75. Fan, J., et al., *Crystal structure and physical properties of ternary phases around the composition Cu5Sn2Se7 with tetrahedral coordination of atoms.* Chemistry of Materials, 2014. **26**(18): p. 5244-5251.
76. Ballikaya, S., et al., *Thermoelectric properties of Ag-doped Cu 2 Se and Cu 2 Te.* Journal of Materials Chemistry A, 2013. **1**(40): p. 12478-12484.
77. Zhao, L., et al., *Improvement of thermoelectric properties and their correlations with electron effective mass in Cu 1.98 S x Se 1− x.* Scientific reports, 2017. **7**: p. 40436.
78. Liu, H., et al., *Ultrahigh thermoelectric performance by electron and phonon critical scattering in Cu2Se1-xIx.* Advanced Materials, 2013. **25**(45): p. 6607-6612.

79. Slack, G.A., *New materials and performance limits for thermoelectric cooling.* CRC Handbook of Thermoelectrics, 1995: p. 407-440.
80. Young, D.M. and S.M. Kauzlarich, *Preparation, structure, and electronic properties of Ca11MSb9 (M= Al, Ga, In).* Chemistry of materials, 1995. **7**(1): p. 206-209.
81. Gascoin, F., et al., *Zintl phases as thermoelectric materials: tuned transport properties of the compounds CaxYb1–xZn2Sb2.* Advanced Functional Materials, 2005. **15**(11): p. 1860-1864.
82. Brown, S.R., et al., *Yb14MnSb11: New high efficiency thermoelectric material for power generation.* Chemistry of materials, 2006. **18**(7): p. 1873-1877.
83. Toberer, E.S., A.F. May, and G.J. Snyder, *Zintl Chemistry for Designing High Efficiency Thermoelectric Materials.* Chemistry of Materials, 2010. **22**(3): p. 624-634.
84. Brown, S.R., et al., *Improved thermoelectric performance in Yb14Mn1− x Zn x Sb11 by the reduction of spin-disorder scattering.* Chemistry of Materials, 2008. **20**(10): p. 3412-3419.
85. Hu, Y., et al., *The remarkable crystal chemistry of the Ca14AlSb11 structure type, magnetic and thermoelectric properties.* Journal of Solid State Chemistry, 2019. **271**: p. 88-102.
86. Zevalkink, A., et al., *Influence of the Triel Elements (M= Al, Ga, In) on the Transport Properties of Ca5 M 2Sb6 Zintl Compounds.* Chemistry of Materials, 2012. **24**(11): p. 2091-2098.
87. Aydemir, U., et al., *Thermoelectric properties of the Zintl phases Yb 5 M 2 Sb 6 (M= Al, Ga, In).* Dalton Transactions, 2015. **44**(15): p. 6767-6774.
88. Aydemir, U., et al., *Thermoelectric enhancement in BaGa2Sb2 by Zn doping.* Chemistry of Materials, 2015. **27**(5): p. 1622-1630.
89. Aydemir, U., et al., *Enhanced thermoelectric properties of the Zintl phase BaGa 2 Sb 2 via doping with Na or K.* Journal of Materials Chemistry A, 2016. **4**(5): p. 1867-1875.
90. Wang, X.-J., et al., *Synthesis and high thermoelectric efficiency of Zintl phase Yb Cd 2− x Zn x Sb 2.* Applied Physics Letters, 2009. **94**(9): p. 092106.
91. Zhang, H., et al., *Thermoelectric properties of Eu (Zn1− xCdx) 2Sb2.* Dalton Transactions, 2010. **39**(4): p. 1101-1104.
92. Zhang, H., et al., *Synthesis and properties of CaCd2Sb2 and EuCd2Sb2.* Intermetallics, 2010. **18**(1): p. 193-198.
93. Zhang, H., et al., *Thermoelectric properties of Yb x Eu 1− x Cd 2 Sb 2.* The Journal of chemical physics, 2010. **133**(19): p. 194701.
94. Zhang, H., et al., *Thermoelectric properties of polycrystalline SrZn 2 Sb 2 prepared by spark plasma sintering.* Journal of electronic materials, 2010. **39**(9): p. 1772-1776.
95. Zhang, H., et al., *A new type of thermoelectric material, Eu Zn 2 Sb 2.* The Journal of chemical physics, 2008. **129**(16): p. 164713.
96. Zevalkink, A., et al., *Nonstoichiometry in the Zintl phase Yb1− δZn2Sb2 as a route to thermoelectric optimization.* Chemistry of Materials, 2014. **26**(19): p. 5710-5717.
97. Shuai, J., et al., *Higher thermoelectric performance of Zintl phases (Eu0. 5Yb0. 5) 1− xCaxMg2Bi2 by band engineering and strain fluctuation.* Proceedings of the National Academy of Sciences, 2016. **113**(29): p. E4125-E4132.
98. May, A.F., et al., *Thermoelectric transport properties of CaMg 2 Bi 2, EuMg 2 Bi 2, and YbMg 2 Bi 2.* Physical Review B, 2012. **85**(3): p. 035202.

99. Zhang, J., et al., *Discovery of high-performance low-cost n-type Mg 3 Sb 2-based thermoelectric materials with multi-valley conduction bands.* Nature communications, 2017. **8**(1): p. 1-8.
100. Tamaki, H., H.K. Sato, and T. Kanno, *Isotropic conduction network and defect chemistry in Mg3+ δSb2-based layered zintl compounds with high thermoelectric performance.* Advanced Materials, 2016. **28**(46): p. 10182-10187.
101. Condron, C.L., et al., *Thermoelectric properties and microstructure of Mg3Sb2.* Journal of Solid State Chemistry, 2006. **179**(8): p. 2252-2257.
102. Mao, J., et al., *Defect engineering for realizing high thermoelectric performance in n-type Mg3Sb2-based materials.* ACS Energy Letters, 2017. **2**(10): p. 2245-2250.
103. Mao, J., et al., *High thermoelectric cooling performance of n-type Mg3Bi2-based materials.* Science, 2019. **365**(6452): p. 495-498.
104. Ozen, M., et al., *Enhanced thermoelectric performance in Mg3+xSb1.5Bi0.49Te0.01 via engineering microstructure through melt-centrifugation.* Journal of Materials Chemistry A, 2021. **9**(3): p. 1733-1742.
105. Gorai, P., et al., *A simple chemical guide for finding novel n-type dopable Zintl pnictide thermoelectric materials.* Journal of Materials Chemistry A, 2019. **7**(33): p. 19385-19395.
106. Ohno, S., et al., *Phase Boundary Mapping to Obtain n-type Mg3Sb2-Based Thermoelectrics.* Joule, 2018. **2**(1): p. 141-154.
107. Qu, J.Q., et al., *Doping by design: finding new n-type dopable ABX(4) Zintl phases for thermoelectrics.* Journal of Materials Chemistry A, 2020. **8**(47): p. 25306-25315.
108. Kauzlarich, S.M., S.R. Brown, and G.J. Snyder, *Zintl phases for thermoelectric devices.* Dalton Transactions, 2007(21): p. 2099-2107.
109. Yang, X., et al., *Low lattice thermal conductivity and excellent thermoelectric behavior in Li3Sb and Li3Bi.* Journal of Physics: Condensed Matter, 2018. **30**(42): p. 425401.
110. Robertson, J., *Electronic structure of zintl compounds (NaTl) and alkali pnictides.* Solid state communications, 1983. **47**(11): p. 899-902.
111. Wei, S.-H. and A. Zunger, *Electronic structure of M 3 I Sb-type filled tetrahedral semiconductors.* Physical Review B, 1987. **35**(8): p. 3952.
112. Leonova, M., et al., *New Cubic Phases in the Li–Na–Sb–Bi System.* Inorganic materials, 2001. **37**(12): p. 1270-1273.
113. Hu, A., et al., *An artificial hybrid interphase for an ultrahigh-rate and practical lithium metal anode.* Energy & Environmental Science, 2021. **14**(7): p. 4115-4124.
114. Weppner, W. and R.A. Huggins, *Electrochemical investigation of the chemical diffusion, partial ionic conductivities, and other kinetic parameters in Li3Sb and Li3Bi.* Journal of Solid State Chemistry, 1977. **22**(3): p. 297-308.
115. Ha, V.-A., et al., *Computationally driven high-throughput identification of CaTe and Li 3 Sb as promising candidates for high-mobility p-type transparent conducting materials.* Physical Review Materials, 2019. **3**(3): p. 034601.
116. Li, W. and N. Mingo, *Thermal conductivity of fully filled skutterudites: Role of the filler.* Physical Review B, 2014. **89**(18): p. 184304.
117. Joshi, G., et al., *Enhancement in thermoelectric figure-of-merit of an N-type half-Heusler compound by the nanocomposite approach.* Advanced Energy Materials, 2011. **1**(4): p. 643-647.

118. Joshi, G., et al., *Enhanced thermoelectric figure-of-merit in nanostructured p-type silicon germanium bulk alloys.* Nano letters, 2008. **8**(12): p. 4670-4674.
119. Mecholsky, N.A., et al., *Theory of band warping and its effects on thermoelectronic transport properties.* Physical Review B, 2014. **89**(15): p. 155131.
120. Gibbs, Z.M., et al., *Effective mass and Fermi surface complexity factor from ab initio band structure calculations.* npj Computational Materials, 2017. **3**(1): p. 1-7.
121. Graf, T., C. Felser, and S.S. Parkin, *Simple rules for the understanding of Heusler compounds.* Progress in solid state chemistry, 2011. **39**(1): p. 1-50.
122. Ma, J., et al., *Computational investigation of half-Heusler compounds for spintronics applications.* Physical Review B, 2017. **95**(2): p. 024411.
123. Roy, A., et al., *Half-Heusler semiconductors as piezoelectrics.* Physical review letters, 2012. **109**(3): p. 037602.
124. Zeier, W.G., et al., *Engineering half-Heusler thermoelectric materials using Zintl chemistry.* Nature Reviews Materials, 2016. **1**(6): p. 1-10.
125. He, R., et al., *Improved thermoelectric performance of n-type half-Heusler MCo1-xNixSb (M= Hf, Zr).* Materials Today Physics, 2017. **1**: p. 24-30.
126. Fu, C., et al., *Enhanced phonon scattering by mass and strain field fluctuations in Nb substituted FeVSb half-Heusler thermoelectric materials.* Journal of Applied Physics, 2012. **112**(12): p. 124915.
127. Buffon, M.L., et al., *Enhancement of thermoelectric properties in the Nb–Co–Sn half-Heusler/Heusler system through spontaneous inclusion of a coherent second phase.* Journal of Applied Physics, 2016. **120**(7): p. 075104.
128. Xie, H., et al., *The intrinsic disorder related alloy scattering in ZrNiSn half-Heusler thermoelectric materials.* Scientific reports, 2014. **4**: p. 6888.
129. Xia, K., et al., *Short-range order in defective half-Heusler thermoelectric crystals.* Energy & Environmental Science, 2019. **12**(5): p. 1568-1574.
130. Zhu, T., et al., *High efficiency half-Heusler thermoelectric materials for energy harvesting.* Advanced Energy Materials, 2015. **5**(19): p. 1500588.
131. He, R., et al., *Enhanced thermoelectric properties of n-type NbCoSn half-Heusler by improving phase purity.* APL Materials, 2016. **4**(10): p. 104804.
132. Bhattacharya, S. and G.K. Madsen, *A novel p-type half-Heusler from high-throughput transport and defect calculations.* Journal of Materials Chemistry C, 2016. **4**(47): p. 11261-11268.
133. Kawaharada, Y., et al., *High temperature thermoelectric properties of CoNb1− xMxSn half-Heusler compounds.* Journal of alloys and compounds, 2004. **384**(1-2): p. 303-307.
134. Kawaharada, Y., et al., *High temperature thermoelectric properties of CoNb1− xHfxSn1− ySby half-Heusler compounds.* Journal of alloys and compounds, 2004. **377**(1-2): p. 312-315.
135. Ferluccio, D.A., et al., *Impact of Nb vacancies and p-type doping of the NbCoSn–NbCoSb half-Heusler thermoelectrics.* Physical Chemistry Chemical Physics, 2018. **20**(6): p. 3979-3987.
136. Suárez, M., et al., *Challenges and opportunities for spark plasma sintering: a key technology for a new generation of materials.* Sintering applications, 2013. **13**: p. 319-342.
137. Cavaliere, P., B. Sadeghi, and A. Shabani, *Spark plasma sintering: process fundamentals.* Spark plasma sintering of materials: advances in processing and applications, 2019: p. 3-20.

138. *STOE WinXPOW, Stoe & Cie GmbH, Darmstadt, ver. 3.11*. 2017.
139. *ICSD database, Fachinformationszentrum (FIZ) Karlsruhe, ver. 4.9,*. 2022.
140. Akselrud, L. and Y. Grin, *WinCSD: software package for crystallographic calculations (Version 4).* Journal of Applied Crystallography, 2014. **47**(2): p. 803-805.
141. Inkson, B.J., *Scanning electron microscopy (SEM) and transmission electron microscopy (TEM) for materials characterization*, in *Materials characterization using nondestructive evaluation (NDE) methods*. 2016, Elsevier. p. 17-43.
142. Vernon-Parry, K.D., *Scanning electron microscopy: an introduction.* III-Vs Review, 2000. **13**(4): p. 40-44.
143. LFA, L.F.A., *467 HyperFlash® Series Method.* Technique, Applications of Thermal Diffusivity and Thermal Conductivity Analyzing and Testing, NETZSCH-Gerätebau GmbH, Selb, Germany.
144. Yahyaoglu, M., et al., *Phase-transition-enhanced thermoelectric transport in rickardite mineral cu3–x te2.* Chemistry of Materials, 2021. **33**(5): p. 1832-1841.
145. Weston, L., et al., *Named Entity Recognition and Normalization Applied to Large-Scale Information Extraction from the Materials Science Literature.* Journal of chemical information and modeling, 2019. **59**(9): p. 3692-3702.
146. Tshitoyan, V., et al., *Unsupervised word embeddings capture latent knowledge from materials science literature.* Nature, 2019. **571**(7763): p. 95-98.
147. Ricci, F., et al., *An ab initio electronic transport database for inorganic materials.* Scientific data, 2017. **4**: p. 170085.
148. Gaultois, M.W., et al., *Data-driven review of thermoelectric materials: performance and resource considerations.* Chemistry of Materials, 2013. **25**(15): p. 2911-2920.
149. Patzak, I., *Uber die struktur und die lage der phasen im system kupfer-tellur.* Zeitschrift für Metallkunde, 1956. **47**(6): p. 418-420.
150. Jia, G., et al., *Sulfur-free synthesis of size tunable rickardite (Cu3− x Te2) spheroids and planar squares.* Royal Society open science, 2019. **6**(2): p. 181602.
151. Pandey, J., et al., *Raman Spectroscopy Study of Phonon Liquid Electron Crystal in Copper Deficient Superionic Thermoelectric Cu2–x Te.* ACS Applied Energy Materials, 2020. **3**(3): p. 2175-2181.
152. Rajkumar, R., et al., *Effect of sintering temperatures on mixed phases and thermoelectric properties of nanostructured copper telluride.* Journal of Alloys and Compounds, 2020: p. 155276.
153. Bouyrie, Y., et al., *High-Temperature Transport Properties of Colusite Cu 24 T 2 V 2 Ge 6 S 32 (T= Ni, Co).* Journal of Electronic Materials, 2017. **46**(5): p. 2684-2690.
154. Lu, X. and D.T. Morelli, *Natural mineral tetrahedrite as a direct source of thermoelectric materials.* Physical Chemistry Chemical Physics, 2013. **15**(16): p. 5762-5766.
155. Thompson, R., *The telluride minerals and their occurrence in Canada.* American Mineralogist: Journal of Earth and Planetary Materials, 1949. **34**(5-6): p. 341-382.
156. Rodriguez, E.E., et al., *Iodine as an Oxidant in the Topotactic Deintercalation of Interstitial Iron in Fe1+ x Te.* Journal of the American Chemical Society, 2010. **132**(29): p. 10006-10008.
157. Ding, Y., Y. Wang, and J. Ni, *Electronic and magnetic properties of 3d transition-metal selenides from first principles.* Solid state communications, 2009. **149**(13-14): p. 505-509.

158. Huang, T.-W., et al., *Doping-driven structural phase transition and loss of superconductivity in M x Fe 1− x Se δ (M= Mn, Cu).* Physical Review B, 2010. **82**(10): p. 104502.
159. Sassi, S., et al., *Assessment of the thermoelectric performance of polycrystalline p-type SnSe.* Applied Physics Letters, 2014. **104**(21): p. 212105.
160. Bansal, D., et al., *Phonon anharmonicity and negative thermal expansion in SnSe.* Physical Review B, 2016. **94**(5): p. 054307.
161. Kawaji, H. and T. Atake, *Heat capacity measurement and thermodynamic study of Ag8GeTe6.* Solid state ionics, 1994. **70**: p. 518-521.
162. Li, L., et al., *High thermoelectric performance of superionic argyrodite compound Ag 8 SnSe 6.* Journal of Materials Chemistry C, 2016. **4**(24): p. 5806-5813.
163. F. J. Blatt , P.A.S., C. L. Foiles and D. Greig, *Thermoelectric Power of Metals*. 1976, New York: Plenum Press.
164. Jones, H., *The Thermoelectric Power of Monovalent Metals.* Proceedings of the Physical Society. Section A, 1955. **68**(12): p. 1191.
165. He, B., et al., *The Fermi surface geometrical origin of axis-dependent conduction polarity in layered materials.* Nature materials, 2019. **18**(6): p. 568-572.
166. Robinson, J.E. and J.D. Dow, *Electron-Phonon Interactions in Solid Alkali Metals. I. Scattering and Transport Coefficients.* Physical Review, 1968. **171**(3): p. 815.
167. Xu, B. and M.J. Verstraete, *First principles explanation of the positive Seebeck coefficient of lithium.* Physical review letters, 2014. **112**(19): p. 196603.
168. Chen, H., et al., *Thermal conductivity during phase transitions.* Advanced Materials, 2019. **31**(6): p. 1806518.
169. Agne, M.T., P.W. Voorhees, and G.J. Snyder, *Phase transformation contributions to heat capacity and impact on thermal diffusivity, thermal conductivity, and thermoelectric performance.* Advanced Materials, 2019. **31**(35): p. 1902980.
170. Kazem, N., et al., *Coinage-metal-stuffed Eu9Cd4Sb9: Metallic compounds with anomalous low thermal conductivities.* Chemistry of Materials, 2015. **27**(21): p. 7508-7519.
171. Qiu, Y., et al., *Realizing high thermoelectric performance in GeTe through decreasing the phase transition temperature via entropy engineering.* Journal of Materials Chemistry A, 2019. **7**(46): p. 26393-26401.
172. Liu, Z., et al., *Phase-transition temperature suppression to achieve cubic GeTe and high thermoelectric performance by Bi and Mn codoping.* Proceedings of the National Academy of Sciences, 2018. **115**(21): p. 5332-5337.
173. Qin, Y., et al., *Doping effect on Cu2Se thermoelectric performance: a review.* Materials, 2020. **13**(24): p. 5704.
174. Shi, D., Z. Geng, and K.H. Lam, *Study of conventional sintered Cu2Se thermoelectric material.* Energies, 2019. **12**(3): p. 401.
175. Yahyaoglu, M., et al., *Stress/pressure-stabilized cubic polymorph of Li 3 Sb with improved thermoelectric performance.* Journal of Materials Chemistry A, 2021. **9**(44): p. 25024-25031.
176. Peng, K., et al., *Thermoelectric performance of binary lithium-based compounds: Li3Sb and Li3Bi.* Applied Physics Letters, 2021. **119**(3): p. 033901.
177. LaLonde, A.D., T. Ikeda, and G.J. Snyder, *Rapid consolidation of powdered materials by induction hot pressing.* Review of Scientific Instruments, 2011. **82**(2): p. 025104.
178. Borup, K.A., et al., *Measurement of the electrical resistivity and Hall coefficient at high temperatures.* Review of Scientific Instruments, 2012. **83**(12): p. 123902.

179. Iwanaga, S., et al., *A high temperature apparatus for measurement of the Seebeck coefficient.* Review of Scientific Instruments, 2011. **82**(6): p. 063905.
180. Beutl, A., D. Cupid, and H. Flandorfer, *The Li-Sb phase diagram part I: new experimental results.* Journal of Alloys and Compounds, 2017. **695**: p. 1052-1060.
181. Brauer, G. and E. Zintl, *Konstitution von Phosphiden, Arseniden, Antimoniden und Wismutiden des Lithiums, Natriums und Kaliums.* Zeitschrift für Physikalische Chemie, 1937. **37B**(1): p. 323-352.
182. Sangster, J. and A. Pelton, *The Li-Sb (lithium-antimony) system.* Journal of phase equilibria, 1993. **14**(4): p. 514-517.
183. Leonova, M., et al., *High-pressure phase transition of hexagonal alkali pnictides.* Inorganic materials, 2003. **39**(3): p. 266-270.
184. Baggetto, L., et al., *Intrinsic thermodynamic and kinetic properties of Sb electrodes for Li-ion and Na-ion batteries: experiment and theory.* Journal of Materials Chemistry A, 2013. **1**(27): p. 7985-7994.
185. Saubanère, M., et al., *Influence of polymorphism on the electrochemical behavior of MxSb negative electrodes in Li/Na batteries.* Journal of Power Sources, 2015. **280**: p. 695-702.
186. Brauer, G. and E. Zintl, *Konstitution von Phosphiden, Arseniden, Antimoniden und Wismutiden des Lithiums, Natriums und Kaliums.* Zeitschrift für physikalische Chemie, 1937. **37**(1): p. 323-352.
187. Leversee, R.A., et al., *High pressure chemical reactivity and structural study of the Na–P and Li–P systems.* Journal of Materials Chemistry A, 2020. **8**(41): p. 21797-21803.
188. Caputo, R., *An insight into sodiation of antimony from first-principles crystal structure prediction.* Journal of Electronic Materials, 2016. **45**(2): p. 999-1010.
189. Madelung, O., *Ix-Vy compounds*, in *Semiconductors: Data Handbook*, O. Madelung, Editor. 2004, Springer Berlin Heidelberg: Berlin, Heidelberg. p. 437-445.
190. Emsley, J., *The Elements.* Oxford University Press, New York, 1989.
191. Shannon, R.D., *Revised effective ionic radii and systematic studies of interatomic distances in halides and chalcogenides.* Acta crystallographica section A: crystal physics, diffraction, theoretical and general crystallography, 1976. **32**(5): p. 751-767.
192. Pauling, L., *The Nature of the Chemical Bond*. Vol. 260. 1960: Cornell university press Ithaca, NY.
193. Peng, W., et al., *An unlikely route to low lattice thermal conductivity: small atoms in a simple layered structure.* Joule, 2018. **2**(9): p. 1879-1893.
194. Toberer, E.S., A. Zevalkink, and G.J. Snyder, *Phonon engineering through crystal chemistry.* Journal of Materials Chemistry, 2011. **21**(40): p. 15843-15852.
195. Chang, D., et al., *Elucidating the origins of phase transformation hysteresis during electrochemical cycling of Li–Sb electrodes.* Journal of Materials Chemistry A, 2015. **3**(37): p. 18928-18943.
196. Beutl, A., H.S. Effenberger, and H. Flandorfer, *The ternary phases CuLi2− x Sb, Cu2− x Li1+ x Sb, and Cu2− x Li1− x Sb and their structural relations to binary alloys in the systems Cu− Sb and Li− Sb.* Zeitschrift für Kristallographie-Crystalline Materials, 2017. **232**(11): p. 735-749.
197. Snyder, G.J., et al., *Weighted mobility.* Advanced Materials, 2020. **32**(25): p. 2001537.
198. Zevalkink, A., et al., *A practical field guide to thermoelectrics: Fundamentals, synthesis, and characterization.* Applied Physics Reviews, 2018. **5**(2): p. 021303.

199. Kim, H.S., et al., *Characterization of Lorenz number with Seebeck coefficient measurement.* Apl Materials, 2015. **3**(4): p. 041506
200. Chen, H., et al., *Thermal Conductivity during Phase Transitions.* Adv Mater, 2019. **31**(6): p. e1806518.
201. Zevalkink, A., et al., *Thermoelectric Properties and Electronic Structure of the Zintl-Phase Sr3AlSb3.* ChemSusChem, 2013. **6**(12): p. 2316-2321.
202. Chanakian, S., et al., *Enhanced thermoelectric properties of Sr5In2Sb6via Zn-doping.* Journal of Materials Chemistry A, 2015. **3**(19): p. 10289-10295.
203. Toberer, E.S., et al., *Traversing the Metal-Insulator Transition in a Zintl Phase: Rational Enhancement of Thermoelectric Efficiency in Yb14Mn1−xAlxSb11.* Advanced Functional Materials, 2008. **18**(18): p. 2795-2800.
204. Yan, R., et al., *Realizing p-type NbCoSn half-Heusler compounds with enhanced thermoelectric performance via Sc substitution.* Science and Technology of Advanced Materials, 2020. **21**(1): p. 122-130.

Appendix A

$Cu_{3-x}Te_2$

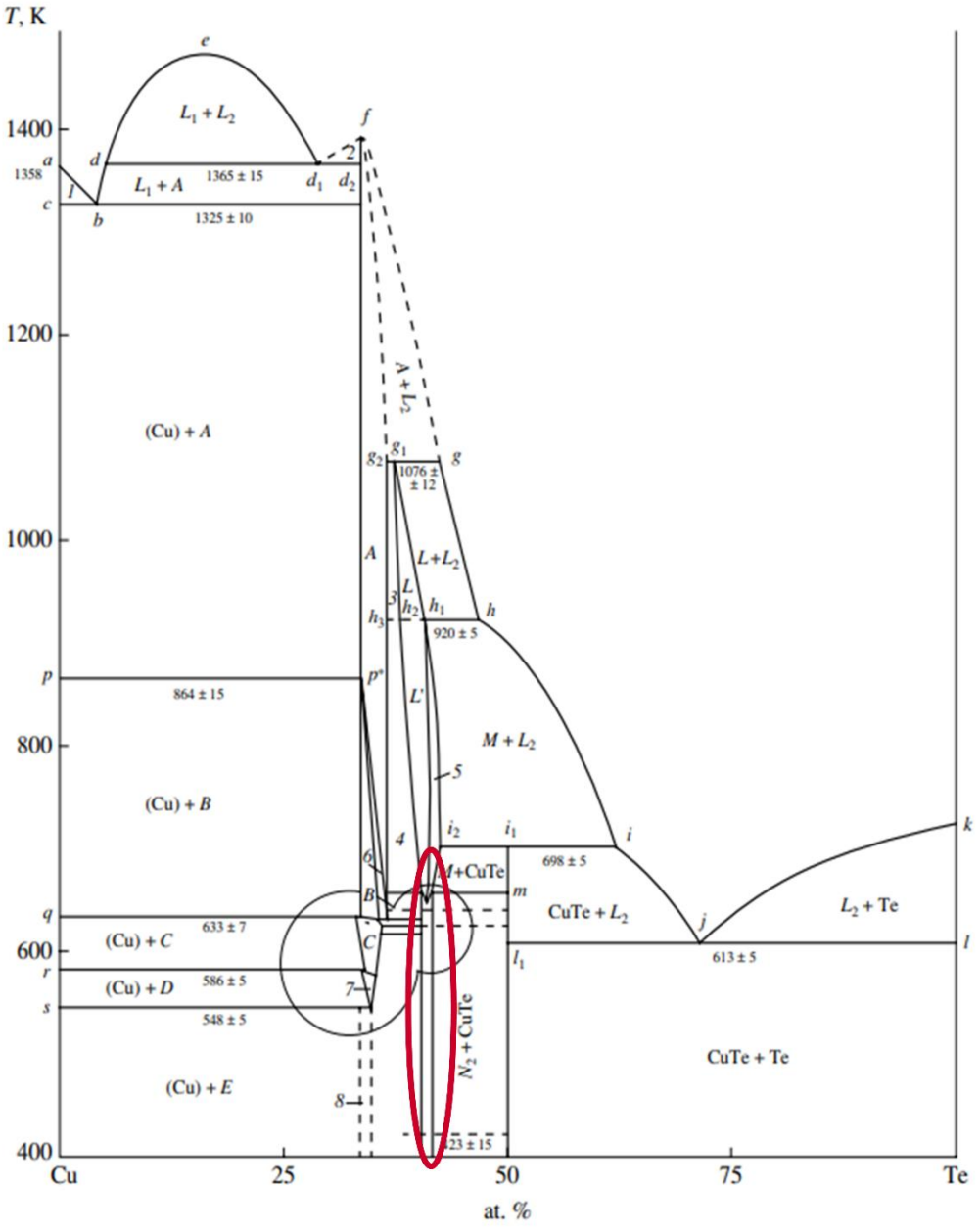

Figure A 1 Phase diagram of the Cu-Te system focuses on the region of $Cu_{3-x}Te_2$ phase [66].

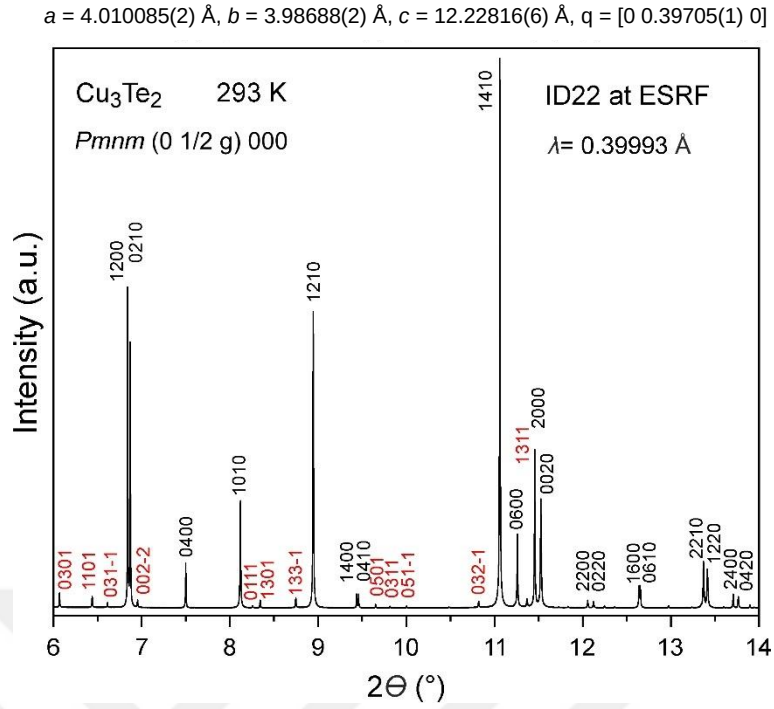

Figure A 2 The selected region of the X-ray powder pattern of the modulated structure of $Cu_{2.9}Te_2$ with indicated main reflections (black) and modulated reflections (red) recorded at ambient conditions with high-resolution synchrotron x-ray powder diffraction. The observed splitting of the reflections is typical for the orthorhombic distortion of the tetragonal unit cell.

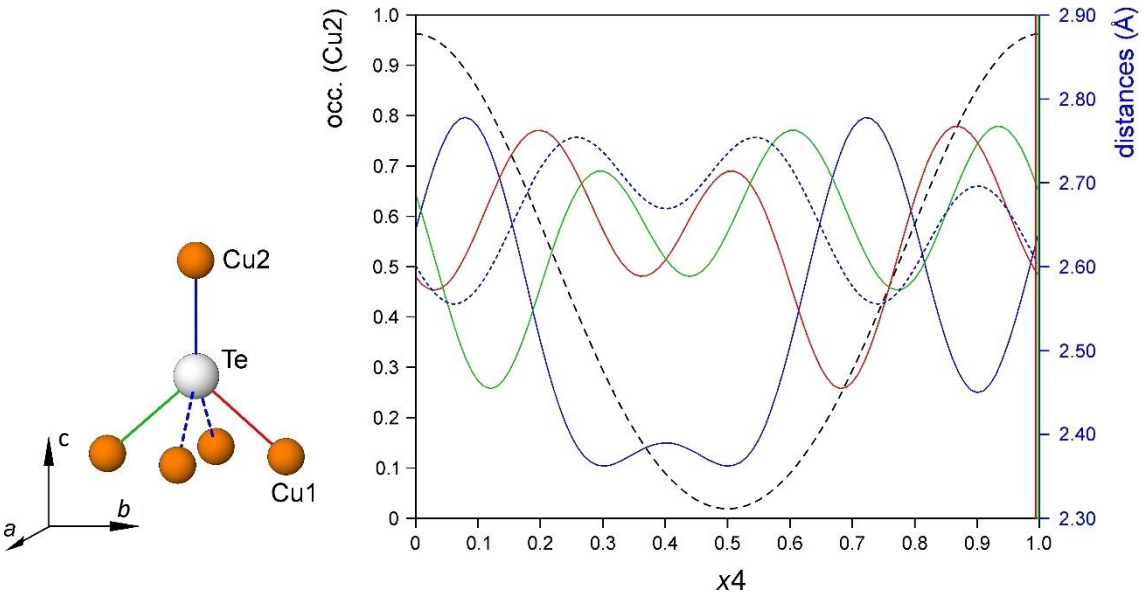

Figure A 3 The diagram describing the variation of the occupancy of Cu2 position and Te-Cu distances as a function of the fourth coordinate (x4) in the orthorhombic modulated structure.

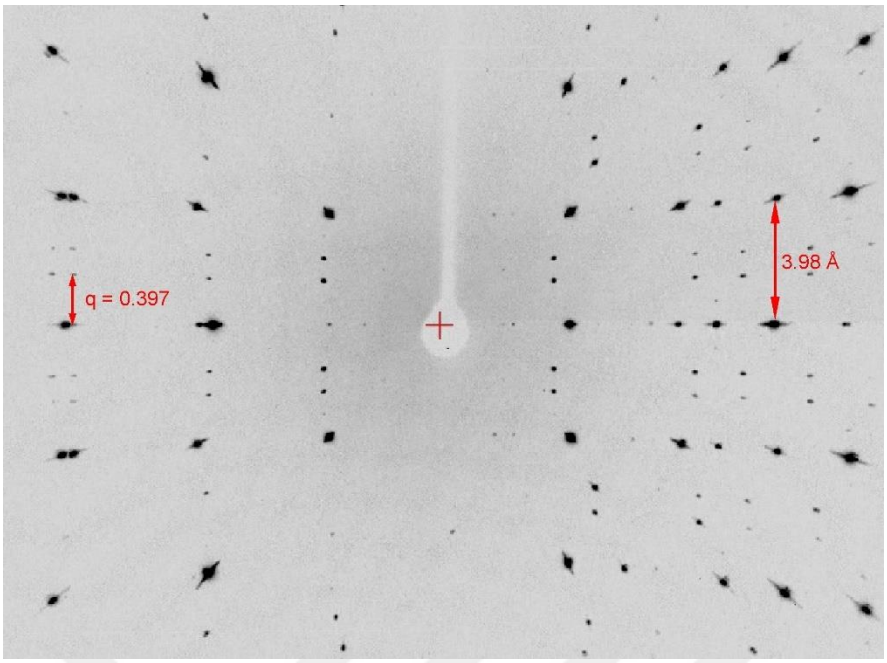

Figure A 4 The oscilation photo about the "b" axis obtained from a single crystal. The strong basic reflections corresponding to the lattice parameter of 3.98 Å and a set of weak modulated reflections with q-vector = 0.397.

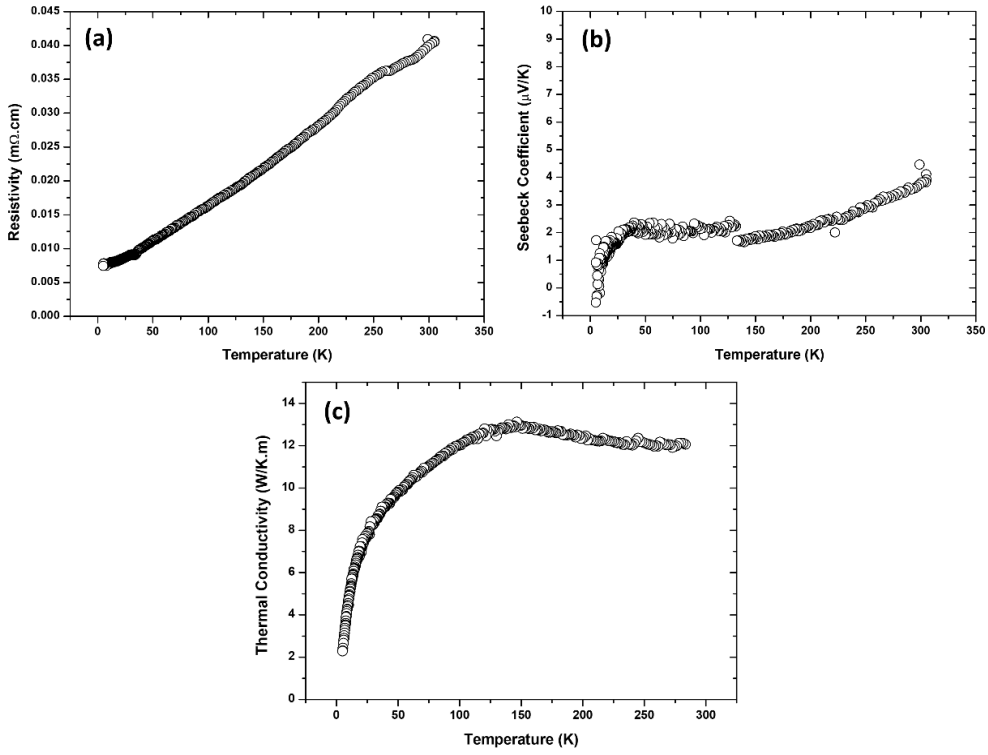

Figure A 5. Low temperature electronic and thermal transport data of $Cu_{2.8}Te_2$.

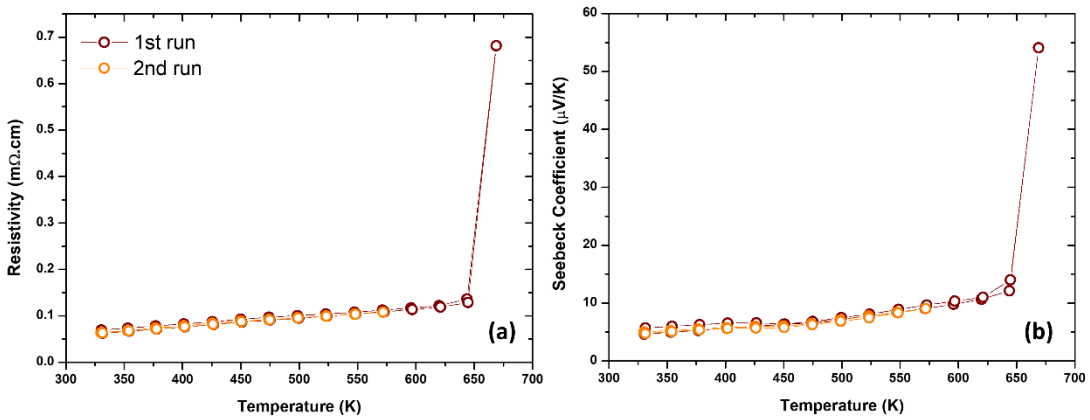

Figure A 6 Resistivity and Seebeck coefficient of $Cu_{2.9}Te_2$ with the second cycle performed to the temperature of 573 K.

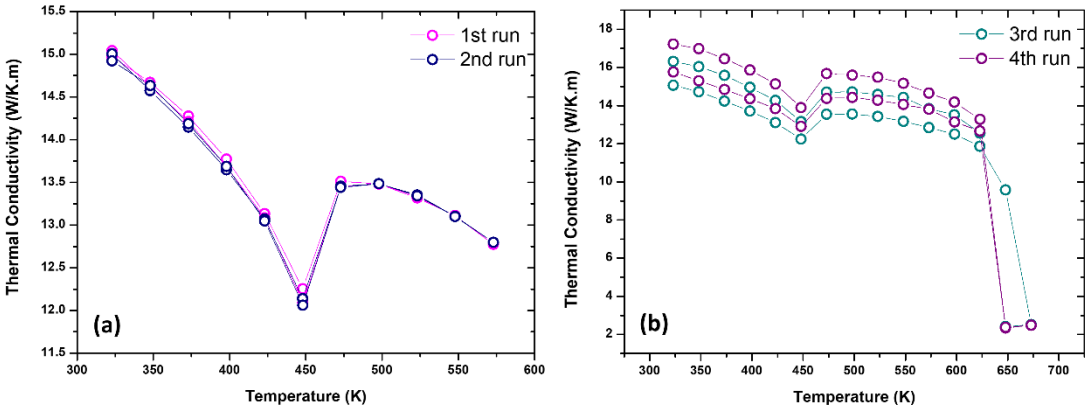

Figure A 7 The repeated thermal conductivity measurements of $Cu_{2.9}Te_2$ to the temperature of a) 573 K and b) 673 K.

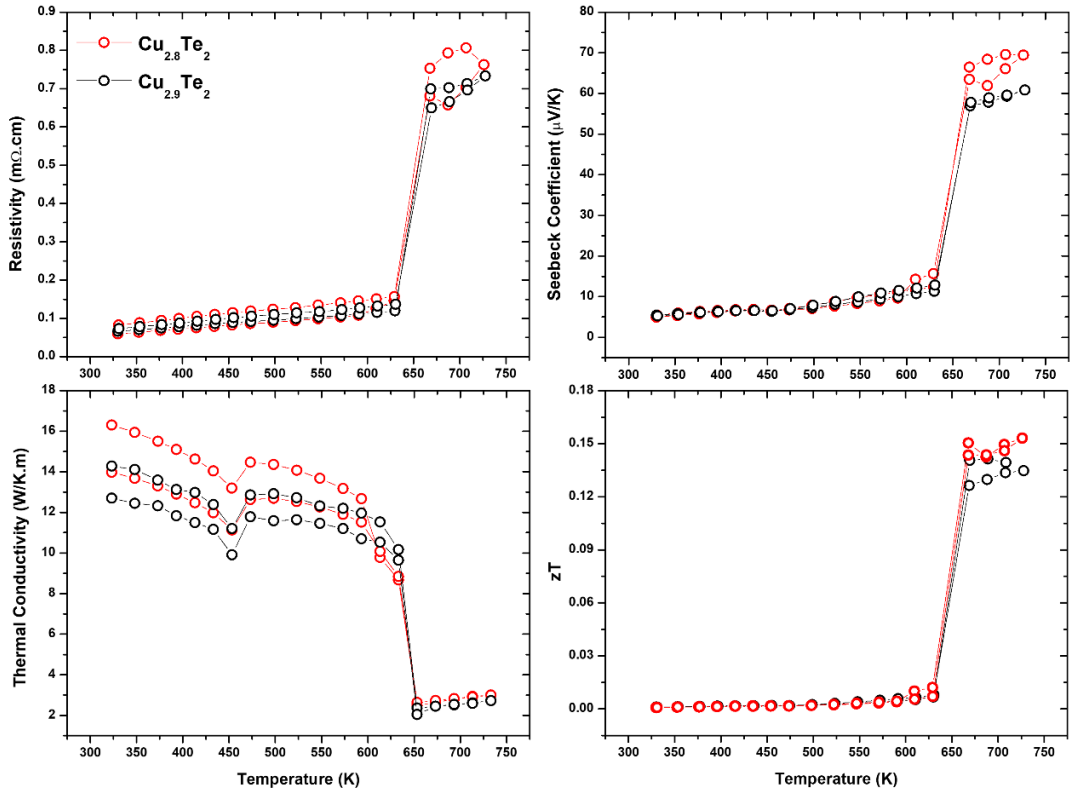

Figure A 8 Comparison of the electronic and thermal transport data of $Cu_{2.8}Te_2$ and $Cu_{2.9}Te_2$.

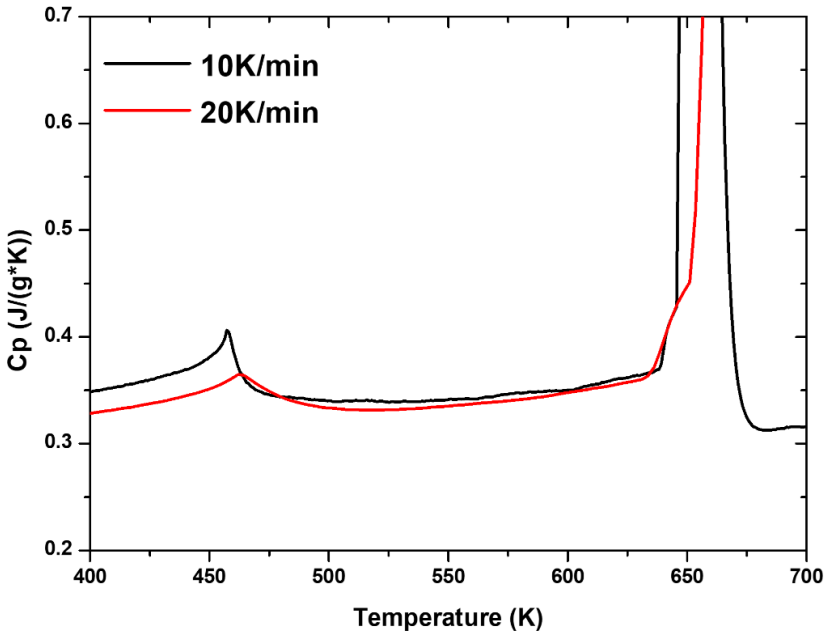

Figure A 9 The C_p of $Cu_{2.9}Te_2$ with heating rate of 10 K/ min and 20 K/ min.

Appendix B

$Cu_{3-x}Te_2$ substitution study

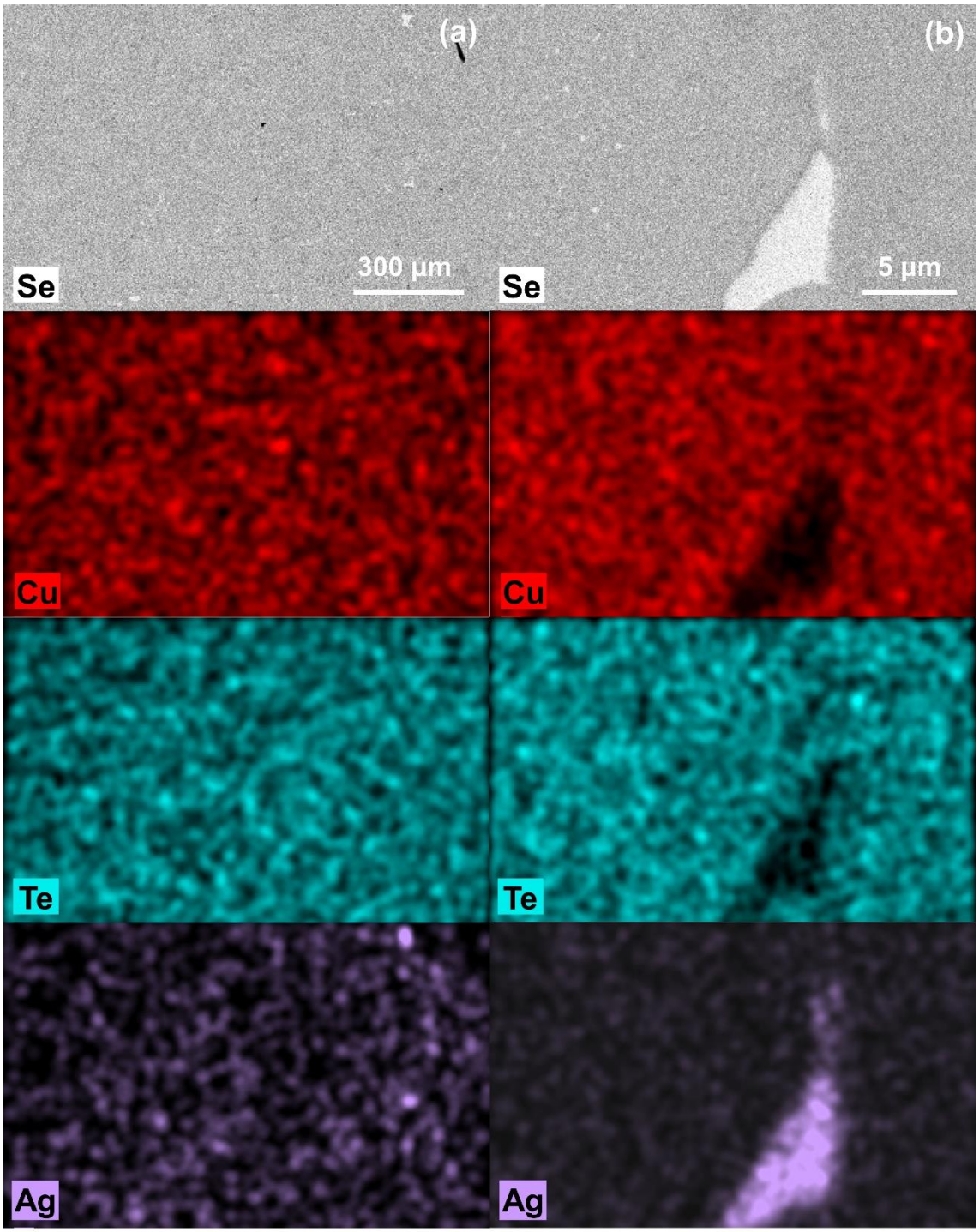

Figure B 1 a) and b) SEM images of $Ag_{0.05}Cu_{2.85}Te_2$ with different magnifications, and the elemental mapping analysis (EDX) of the same SEM images showing the distribution of Cu, Te, and Ag distributions

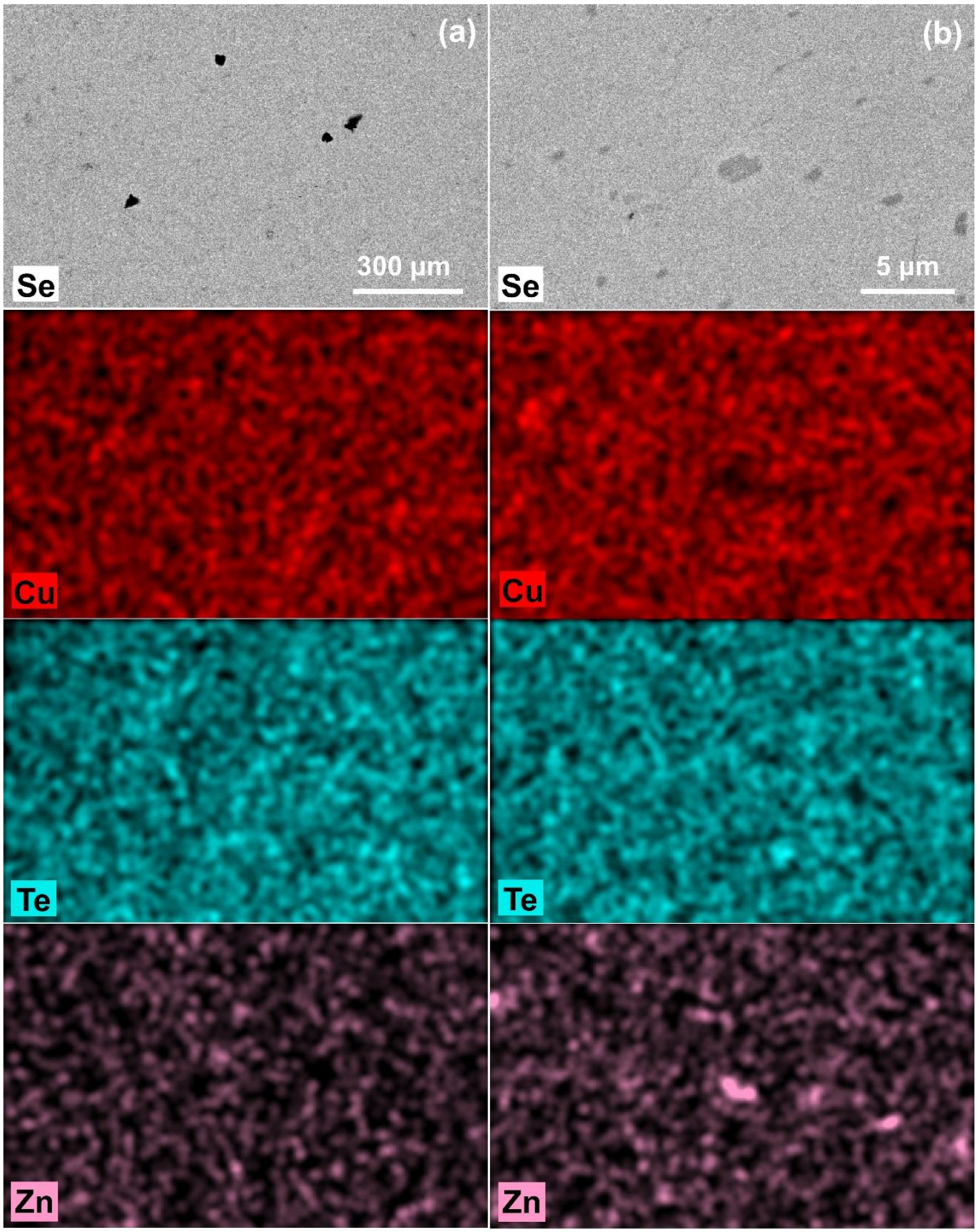

Figure B 2 a) and b) SEM images of $Zn_{0.10}Cu_{2.80}Te_2$ with different magnifications, and the elemental mapping analysis (EDX) of the same SEM images showing the distribution of Cu, Te, and Zn distributions

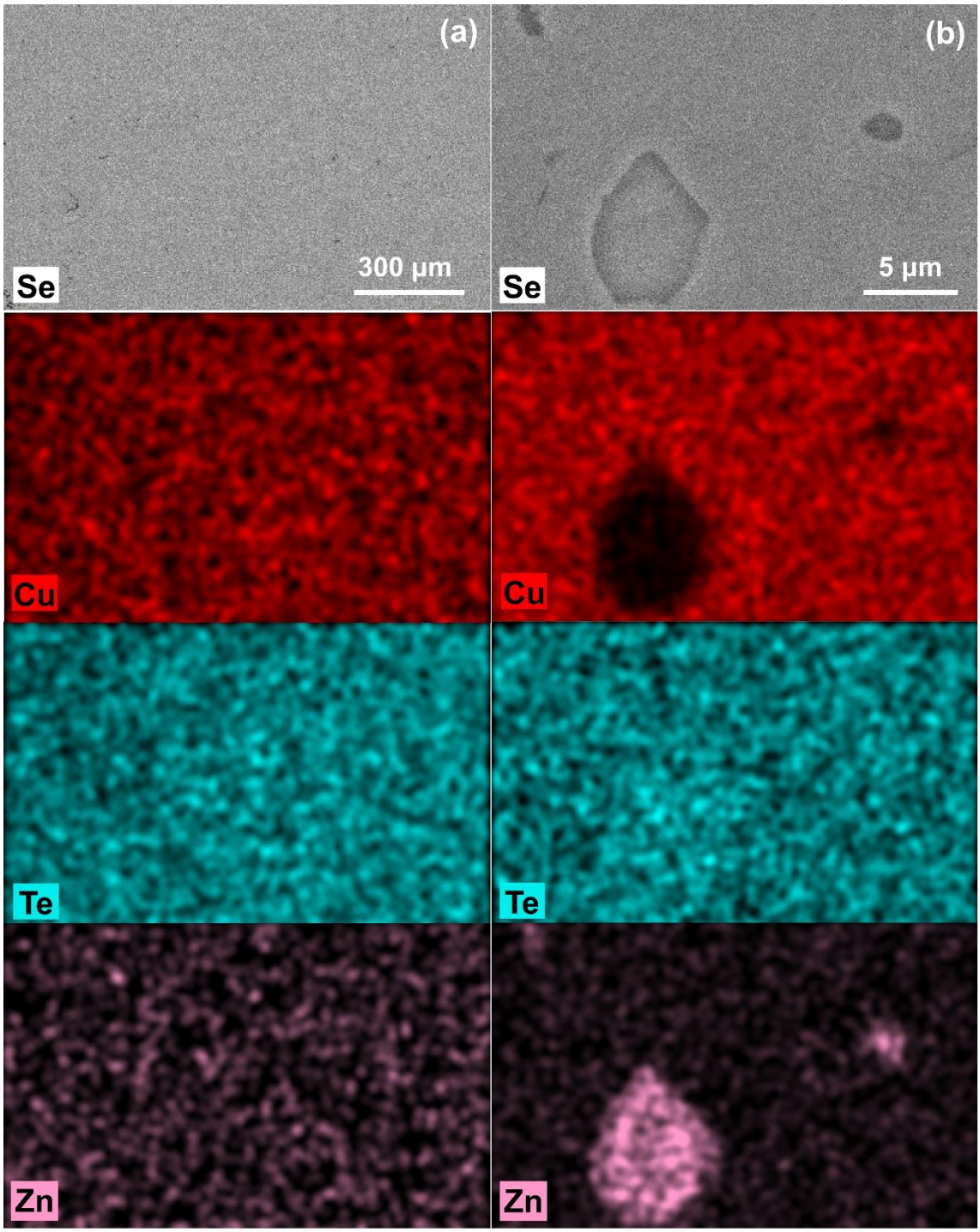

Figure B 3 a) and b) SEM images of $Zn_{0.05}Cu_{2.85}Te_2$ with different magnifications, and the elemental mapping analysis (EDX) of the same SEM images showing the distribution of Cu, Te, and Zn distributions

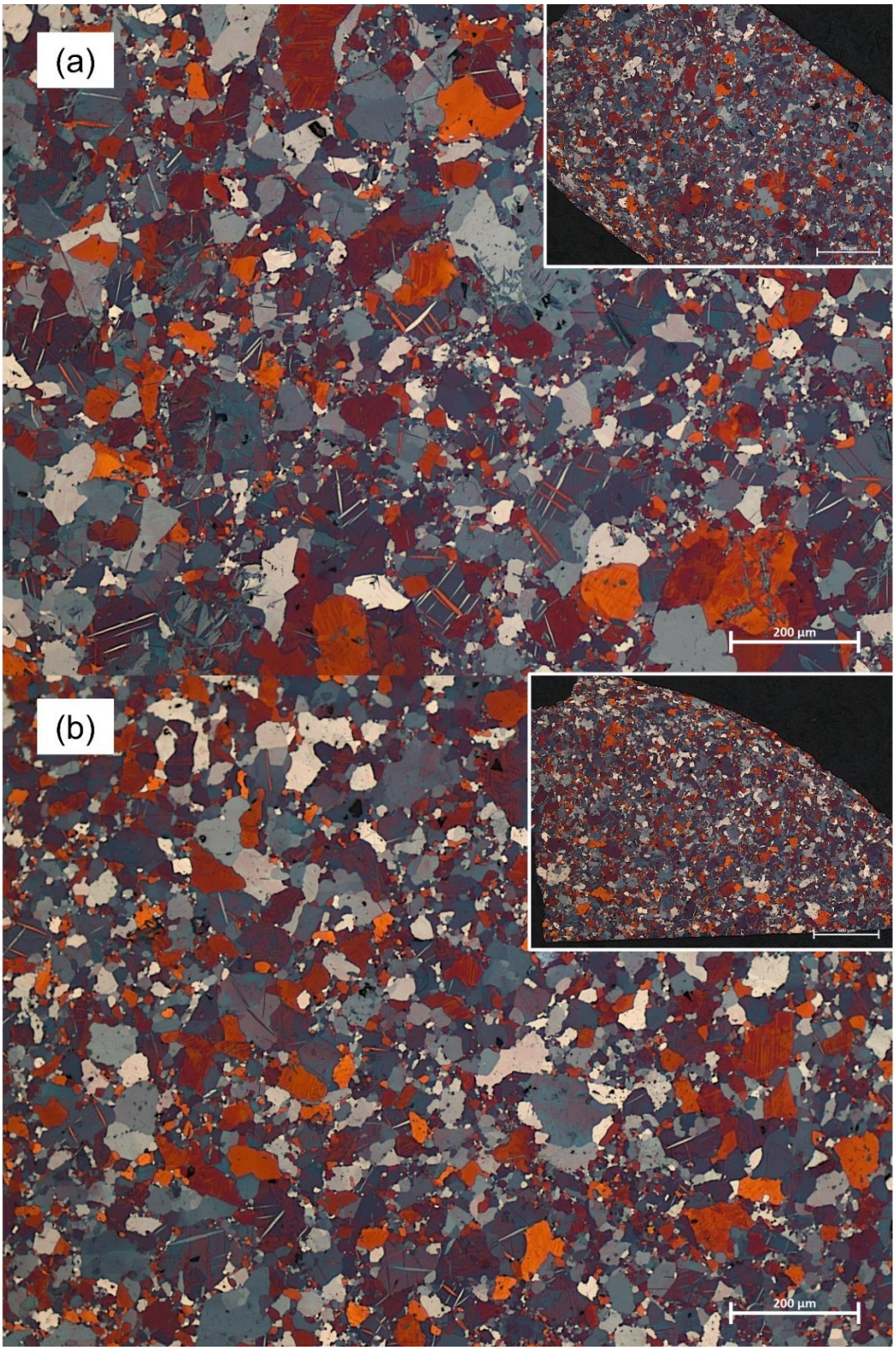

Figure B 4 OM images of Zn- substituted $Cu_{2.9}Te_2$ samples: (a) $Zn_{0.05}Cu_{2.85}Te_2$ and (b) $Zn_{0.10}Cu_{2.80}Te_2$ sps piece under polarized light with 10X magnification, inset images are with 5X magnification with 500µm scale bar.

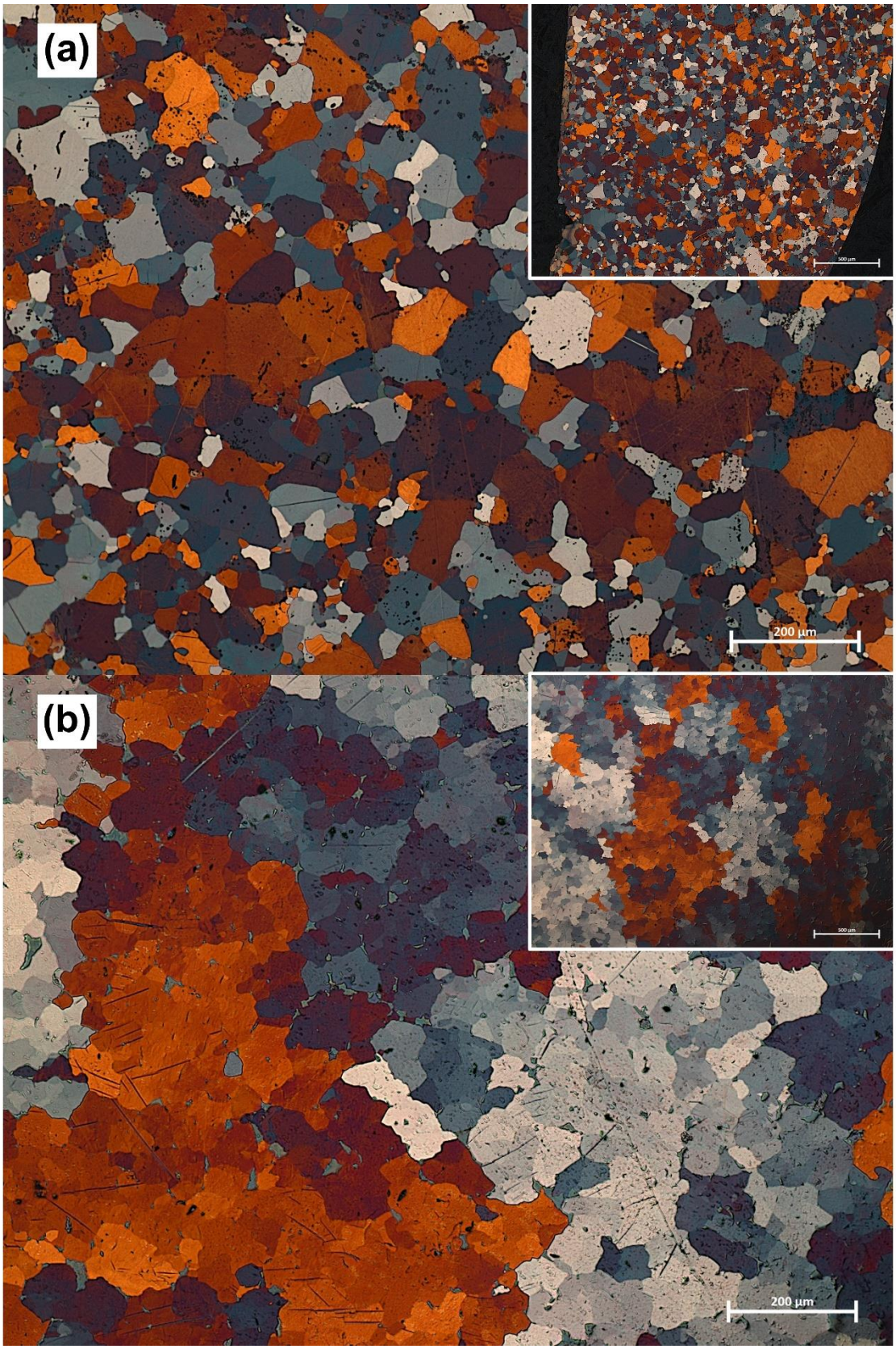

Figure B 5 OM images of Ag- substituted $Cu_{2.9}Te_2$ samples: (a) $Ag_{0.05}Cu_{2.85}Te_2$ and (b) $Ag_{0.10}Cu_{2.80}Te_2$ sps piece under polarized light with 10X magnification, inset images are with 5X magnification with 500µm scale bar (left side: dark, right side: light).

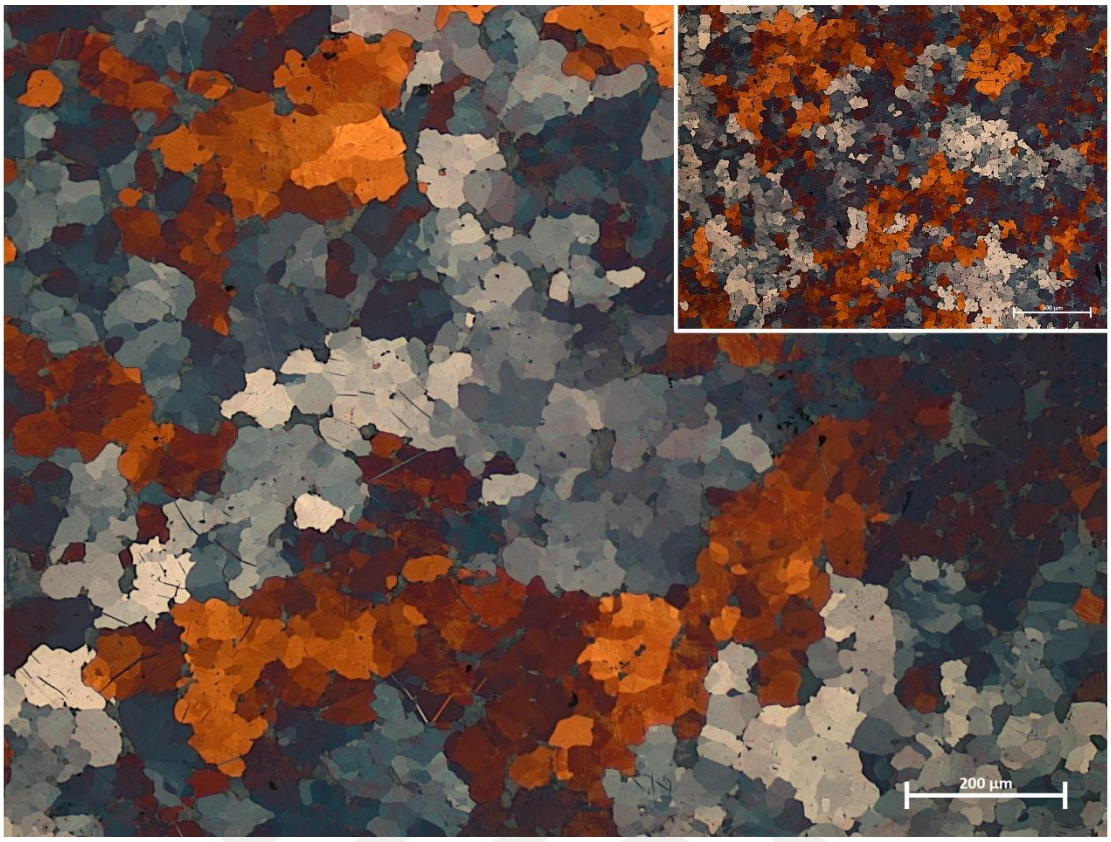

Figure B 6 OM images of Ag- substituted $Cu_{2.9}Te_2$ sample; $Ag_{0.20}Cu_{2.70}Te_2$ sps piece under polarized light with 10X magnification, inset images are with 5X magnification with 500µm scale bar (left side: dark, right side: light).

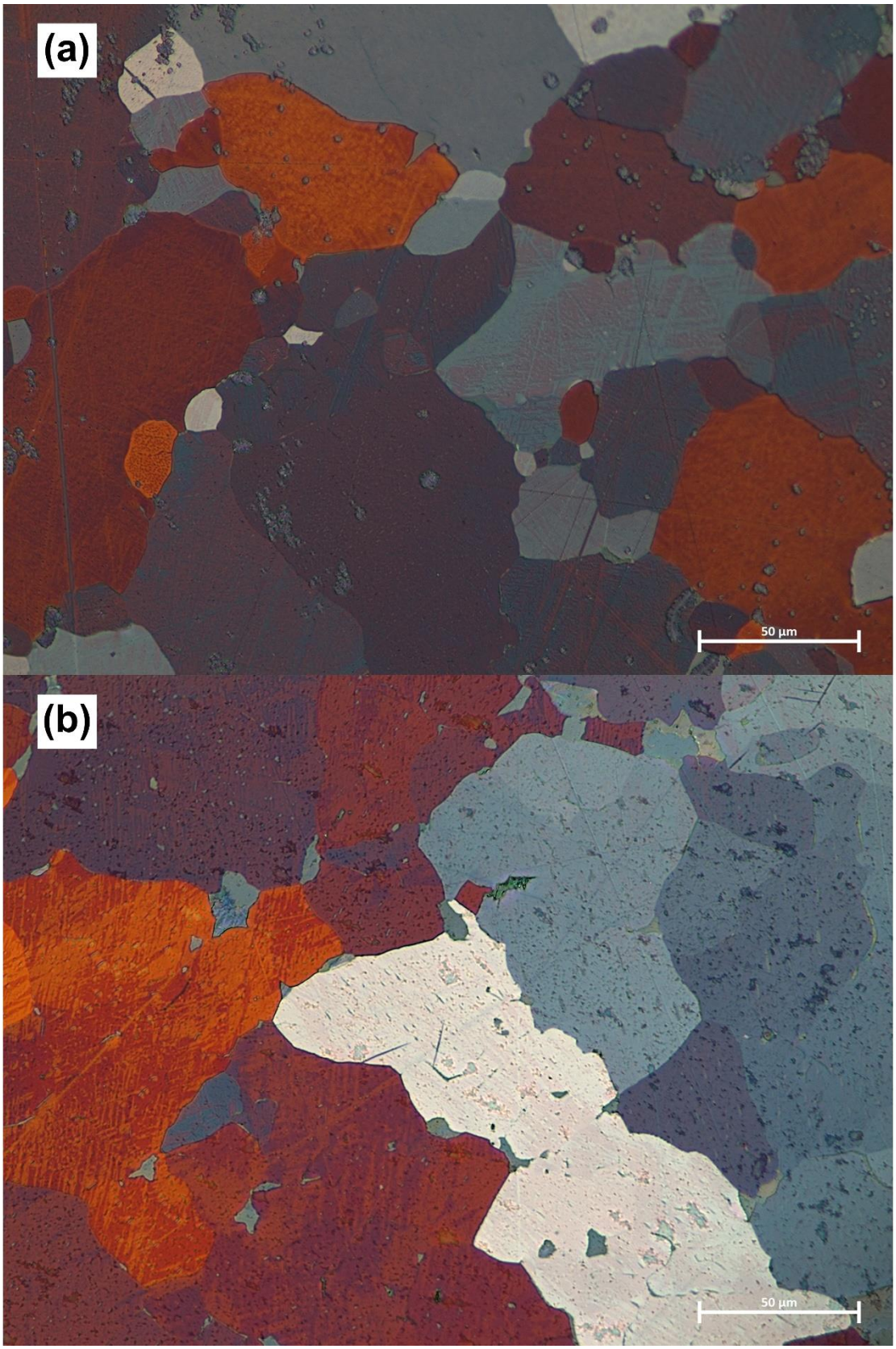

Figure B 7 OM images of Ag- substituted $Cu_{2.9}Te_2$ sample; (a) $Ag_{0.05}Cu_{2.85}Te_2$ sps piece and (b) $Ag_{0.10}Cu_{2.80}Te_2$ sps piece under polarized light with 50X magnification.

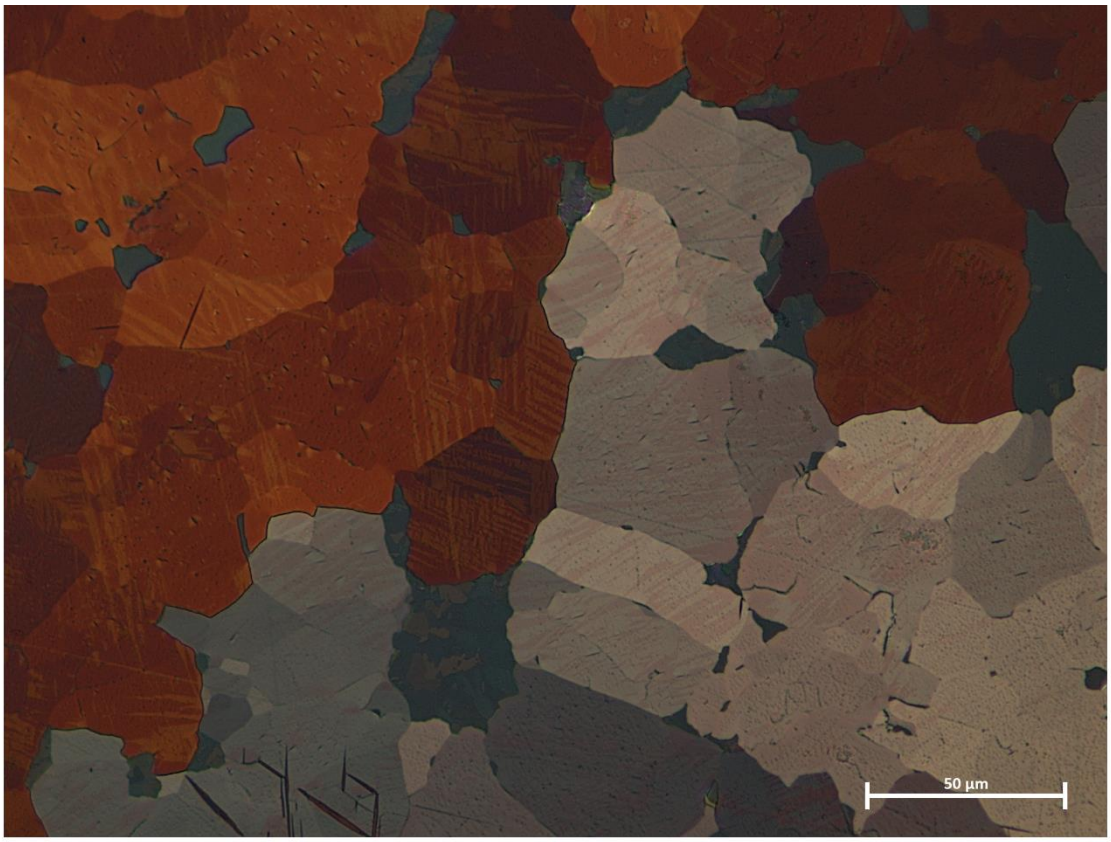

Figure B 8 OM images of Ag- substituted $Cu_{2.9}Te_2$ sample; $Ag_{0.20}Cu_{2.70}Te_2$ sps piece under polarized light with 50X magnification.

Appendix C

Cu_2Se

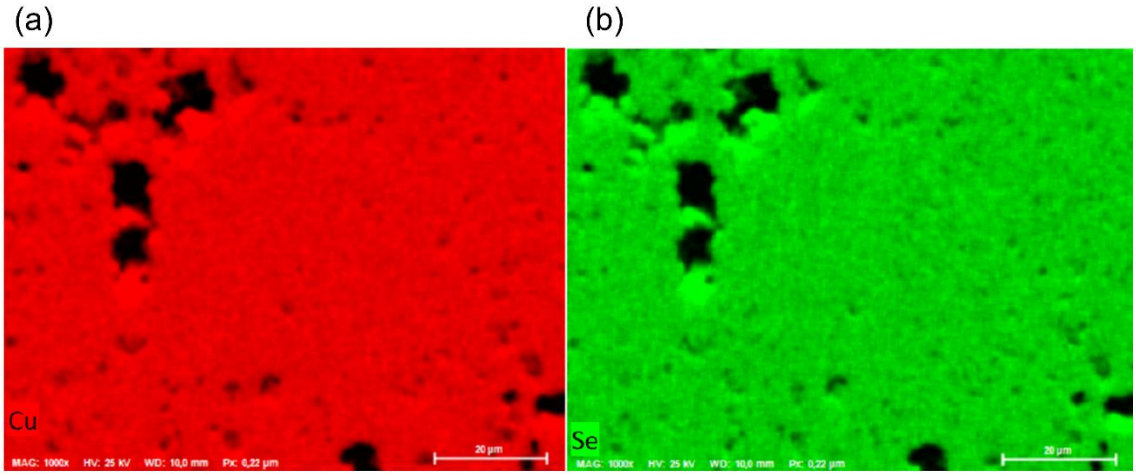

Figure C 1 EDX elemental mapping of Cu_2Se sample-1.

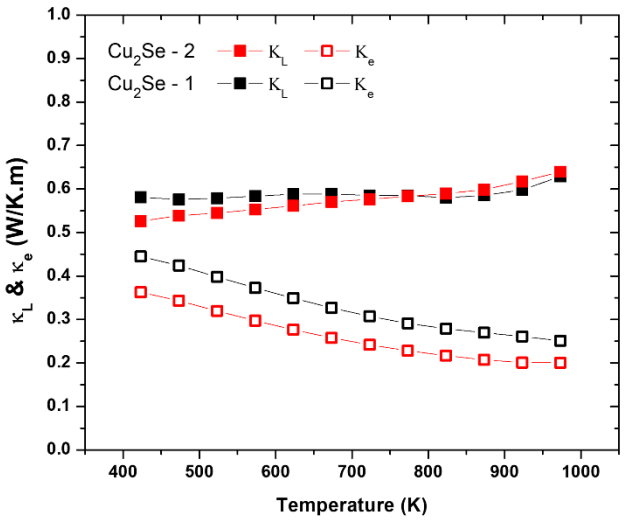

Figure C 2 Temperature dependence of the lattice thermal conductivity and electronic thermal conductivity of Cu_2Se samples.

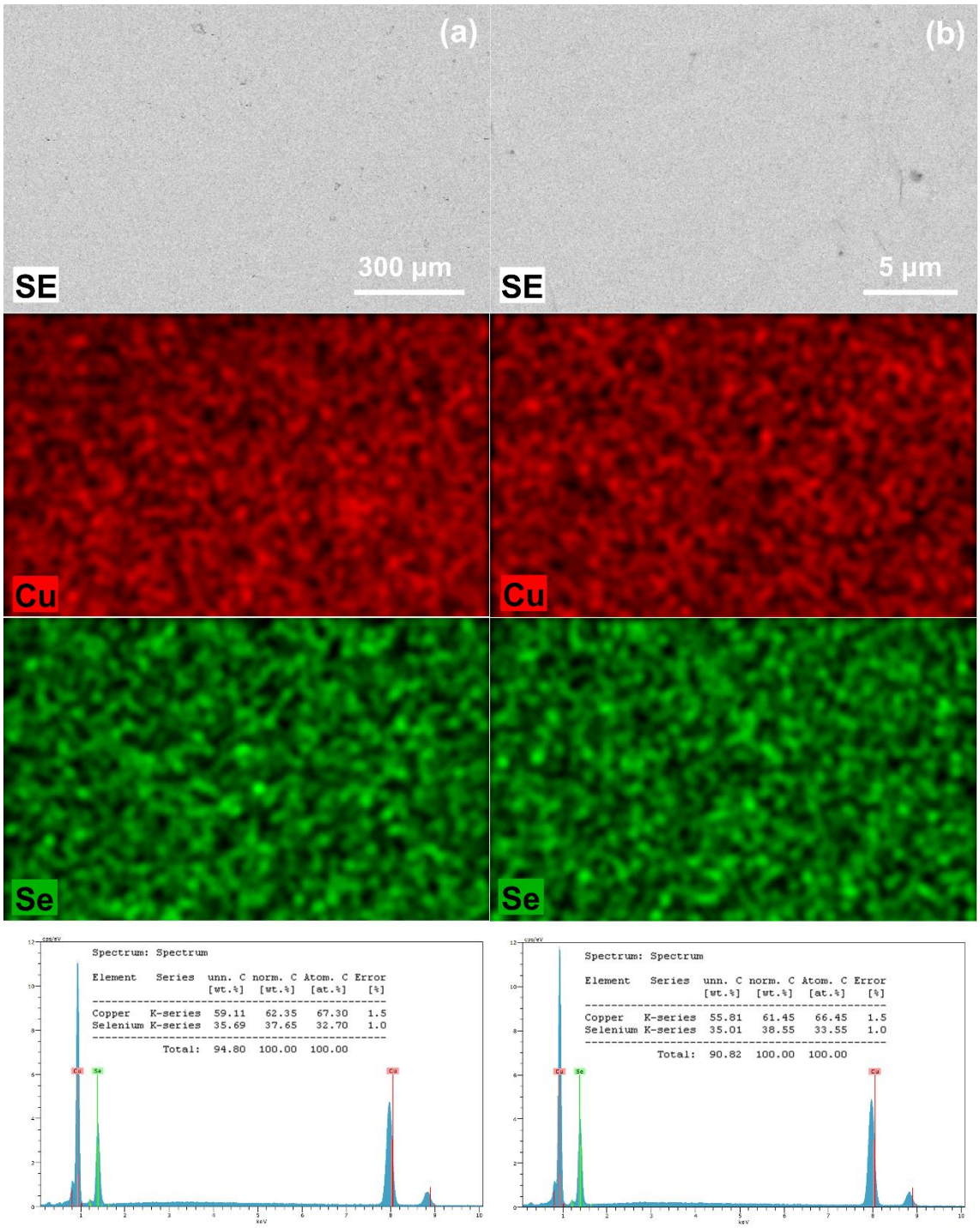

Figure C 3 SEM images of pristine Cu_2Se samples used for a) nano-B and b) C-coated nano-B incorporation studies. The elemental mapping analysis (EDX) of the same SEM images showing the distribution of Cu and Se distributions.

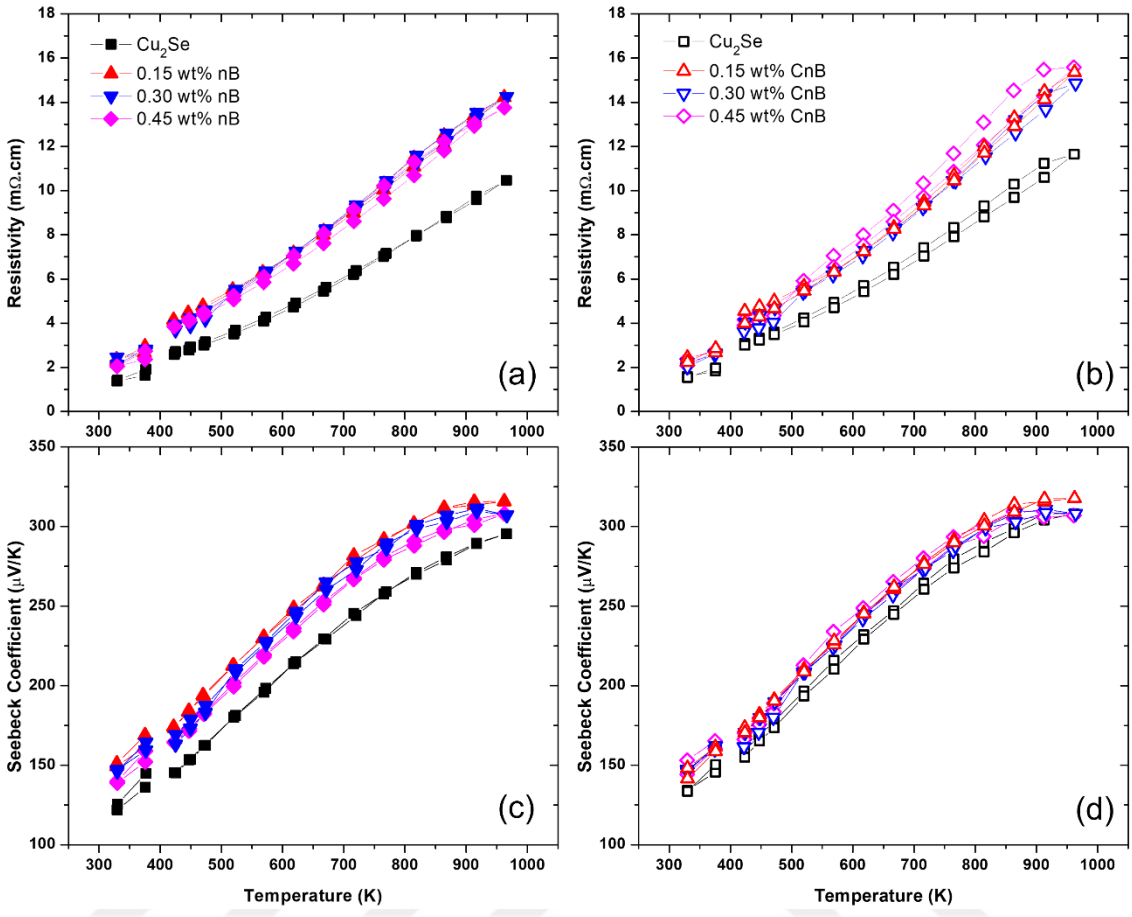

Figure C 4 Thermoelectric properties of the low-temperature and high-temperature phases in pristine, nano-B and C-coated nano-B incorporated Cu_2Se samples. Temperature dependences of electrical resistivity (a and b) and Seebeck coefficient (c and d) with cooling data.

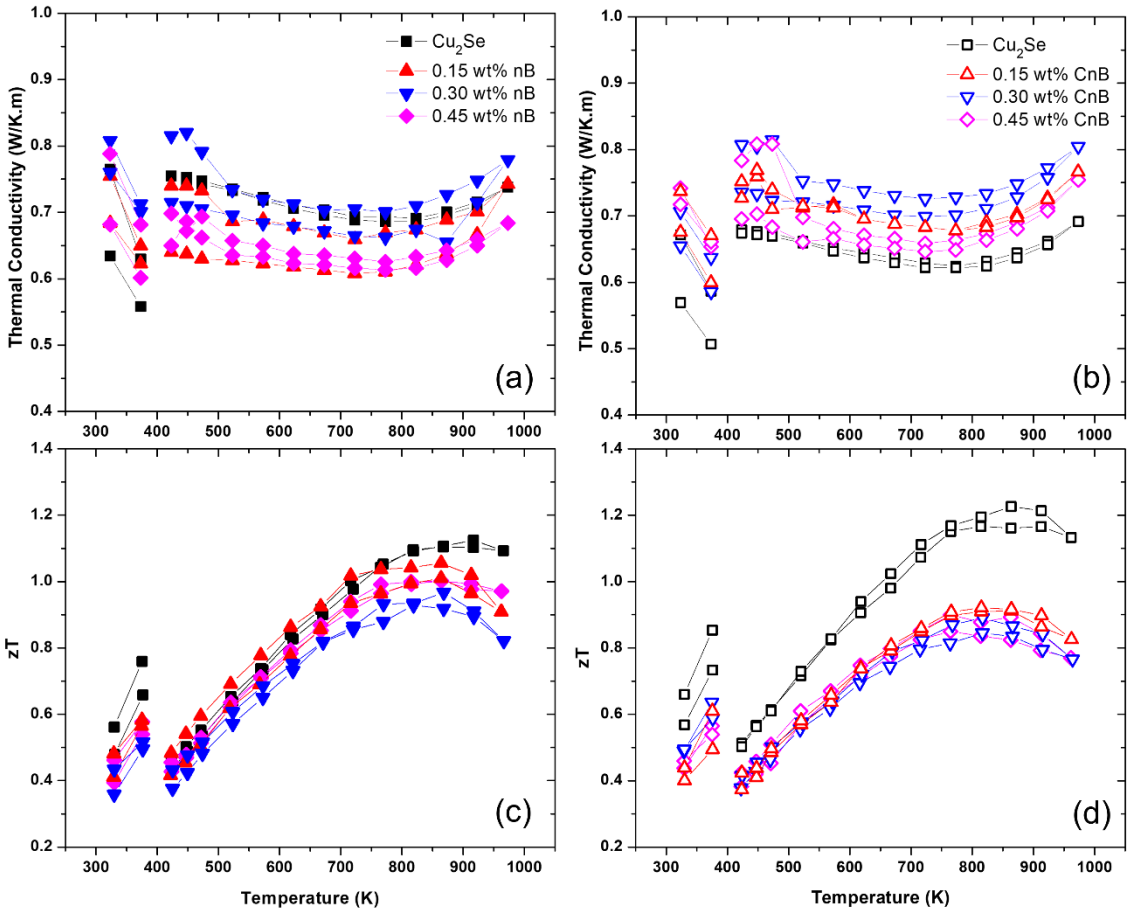

Figure C 5 Thermoelectric properties of the low-temperature and high-temperature phases in pristine, nano-B and C-coated nano-B incorporated Cu_2Se samples. Temperature dependences of total thermal conductivity (a and b) and *zT* (c and d) with cooling data.

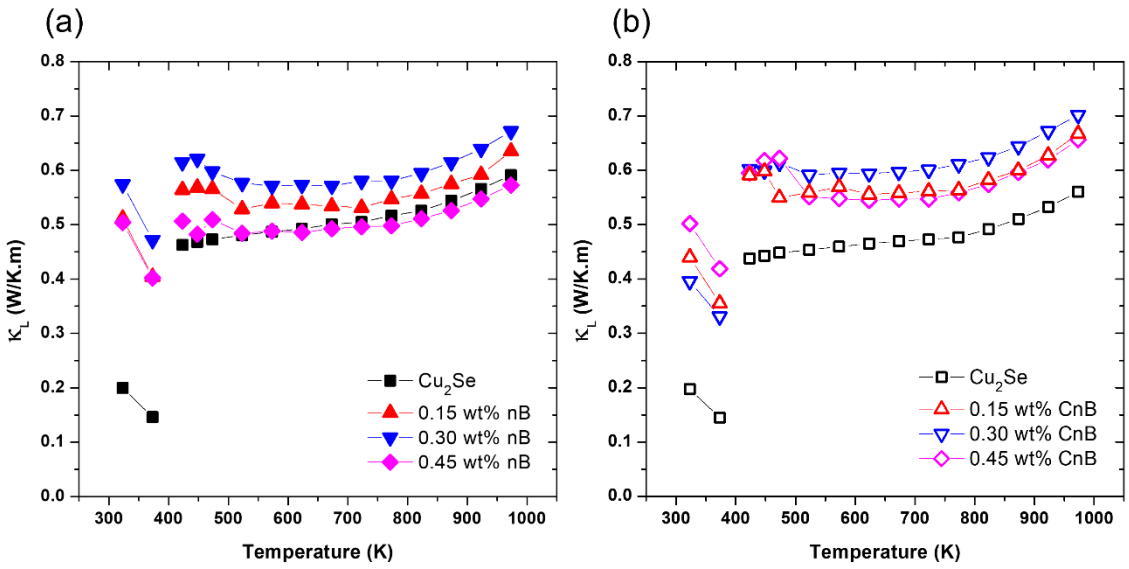

Figure C 6 Temperature dependence of the lattice thermal conductivity of incorporated Cu_2Se samples.

Appendix D

Li_3Sb

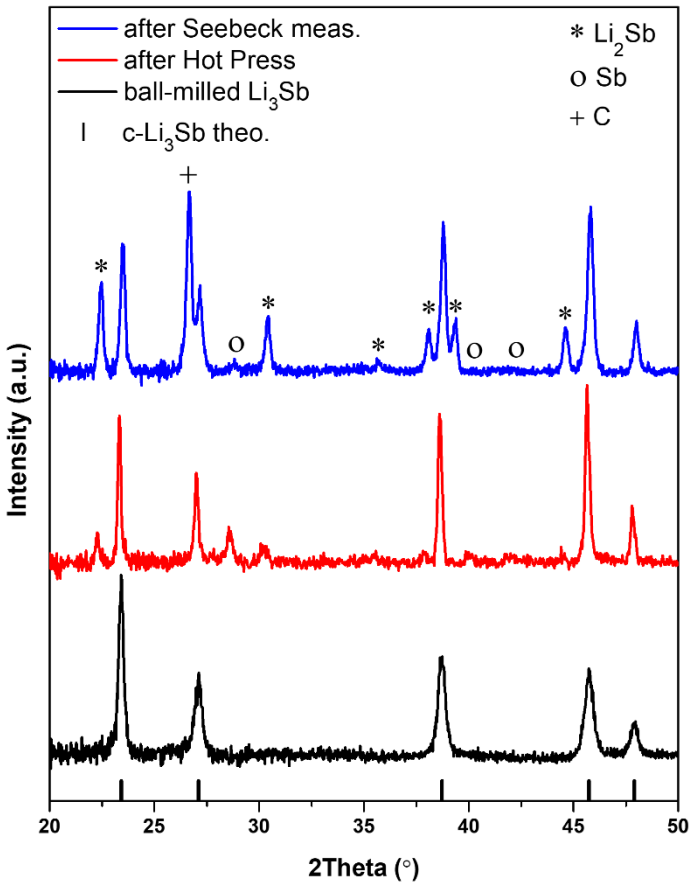

Figure D 1 Experimental XRD patterns (Cu Kα) of as synthesized powder (black) and hot pressed (red) Li_3Sb samples along with the data after Seebeck measurement (blue). Ticks mark the calculated reflection positions of the c-Li_3Sb.

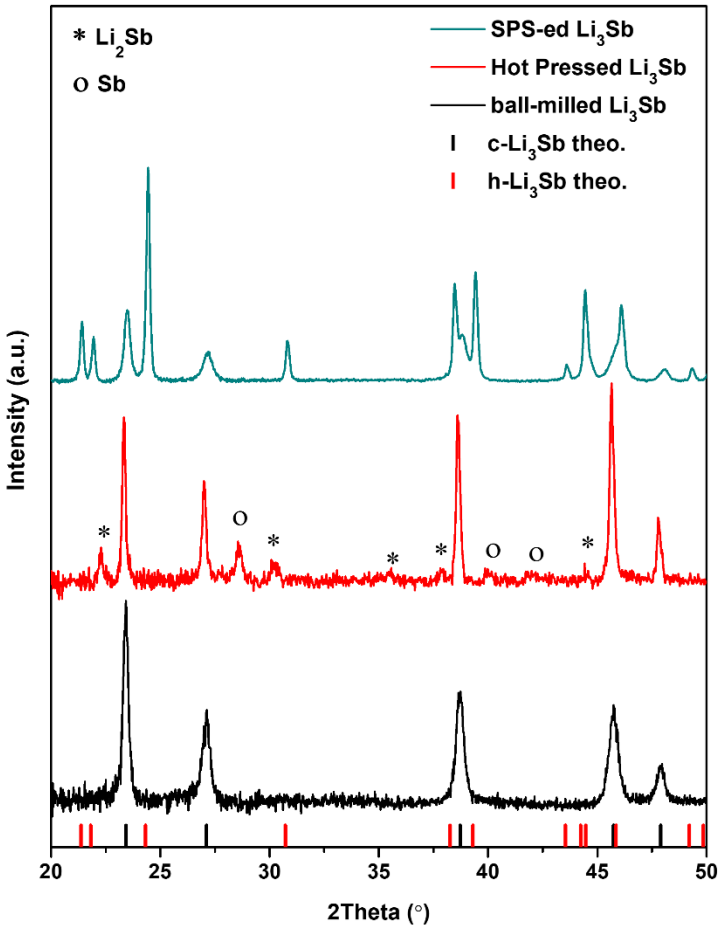

Figure D 2 Experimental XRD patterns (Cu Kα) of as synthesized powder (black), hot pressed (red), and SPS-ed (green) Li_3Sb samples. Black and red ticks mark the calculated reflection positions of the c-Li_3Sb and h-Li_3Sb, respectively.

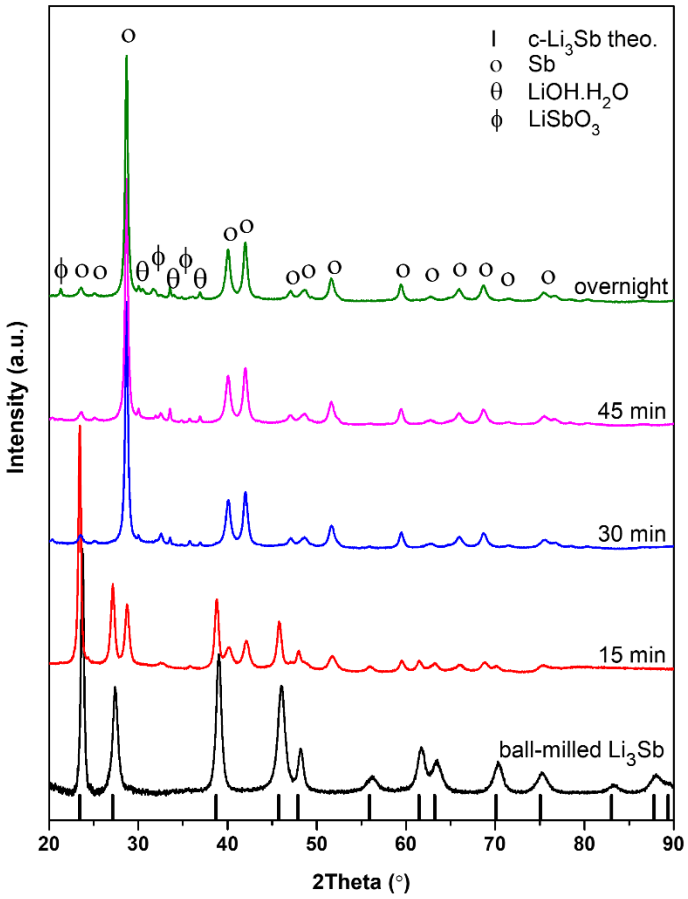

Figure D 3 Experimental XRD patterns (Cu Kα) of as synthesized powder (with Kapton foil) and air exposed Li_3Sb samples. Each scan corresponds to about 15 minutes of exposure (red, blue, and pink) and an overnight exposure (green). Ticks mark the calculated reflection positions of the c-Li_3Sb.

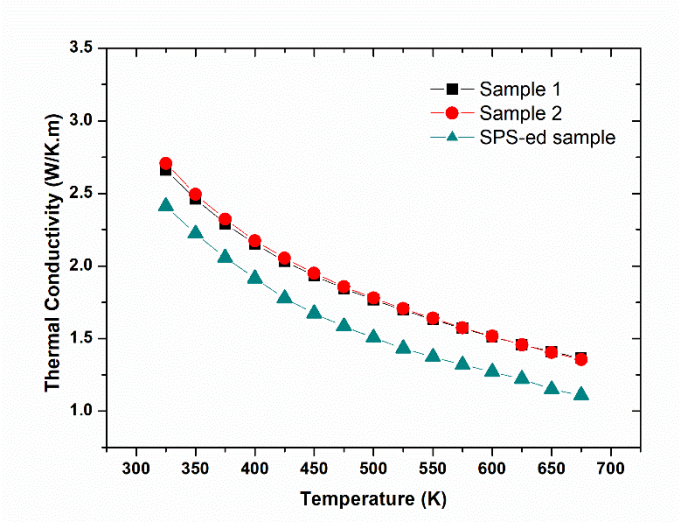

Figure D 4 Temperature dependence of the total thermal conductivity of hot pressed (sample 1 and sample 2) and SPS treated (green) Li_3Sb samples.